Department Biologie II
Anthropologie und Humangenetik
Ludwig-Maximilians-Universität München

Manipulation of global chromatin architecture in the human cell nucleus and critical assessment of current model views

Heiner Albiez

Dissertation der Fakultät für Biologie der Ludwig-Maximilians-Universität München
Eingereicht am 5. April 2007

Manipulation of global chromatin architecture in the human cell nucleus and critical assessment of current model views

Dissertation der Fakultät für Biologie
der Ludwig Maximilians Universität München (LMU)
vorgelegt von
Dipl. Biol. Heiner Albiez
aus Bonn
Gutachter:
1. Prof. Dr. Thomas Cremer
2. Prof. Dr. Peter Becker
Tag der mündlichen Prüfung: 25. September 2007

1 CONTENTS

2 SUMMARY

In spite of strong evidence that the mammalian cell nucleus is a highly organized organelle, a consensus on basic principles of global nuclear architecture has not so far been achieved. The existence of major architectural features such as an organized interchromatin compartment and higher order organization of chromatin postulated by some of the models is questioned or even refused by the others. This study was set up to test predictions of the various model views after manipulating nuclear architecture by applying the induced formation of hypercondensed chromatin (HCC). This method leads to massive but completely reversible conformational changes of chromatin arrangements in living cell nuclei, but does not affect the cells survivability.

Nuclear functions like transcription, replication and cell cycling were immediately stalled when HCC formation was induced, but were rapidly recovered upon recovery of normal chromatin configurations. The emerging pattern of HCC revealed a 3D network of interconnected chromosome territories. The surface of the emerging HCC bundles was the site of preceding activity like RNA transcription or DNA replication, which confirmed the existence of a distinct topological arrangement of functional processes with respect to the architecture of chromatin. This arrangement could further be demonstrated by analyzing the topography of defined chromatin modifications, showing that active chromatin is preferentially located at the HCC bundle surfaces, whereas inactive chromatin regions are preferentially found in the HCC bundle interior. The emerging patterns of HCC were further strikingly similar in consecutively repeated cycles of HCC formation and recovery, demonstrating a non-random but pre-existing and defined chromatin and interchromatin topography. All results of this study were obtained using confocal laser scanning microscopy. A protocol for deconvolution of confocal images was established to enhance confocal image quality to an extent sufficient for subsequent image analysis.

In contribution to the present model views this study demonstrates: [1] That most chromatin exists in the form of higher-order sub-compartments ('~1 Mb chromatin domains') above the level of extended 30 nm fibers and [2] That an interchromatin compartment exists as a dynamic, structurally distinct nuclear compartment, which is functionally linked with the chromatin compartment.

An updated chromosome territory-interchromatin compartment model on the basis of the gained results is presented at the end of this thesis together with an attempt to provide a comprehensive view linking ultrastructural with light microscopic insights.

3 PREFACE

It has been a long history ever since man started to satisfy the curiosity for knowledge on the functionality of the world. Particularly the functionality of life fascinated generations of scientists. In the course of the last century man managed to discover, understand and even manipulate the molecular basis which encodes the construction plan of all living beings: the deoxyribonucleic acid (DNA). Up to now, we gained an overwhelming knowledge about how the code works how it is translated and finally used to build molecular machines. We discovered complex interactions of these molecular machines, ensuring the functionality of cells, the basic unit of all living beings. Only a correct functionality of cells grants the proper functionality of organs and whole organisms.

Accompanying the success in discovering these basic principles, natural sciences gained a nimbus of being able to become omniscient. The great majority of western society people nowadays consider scientific results as unbeatable facts. This attitude is accompanied by the hope and desire that science and especially the field of molecular genetics will soon be able to provide key insights in the cure of cancer and in the cure of many other major present-day diseases.

Scientists themselves, however, know about the complexity of results, about the interpretability of statistics and about the problems faced when performing experiments. Studies designed to address an interesting question do provide a single answer only in the best but rare cases. In most of the cases a bunch of new questions is raised and formerly unknown enigmas given by nature are revealed. Quite contrary to the public belief, it arises that the more we discover in absolute terms, the less we know in relative terms, or to exaggerate it with Mark Twain: *The researches of many commentators have already thrown much darkness on this subject, and it is probable that, if they continue, we shall soon know nothing at all about it*. This statement held e.g. true for the deciphering of the entire human genome: This very remarkable success was much less providing a final answer in the field of human genetics, but opened to a much greater extent a new avenue for scientists to address countless questions, which nobody could think of before. One example is the research on the flow of information from a gene-coding DNA sequence to its messenger molecule which exports the information out of the cell nucleus. After the first linear protein-protein interactions were demonstrated at that molecular level (e.g. transcription factors and corresponding DNA binding motives), it became clear that many such linear interactions could locally build up highly complex interaction networks (e.g. the orchestrated interplay of many factors and sequences in cis and trans). The demonstration of the existence of complex interaction networks was followed by the claim that additionally the large-scale environment, in which all these reactions take place, has to be considered (e.g. the higher order compartments of a

cell nucleus). Step by step, the simple views of molecular interactions had to be modified and evolved to more and more complex views and theories. Nowadays, molecules involved in transcription have to be considered as components of larger machines acting in crowded environments and being implemented in processes taking place in a highly organized 3D nuclear space.

From different fields of research it is a long known fact that the organization of a 3D space, so to say its architecture has a huge impact on the functionality of its components. It was Louis Henry Sullivan (1856-1924), the famous American architect who manifested the phrase '*form follows function*' (Sullivan, 1896). From his point of view, function was defined first and the form was its consequence or at least based on function. In terms of architecture this argument was naturally pointing to the trade-off between function and design. Nevertheless, reversing the phrase, the existence of functional processes can be deduced by analyzing the form in which they occur like in the fictional statement: '*since there is an elevator, it is likely that there is traffic from the first to other floors* '. Applying this conception to biological objects can help to deduce functional processes from the investigation on the body within they are located. For example, the common wolf (*Canis lupus,* mammals, Europe) and its extinguished counter-part the tasmanian wolf (*Thylacinus cynocephalus,* marsupials, Australia) do not exhibit a very similar appearance (form) just by chance, but analyzing their anatomy allowed to deduce that similar life strategies (function) were adopted by both to survive in the same ecological niche.

The biological object of interest of this thesis is the cell nucleus, which serves as the 'form', where various functional processes take place. The nucleus is the cellular organelle harboring the genetic material, which has to be maintained, transmitted and read-off. Its higher order architecture, in scales much beyond the naked DNA molecule, has become a topic of interest since it seems to have a great impact on proper functioning of the nucleus. The most prominent nuclear module is the DNA and the chromatin formed out of it by the tight association of the DNA molecule with histone proteins. Of at least similar importance are the non chromatin nuclear components, the proteins, ions and fluids roaming the nuclear volume and contributing to its higher order architecture.

This study was performed with the aim to reveal further architectural features of the living cell nucleus to be able to further develop existing model views on nuclear architecture. As a matter of course, the presented results do not accomplish the endeavors of nuclear exploration, but open new avenues for future research.

4 INTRODUCTION

4.1 Chromatin architecture

Nuclear architecture is a system, which can be surveyed at different hierarchical levels. This introduction starts from a global view on chromatin organization with its compartmentalization in chromosome territories and their topology. The subjacent structural level of sub-chromosomal domains is overviewed thereafter before descending to the level of epigenetics and finally viewing the organization of the naked DNA molecule.

4.1.1 Chromosome territories

The whole human genome consists of 23 chromosomes with two copies (homologues) in every cell, one transmitted of each parent. The term chromosome, which refers to 'stainable body', was introduced originally for the distinct appearance of chromosomes in their highly condensed state during mitosis (X-shaped bodies). However, when cell cycle proceeds, the formation of the nucleus is accompanied by a decondensation of chromosomes leading to their 'disappearance' as separate entities since they become indistinguishable at the light- as well as at the electron-microscopy level (Wischnitzer, 1973). Since the extent of decondensation was and still is unknown, and since the DNA molecule is a long helical fiber, it was postulated that chromosomes were indistinguishable due to an extent of decondensation that results in an intermingling of decondensed fibers like spaghetti on a plate. Indeed, this kind of view was still the text books opinion some years ago (Alberts, 2002; Wolfe, 1993). However, in the 1980ths Thomas Cremer and colleagues managed to demonstrate that single interphase chromosomes are confined to discrete 3D volumes, the 'chromosome territories' (CT) a term which Theodor Boveri introduced already in the beginning of the 20th century for the interphase state of chromosomes (Cremer et al., 1980; Cremer et al., 1982; Cremer and Cremer, 2006a). While Cremer and colleagues obtained their results by indirect evidences, the development of In-Situ-Hybridization (ISH) allowed the direct visualization of single chromosomes by hybridizing labeled complementary DNA probes, specific for each chromosome, to the target nuclear DNA in-situ (e.g in (Manuelidis, 1985; Schardin et al., 1985). Today, Fluorescent-in-situ-Hybridization (FISH) allows the direct visualization of CTs in intact nuclei, distinguishable by fluorochromes with different spectral signatures (Cremer and Cremer, 2006b). Recently, Bolzer et al. managed to simultaneously visualize all 23 CT pairs by applying a combinatorial labeling scheme overbearing the still limited number of available fluorochromes (Bolzer et al., 2005). All chromosomes occupy largely separated territories with only little or even no overlap (Albiez et al., 2006; Bolzer et al., 2005; Cremer and Cremer, 2001).

The mechanism ensuring the territorial arrangement of chromosomes is not well understood, leading to the formulation of various hypothesis and model views (see 4.3). The question on the benefit of a territorial organization of interphase chromosomes becomes obvious, when considering the integrity of a chromosome as being highly important to keep the number and composition of chromosomes constant. The loss of a chromosome or parts of it over the cell cycle or a higher frequency of chromosomal rearrangements, which would have to be expected if thin DNA fibers were widely intermingling, would highly increase the risk of lethal consequences and would concomitantly not be favored over evolution. Nevertheless the view of chromosome territories as distinct structural units was recently challenged, and a less distinct configuration with a considerable overlap between chromosomes in interphase was postulated (Branco and Pombo, 2006; Chubb and Bickmore, 2003). These new views will be introduced later in this introduction when reviewing the present model views on nuclear architecture (see 4.3.5).

4.1.2 Topology of chromosome territories

Many studies on the localization of CTs in the cell nucleus have been performed and demonstrated a non-random pattern of CT arrangement in regard to the relative radial position in the nucleus (for reviews see Cremer and Cremer, 2001; Foster and Bridger, 2005). CTs mapped according to their size (in megabases, Mb, Cremer et al., 2001; Sun et al., 2000) or their gene density (genes per Mb, Boyle et al., 2001) displayed a non-random distribution with small and/or gene-dense CTs located more towards the nuclear interior. While the gene-density and size related distribution pattern have both been shown for spherical nuclei and rather spherical nuclei (e.g. human lymphocytes), the topology was not so clear in flat ellipsoidal nuclei (e.g. human fibroblasts), where rather a size related difference was found (Bolzer et al., 2005).

The mechanism establishing this radial pattern of CT localization has not so far been revealed. Chromatin can bind to the nuclear lamina, the protein layer at the nuclear membrane which stabilizes the nucleus (Gruenbaum et al., 2005). This lamina disassembles in prophase and is re-established at the beginning of telophase. If only chromatin regions with gene poor material, e.g. heterochromatic regions, got bound to the lamina, gene-poor material and concomitantly the corresponding chromosomes would get pilled to the nuclear periphery when the nucleus forms, leaving the gene-dense material and corresponding CTs in the nuclear interior (Bolzer et al., 2005). In accordance with this hypothesis, most chromatin binding partners involved in the lamina attachment preferentially bind gene-poor heterochromatic sequences (Bolzer et al., 2005; Hutchison, 2002). This scenario could also account for the failure of detecting a radial arrangement in flat nuclei since the formation of these nuclei is not accompanied by a significant volume enlargement. Chromosomal material

of gene-poor CTs could be in close spatial proximity to the nuclear lamina, wherever it is localized since every position in a flat body is close to the surface in absolute terms.

In addition, also chromosome arrangements during mitosis have to be considered (Bolzer et al., 2005; Habermann et al., 2001). During mitosis, chromosomes get attached to the spindle apparatus and form a rosette like ring. Here, small chromosomes tend to locate more in the interior of the rosette just by geometrical constrains, whereas large chromosomes need to expand more to the periphery. Whether or not this arrangement is transmitted to the daughter nuclei may then depend on the final shape of the nucleus (Bolzer et al., 2005; Habermann et al., 2001).

The gene-density related pattern of CT arrangement was conserved over a evolution period of more than 300 million years, since it was found in nuclei of mammals (primates and mice, Mayer et al., 2005; Tanabe et al., 2002a; Tanabe et al., 2005) as well as of chicken (Habermann et al., 2001). This evolutionary conservation argues strongly for a significant benefit of such a probabilistic gene-density related arrangement (Parada et al., 2002). The most prominent postulation claiming such a benefit is the '*bodyguard hypothesis*' (Gazave et al., 2005; Hsu, 1975). It postulates that the storage of important gene dense chromatin material in the nuclear interior is protective since it prevents damaging impact originating from exterior. Harming agents would be absorbed by the tightly packed gene poor material at the periphery. Damage in the sense of the bodyguard hypothesis could be free radicals (e.g. deriving from the respiration in mitochondria, which are packed around the nucleus) or by any other DNA damaging agent like chemicals or radiation. However, a study counting the damage after nuclear exposure to UV-radiation (Gazave et al., 2005) could neither reveal any significant difference in damage susceptibility between gene-dense or gene-poor material nor between peripheral or centrally located chromatin. Alternative hypothesis consider the densely packed gene-poor chromatin material at the periphery as a buffer for shifts in tonicity (Vinogradov, 1998; Vinogradov, 2005) or a buffer of external mechanical forces (Caille et al., 2002; Gladilin et al., 2006; Maniotis et al., 1997b), but both still need to be experimentally tested.

An assumption that the CT gene-density alone would determine its nuclear position is a too simplistic view (Meaburn et al., 2007). This would not account for the results that different tissues or cell differentiation states of the same species or cells in different cell cycle stages can significantly differ in their radial CT distribution (Bridger et al., 2000; Kuroda et al., 2004; Stadler et al., 2004). Accordingly, additional differences in expression profiles may have considerable impact. This suggests that the position of a CT in addition to its gene density is strongly affected by the functional status of its genes (Meaburn et al., 2007).

4.1.3 Neighborhoods of chromosome territories

Since a non-random radial organization exists, the question arises, whether certain CTs are more frequently neighboring than others. An increased frequency of certain neighborhoods has already to be expected from the probabilistic preference in radial CT positioning: CTs preferentially locating in the nuclear interior will necessarily more often meet CTs with the same tendency and vice versa.

FISH painting of CTs in different tissues of the mouse confirmed this expectation since distinct types of spatial CT clusters were more often neighboring than would be expected by chance (Parada et al., 2004; Parada et al., 2002). Depending on the cell type or tissue investigated, different pairs of CTs displayed the increased frequency of neighborhood. These findings correlated with the measured translocation frequencies of the corresponding CTs in the respective cell lines or tissues, stressing the functional impact of CT localization (Misteli, 2004; Parada et al., 2004).

Notwithstanding the importance of preferred positioning, a deterministic view on CT neighborhoods, as earlier suggested (Nagele et al., 1995; Nagele et al., 1998), is not supported by this data. A deterministic view on CT positioning and neighborhoods would necessarily implicate a high similar arrangement of all CTs in different cells, which is not the case (Gerlich et al., 2003; Walter et al., 2003; Williams and Fisher, 2003). In human fibroblasts, where all CTs were labeled simultaneously and the distances and angles between pairs were measured and compared with random distribution, no significant evidence for deterministic CT arrangements/neighborhoods was found (Bolzer et al., 2005).

Living cell observations of labeled CTs demonstrated a similarity of chromatin positioning only between daughter cells (Gerlich et al., 2003; Walter et al., 2003). This similarity, however, was already lost after a second cell division. In conclusion, the reported CT clusters seem not to be a consequence of a preferred neighborhood but are rather caused indirectly by a radial preference of CT positioning according to gene-density (Bolzer et al., 2005; Williams and Fisher, 2003).

4.1.4 Topology of sub-chromosomal domains

Chromosome arms, centromeres and telomeres

CTs can further be classified in sub-chromosomal domains like chromosome arms, centromeres or telomeres. It has been demonstrated that not only CTs as a whole, but also sub-domains like the chromosome arms occupy discrete areas in the nuclear volume (Dietzel et al., 1998). Centromeres and Telomeres, whose main functional role is to maintain the chromosome integrity, do also locate in distinct sub-volumes shown in various FISH experiments with specific probes (Molenaar et al., 2003; Weierich et al., 2003). Telomeres act as protective caps at both ends of the linear DNA molecules and ensure due to their

repetitive sequence a complete duplication of each chromosome during S-phase (Alberts, 2002). The major function of centromeres is to provide a binding platform for the kinetochore complex, the attachment site for microtubules, separating chromatids during mitosis. Due to the attachment of microtubules to the kinetochore and the subsequent pulling forces, centromeres and telomeres end up on different poles of late anaphase rosettes (centromeres ahead, telomeres behind, see Solovei et al., 2004b). The 'fallen rosettes' scenario (Habermann et al., 2001; Solovei et al., 2004b), assumes that no major chromatin rearrangements occur thereafter, but each rosette just 'falls' on one of its flat sides. This event would lead to a polar orientation of centromeres and telomeres termed 'Rabl configuration' after Carl Rabl who was the first to postulate such an orientation of CTs in interphase nuclei based on observations on mitotic cells of *Salamandra maculata* and *Proteus* (Cremer and Cremer, 2006a; Rabl, 1885). This Rabl configuration was indeed demonstrated for a variety of plant cells and some mammalian cells (Abranches et al., 1998; van Driel and Fransz, 2004). However, a clear nuclear polarity between centromeres and telomeres is not a general phenomenon (Vourc'h et al., 1993) implying that chromatin movements after the end of mitosis cause changes in chromatin configurations (Solovei et al., 2004b; Weierich et al., 2003). Still, centromeres preferentially keep their peripheral localization, but are not necessarily found on only one pole or side of the nucleus. This peripheral positioning, however, has mainly been demonstrated for cells in G0, whereas cycling cells can also display a more internal localization (Solovei et al., 2004b; Weierich et al., 2003). Centromeres further tend to cluster, which is very prominent phenomenon in murine cells ('chromocenters') but was demonstrated for human cell nuclei as well (Weierich et al., 2003). Such a cluster formation was also reported for telomeres (Nagele et al., 2001; Weierich et al., 2003) with peripheral positions in murine but internal positions in human cells (Weierich et al., 2003).

~1 Mb chromatin domains

When treating living cells during S-phase with labeled nucleotides, these get incorporated in the growing DNA duplicate. However, replication is not processed evenly over the entire nuclear volume, but is organized in individual replication foci with DNA contents from a few hundred kb to several Mb (Berezney et al., 2000; Jackson and Pombo, 1998; Koberna et al., 2005). It was found that replication foci once duplicated and labeled during S-phase, can be detected as persistent chromatin units at any subsequent cell cycle stage (for review see Berezney et al., 2000). According to their estimated DNA content (ranging from several 100 kb up to some Mb), these foci were called '~1 Mb chromatin domains' (Ma et al., 1998; Nakamura et al., 1986). The internal structure of a replication focus or ~1 Mb chromatin domain is unknown leading to postulations of different model views described later in this

introduction (see 4.3). Despite the accepted evidence on the persistence of the labeled foci, not all of present models on nuclear architecture consider ~1 Mb chromatin domains as considerable architectural components. This may partly be due to the lack of detection of a focal substructure in electron microscopy sections, when chromatin as a whole is contrasted. Nevertheless, although there is also no such evidence for the existence of CTs at the EM level (Wischnitzer, 1973), the concept of a territorial chromosome organization in interphase is widely accepted amongst electron microscopy scientist. The reason for not being detectable may be the same as for the CTs. Possibly ~1 Mb chromatin domains are not strictly separated from each other but in close spatial association (Visser et al., 2000) leaving no gap of non-chromatin areas obligate to separate them just by chromatin staining.

Recently, the existence of replication foci was demonstrated in HeLa cell nuclei in an electron microscopy study (Koberna et al., 2005). Preceding incorporation of marked nucleotides was followed by their immunodetection with specific primary and gold-coupled secondary antibodies. Accordingly, accumulations of gold grains marked sites of pre-ceding replication (nucleotide incorporation). The underlying chromatin contrast displayed, as expected, no clear separation between adjacent foci. The size of the immuno-detected foci was measured to be ~100 nm. Replication domains appearing larger at the light microscopy level were demonstrated to be composed of several such ~100 nm foci (Koberna et al., 2005).

Replication pattern

Replication foci are not evenly distributed throughout the nuclear volume, but appear in globally separated patterns correlating with the respective time point of replication (Ferreira et al., 1997; O'Keefe et al., 1992; Sadoni et al., 2004; Sadoni et al., 1999). Early replicated chromatin locates more internally, whereas mid to late replicating chromatin locates in close association to the nuclear periphery and peri-nucleolar. The very late replicating chromatin, found in the entire nucleus, can be distinguished from the other replication patterns at the light microscopy level by its much more bulky appearance with viewer loci, which are, according to EM, built up by closely associated smaller foci (Koberna et al., 2005, see above). These roughly classified and seamless three patterns of chromatin distribution with respect to replication timing are highly conserved through evolutionary history since they have been demonstrated in nuclei of mammals (primates, mice, Mayer et al., 2005; Tanabe et al., 2002b), birds (chicken, Habermann et al., 2001), cnidaria (hydra, Alexandrova et al., 2003) and ciliates (Postberg et al., 2005) which are species spanning an evolution period of >500 million years.

The three types of replication patterns are further characterized by their gene content. Gene dense chromatin regions replicate during early stages of S-phase, whereas the more

gene-poor and inactive chromatin replicates in mid to late stages of S-phase (Federico et al., 1998; Goren and Cedar, 2003; Sadoni et al., 1999). Since the described radial arrangements of the replication patterns reflect the findings for the gene-density related radial positioning of whole chromosomes (see 4.1.2) it seems likely that this organization is triggered by the same mechanism. Probably this mechanism applies at the local level of chromatin domains and radial CT arrangements are only the global consequence. Murmann et al. plotted chromatin regions with a similar size of 2 Mb but a different gene density in regard to their radial arrangement in the nucleus. The obtained distributions delivered a much better correlation between the region's gene density and their radial position than was earlier obtained for entire CT plots. The driving force organizing the gene-density related arrangements may therefore act at the local level of some ~1 Mb chromatin domains (Kupper et al., 2007; Murmann et al., 2005). However, in addition to gene-density, the transcriptional activity of a domain could have an additional impact on its localization.

Protrusion of highly expressed gene clusters

It was demonstrated for several sub-chromosomal regions that they can locate remote from their respective CT. The first region which was reported to frequently protrude from its CT was the MHC locus on HSA 6p21.3 (Musoski, 2005; Volpi et al., 2000) after interferon-γ activation. These protrusions were measured to end in distances up to ~1.5 µm from the respective CTs surface delineated by a HSA 6 paint probe (Volpi et al., 2000). The fact that these regions were not depicted by the chromosome paint itself is presently not understood but depends most probably on the quality of the paint (complexity), the general efficiency of hybridization and the competition of the respective locus probe and the corresponding CT paint probe for the same nuclear target. A similar pattern of arrangement was found for a sub-telomeric region on HSA 11p15.5 (Albiez et al., 2006; Dittrich, 2006; Kupper et al., 2007; Mahy et al., 2002a). A high frequency of protrusion was found for this locus, which could be lowered if transcriptional activity was inhibited by 5,6-Dichlorobenzimidazole riboside (DRB) or actinomycin treatment (Chubb and Bickmore, 2003; Mahy et al., 2002a). The extensions of this out-looped region are comparable to data found for the MHC-locus and reached maximal distances of ~1.5 µm as well.

For both, the MHC as well as the HSA 11p15.5 regions, the frequency of extended protrusions was correlating with the activity state of that particular region. Protrusion of specific loci were additionally demonstrated for: [1] the epidermal differentiation complex (EDC, Williams et al., 2002) on 1q21, when comparing differentiated keratinocytes (active EDC-locus) with lymphoblasts (inactive EDC locus), [2] the β-globin-locus on 11p15.4 in interleukin-3 stimulated versus non-stimulated leukemia cells (Galiova et al., 2004) and the Hox-b and Hox-d locus (MMU 11 resp. 2) in differentiated or non-differentiated cells

(Chambeyron et al., 2005; Morey et al., 2007). Common for all these regions is that they represent large clusters of active genes. The MHC locus for example comprises >3 Mb of coding sequences and the gene dense 11p15.5 region was classified as a '**r**egion of **i**ncrease**d** **g**ene **e**xpression' ('RIDGE', Caron et al., 2001; Versteeg et al., 2003). Whether the protruding occurs before or after transcriptional activation is not yet clear, but it has been demonstrated for the β -globin locus that transcription was detected before any protrusion was obvious. Increased transcription was measured with larger extensions of the locus (Ragoczy et al., 2006; Ragoczy et al., 2003).

Whether the extended 'out-looping' or protruding of loci should be considered as a common phenomenon of active and/or gene-rich chromatin sites (Chubb and Bickmore, 2003; Mahy et al., 2002a), or whether it is a rare event (Kupper et al., 2007) detectable only for huge clusters of activated genes has still to be addressed.

4.1.5 Chromatin mobility

The observation of extensive protrusions of highly expressed gene clusters suggests a high mobility of chromatin domains over the cell cycle. What in fact is the degree of freedom for chromatin domain movements and when does 'out-looping' take place?

Marshall et al. found that there is indeed significant diffusive motion of chromatin domains in interphase nuclei (Marshall et al., 1997). However, this diffusion was constrained within only a limited sub-region of the nucleus. They tagged *lac* operator sites inserted in the yeast genome by the expression of Lac-repressor-GFP fusion constructs. According to their measurements, chromatin diffusion was confined to scales less than 0.3 µm. This finding is consistent with FRAP studies on HeLa and Swiss 3T3 cell nuclei labeled by dihydroethidium, a membrane-permeable derivative of ethidium bromide (Abney et al., 1997). No significant recovery of bleached spots with diameters of ~0.4 µm was measured and the bleached spots persisted for more than 1 h. These results allowed to conclude that chromatin domains, or more precisely the loci investigated, were largely immobile over distance scales ≥ 0.4 µm. Studies on interphase chromatin mobility beyond the sub-chromosomal level (>1 µm scale) further suggested an immobility of global chromatin over large parts of the cell cycle from late G1- until the end of G2-phase (Walter et al., 2003). Monitoring the intensity gravity center of labeled CTs in living HeLa cell nuclei revealed significant movements only in the early G1-phase (Walter et al., 2003). This result is in accordance with further mobility studies on yeast chromatin (Heun et al., 2001), which reported movements of >0.5 µm in 10 s in G1-phase delineated by the *lac* operator / Lac repressor-GFP system as described above and with another study monitoring tagged telomere dynamics in living U2OS cells, which reported constrained movements within a region with a diameter of 0.5 µm (Molenaar et al., 2003). Major changes of e.g. CT neighborhoods and large scale protrusions would accordingly have

to be established during mitosis or early G1. This assumption is supported by H2B-GFP bleaching experiments in living HeLa cells monitored from late G2 to early G1 (Gerlich et al., 2003; Walter et al., 2003). Bleached respectively unbleached chromatin regions adopted patterns with a certain pattern of symmetry in the daughter nuclei, dissimilar from the mother nucleus, which demonstrated changed global chromatin arrangements from one generation to the next established over mitosis (Gerlich et al., 2003; Walter et al., 2003).

In a recent study, however, migration of a small tagged chromosome site (lac O/lac r-GFP) from the nuclear periphery to the interior upon targeting a transcriptional activator to this site demonstrated inducible repositioning over distances of up to 5 µm over 1-2 h during interphase (Chuang et al., 2006). It will have to be proven, if these observations will be confirmed for non-genetically engineered loci as well. Nevertheless, this study stresses the fact that besides the widely accepted view on global chromatin immobility, the dynamic properties of sub-chromosomal domains are a still poorly understood subject of nuclear architecture (Lanctot et al., 2007).

4.1.6 Epigenetics

Before descending to the level of the sheer DNA sequence, the level of epigenetics, which comprises genetically inheritable features, which are not part of the DNA sequence itself, has to be viewed, since this topic has become one of the main directions of molecular biology research over the last ten years. Modifications on the epigenetic level have been linked with human diseases (Okada et al., 2005; Seligson et al., 2005; Varambally et al., 2002) and were demonstrated to have a significant impact on nuclear functions like replication or transcription and affect chromatin architecture (for reviews see Craig, 2005; Fuchs et al., 2006; Martin and Zhang, 2005; Peters et al., 2003). The epigenetic level comprises modifications of DNA and modifications on DNA associated proteins.

DNA is never found in its naked form *in-vivo* but is always wrapped around nucleosomes (for review see Olins and Olins, 2003). These are protein complexes generally composed of the four histone variants H2A, H2B, H3 and H4. Each histone harbors an N-terminal aminoacid tail protruded from the histone core. The amino acids of these protruded histone tails can carry a variety of biochemical modifications like e.g. methylation, acetylation or ubiquitinylation (Fuchs et al., 2006). These modifications have the potential to trigger the activity state of the wrapped DNA, for example by acting as landing platforms for chromatin remodeling factors. The found complexity of possible combinations of the epigenetic marks and the respective impact on functions led to the proposal of the term 'histone code”, stressing the important role of this epigenetic level juxtaposed to the genetic code (Jenuwein and Allis, 2001).

Besides the high impact on functions at the molecular level, histone modifications are spatially organized in a higher order in the nucleus (Cremer et al., 2004a; Fuchs et al., 2006; Zinner et al., 2006). Zinner et al., 2006 demonstrated that functionally classified histone modifications locate in distinct compartments on the global level of nuclear architecture. A well described epigenetic marker for active chromatin (Bernstein et al., 2005; Santos-Rosa et al., 2002), trimethylated lysine 4 at the histone tail of histone H3 (3meH3K4) displayed a strikingly similar arrangement compared to early replicating chromatin (Fuchs et al., 2006; Zinner et al., 2006), namely an exclusive localization in the nuclear interior but not at the periphery. The nuclear periphery as well as perinucleolar regions, on the other hand, were shown to be covered by chromatin delineated by trimethylated lysine 27 on histone H3 (3meH3K27). This modification had been classified as a marker for facultative inactive chromatin and e.g. decorates the inactivated X-chromosome in female cell nuclei (Chadwick and Willard, 2004; Rougeulle et al., 2004). The global nuclear arrangement of 3meH3K27 mimics that of mid replicating chromatin so that in addition to the nuclear periphery, 3meH3K27 signals were also detected at perinucleolar sites (Zinner et al., 2006). The best described marker for constitutive inactive chromatin is the trimethylated lysine 9 on histone H3 (3meH3K9). This modification was assigned to the constitutively repressed chromatin regions like e.g. centromeres (Lachner et al., 2003). Its global pattern in the nucleus reflects that of late replicating chromatin i.e. a co-localization with few spots of more compacted chromatin throughout the entire nuclear volume as described for late replicating chromatin (Zinner et al., 2006).

In addition to their high impact on the functioning of molecular nuclear processes and in spite of the high complexity of the histone code, some epigenetic modifications can be used as markers for different activity states of chromatin on the global level of nuclear architecture.

4.1.7 Basic architecture of chromatin fibers

An average human metaphase chromosome has a physical length of ~2 µm and an average DNA content of about 50-250 Mb (e.g. 60 Mb for HSA 6). The physical length of the naked DNA fiber of such a chromosome, however, could theoretically be stretched to a total length of ~20 cm (Alberts, 2002). An average human metaphase chromosome is therefore compacted with a ratio of ~1:10,000 (Alberts, 2002). How is such a higher order compaction achieved? As already stated above, DNA does not exist as the sheer helical molecule *in-vivo* but is always wrapped around nucleosomes (for review see Olins and Olins, 2003). The DNA helix is wrapped around these nucleosomes in 1.65 rounds (~146 base pairs) and a ~30 base pair long DNA segment interconnects adjacent nucleosomes. This configuration results in a 10 nm thick chromatin fiber termed according to its appearance 'beads-on-a-string' configuration. Evidence for the existence of this configuration was

provided by electron microscopy on low ionic-strength chromatin spreads (for review see Olins and Olins, 2003). The compaction ratio reached with the 10 nm chromatin fiber compared to the naked DNA fiber is 1:10. The 'beads-on-a-string' configuration could only be demonstrated applying the harsh treatments on isolated nuclei and is postulated to only rarely exist as such *in-vivo*. More likely, 10 nm chromatin fibers are further compacted by the formation of a solenoid (Adkins et al., 2004). This is a 30 nm thick fiber formed by the helical configuration of the 10 nm nucleosome fiber. Compared with naked DNA, the compaction reached with this configuration is ~1:35. Evidence for the existence of the solenoid was provided by electron microscopy in *in-vitro* preparations of chromatin fibers (Finch and Klug, 1976; Hansen, 2002; Thoma et al., 1979; Woodcock and Dimitrov, 2001).

4.2 Present models on mitotic chromosome architecture

But how is the chromatin fiber in metaphase or interphase organized beyond the level of the 30 nm solenoid to achieve the final compaction of 1:10,000? Several model views addressing that question have been proposed. The postulations range from a looped formation of the 30 nm solenoid forming sub-compartments (Munkel and Langowski, 1998; Sachs et al., 1995), to supercoiling by a hierarchy of helices (Belmont et al., 1987; Sedat and Manuelidis, 1978) or by anchoring of chromatin fibers/loops to an axial fibrous element (Berezney et al., 1995; Maeshima et al., 2005; Marsden and Laemmli, 1979; Wanner and Formanek, 2000).

The present plurality of models points to the actual lack of knowledge considering the architecture of chromatin at this level and stresses the importance of further studies exploring the basics of nuclear organization.

4.2.1 Loop-scaffold model of mitotic chromosome architecture

An organization of mitotic chromosomes in chromatin loops attached to an underlying contiguous scaffold was first suggested by experiments of Ulrich Karl Laemmli and colleagues (Adolphs et al., 1977; Laemmli et al., 1978). Treating isolated metaphase chromosomes with a low salt protein extraction method or by stripping off their histones released a huge halo of expanded chromatin loops and led to the detection of a residual non-histone protein scaffold at the axis of the chromosomes (Earnshaw and Laemmli, 1983; Laemmli et al., 1978; Maeshima et al., 2005; Paulson and Laemmli, 1977). The protein composition building up this scaffold is still unknown, but proposed candidates are condensin and topoisomerase-II-α since they were detected in the center of intact metaphase chromosomes by immunofluorescence (Earnshaw and Heck, 1985; Maeshima and Laemmli, 2003) as well as by transmission electron microscopy (Maeshima et al., 2005). The signals deriving from topoisomerase-II-α immuno-labeling were not distributed homogeneously, but

displayed striations or coils in some regions alternating with rather straight configurations along the axis of a chromosome (Earnshaw and Heck, 1985). According to the **loop-scaffold model** (Saitoh and Laemmli, 1994) this arrangement reflects the fact that different sub-regions of a chromosome are differentially packed in smaller or larger loops. The difference was postulated to be caused by differences in the AT- versus GC-content of the respective genome regions and by a different affinity of these sequences to attach to the underlying scaffold (Saitoh and Laemmli, 1994). The regions mediating the attachment are termed scaffold attachment regions (SARs), which comprise AT-rich chromatin segments. Accordingly, regions enriched in AT-pairings (and correlative enriched in SARs) are more frequently attached and build smaller loops than segments of GC-rich regions. Following this postulation, the observed banding patterns by staining with Giemsa, a DNA dye with a higher affinity to AT-rich sequences, would be caused by a more intense staining of the tightly packed AT-rich loops (G-bands) compared to the larger and less compact GC-rich loops (R-bands, Saitoh and Laemmli, 1994).

4.2.2 Dynamic Matrix Model

Further evidence for the postulation of a scaffold based organization of chromatin in metaphase chromosomes stems from experiments performed by Gerhard Wanner and colleagues (Wanner and Formanek, 2000; Wanner et al., 2005). They investigated the ultra-structure of mitotic chromosomes and interphase chromatin of barley by Scanning Electron Microscopy (SEM). The enhancement of their setup allowed a separate visualization of DNA and proteins in a high resolution microscopy approach (lateral resolution <10 nm) using the back scattered electrons detection in a SEM device (Wanner et al., 2005). They found a predominant chromatin fiber size of 30 nm matching the dimension of the solenoid, with some of these fibers being coiled and forming clusters with diameters of 200-400 nm termed 'chromomeres'. These chromomeres were also detected in mitotic chromosomes (here with diameters of 200-300 nm) again built up by detectable 30 nm fibers. Continuing their approach, Wanner and colleagues found that the chromomeres of mitotic chromosomes were interconnected by 'matrix fibers'. When artificially stretching the chromosomes by a citrate buffer treatment, an exaggerated X-shape of the chromosomes was induced and a much more defined visualization of the chromomeres and 'matrix fibers' was obtained (Wanner and Formanek, 2000). The separated visualization of DNA and proteins demonstrated that chromomeres were enriched in DNA molecules, whereas the interconnecting 'matrix fibers' were predominantly composed of proteins. From the observation that 'matrix fibers' are less frequently found in cross-sections of thin and long chromosomes but frequently in cross-section of short, thick and highly condensed chromosomes, Wanner and Formanek, 2000 deduced their **Dynamic Matrix Model** with two

dominant structural elements: [1] Coiled solenoid fibers (chromomeres), which are attached to [2] protein-rich 'matrix fibers'. The motor of chromatin condensation was postulated to be the movement of the parallel arranged 'matrix fibers', possibly driven by attached linker proteins. During this condensation process, chromomeres with diameters of 200-300 nm would be formed with the support of loop stabilizing proteins. The further progression of the 'matrix fibers' shift parallel to each other, accompanied by the formation of more and more chromomeres would finally lead to the compact appearance of mitotic chromosomes (Wanner and Formanek, 2000; Wanner et al., 2005). Decondensation, the process observed when chromosomes leave mitosis and enter interphase was postulated to be the reverse process (Wanner and Formanek, 2000): 'Matrix fibers' would shift away from each other leading first to a separation of chromomeres and second to either their disintegration or preservation at sites of euchromatin or heterochromatin respectively. Concluding from this model view, the configuration of interphase chromosomes would differ from their mitotic counterparts predominantly in their axial but not transversal extension (Wanner and Formanek, 2000).

4.2.3 Transition from mitotic to interphase chromosomes

In contrast, Uwe Claussen and colleagues (Lemke et al., 2002) demonstrated that interphase chromosomes were mainly thicker but not significantly longer than their mitotic counterparts. They labeled several sub-domains of the HSA 2 and 5 and compared the linear continuity of the labeled domains in mitotic as well as in interphase chromosomes (Lemke et al., 2002; Weise et al., 2002). Both, CTs and corresponding metaphase chromosomes, displayed the same axial succession of labeled domains in their experiments. They drew the conclusion that no significant decondensation or out-looping of DNA fibers takes place, but demonstrated that the continuity in the axial direction of chromosomes is widely conserved. Accordingly, interphase chromosomes would just be 'swollen' versions of their mitotic counterparts. Claussens postulations culminated in the claim that the term 'chromosome territories' should no longer be used but substituted by the term 'interphase chromosomes' (Claussen, 2005). However, the strict linearity found in the depicted FISH experiments by Claussen and colleagues could not be demonstrated for other CTs by FISH experiments on 3D preserved nuclei in subsequent studies (Boutanaev et al., 2005; Kupper et al., 2007). Irregularities in the linear continuity of successively labeled domains in experiments provided by Küpper et al. reached to some extent a complexity making it impossible to identify the original sequence of labels (Kupper et al., 2007). Increasing evidence for the existence of extensive protruding of highly transcribed gene clusters (Albiez et al., 2006; Mahy et al., 2002a; Volpi et al., 2000) additionally adds to the disintegration of chromosome continuity. Incorporating these contrary results suggests the conclusion that chromosome

decondensation and deformation is a gradual process, able to reach varying extents and concomitantly different degrees of chromosome disintegration.

4.3 Present models on interphase chromatin architecture

4.3.1 The 'nuclear matrix'

Following the postulation that metaphase chromosomes are organized in scaffold attached fibers, leaving space for different degrees of disintegration when transforming into an interphase chromosome (Claussen, 2005; Maeshima et al., 2005; Wanner and Formanek, 2000), what is the fate of the postulated scaffold?

With no direct link to the mitotic chromosome scaffold, a postulated interphase counterpart of a structure organizing chromatin was termed the '**nuclear matrix**' (Berezney and Coffey, 1974; Berezney et al., 1995; Fawcett, 1966; Pederson, 1998). This structural element was postulated to essentially contribute to the function and higher order organization of chromatin, similar as the cytoskeleton organizes the cytoplasm. Evidence for the existence of such a nucleo-skeleton was first derived from high-salt extraction and DNase digestion of isolated nuclei pre-treated by extensive crosslinking. This procedure removed 95% of DNA and histones from the nucleus and left over a 3D network of protein fibers roaming the entire nuclear volume (Nickerson, 2001; Nickerson et al., 1997). Analysis of the content of these biochemical 'nuclear matrix' preparations revealed a huge number of proteins involved amongst others in the assembly of nuclear speckles, bodies and functional machineries (Nickerson, 2001). The structural integrity of the 'nuclear matrix' was proposed to be based on intermediate protein filaments (Nickerson, 2001). In support of this claim, lamin proteins were detected in the interior of DNase treated HeLa nuclei (Hozak et al., 1995; Neri et al., 1999). The fact that untreated nuclei do only reveal peripheral lamins was suggested to be due to a localization of these 'nuclear matrix' filaments in the interior of normally inaccessible compact chromatin domains (Hozak et al., 1995).

The proposed 'nuclear matrix' concept fueled a controversial discussion on the potential experimental artifacts generated by the harsh treatments obligate to visualize it (Nickerson, 2001; Pederson, 2000). It was proposed that salt-extraction itself could cause the artificial formation of the detected protein network by a precipitation of interchromatin proteins (Cremer et al., 1995; Pederson, 2000), irrespective of whether they derive from a real scaffold or were just roaming the interchromatin space by diffusion. Additionally it was argued that the principal organization of the nucleus, e.g. the compartmentalization of CTs, could be fully explained by chromatin self-organization with no need for additional structural components (Cremer and Cremer, 2001; Hancock, 2000). This claim was supported by computer based model simulations, which assumed a chromatin organization based on

chains of stable ~1 Mb chromatin domains connected by flexible linkers (Kreth et al., 2004b; Munkel et al., 1999).

Nevertheless, the existence of a nucleo-skeleton is postulated by model views on the organization of processes like transcription and replication (Cook, 1999), to ensure the mechanical fixation of the transcriptional or replicational machinery and the successful reeling of the DNA template (Cook, 1999, see also Discussion: 7.6.2).

4.3.2 The chromonema model

Andrew Belmont and colleagues provided evidence for a hierarchical folding of chromatin fibers in mitotic chromosomes of Drosophila (Belmont et al., 1987). Later a similar organization of interphase nuclei was postulated in their **chromonema model** (Belmont and Bruce, 1994) based on electron microscopy observations of chromatin morphology in early G1 nuclei. They detected chromatin fibers with thicknesses of either 60-80 nm or 100-130 nm they termed chromonema fibers. These results also conform to fiber size estimations obtained from light microscopic investigations of H2B-GFP tagged chromatin (Belmont and Bruce, 1994; Sadoni et al., 2001). Belmont and colleagues presumed that these fibers are basically built up by tight packing of 10 and 30 nm fibers (Fig. 1 A). Since they did not detect gradual intermediates, but only the two distinct classes of fiber diameters, a hierarchical folding model matched their observations best (Belmont and Bruce, 1994; Shopland et al., 2006). Further folding of the 100-130 nm chromonema fiber was suggested to finally lead to the compaction level of mitotic chromosomes. Though not rejecting, the chromonema model does not necessarily demand an anchoring scaffold, but could be stabilized by unspecific interchromatin linkers.

4.3.3 The random walk-giant loop model

A further proposed view on chromatin organization without the need of a stiff protein scaffold is the **random walk/giant loop model** (RW-GL) proposed by Sachs et al., 1995. This is a quantitative mathematical model, which was developed to account for experimental data gained by FISH on genomic loci with a defined genomic separation (Yokota et al., 1995). The relationship between mean-square interphase distances and genomic separation was demonstrated in the experimental data to have two linear phases with a transition point at approximately 2 Mb (Yokota et al., 1995). This implied a lower level, spanning at most 3 Mb building up a randomly folded chromatin loop, which is attached to a backbone like structure (Fig. 1 B). Genomic loci more far apart from this loop are organized in a further loop also attached to the backbone. Giving the backbone a freedom of a random walk in computer model (Sachs et al., 1995) still accounted for the measured physical and genomic distances.

Sachs et al. accordingly claimed that their model was at that time the most simple to explain the given experimental data.

4.3.4 The multi-loop sub-compartment model

In contrast to the random walk/giant loop model Christian Münkel and Jörg Langowski developed the **multi-loop sub-compartment model** (MLS model) based on chromatin loops of much smaller size (Langowski, 2006; Munkel et al., 1999; Munkel and Langowski, 1998). Their aim was to bridge the gap between electron- and light microscopy by computer modeling of chromatin organization. In the MLS computer model, chromatin is organized as a polymer building up small scale loops in the order of ~120 kb. They further postulated that several such loops, comprising ~1 Mb, were interconnected by stiff springs of unknown nature building up a rosette-like sub-compartment (Fig. 1 C). Adjacent ~1Mb sub-compartments were interconnected by chromatin fibers with the size of the loops. A rosette-like organization of chromatin was observed in EM preparations (Okada and Comings, 1979) of ammonium acetate treated and spread hamster metaphase chromosomes. However, direct evidence that these structures match the scales delineated above was not provided. The computer MLS model, fed with the stated assumptions on chromatin organization, was executed and the results were compared with experimental data sets (Munkel et al., 1999). To assure the comparability between the real and synthetic data, a virtual microscopy was performed on the synthetic data sets accounting for the limitations in resolution of light microscopy. In accordance with real data, the model generated a separation of chromosome arms in interphase nuclei, as well as integer and non-overlapping ~1 Mb chromatin sub-domains (sub-compartments). The MLS model was further in accordance with the experimental data showing chromonema fibers (Belmont and Bruce, 1994), since it generated 100 – 150 nm thick chromatin bundles (Munkel et al., 1999).

When comparing experimental data on distances between loci spanning a telomeric 4 Mb long genomic distance on HSA 4, the MLS model performed better than the RW-GL model, when considering data from nuclei fixed under conditions, which preserved the 3D organization of chromatin (Munkel et al., 1999; Munkel and Langowski, 1998).

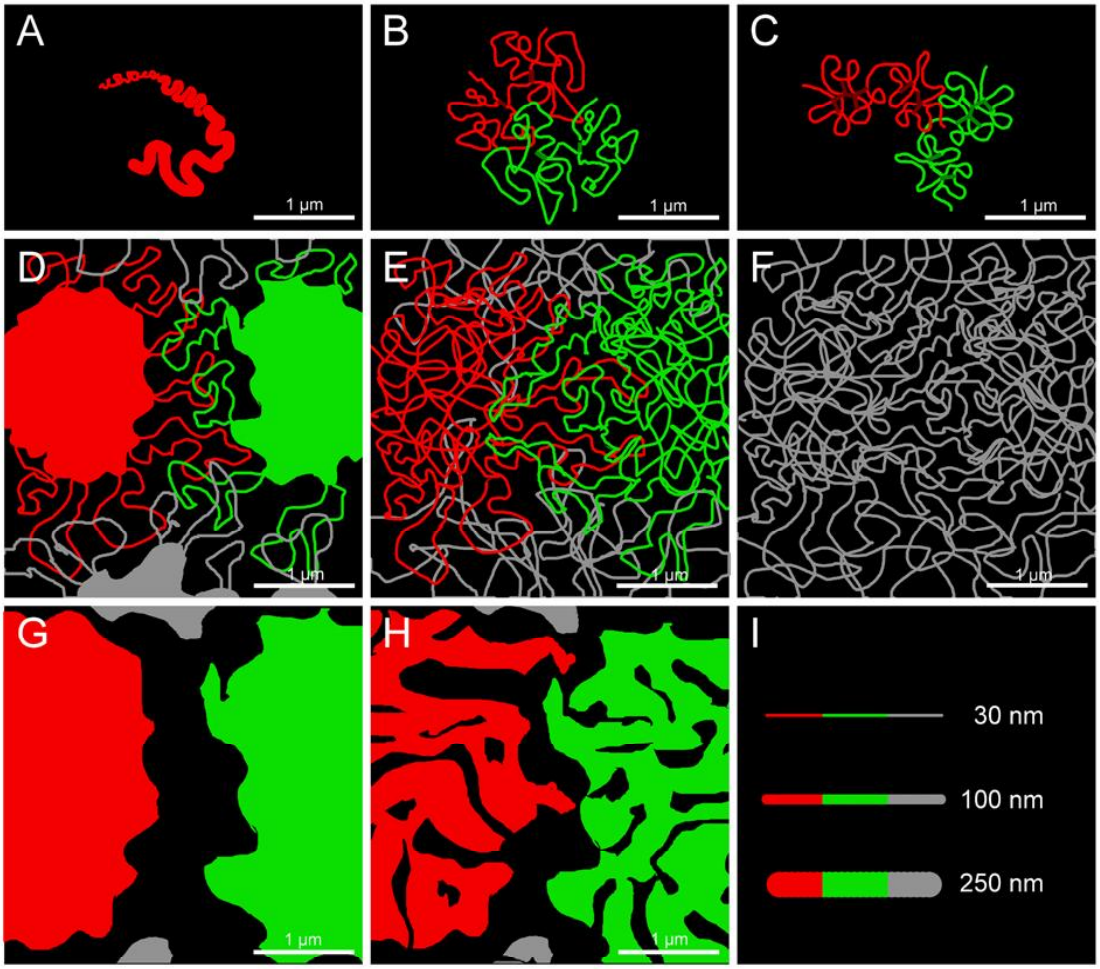

Figure 1: Overview over present model views on nuclear architecture

Displayed are the model views on small scale organization of 30 nm chromatin fibers (A-C) and the large scale model views (D-H) comprising two CTs (red and green) and neighboring CTs (gray). A corresponding scale of fiber thicknesses is given in (I). All images are similar scaled, bars = 1µm.

A) The chromonema model claims a hierarchical folding of the 30 nm fiber leading to distinct classes of fiber diameters with 60-80 nm fibers (folding of the 30 nm fiber) and 100-130 nm fibers (further folding).

B) The RW-GL model postulates a small scale organization of chromatin in giant (~2 Mb) chromatin loops (displayed are 2 loops in green and 2 in red) interconnected by small backbone like structures.

C) The MLS model postulates several small scale loops (~150 kb) forming a ~1 Mb chromatin sub-compartment, (displayed are 2 compartments in green and 2 in red) kept together by small linkers.

D) Bickmore and colleagues postulated that CTs are organized in a core region (filled green area) surrounded by giant loops, intermingling in a broad zone with loops of neighboring CTs.

E) The ICN model postulates extensive intermingling between neighboring CTs (~33% of each CTs volume) and no higher order compartmentalization of interchromatin spaces (black background). Chromatin loops can invade deeply in neighboring CTs.

F) The lattice model postulates an organization of chromatin in only 30 nm fibers with no higher order compartmentalization of chromatin (gray) and non-chromatin (black) regions.

G) The ICD model postulates CTs to be surrounded by a chromatin free interchromatin domain (black), where functional processes are restricted to the CTs periphery

H) The CT-IC model claims that CTs are build like sponges with deep invaginations of the interchromatin compartment (black channels), where functional processes are restricted to the chromatin surface in the periphery and the interior of CTs.

4.3.5 Chromosome territories and giant loops of chromatin fibers

As described above, particular clusters of highly transcribed gene loci were detected to protrude for up to 1.5 µm from the surface of the corresponding CTs (Kupper et al., 2007; Mahy et al., 2002a; Volpi et al., 2000, see 4.1.4). Based on these data, Wendy Bickmore and colleagues argued that a strict territorial organization of chromosomes would not be supported any longer (Chubb and Bickmore, 2003; Mahy et al., 2002a). Their model view of the nucleus, provided in Chubb and Bickmore, 2003, postulates that CTs were composed of a central core territory surrounded by a field of chromatin fibers (Fig. 1 D), which can build giant loops of chromatin fibers depending on the transcriptional status of the inherent loci. Though Bickmore and co-workers agree that the giant fibers could posses a higher order organization (Gilbert et al., 2004), the schematic draft (Chubb and Bickmore, 2003) suggests dimensions of giant loops, demanding an extensive decondensation of chromatin fibers down to the level of 30 nm fibers.

4.3.6 The interchromosomal network model

Recently, the view of 'out-looping' fibers was extended and led Ana Pombo and Miguel Branco to claim a new model of nuclear architecture named the **interchromosomal network model** (ICN model, Branco and Pombo, 2006). It follows the claim of rethinking of a CT as a distinct compartment, but suggests that CTs, besides occupying discrete volumes, additionally share wide fields of intermingling chromatin fibers with their neighboring chromosomes (Fig. 1 E). Evidences in favor of their view were obtained by light microscopy on chromosomes detected by FISH on ultra-thin (80-150 nm) cryosections. By this physical sectioning Branco et al. could overbear the limitations in axial resolution in light microscopy. After applying subjectively chosen gray value thresholds, the partial overlap between neighboring CTs was measured and they claimed that these overlapping zones make up 33% of a given CTs volume on average. To strengthen their findings, they plotted the specifically found overlay between certain CT pairs against the corresponding translocation frequency measured in the same cell line. A highly significant correlation was found (Branco and Pombo, 2006). The ICN model does not consider ~1 Mb chromatin domains as fundamental organizing units but prefers the view of chromatin organization made up by a network of intermingling fibers (Branco and Pombo, 2006; Branco and Pombo, 2007).

4.3.7 The lattice model of chromatin organization

These postulations of the ICN model are supported by the **lattice model** of chromatin organization proposed by David Bazett-Jones and colleagues (Dehghani et al., 2005). They carried out extensive studies on chromatin architecture with the use of electron spectroscopic imaging (ESI). This method is based on the electron energy loss spectroscopy, where

electrons loose specific amounts of energy depending on the different elements they hit in the specimen. An instrument that acts both as an electron spectrometer and as a lens is required to detect these energy differences. The elements of interest for studies on nuclear architecture are nitrogen and phosphorus, with the first enriched in proteins and the latter delineating sites of DNA with its phosphate backbone. This technique enabled the resolving of distributions of nucleic acids in the nucleus with a high resolution. Using ESI, chromatin appears to be organized as a network of DNA fibers with a diameter of 10-30 nm (Fig. 1 F). Dehghani et al claim that no fibers with diameters beyond 30 nm could be found in euchromatin of G1 nuclei (Dehghani et al., 2005). Large channels between CTs were not apparent. According to Dehghani et al. chromatin of neighboring CTs may form overlapping lattices of chromatin fibers. Inter- and intra-chromosomal spaces would be joined to form an 'almost contiguous nucleoplasmic space' (Dehghani et al., 2005).

4.4 Architecture of the interchromatin space

When estimating the volume, which is physically occupied by the whole amount of 10 nm chromatin fibers (DNA plus histones; calculation based on the volume of nucleosomes = ~580 nm^3), a typical fibroblast nucleus would be filled to only 16.5% of its average volume (Dehghani et al., 2005). This calculation stresses the importance of addressing questions regarding the architecture of this interchromatin space, its content and its impact on nuclear functions. According to the lattice model this space is considered as the unstructured channels between the networks of 10-30 nm chromatin fibers (Dehghani et al., 2005). In contrast to this view, many other studies demonstrated a significant compartmentalization of the interchromatin space suggesting a significant functional impact (Cremer and Cremer, 2001).

4.4.1 The interchromatin space

Already at the resolution level of a light microscope, huge lacunas of chromatin-free areas can be observed (Cremer and Cremer, 2001). Especially the accumulation of splicing factors in nuclear speckles (Lamond and Spector, 2003) or the accumulation of other proteins in aggregates like the PML-bodies (Ching et al., 2005), Cajal-bodies (Zirbel et al., 1993) or Rad51-foci (Tashiro et al., 2000) were observed in these interchromatin spaces at the light as well as at the electron microscopy level (Fakan and Puvion, 1980; Monneron and Bernhard, 1969; Richter et al., 2005; Spector, 2001). Further and finer interchromatin channels were observed in ultra-thin sections of nuclei examined with transmission electron microscopy and highly specific chromatin staining (Esquivel et al., 1989; Fakan, 2004a; Fakan, 2004b). This technique contrasts chromatin by osmium ammine staining and is based on a Feulgen-type reaction (Cogliati and Gautier, 1973). Its sensitivity was reported to be

sufficient to detect individual DNA molecules (Cogliati and Gautier, 1973, reviewed in Cremer et al., 2006). These smaller interchromatin channels with diameters below the light resolution limit (<500 nm) add to a complex system of channels and lacunas pervading the entire nuclear volume. In addition to the prominent protein aggregations observed in micron-sized interchromatin lacunas, the finer channels are roamed by nuclear proteins involved in transcription, like the transcription factor TFIIH or RNA polymerases as well as RNA processing proteins (hnRNP-U, Verschure et al., 2002). In contrast, sub-chromosomal domains intensely labeled by FISH of chromosome paint probes, were devoid of nascent transcripts, which were almost exclusively detected in interchromatin areas (Verschure et al., 1999). This report is in accordance with the observation of a reticular network of mRNA delineated in nuclei by RNA-only-FISH against specific RNA transcripts of transfected genes (Bridger et al., 2005; Lawrence et al., 1989; Raap et al., 1991). These results on the localization of transcription involved processes support the view of a compartmentalized interchromatin channel system aligning chromatin domains and guiding transcripts to the nuclear pores (Cremer and Cremer, 2001). After (over-)expression of a the intermediate filament protein vimentin tagged to GFP in human cell nuclei, a growing network of protein filaments along, but never inside patches of compact chromatin and whole CTs was observed holding as a rough marker for the interchromatin channel system (Bridger et al., 1998; Reichenzeller et al., 2000). Following the movements of poly(A) RNA throughout the nuclear volume in living cells by fluorescein tagged oligo(dT) probes allowed Politz et al. to visualize defined tracks of movements in channels between intensely stained chromatin regions within which a free diffusion of the transcripts was observed (Politz, 1999; Politz et al., 1998).

4.4.2 Mobility of interchromatin proteins

Despite the distinct compartmentalization of nuclear architecture and despite the observed immobility of chromatin at the global level, considering the nucleus as a static structure would not meet its real nature. In fact, most nuclear proteins are highly dynamic and interchange rapidly between different compartments (Misteli, 2001; Phair and Misteli, 2000). These insights were mainly gained by *in-vivo* observations of GFP-fusion proteins and the application of FRAP (fluorescence recovery after photobleaching) or FLIP (fluorescence loss in photobleaching). Both techniques take advantage of the possibility to bleach GFP-signals in a defined region by an intense laser beam. Bleaching such a region of interest and measuring the recovery of fluorescence intensity at the bleached spot (FRAP) could demonstrate the invasion of unbleached molecules from other regions, if increasing intensity at the bleached spot was observed. Applying a continuous intense laser beam and measuring the intensity of a spot outside that region (FLIP), could reveal a loss of intensity at

monitored untreated spot indicating molecules leaving the spot and invading the bleaching area. Both FRAP and FLIP analyses deliver curves of fluorescence intensities, which can be evaluated to determine the kinetic properties of the investigated proteins (Misteli, 2001; Phair and Misteli, 2000). Applying further modeling on these curves allowed for determining residence times and steady-state fluxes of the investigated molecules (Phair et al., 2004; Phair and Misteli, 2000). Such studies have shown that '*many nuclear proteins roam the entire nuclear space in-vivo and that compartments are the reflection of the steady-state association/dissociation of its residents with the nucleoplasmic space*' (Phair and Misteli, 2000).

4.4.3 The perichromatin region

The intranuclear localization of proteins involved in transcription has further been extensively investigated by electron microscopy (for reviews see Fakan, 2004a; Fakan, 2004b). Stanislav Fakan and colleagues demonstrated that perichromatin fibrils, first described in the late 60ies (Monneron and Bernhard, 1969) are the in-situ form of hnRNP transcripts (Fakan, 1994). These fibrils are regularly detected in a region at the periphery of compact chromatin domains consisting of decondensed chromatin with a width of 100-200 nm. This compartment, termed the perichromatin region (Fakan and Bernhard, 1971), attracted more and more attention, since it seems to be the site of all major active processes. In addition to RNA synthesis (Cmarko et al., 1999; Fakan et al., 1976; Nash et al., 1975; Trentani et al., 2003), the transcription factor TFIIH and RNA polymerase II (Cmarko et al., 1999) and pre-mRNA processing steps, detected by poly(A) polymerase and oligo-dT probes, were localized at the perichromatin region (Cmarko et al., 1999; Fakan, 2004a; Fakan, 2004b). Since polycomp group silencing proteins are also concentrated in the perichromatin region, it was concluded that not only active, but also inactive but coding regions are exposed at the surface of the compact chromatin clumps (Cmarko et al., 1999).

Short pulses with labeled deoxy-nucleotides in S-phase cells revealed active replication sites at the perichromatin region with no respect to the size of the underlying chromatin clump (Fakan and Hancock, 1974). Pulse-chase experiments demonstrated that chromatin, after being replicated at the surface is moved to the chromatin clump interior so that active replication only occurs at the surface of the clumps (Jaunin and Fakan, 2002; Jaunin et al., 2000). Nascent DNA co-localized with DNA polymerase, cyclin A and PCNA (Sobczak-Thepot et al., 1993).

Taken together, the mentioned data indicates that the perichromatin region is the compartment, where the main functional processes transcription, pre-mRNA splicing and poly-adenylation and replication take place (Cremer et al., 2004b).

4.4.4 Transcription factories

The perichromatin region is too small to be resolved by conventional light microscopy approaches. Accordingly, considering solely the findings of electron microscopy studies on the localization of transcription, a rather homogeneously distributed nucleus-wide signal would be expected, when detecting the same sites by light microscopy.

However, the detection of incorporated BrUTP nucleotides in nascent RNA revealed a compartmentalized signal appearing in countless but distinct small fluorescent foci (Albiez et al., 2006; Pombo and Cook, 1996; Wansink et al., 1993). These findings and the corresponding view on replication sites (see 4.3.1), gave rise to the perception of small 'factories' being the places of ongoing transcription (Cook, 1999; Jackson, 2003; Martin and Pombo, 2003). According to this view, a few polymerases are arranged in a small fixed cluster, the 'factory, and twine the mobile DNA template to transcribe active loci. This view solves two topological problems, which occur during transcription of helical templates (Cook and Gove, 1992). These problems would turn up if polymerases are regarded as mobile and the DNA template as fixed. The first problem would be the generation of torsional stress induced by the progressive opening of the DNA double strand, which could be solved by topoisomerase action (Liu and Wang, 1987). The second problem would arise when a polymerase tracks along the helical template: The transcript would become entwined about the template with progressing transcription. An untwining mechanism would have to work perfectly, since leaving only one entwinement would prevent the successful export of the transcript. In contrast, this untwining problem would not occur if the polymerases were fixed and DNA rotated instead. The concept of transcription factories naturally depends on the existence of anchorage sites for the postulated transcription factories. The postulated 'nuclear matrix', serving as a nucleo-skeleton (see 4.3.1), could fulfill this demand.

4.5 Present models on interchromatin architecture

4.5.1 The interchromosome domain model

A functional importance of interchromatin space was postulated by Peter Lichter and colleagues (Zirbel et al., 1993). Accordingly interchromatin spaces would define a 3D network-like compartment, termed the **interchromosome domain** (ICD), which starts from nuclear pores and invades the nuclear interior in channels surrounding CTs (Zirbel et al., 1993, Fig. 1 G). The model was based on the finding that RNA transcripts and components of the splicing machinery are basically excluded from the interior of CTs, since CTs and RNA transcripts seemed to be spatially exclusive (Zirbel et al., 1993). The space of the ICD was postulated to define a structural and functional compartment, where nuclear components involved in transcription and mRNA processing are accumulated. The model implicates that

transcribed genes are located in the periphery of the corresponding CT. Investigations on the localization of a set of active and inactive genes with respect to their CT was performed in different cell lines and compared with the localization of non-coding sequences (Kurz et al., 1996). In support of the ICD model, genes were localized at the periphery of the respective CTs with no respect to their transcriptional status. Studies on the localization of highly expressed loci (see 4.1.4) are in accordance with the ICD model as well.
Additionally, the detection of a network of vimentin fibers in interchromatin areas (Bridger et al., 1998), which was aligning but never invading CTs, further supported the view of a CT surrounding channel system of functional importance.
The ICD model was challenged, however, when active loci were found within the very interior of a CT as well (Mahy et al., 2002b), and when it was demonstrated that a strict organization of active chromatin regions with respect to the CT periphery does not exist (Kupper et al., 2007).

4.5.2 The chromosome territory-interchromatin compartment model

Further subsequent studies also challenged the view of active processes exclusively localized at the periphery of CTs, since also ongoing transcription (Abranches et al., 1998; Cmarko et al., 1999; Verschure et al., 1999) was reported to localize in the deep interior of FISH painted CTs. The **chromosome territory- interchromatin compartment model** (CT-IC model) accounted for these findings and was introduced by Thomas and Christoph Cremer (Cremer and Cremer, 2001). It basically represents an advancement of the preceding ICD model (Cremer and Cremer, 2001; Cremer et al., 2004b). Now, CTs are considered to be built with a sponge like conformation with extensions and invaginations which invade the CTs interior (Fig. 1 H). This architecture of a CT would be mediated by a hierarchy of domains as described by the MLS model (Munkel et al., 1999; Sadoni et al., 2004): Several DNA loops with a length of 30-200 kb (~100 kb domains) build up sub-compartments termed according to their rough DNA content '~1 Mb chromatin domains', which correspond to foci detected by replication labeling (Jackson and Pombo, 1998, see 4.1.4). Computer modeling of CTs built up from such sphere-like ~1 Mb chromatin domains, yielded an interchromatin space of variable width expanding between the spherical domains (Kreth et al., 2004b). In such a porous architecture of a CT, with interchromatin channels pervading its entire volume, the functional machinery can access the interior of a CT. Accordingly, active processes are no longer restricted to locate at the CTs periphery (ICD model), but can be situated at the surface of a chromatin domain within a CT, which is in full agreement with the experimental data stated above. Still, a topological separation of chromatin and interchromatin spaces is postulated, since active processes are still postulated to locate at the border between chromatin and interchromatin space (Cremer and

Cremer, 2001). This proposed complex architecture of the interchromatin space was emphasized by terming it the interchromatin compartment (IC). The postulated restriction of functional processes to the border of chromatin domains is further consistent with the mentioned EM observations, which demonstrated that ongoing transcription, splicing and replication are exclusively observed at the perichromatin region (Cremer et al., 2004b, see 4.4.3)

4.5.2.1 In-/Accessibility of chromatin domains

The postulation that active processes are restricted to the surfaces of chromatin domains raised the question if the interior of these compact chromatin domains is indeed physically inaccessible for molecules in the size range of e.g. transcription factors or preassembled functional machineries. Several studies addressed that question by the use of micro-injected FITC-conjugated dextrans of varying size or FITC-poly-L-lysine in the nuclei of living cells. Accordingly, small dextrans (3-42 kDa) displayed homogeneous signal distributions with no preferential exclusion from chromatin regions (Gorisch et al., 2003; Verschure et al., 2003). With increasing masses (77- 2500 kDa), however, FITC dextrans were progressively excluded from chromatin regions (Verschure et al., 2003) and accumulated in interchromatin channels (Gorisch et al., 2003). However, 70-kDa dextrans were detected in some compact chromatin regions, demonstrating that the overall exclusion is not necessarily due to a strict size threshold at this level (Verschure et al., 2003). These results implied that different types of condensed chromatin domains may exist, distinguishable by their accessibility to 70-kDa dextrans. Anionic FITC-dextrans (500-kDa) were exclusively observed in interchromatin spaces, whereas positively charged FITC-poly-L-lysine was to some extent also detected within the chromatin regions (Gorisch et al., 2003). Görisch et al. therefore concluded that the nucleoplasmic accessibility for macromolecules not only depends on molecule size but additionally on electrical charge properties.

However, limitations in accessibility were only detected in size ranges greater than that of components of the transcription machinery. This result suggested that these molecules can diffuse freely also inside condensed chromatin domains. In accordance with this claim RNA-polymerase II as well as the transcription factor TFIIH was found homogenously distributed throughout the nucleoplasm (Verschure et al., 2003). Nevertheless there seems to be a size threshold in the range of 70 kDa dextrans, consistent with the observation that large hnRNP particles localized in interchromatin channels demonstrated when poly-(A) RNA molecules were tagged in living cells (Politz et al., 1999, see 4.4.1).

The claim of limited accessibility was further challenged by living cell studies and diffusion measurements obtained by the observation of transfected GFP-tagged nuclear proteins. Applying either FRAP (fluorescence recovery after photobleaching) or FCS (fluorescence correlation spectroscopy) unlimited access to compact chromatin regions was demonstrated

for the heterochromatin protein HP1 (Cheutin et al., 2003; Festenstein et al., 2003). It is important to note, however, that a decreased mobility of HP1 was observed in heterochromatic (compact) versus euchromatic (decondensed) chromatin regions in unstimulated T cells (Festenstein et al., 2003).

Taken together, simple steric exclusions are not sufficient to explain the restricted localization of active processes to chromatin domain surfaces. Considering these results two functional scenarios were put up (Cremer and Cremer, 2006b) to explain the observed topology of functional processes: [1] parts of functional machineries may pre-assemble in the IC forming macromolecules with limited access to the interior of domains according to a size threshold and/or [2] a cascade of protein binding interactions forming a functional machinery would start at promoters exposed at a domain surface, which is the closest region for proteins released from neighboring aggregates like speckles or bodies. The advantage of the second scenario would be a closer pathway for the interactions increasing the probability for binding partners to meet.

4.6 Induced formation of hypercondensed chromatin

Precise descriptions of the higher order topology of chromatin and interchromatin spaces is very important to gain knowledge on the organization of nuclear architecture. Of similar importance, however, is to experimentally manipulate nuclear architecture enabling to proof postulated topology-function relationships.

A phenomenon that was already described in the beginning of the last century in plant cells is the formation of hypercondensed chromatin (HCC) by incubating living cells in hyper-osmotic media (Bank, 1939; Sakamura, 1927). This treatment causes dramatic changes in chromatin morphology. Cells incubated in these conditions displayed a chromatin pattern reminding on prophase nuclei with condensed patches of chromatin. Surprisingly, despite its obvious impact on nuclear architecture, only two studies in the 1970ies applied this approach (Pederson and Robbins, 1970; Robbins et al., 1970) and investigated the effect on nuclear functions accompanying the induced changes in chromatin compaction. Since then, the approach was not used until Gerd Maul and colleagues reported a transient shift in chromatin compaction in heat shocked (42°C) cells, which were covered only by a thin film of culture medium (Plehn-Dujowich et al., 2000). Motivated by this study we investigated this effect in more detail and found that the observed formation of hypercondensed chromatin (HCC) was also inducible just by raising the osmolarity of the culture medium (Albiez, 2003). This discovery guided us to re-discover the forgotten former publications on that topic. In the resulting Diploma thesis first insights in the physiological characteristics and topological changes were explored culminating in the assumption, that the method of induced formation of HCC *had the potential to become a helpful tool for future investigations on nuclear*

architecture (Albiez, 2003). Following this claim, the present study was put up to manipulate nuclear architecture by the induced formation of HCC to test the conflicting postulations of present model views.

4.7 Imaging

A highly important, though not regularly addressed topic in 3D imaging is the method of imaging. Most publications cited in this introduction were obtained by applying either light or electron microscopy with different types of microscopes. However, it is important to know about the limitations of each of the microscopes as well as about the pitfalls occurring, when working with images. Obligate processing steps preceding electron microscopy (EM), for example, include dehydration, resin embedding, ultra-cutting and a facultative contrast- or immuno-staining. EM recordings can reach a resolution level of several nanometers. However, each of the mentioned processing steps may introduce artifacts and potentially affect the morphology of nuclear material in scales considerably larger than nanometers. Light microscopes are much more limited in resolution compared to EM (<300 nm in lateral and <500 nm in axial direction). Nevertheless there are certain advantages, especially in the specimen preparation. Physical sectioning is not demanded and water, the major component of all biological specimen, is not hindering successful imaging like in EM. Nevertheless besides the limited resolution, additional problems, elucidated below, need to be considered when dealing with data gained by light microscopy.

Fluorescence light microscopy is widely used to investigate the topography and function of cellular organelles and substructures. The development of a wide range of fluorochromes differing in their spectral signatures enabled the simultaneous visualization of various fluorescent objects in the nucleus. The output of a confocal microscope typically consists of a series of 2D images that make up the complete fluorescent 3D object of interest, with each image taken from consecutive focus planes (Conchello and Lichtman, 2005). These images are built up as matrices of voxels (=pixels in 3D data sets) with gray values within a range set by the digital data format of the image (e.g. gray value ranges from 0 to 255 for 8-bit images). Quantification of these fluorescent objects, e.g. based on distance measurements or gray value ratios between the voxels of the objects, is necessary for determining their size, topography or position. Evaluation software usually require the user to set a threshold value (TH) above which a voxel is included in the analysis and below which it is assigned to background and therefore not considered in subsequent calculations. Although TH-independent evaluation algorithms that analyze variations in gray value or evaluations that consider TH ranges are being developed (Albiez et al., 2006; Stadler et al., 2004), most of the currently used software tools still demand the input of a single TH value as key parameter. Several algorithms for automated TH determination based on gray value

histograms of the 3D data sets or on pattern or edge recognition have been developed (Hu et al., 2006; Vasilic and Wehrli, 2005; Yi and Coppolino, 2006). However, a sampling of recent publications using confocal microscopy imaging in the field of cell biology reveals that researchers still prefer to perform thresholding themselves (Bacher et al., 2006; Branco and Pombo, 2006), suggesting that automated procedures for TH determination are still not working satisfactorily.

One of the difficulties that hinders the choice of an optimal TH is that recorded images not only comprise signals derived from the focused optical plane, but also exhibit signals from fluorescent objects above and/or below this plane. This out-of-focus light leads to blurred (i.e. lower contrasted) data sets which can not be segmented using a single TH value because either additional out-of-focus light is at least to some extent included (low TH value) or true signals would be excluded (high TH value).

The use of monochromatic laser lines for excitation and the introduction of a pinhole in the pathway of light detection in order to reduce the amount of out-of-focus light (Pawley, 2006) allowed the development of confocal microscopes, a significant advance in the field of fluorescence microscopy. However, even confocal images suffer from blurred light (Pawley, 2006). This blurring occurs according to the point-spread function (PSF), which is the mathematical description of how a point-like light source would appear in a microscope data set (Shaw and Rawlins, 1991). Fluorescence microscopes can be understood as linear systems, where any two different light signals coming from two different points of the object do not interfere with each other and do contribute additively to the total image. Therefore, for a given object, the expected image can be obtained by breaking the object down into a set of points and adding a copy of the PSF to the image at the location of each point. The PSF depends mainly on the objective that is used to acquire the image. Since a point-like light source is blurred to a greater extent in the axial direction, it appears elongated rather than spherical (Pawley, 2006; Shaw and Rawlins, 1991; see Fig. 2). One way to correct for this mathematically-defined distortion is to apply deconvolution (McNally et al., 1999). Deconvolution is a mathematical procedure that applies the reverse PSF on the raw images obtained from the microscope. The results are images which are less blurred and therefore more contrasted (Pawley, 2006). Deconvolution was shown to increase the resolution of confocal data sets (Dey et al., 2006; Pawley, 2006; van der Voort and Strasters, 1995) and to emhance image quality more than could be achieved by image filtering techniques, as proven by co-localization analysis (Landmann, 2002; Sedarat et al., 2004). The PSF can be measured by imaging fluorescent spheres with diameters much smaller than the optical resolution limit of the microscope, thereby serving as a point-like light source (Hiraoka et al., 1990) which can subsequently be converted into a PSF by appropriate software. Specialized deconvolution programs, additionally allow sensible PSF estimates to be extracted from

slightly larger objects (e.g. 175 nm beads), which have a considerable advantage with respect to the signal-to-noise ratio (SNR).

Nevertheless, although deconvolution is routinely and successfully used in the processing of wide-field microscopy images, its usefulness is considered with skepticism when it comes to confocal data sets. While some scientists consider raw confocal images as the best possible resolved and therefore not improvable, others fear that the 'black-box'-procedure deconvolution could add artifacts to confocal images (Kriete et al., 2001; Markham and Conchello, 2001; McNally et al., 1999; Wallace et al., 2001) and therefore prefer to evaluate unprocessed raw data sets (Sadoni and Zink, 2004). Accordingly, the first aim of this study was to establish a working protocol for deconvolution of confocal images to provide 3D data sets of a quality sufficient for subsequent studies on nuclear architecture.

4.8 Goals of the present work

Present models on global principles of nuclear architecture are conflicting in several issues. Most notably, the existence of major architectural features like the interchromatin compartment, the 'nuclear matrix' or the higher order configuration of chromatin postulated by different models is questioned or even refused by others. This study was set up to manipulate nuclear architecture with the use of hypercondensed chromatin formation and revisit the postulations of the present models under the light of the obtained results.

The main questions addressed in this context were:

- Can major components like the interchromatin compartment or the 'nuclear matrix' be demonstrated at the light microscopy level?
- Are functional processes restricted to the surface of chromatin domains at the border to the interchromatin compartment?
- Do DNA fibers regularly loop-out from their respective bulk CTs and what is the configuration of these protruded regions?
- Are active and inactive chromatin regions arranged in a certain pattern in regard to the chromatin-interchromatin border zone?
- Do chromosome territories exist as separate entities or are they interconnected?

These questions were addressed with the use of modern cell biology methods including transfection of expression constructs, transgenic cells, immuno-labeling and advanced microscopy. Confocal laser scanning microscopy was performed with fixed cells as well as using living cell observation technologies. State of the art electron microscopy was used to confirm results on the ultrastructural level in a collaborative project with the EM laboratory of Prof. Stanislav Fakan in Lausanne. Deconvolution of confocal images is an image restoration procedure enhancing image quality. Since it was not routinely applied at the beginning of this thesis, the first aim was to establish a protocol for deconvolution demonstrating an enhanced image quality without the introduction of artifacts.

5 MATERIAL AND METHODS

5.1 Cell culture and Transfection

5.1.1 Cell cultivation

All cells were cultured at 37°C with a 5% CO_2 atmosphere in a humidified incubator. Cell culture growth media were supplemented with 10% FCS, 100 U Penicillin, 100 µg/ml Streptomycin and in case of live cell observations additionally with 25 mM HEPES.
The growth media used were D-MEM (***D**ulbeccos **M**odified-**E**agle-**M**edium*) or RPMI-1640 (***R**oswell-**P**ark-**M**emorial-**I**nstitute*). For the cell types and cell lines used see 8.1.

5.1.2 Thawing cells

Materials:
Cryotube with deep-frozen cell suspension stored in liquid nitrogen tank
Appropriate growth medium, pre-warmed to 37°C
Sterile tissue culture flask (25 cm²)
Water bath 37°C
Incubator (37°C, 5% CO2 humidified atmosphere)

Method:

- Take cryotube from liquid nitrogen tank and transfer it quickly to the water bath (37°C)
- Transfer the solution in the culture flask, immediately after the cell suspension melted, and fill it up to ~10 ml with pre-warmed growth medium
- Incubate culture flask with cells for 30 min in incubator to allow proper cell adherence
- Exchange medium to remove DMSO remnants
- Place culture flask with cells back in incubator

5.1.3 Sub-culturing

Materials:
CMF-PBS, pre-warmed to 37°C
Appropriate growth medium, pre-warmed to 37°C
Sterile tissue culture flasks (25 cm², 75 cm²)
Trypsin/EDTA solution (0.05% / 0.02% in CMF-PBS), pre-warmed to 37°C
Centrifuge
Incubator (37°C, 5% CO2 humidified atmosphere)

Method:

- Cultivate cells in culture flasks of appropriate size

- Discard supernatant medium by decantation (adherent cells) or centrifugation with 1000 rpm for 10 min (suspension cells)
- Wash cells with CMF-PBS
- Incubate adherent cells in Trypsin/EDTA solution for some minutes in the incubator
- Re-suspend cells in adequate amounts of growth medium and dilute as required

5.1.4 Seeding cells on coverslips

Materials:

Appropriate growth medium, pre-warmed to 37°C

Appropriate coverslips (see 8.4) stored in 100% ethanol

Petri-dishes (35 mm, 60 mm) or 6-well plates

Poly-L-Lysine (1 mg/ml)

Water bath 37°C

Bunsen burner

Incubator (37°C, 5% CO2 humidified atmosphere)

Method:

- Flame coverslips with Bunsen burner
- For suspension cells: prepare Poly-L-Lysine covered coverslips by incubation of coverslips for 30 min with a drop of Poly-L-Lysine solution on top. Wash coverslips with CMF-PBS to remove left over Poly-L-Lysine
- Place coverslips in Petri-dishes or 6-well plates
- Re-suspend cells in adequate amount of medium as described in 5.1.3
- Distribute cell suspensions on dishes/wells with coverslips
- Place cells in incubator for at least 30 min to assure proper cell adherence

5.1.5 Deep-freezing cells

Materials:

Appropriate growth medium, pre-warmed to 37°C

Freezing medium: Growth medium additionally supplemented with 10% DMSO

Cryotubes

Cooling box (containing isopropanol)

Freezer (-80°C)

Liquid nitrogen tank with rackets

Method:

- Cultivate cells as described in 5.1.3
- Re-suspend cells in adequate amounts of freezing medium

- Distribute 1.5 ml cell suspension in each cryotube
- Place cryotubes in cooling box
- Incubate cooling box with cryotubes for approx. 24 h in freezer at -80°C
- Place cryotubes in rackets in liquid nitrogen tank for long-term storage

5.1.6 Transfection of cells

Materials:

Growing cells on coverslips (semi-confluent) in Petri-dishes / 6-well plates

Serum-free (w/o FCS) growth medium

FuGene 6 transfection kit

1 ml Eppendorf tube

Expression construct: Plasmid DNA in H_2O dd (for list of constructs used see 8.1)

Incubator (37°C, 5% CO2 humidified atmosphere)

Method:

The given concentrations match the transfection of cells in one 35 mm Petri-dish.

- Thaw FuGene 6 reagent for 15 min at RT
- Prepare transfection solution:
  - Pipette 97 µl serum-free medium in Eppendorf tube
  - Add 3 µl of FuGene 6 reagent directly in the serum-free medium under careful avoidance of touching the tubes wall
  - Add adequate volume of Plasmid DNA solution containing ~1 µg DNA
  - Mix transfection solution by gently tapping the tube and incubate for 15 min at RT

- Add 100 µl of transfection solution drop-wise to a 35 mm Petri-dish with cells
- Incubate cells in incubator for at least 24 h to achieve sufficient transfection and expression

5.2 Inhibition protocols

5.2.1 Inhibition of RNA polymerase-II activity by α-Amanitin

Materials:

Growing cells on coverslips (semi-confluent) in Petri-dishes / 6-well plates

Appropriate growth medium, pre-warmed to 37°C

α-Amanitin stock solution (2 mg/ml)

Incubator (37°C, 5% CO2 humidified atmosphere)

Method:

- Prepare α-Amanitin working solution (2µg/ml) by diluting the stock solution in growth medium
- Incubate cells for >2 h in α-Amanitin working solution to inhibit RNA-Pol-II activity

5.2.2 Depletion of cellular ATP levels

Materials:

Growing cells on coverslips (semi-confluent) in Petri-dishes / 6-well plates

Appropriate glucose-free growth medium, pre-warmed to 37°C

Sodium azide stock solution (1 M)

2-deoxyglucose stock solution (60 mM)

Incubator (37°C, 5% CO2 humidified atmosphere)

Background:

The ATP-depletion protocol was mainly adopted from Dingwall et al., 1987 and Phair and Misteli, 2000. The aim of this method is to block the two ATP synthesis pathways by [1] blocking the respiratory chain (inhibition with sodium azide) and by [2] blocking the glycolysis (substitution of glucose by 2-deoxyglucose). By incubation of cells in these conditions, cellular ATP levels get depleted over time. However, cellular and nuclear morphology have to be carefully watched over the course of the treatment since effects on chromatin compaction have been observed (see Results 6.2.6.3 and Shav-Tal et al., 2004).

Method:

- Prepare depletion medium containing glucose-free growth medium, sodium azide (10 mM) and 2-deoxyglucose (6 mM)
- Exchange standard growth medium of cells and incubate for >30 min in depletion medium to largely decrease the cellular ATP level

5.3 Labeling of RNA/DNA

5.3.1 Labeling of replication foci with BrdU

Materials:

Growing cells on coverslips (semi-confluent) in Petri-dishes / 6-well plates

Appropriate growth medium, pre-warmed to 37°C

BrdU stock solution (50 mM)

Incubator (37°C, 5% CO2 humidified atmosphere)

Method:

- Add BrdU solution to Petri-dishes to a final concentration of 50 µM
- Incubate cells for 30 min to 1 h to achieve BrdU-incorporation in replication foci in S-phase cells, or
- Incubate cells for several hours (covering the entire S-phase of the respective cells) to achieve BrdU-incorporation in most of the chromatin of S-phase cell nuclei
- Perform immuno-detection with primary antibodies directed against bromine as described in 5.5

5.3.2 Labeling of replication foci and / or chromosomes in living cells

Materials:

Cells growing on 15x15 mm coverslip (semi-confluent) in Petri-dishes / 6-well plates

Appropriate growth medium, pre-warmed to 37°C

Cyanin-3-deoxy-triphosphate (Cy3-dUTP) stock solution (~1 mM)

Petri-dishes (60 mm)

Hypodermic needle (0.9x40 mm)

Paper wipes

Incubator (37°C, 5% CO2 humidified atmosphere)

Background:

To visualize replication foci in living cells fluorochrome-tagged nucleotides (e.g. Cy3-dUTP) need to be incorporated during S-phase. Since these nucleotides carry a triphosphate group they are not membrane-permeable. Transient membrane damage has to be induced to allow an uptake of these nucleotides. This can be achieved either by microinjection (see 5.7.2) or in a much less sophisticated way by the scratch-labeling method introduced by Dr. L. Schermelleh (Schermelleh et al., 2001). This treatment leads to a high number of cells harboring fluorescently labeled replication foci even in un-synchronized cultures (Schermelleh et al., 2001). When replication labeled cells are cultivated for several days,

labeled and non-labeled chromosomes get randomly passed to daughter cells yielding nuclei with segregated and fluorescently tagged chromosomes.

Method:

- Prepare labeling solution containing growth medium and Cy3-dUTP (~50 µM)
- Take coverslip with adherent cells out of Petri-dish, dry the bottom with a paper wipe and place the coverslip in the middle of a 60 mm Petri-dish
- Add ~10 µl of labeling solution on top of the coverslip
- Apply parallel scratches on the cell layer with the hypodermic needle as if hatching. The procedure should not take long to avoid drying of the cells
- Add several ml of growth medium to cover the cells and incubate for 30 min to 1 h in the incubator to achieve Cy3-dUTP-incorporation in replication foci in S-phase cells
- To obtain nuclei with segregated labeled and unlabeled chromosomes, sub-culture replication labeled cells for several cell cycles prior to observation

5.3.3 Labeling of nascent RNA (transcription foci)

Background:

Nascent RNA (transcription foci) can be labeled by the incorporation of bromo-uridin-triphosphate (BrUTP) (Albiez, 2003; Wansink et al., 1993). Again, microinjection (see 5.7.2) or the scratch-labeling method is suited to achieve nucleotide uptake and incorporation in a high amount of cells. Scratch-labeling was performed mostly as described in 5.3.2 by substituting Cy3-dUTP with BrUTP which was used in a final concentration of 5 mM. Since the bromo-labeled transcripts have to be detected by immuno-detection to allow visualization, it was desirable to substitute BrUTP with nucleotides directly coupled to fluorochromes. However, neither Cy3-uridine-triphosphate nor Cy3-uridine yielded a successful visualization of transcription foci as known from BrUTP labeling experiments.

5.4 Fixation and permeabilization

5.4.1 Standard protocol

Materials:

Cells growing on coverslip (semi-confluent) in Petri-dishes / 6-well plates

Formaldehyde stock solution (37%)

CMF-PBS

PBST (0.01% Tween / PBS)

Triton X-100

Method:

- Prepare fixation solution containing 4% formaldehyde in CMF-PBS
- Prepare permeabilization solution containing 0.2% Triton in PBST
- Take coverslip with adherent cells out of Petri-dish and wash in CMF-PBS
- Incubate coverslip with cells for 10 min in fixation solution
- Wash coverslip with fixed cells few times with PBST
- Incubate coverslip with fixed cells for 5 min in permeabilization solution
- Wash coverslip with fixed cells with PBST

5.4.2 RNase treatment

Materials:

Fixed and permeabilized cells on coverslip in PBST (see 5.4)

RNase stock solution (1%)

Water bath 37°C

Humidified chamber

Method:

- Prepare RNase working solution (0.02%) by diluting the stock 1:50 in PBST
- Incubate coverslip in RNase working solution for 1 h at 37°C in a humidified chamber
- Wash coverslip with cells few times with PBST

5.4.3 Preparation for transmission electron microscopy (EM)

Materials:

Cells growing on microgrid coverslip (semi-confluent) in Petri-dishes / 6-well plates
Paraformaldehyde (powder)
Soerensen phosphate buffer (0.1M, pH 7.4)
Ethanol concentration series (30%, 50%, 70%, 90% and 100%)
Resin LR White
Glass embryo dishes (for incubations with resin, which dissolves plastics)
Embedding capsules (BEEM)

Background:

One aim of this study was to compare the morphology of the same nuclei, recorded at the confocal light microscope and subsequently at the electron microscope, where the same nuclei had to be retrieved. For this purpose cells were seeded on coverslips with an etched surface (grid), which was recordable at the light microscope (phase contrast). The incubation of these coverslips in the polymerization resin imprinted the grid pattern in the resin so that the recorded location was retrievable.

Method:

- Prepare fresh fixation solution (4%) by dissolving 4 g paraformaldehyde in 100 ml Soerensen phosphate buffer (dissolving best > 60°C)
- Cool fixation solution down to 4°C
- Wash coverslip with cells in Soerensen phosphate buffer
- Incubate coverslip with cells for 1 h in fixation solution at 4°C
- Wash coverslip 5x 1 min in Soerensen phosphate buffer (RT)
- Incubate coverslip in increasing ethanol series at RT:
  2x 2 min in 30%, 2x 5 min in 50%, 2x 10 min in 70%, 2x 10 min in 90%,
  2x 10 min in 100%
- Incubate coverslip for 30 min with resin in embryo dishes at RT
- Incubate coverslip O/N with resin in embryo dishes at 4°C
- Fill embedding capsule with resin without air bubbles and place coverslip with cells upside-down on the filled capsule
- Overturn capsule together with coverslip and place on even ground covered with an aluminum sheet
- Incubate coverslip with resin filled capsule on top of it for 48 h at 60°C to polymerize the resin

These preparations were sent to our collaborators at the electron microscopy laboratory of Prof. S. Fakan in Lausanne and were further processed by Cinzia Tiberi and Lorella Vecchio. Briefly, further steps included:

- Detachment of cells from the capsule by a short thermal shock (dipping in liquid nitrogen).
- Relocation of cells of interest according to the imprinted grid pattern on the resin block
- Ultra-cutting (~80 nm) of the resin blocks with embedded cells at the regions of interest
- Contrasting of chromatin with the osmium ammine staining solution to specifically visualize DNA by the Feulgen-type method (Cogliati and Gautier, 1973)
- Immuno-cytochemistry
- Transmission electron microscopy

5.5 Immuno-cytochemistry and DNA counterstaining

5.5.1 Standard protocol

Materials:

Fixed and permeabilized cells on coverslip in PBST (see 5.4)
Bovine serum albumin (BSA)
PBST (0.01% Tween/PBS)
Primary antibody stock solution (see list in 8.2)
Secondary antibody stock solution (see list in 8.2)
Water bath 37°C
Humidified chamber
Parafilm
Vectashield embedding medium (antifade)
Object slide
Counterstain solution (see 8.3)
Nail polish
optional: HCl (0.1N) and DNase stock solution (2 U/µl)

Method:

- Prepare blocking solution (2%BSA) by dissolving 2 g BSA in 100 ml PBST
- Prepare primary and secondary antibody working solutions (according to dilutions listed in 8.2) by dilution in blocking solution
- Incubate fixed and permeabilized cells on coverslips for >10 min in blocking solution
- Wash coverslip with cells 3x 5 min in PBST

- Place drop of primary antibody solution (~50µl) on a piece of Parafilm and incubate coverslip with cells for >45 min (or overnight) upside-down on this solution in a humidified chamber at 37°C
- Wash coverslip with cells 3x 5 min in PBST
- Place drop of secondary antibody solution (~50µl) on a piece of Parafilm and incubate coverslip with cells for ~30 min upside-down on this solution in a humidified chamber at 37°C
- Wash coverslip with cells 3x 5 min in PBST
- Place drop of counterstain solution (~50µl) on a piece of Parafilm and incubate coverslip with cells for 2-5 min (according the dye used, see 8.3) upside-down on this solution
- Wash coverslip with cells 1x in PBST
- Embed coverslip with cells upside down on an object slide with Vectashield antifade medium
- Seal specimen with nail polish

Optional modifications to ensure antibody accessibility to the interior of compact chromatin:

- incubate coverslip before blocking with cells for 10 min in 0.1 N HCl
- Add DNase to the primary antibody solution to a working concentration of 20 µg/ml

5.5.2 Sequential Immuno-labeling protocol

Materials:

All material listed in 5.5.1

Cy3-conjugated Fab fragment (see 8.2)

Non-conjugated Fab fragment (see 8.2)

Background:

If two primary antibodies raised in the same animal are to be used in the same experiment, a modified protocol for immuno-labeling has to be applied to prevent cross-detection. The main steps of this protocol are: [1] incubation with the first antibody followed by [2] its detection with a fluorochrome-coupled secondary antibody Fab fragment. This is followed by incubation [3] with a non-coupled secondary antibody Fab fragment. This small molecule binds all accessible left over binding sites. After the subsequent incubation with the next primary antibody [4], its specific detection with another fluorochrome-coupled secondary antibody [5] can not lead to cross detection anymore.

Method:

- Follow protocol 5.5.1 to the washing step after the primary antibody detection

- Incubate coverslip with cells in Cy3-conjugated Fab fragment for 45 min at 37°C in humidified chamber
- Wash 2x 10 min in PBST
- Incubate coverslip with cells in non-conjugated Fab fragment for 45 min at 37°C in humidified chamber
- Wash 2x 10 min in PBST
- Proceed with secondary antibody detection and further steps as in protocol 5.5.1

5.6 Treatment of living cells

5.6.1 Permeabilization of living cells

Materials:

Cells growing on coverslip (semi-confluent) in Petri-dishes / 6-well plates
Appropriate growth medium, pre-warmed to 37°C
Digitonin stock solution (10 mg/ml)
CMF-PBS
Trypan blue (0.5 %)
Phase contrast microscope

Background:

This treatment leads to a 'mild' permeabilization of the membrane of living adherent cells by means of no obvious cell destruction or detachment from the coverslip. The given protocol results in 95% permeabilized cells of a HeLa cell culture. Longer incubations as well as higher concentrations of Digitonin lead to detachment and destruction of cell integrity. Since the effect of Digitonin permeabilization is not transient, cells will die after longer subsequent incubation.

Method:

- Vortex Digitonin stock solution
- Take an appropriate aliquot (>20 µl) and solubilize for 20 sec at 95°C
- Prepare permeabilization solution by diluting the solubilized aliquot 1:250 in growth medium to a final concentration of 40 µg/ml
- Incubate cells for 2 min in permeabilization solution
- To check the efficiency of permeabilization apply a drop of Trypan blue solution to 2 ml of the permeabilization solution and observe cells under the phase contrast microscope. Since an intact cell membrane is impermeable for Trypan blue molecules, efficient permeabilization can be confirmed for cells getting stained blue.

5.6.2 Induced formation of hypercondensed chromatin (HCC)

Materials:

Cells on coverslip (semi-confluent) in Petri-dishes / 6-well plates

Appropriate growth medium, pre-warmed to 37°C

20x PBS

Background:

This treatment leads to the formation of hypercondensed chromatin (HCC). The effective factor is the osmolarity of the condensation medium. Standard growth medium has a physiological osmolarity of 290 mOsm. Hypercondensation of chromatin occurs at concentrations of >500 mOsm. The condensation medium of this protocol was measured to be ~750 mOsm. Using higher concentrations does not effect further condensation if not longer incubation periods are applied.

Method:

- Prepare condensation medium (~750 mOsm) by adding 1 ml of 20x PBS to 9 ml of growth medium (~290 mOsm)
- Incubate cells for 5 min in condensation medium

If cells with hypercondensed chromatin are to be fixed

- carry on immediately with transferring coverslips with cells to the fixation solution without any washings in CMF-PBS since this would instantly result in the reversal of the effect.

To reverse the effect of hypercondensation back to normal condensed chromatin:

- Incubate cells for 5 min in growth medium (or any other solution with 290 mOsm)

Excursus: hyper-osmotic fixation solutions

Since hyper-osmotic conditions immediately trigger the described chromatin condensation effect (see Results 6.2), why do untreated living cells, fixed for 10 min in a hyper-osmotic solution (e.g. 3.7% formaldehyde: ~1750 mOsm), not display hyper-condensed chromatin as well? An explanation could be that the osmotic equilibrium is achieved faster by a huge amount of paraformaldehyde penetrating the cells than by the small amount of water evaporating from the cells due to external hyper-osmotic conditions. The osmotic gradient between the cells interior and exterior would accordingly be compensated immediately keeping the volume of the cells and nuclei constant.

5.7 Technical protocols

5.7.1 Measuring osmolarity

Materials:

Solutions with unknown osmolarity

dd H_2O (0 mOsm)

Calibrated solution (300 mOsm) (=946.3 mg NaCl in 100 g dd H_2O)

Freezing point Osmometer with tubes

Background:

This method measures the osmolarity of a solution. Osmolarity is the concentration of all osmotic active particles in a solution (e.g.: 1M NaCl ~ 2 Osm, since 1 molecule NaCl dissociates to two atoms: 1 Na^+ and 1 Cl^-). Osmolarity can be measured by the freezing point depression of a given solution due to its solved particles. An osmometer starts with fast deep-cooling of a solution down to -7°C without effecting crystallization. Immediately thereafter a needle is shot in the solution which acts as a seed crystal yielding crystallization of the solution accompanied by an increase of the temperature of the solution. As soon as this temperature reaches a constant value, the osmolarity is calculated and displayed.

Method:

- Pipette appropriate amount of calibration solutions (0 mOsm and 300 mOsm) in separate tubes
- Perform a two-point-calibration with these samples according to the manual
- Pipette appropriate amounts (~200 µl) of the solutions with unknown osmolarity in tubes
- Measure osmolarity of these samples according to manual approx. 3x and calculate the mean

Osmotic values measured for the solutions used in this thesis:

Solution	**composed of:**	**mOsm**
standard treatments		
hyper-osmotic solution 1	1/10 20xPBS in medium	750
hyper-osmotic solution 2	1/20 20xPBS in medium	570
hyper-osmotic solution 3	1/25 20xPBS in medium	480
hyper-osmotic solution 4	1/33 20xPBS in medium	425
hyper-osmotic solution 5	1/50 20xPBS in medium	380
hyper-osmotic solution 6	1/100 20xPBS in medium	340
extreme treatments		
hyper-osmotic solution 7	6/100 20xPBS in medium	570
hyper-osmotic solution 8	7/100 20xPBS in medium	610
hyper-osmotic solution 9	1/4 20xPBS in medium	1310
hyper-osmotic solution 10	1/3 20xPBS in medium	2010
hyper-osmotic solution 11	1/2 20xPBS in medium	3050
hypo-osmotic treatment		
hypo-osmotic solution 1	1/5 water in medium	260
hypo-osmotic solution 1	1/3 water in medium	180
hypo-osmotic solution 1	1/2 water in medium	145
hyper-osmotic salts		
hyper-osmotic NaAc	220 µl 3M NaAc in 2 ml medium	820
hyper-osmotic Saccharose	220 µl 3M Sac. in 2 ml medium	450
hyper-osmotic NaCl	110 µl 3M NaCl in 2 ml medium	540
hyper-osmotic KCl	100 µl 3M KCl in 2 ml medium	500
buffers and fixatives	*diluted in*	
1xPBS	water	310
0.75xPBS	water	235
0.5xPBS	water	160
0.3xPBS	water	100
1x PBS	3.7% formaldehyde (from solution)	1750
1x PBS	4% PFA (from powder)	1380
0.75x PBS	4% PFA (from powder)	1340
0.5x PBS	4% PFA (from powder)	1300
0.3x PBS	4% PFA (from powder)	1200

5.7.2 Microinjection

Materials:

Adherent cells growing on round (42 mm) coverslip (semi-confluent)
living cell chamber system *POC*
Centrifuge (Biofuge pico)
Appropriate growth medium, HEPES buffered and pre-warmed to 37°C
Injection solution
Microloader tip
Microinjection capillary
Microscope stage with heating chamber
Microinjection device
Alexa-633

Background:

This protocol works for the Eppendorf Microinjection device '*FemtoJet*' coupled to '*InjectMan*'. For a detailed description of the system see manual. To calibrate the system and to have a better control on the injection process, it is advisable to always include a fluorescent marker in the injection solution. Over the course of this study dextran-conjugates (e.g. FITC-dextran) as well as the alexa-633 hydrazide have successfully been used as markers, which do not harm the cell if used in appropriate concentrations, but which allow the visual inspection of the progress of injection.

Since microinjection is a very sophisticated application, it is not suited to label or treat a large amount of cells (>300). For such experiments it is indicated to apply the scratch-labeling technique (see 5.3.2). However, microinjection is the only approach which enables an observation before and after the labeling of single living cells.

Method:

- Mount *POC* chamber in the 'open' configuration and install it on the microscope stage with a running heating chamber (37°C)
- Centrifuge injection solution for 30 min at 13000 rpm to spin down unsolved particles which might block the capillary
- Pipette 3 µl of injection solution with a Microloader tip
- Open a capillary by removing its cap and gently load the capillary with the Microloader so that the solution comes as close as possible to the tip of the capillary without any air bubbles inside the solution
- Install the loaded capillary at the microscope stage and apply pressure to push the solution to the very front of the tip of the capillary
- Bring the capillary down to the solution and close to the cells

- Start microinjection with default parameters for injection pressure [Pi], compensation pressure [Pc] and injection time [t]
  (e.g. for HeLa cells: Pi 130-180 hPa; Pc: 30 hPa; t=0.3 sec)
- Calibrate parameters [Pi and t] so that cells are not 'blown-up' but still take-up sufficient amounts of injection solution and [Pc] so that the injection solution is continuously leaking from the capillary inhibiting a soaking up of solutions by capillary forces

5.8 Microscopy

5.8.1 Confocal laser scanning microscopy

The confocal microscopes used over the course of this thesis comprised a *Zeiss LSM 410*, a *Zeiss LSM 510* and a *Leica TCS SP2*. These systems differ to some extent in their specific compositions and equipments (see 8.4). In general confocal microscopy of fixed specimen was performed with the following parameters:

- Laser excitation power was set to the highest possible value not causing obvious photobleaching
- Photomultiplier sensitivity was adjusted as low as possible to prevent overexposure and 'electronic noise', but to yield images which cover the whole range of gray values (0-255 for the 8-bit image format)
- the filters (*LSM 410*) respectively the filter ranges (*LSM 510* and *Leica SP2*) were adjusted not to implement light emitted by other channels
- The 'Contrast' (*LSM 410*) respectively the 'Offset' (*LSM 510* and *Leica SP2*) were adjusted to prevent underexposure, but to yield images which cover the complete range of gray values
- The zoom was set to obtain a lateral voxel resolution of 50x50 nm
- The z-step size was set to 200 nm (LSM 410) respectively 120 nm (*LSM 510* and *Leica SP2*)
- The 4x 'averaging' was used
- The pinhole size was adjusted to ~1 airy unit
- Chromatic shifts were measured and corrected as described in 5.8.3 and 5.9.1

5.8.2 Living cell observations

Materials:

Adherent cells growing on round (42 mm) coverslip (semi-confluent)

Living cell chamber systems *POC*, or *FCS-II*, or living cell culture dish *µ-slide-I*

Appropriate growth medium, HEPES buffered and pre-warmed to 37°C

Trolox (100 mM)

Microscope stage with heating chamber

Confocal microscopes (Zeiss *LSM 410, LSM 510; Leica SP2*)

Background:

To perform living cell observations some particular acquisition parameters have to be adapted in regard to the high sensitivity of living cells to light exposure:

- Laser excitation power has to be set to the lowest possible value which still leads to a sufficient excitation of the fluorochromes
- Photomultiplier sensitivity has to be adjusted with a higher voltage as usual, since the low excitation and concomitant low emission demand a more sensible detection
- The zoom was kept to obtain a lateral voxel resolution of 50x50 nm, unless a lower resolution (~200x200 nm) was of similar sufficiency
- The z-step size was increased in some cases to further minimize total light exposure
- The 'averaging' was set to 1x or maximal 2x
- In rare cases (mainly the FRAP experiments) pinhole size was opened to >1 airy unit to allow an enhanced signal detection

Methods:

- Short-term observations:

- Mount *POC* chamber in the 'closed' configuration and install it at the microscope stage with a running heating chamber (37°C)
- Start microscopy with light exposure kept to a minimum

- Long-term observations:

- Mount *FCS2* chamber as described in Schermelleh, 2003 and Walter et al., 2003 and install it at the *Zeiss LSM 410* microscope stage with a running objective heater (37°C)
- Use the setup described in Schermelleh, 2003 and Walter et al., 2003 and perform microscopy with light exposures kept to a minimum

- Fluorescence-Recovery-after-Photobleaching (FRAP):

- Mount *POC* chamber in the 'closed' configuration and install it at the *Zeiss LSM 510* microscope stage with a running heating block (37°C)
- Use the 'FRAP' module of the *Zeiss LSM 510* software
- Center a nucleus of interest and define a region-of-interest (ROI) to be bleached

- Bleach ROI to background level with the maximal laser power and as little averages as sufficient (calibrate these parameters with fixed specimen)
- Record time series of the optical section in minimal time steps covering the fast fluorescence recovery period in the beginning
- Increase time step duration to minimize light exposure and allow a prolonged observation until no obvious further recovery is detected
- Proceed with Image analysis as described in 5.10.6

5.8.3 Measuring the chromatic shift

Materials:
Fluorescent beads: *Tetraspeck*
Coverslip
Object slide
Vectashield embedding medium (antifade)
Nail polish
Confocal microscope

Background:

Different laser lines of a confocal microscope can never be calibrated 100% to exactly the same optical focus. Slight misalignments (shifts) between different color channels are the consequence, which [1] can be measured and [2] can be corrected after image recording. These measurements are performed by imaging fluorescent beads with spectral signatures matching the laser lines used.

Method:

- Preparation of *Tetraspeck*-bead slide:

- Pipette appropriate amount of *Tetraspeck*-bead solution on coverslip
- Incubate coverslip overnight or till the complete evaporation of the added solution. The desiccation usually leads to the permanent adherence of beads to the coverslip. If detachment of beads is still observed, the use of coverslips covered with Poly-L-Lysine (see 5.1.4) is recommended
- Mount coverslip on object slide with Vectashield
- Seal specimen with nail polish

- Measurement of chromatic shift:

- Install *Tetraspeck*-bead slide on microscope stage
- Focus beads so that ~10 beads are comprised in an 512x512 pixels image at a resolution of 50x50 nm pixel size

- Record image stacks (comprising the entire volume of the beads) separately for all color channels with a voxel-size of 50x50x120 nm and a 4x average
- Proceed with image processing and analysis as described in 5.9.1

5.9 Image Processing

5.9.1 Correction of the chromatic shift

Materials:

Image stacks of different color channels comprising ~10 *Tetraspeck* beads

raw Leica file series to be Z-shift corrected

ImageJ, including the plugins *Sync Measure 3D* and *StackGroom / Shiftcorrector*

Excel

Background:

The chromatic shift gets obvious when overlaying different color channels which contain the same fluorescent object (e.g. a *Tetraspeck* bead). Calculating the coordinates of the barycenter of the same bead in different channels delivers the geometrical vector of the shift between the channels, with which they can be corrected thereafter. Since confocal images are limited to the dimensions of single voxels, image shift corrections can only be executed with full-voxel step sizes. Since the lateral shifts (x-y) are usually only very small (~50-150 nm) only Z-shifts are commonly corrected. Z-shift correction can be performed with the plugin *Shiftcorrector* developed by Dr. B. Joffe, which deletes the first or last slices of the image stacks to yield a best-fitting alignment in Z compensating for the chromatic shift. *Shiftcorrector* has a defined demand on the file naming and works well with raw Leica file series. Note that every nucleus has to be saved in a subfolder and no additional files are allowed in the main folder as this leads to a crash of the plugin. The plugin reads the information on chromatic shift out of a text-file in which the different channels are sorted according to their emission lights: (b)lue, (g)reen, (o)range, (r)ed and (f)ar red. Since one channel has to act as referee, where all other channels will be aligned to, one should choose the particular channel, where all other channels have a positive shift to. This channel will be given the value 0 (no beginning slice of the stack will be deleted). According to the measured chromatic shifts, a certain number of beginning slices of the stacks of the other channels have to be deleted (e.g. 1= the first; 2= the first and the second or 0= no slice). To equalize the number of slices obtained in the different channels after Z-shift correction, the software automatically deletes slices in the end of the channels till all channels have the same amount of slices

Methods:

- Measure chromatic shift

- Load bead image stacks in *ImageJ* and analyze chromatic shift with the use of the plugin *Sync Measure 3D* developed by Dr J. Walter.
- Save chromatic shift vector information for subsequent shift corrections in an *Excel* file

- Correct chromatic shift

- round Z-shift vectors to whole voxel values according to the voxel-size in the data sets which are to be corrected. Thereby, minimize the left-over shift summed up for all color channels after shift correction (e.g.: Z-voxel-size: 250 nm; Z-shift: 300 nm → left-over shift of 50 nm)
- Create a text-file (e.g. *actual_shift.txt*) matching the demands of the plugin *Shiftcorrector*
- Start the plugin *Shiftcorrector* and choose the text-file containing the actual shift
- Define the order in which the different color channels had been recorded (leave out non-recorded channels)
- Choose the main folder in which the raw Leica image series are saved

The plugin will automatically open all stacks consecutively, will delete first or last slices according to the text-file and will save shift corrected files in a new folder

5.9.2 Deconvolution

Materials:
Raw confocal stacks
Deconvolution software *Huygens (SVI) Essential 3.5*
For all deconvolution parameters to be set see list in 8.5
Fluorescent beads: 175 nm, for each color channel
Confocal microscope

Background:

Since deconvolution of confocal images was not commonly applied in the beginning of this thesis, its establishment and standardization was the first aim of this study. The methodological part comprehending deconvolution is therefore kept short since the proof of reliability is described and discussed in detail in the corresponding results chapter (see Results 6.1).

Methods:

- Preparation of 175 nm-beads slide:

- Follow protocol 5.8.3 but substitute the *Tetraspeck*-beads with the fluorescent 175 nm beads. Since these beads are available with different spectral signatures (blue, green,

orange and red), it is advisable to make separate slides for each signature to facilitate the subsequent recording.

- Measuring the Point-Spread-Function (PSF):

- Record stacks for each laser line with the 175 nm-beads slide best-matching with its spectral signature. Thereby, use an image size of 512x512 pixels and a voxel dimension of 50x50x120 nm.
- Open the recorded image stacks with the *Huygens* software and distill the corresponding PSFs according to the manual (for detailed description of the parameters see 8.5)
- Save PSF files for subsequent deconvolution of confocal image stacks separately for each spectral signature in the '.ics' and '.ids' file format

- Deconvolution of single stacks:

- To deconvolve a single image stack, open it with the *Huygens Essential* software
- Additionally open the corresponding PSF file
- Start deconvolution according to the manual (for parameters see 8.5)
- Save deconvolved image stacks

- Deconvolution of multiple stacks (batch mode):

- To deconvolve multiple stacks start the computer in the Linux mode
- Save the raw image stacks, the corresponding PSF files and the three *Huygens* files ('batchCtl.tcl', 'restOneImage.tcl' and 'doBatch.tcl') in the same folder
- Open the 'batchCtl.tcl' file with *Kwrite*, adapt all parameters (see 8.5), define the stacks to be deconvolved and save the processed 'batchCtl.tcl' file
- Start deconvolution by executing the 'doBatch.tcl' file

The software will deconvolve all selected image stacks according to the information in the 'batchCtl.tcl' and 'restOneImage.tcl' files and will save them in a subfolder named 'Results'.

5.10 Image analyses

Image analyses were predominantly performed with the public domain program *ImageJ* (http://rsb.info.nih.gov/ij/) and its implemented plugins down-loaded from the *ImageJ* website or the website of the *Wright Cell Imaging Facility* (WCIF), Toronto, Canada (http://www.uhnresearch.ca/facilities/wcif/imagej/). This methodological part is limited to special measurements performed over the course of this thesis. For standard measurements (e.g. lengths, areas or intensity histograms) see the *ImageJ* manual (http://rsb.info.nih.gov/ij/download.html).

5.10.1 Measuring co-localization

- Start *ImageJ*
- Open the two color channel stacks whose co-localization is to be determined
- Apply a gray value threshold separately for each stack, which sets every out-of-signal voxel to zero, but leaves the signal voxels unchanged with their original gray values
- Run the plugin *Manders coefficients*

The calculated values are the Pearson correlation coefficient (Rr), the Manders overlap coefficient (Rc) and the Manders colocalization coefficients M1 and M2 (for detailed description of the values see Manders et al., 1993).

The Pearson coefficient (Rr) adopts values between [-1 and +1] and is only suited, if a trend inside of one population of data points is to be measured. Since co-localization analysis in case of images includes a comparison between two (potentially completely separated) populations of data points, Rr is an inadequate coefficient for this kind of evaluation. This fact becomes obvious, when evaluating two completely separated signals, where Rr will never adopt its negative extreme [-1], but a value around [0]. In fact, [-1] would correspond to a perfect inverse correlation (the strict concurrence of the highest value in image A falls with the lowest value in image B, the second highest in A with the second lowest in B, etc.) which can not be expected in the images investigated.

The Manders overlap coefficient Rc, on the other hand, is a value providing information on the percentage of overlap between two different populations of data points and adopts values between 0 (complete separation) and 1 (perfect co-localization). The limitation of this value consists in the amount of signal voxels of the two channels, which needs to be roughly similar. If the first channel comprises considerably less voxels than the second, a complete overlap (e.g. image A embedded completely in image B) would deliver a value below 1, since not all voxels of the bigger channel are in concurrence with voxels of the smaller channel.

In these cases it is advisable to limit the analysis to the Manders colocalization coefficients M1 and M2 to describe the data overlap. These values deliver the percentage of overlap separately for each channel (how many overlap of image A with image B; and how many overlap of image B with image A). However these coefficients do not integrate the information on the gray value ratio between the two channels at each single voxel
In summary, all values consider the intensity of the corresponding voxels. Rr and Rc compare the data sets on a voxel-by-voxel based analysis, whereas M1 and M2 consider both data sets only as complete units.

5.10.2 Measuring circularity and Feret's diameter

Background:

The circularity of an object in 2D can be defined by ($c= 4\pi$ X area/perimeter^2) and is a description of the roundness of the object (a perfect circle adopts the value 1). The Feret's diameter is defined as the largest diameter of an object in 2D. Both values can be easily obtained by measurements in ImageJ.

Method:

- Start *ImageJ*
- Load the 2D image comprising the objects to be measured
- Set voxel dimensions in *Image/Properties…*
- Select *Analyze/Set Measurements/*
- Activate *Circularity* and *Feret's diameter*
- Select *Image/Adjust threshold*
- Select the gray value threshold yielding the best-matching segmentation of the object of interest (no applying of the threshold needed)
- Outline the thresholded object by clicking it with the magic wand tool
- Select *Analyze/Analyze Particles*

5.10.3 Measuring intensity shifts

Background:

Shifts in the frequency distribution of gray values of a 3D image stack can occur, when e.g. chromatin of a nucleus gets more compacted over time (e.g. by induced formation of hypercondensation). This leads to an increase of the amount of bright voxels accompanied by a decrease of frequencies for lower gray values.

Method:

- Start *ImageJ*
- Load the 3D image stacks comprising the object during the different treatments

- Activate the first image stack and select *Edit/Selection/ Select All*
- Select *Analyze/Histogram/* and include all sections of the stack
- Select *Copy* in the Histograms window
- Open an *Excel* sheet and paste the copied histogram values
- Repeat all steps for the other channels
- Calculate all values to a logarithmic scale for better readability
- Calculate the total sum of intensity obtained for each stack
- Normalize all values for each stack to its total sum of intensity

5.10.4 Measuring intensity profiles

Background:

Intensity profiles allow an easy insight into gray value progressions, especially for comparisons of the intensities between two channels which are plotted correspondingly.

Method:

- Start *ImageJ*
- Load the 3D image stacks comprising the two channels
- Synchronize the stacks by selecting *Analyze/Tools/ Synch Windows*
- Draw a line with the Line tool (or region of interest with the Rectangular tool)
- Select *Analyze/Plot Profile* in the Histograms window
- Select *Copy* in the Histograms window
- Open an *Excel* sheet and paste the copied histogram values
- Repeat all steps for the second channels (where the same line was drawn)
- Plot values for each channel

5.10.5 Measuring the similarity of image stacks

These measurements were performed in the laboratory of Prof. R. Eils at the DKFZ, Heidelberg by S. Yang under the supervision of Dr. K. Rohr. For a detailed description see Albiez et al., 2006. Briefly, the sum-of-squared-differences was calculated for normalized histograms of two image stacks comprising the same nucleus after different treatments. Finally the mean squared error (MSE) of these differences was computed and held as a value for similarity/dissimilarity (MSE = 0 for comparing the same data set with itself). For reasons of better readability all resulting values were multiplied with 10^7.

5.10.6 Analyzing FRAP data sets

Background:

FRAP data sets comprise an image series of the same optical section before any treatment ('pre-bleach') and sections recorded in dedicated time steps after the bleaching ('post-

bleach') (see 5.8.2). The matter of interest is the recovery of intensity over time in the bleached region. Before plotting the recovery in the post-bleach series, the raw data set has to be corrected for background fluorescence (e.g. detector read-out noise), and for the amount of fluorescing molecules over time, which changes by laser fluctuations, acquisition photobleaching and due to the loss of intensity during photobleaching. Finally the data sets are normalized to the pre-bleach values to enable comparisons between different experiments.

Method:

- Start *ImageJ*
- Load the FRAP data set
- Run the plugin *TurboReg* to correct for movements of the fluorescent object over time
- Outline the bleached region-of-interest (ROI)
- Measure the mean pixel intensity of ROI for the complete data set (comprising pre- and post-bleach series) by *Analyze/Plot Profile* and copy the resulting values in an Excel-sheet
- Define the mean background intensity for the complete data set by outlining an out-of-object region (with a similar size as the ROI) and measure and save the mean pixel intensity accordingly
- Outline the complete fluorescent object (comprising bleached and un-bleached regions) and determine and save the mean total object intensity for the complete data set accordingly
- Change to the *Excel* sheet containing the obtained values
- Subtract the mean background intensity value of the mean values of the ROI for each time point (pre- and post-bleach)
- To correct for fluctuations of total intensity, divide each background subtracted ROI value by its corresponding mean total object intensity value for each time point
- Determine the mean pre-bleach value of the ROI out of the sections comprising only the pre-bleach phase
- Normalize data set to the pre-bleach phase (=pre-bleach values are set to 1) by dividing each corrected ROI value with the mean pre-bleach value

5.10.7 Enhanced Distance Measurement Tool (EDMT)

Materials:

Confocal image stacks ('signal stacks')

Confocal image stack ('reference stack')

EDMT software including *EDMT* (v 3.00a) and the *Filemaker* (v 2.10)

Background:

In the course of this thesis, the existing ADS program (**A**bsolute-**D**istance-to-**S**urface) developed by Dr. J. von Hase (Kirchhoff Institute for Physics, University of Heidelberg) was enhanced and essentially improved (all related programming work kindly done by the diploma student T. Thormeyer (Albiez et al., 2006; Thormeyer, 2005). The outcome was a software tool, which allows distance measurements between signals of different color channels (*EDMT*: **E**nhanced **D**istance **M**easurement **T**ool). This basic application is capable of a variety of sub-routines, one of which is eADS (enhanced Absolute-Distance-to-Surface), which performs measurements of the shortest distance of a signal to the surface of a signal depicted in a second channel. The advancement achieved with eADS comprises its much more transparent algorithm, the easy-to-use Windows-based interface and the extreme speedup (>100x) of computation time compared to the old ADS. A detailed description of the algorithm can be found in Thormeyer, 2005.

Methods:

- Generating a parameter text file:

- Start the *Filemaker* and fill out the form according to the manual (see Thormeyer, 2005).One can implement several signal channels and one reference channel, which comprises the surface to which the distances will be measured
- Save filled-out form as a parameter text file (with the ending '.ads.txt') for subsequent measurements and evaluations

  Important notes:

  a) Always use the *Filemaker* to change parameter files, since the software is very sensitive to tiny errors like comma displacements, left-out spaces, etc.

  b) Do never use minus (-) or plus (+) or space ( ) in your file naming since these may be interpreted by the program as functional commands

  c) Do not use 01, 02, 03,…to start the consecutive numbers in your file names but start with 1, 2, 3, …

  d) If you have to leave out nuclei: Do never exclude the last nucleus, but just end the evaluation with the one before

- Run a distance-to-surface measurement and a distances evaluation:

- Start *EDMT*

- Check the parameter text file by selecting '5' (*Start parameter file check*) and choosing the parameter text file. Correct parameter-file if necessary
- Run the distance measurements by selecting '3' (*Start Ultra Rapid Distance Measurement*) and choosing the parameter text file

- Run distance evaluation only:

- Start *EDMT*
- Run the distance evaluation by selecting '4' (*Start Distance Evaluation*) and choosing the parameter text file

The program will measure the distances of all signals in the different channels to the closest surface of signals in the reference channel and will weight them according to the intensity gray value of the corresponding voxel. It will save ASCII-sheets (readable e.g. by Excel) containing the percentages of distance frequencies assigned to classes of distances separately for each channel and nucleus and the corresponding means calculated over all nuclei. Additionally a multitude of statistical values including medians, quartiles and inter-quartiles (weighted by intensity and non-weighted), are given at the end of the sheet. A macro written by T. Thormeyer for *Excel* ('*EDMT-Excel*') working on theses ASCII-sheets facilitates the generation of graphs representing the data.

Important notes:

a) The options '1' (*Start Iterative Distance Measurement*) and '2' (*Start Non-Iterative Distance Measurement)* start measurements based on outdated algorithms and are no longer required.

b) The error message '*…File… does not exist…*' indicates that (1) the file naming in the parameter file does not correspond to the real file naming or (2) the assigned file path does not exist or (3) the files are not placed in the assigned file path.

c) The error message '*…exceeds matrix dimensions…*' indicates that (1) the stacks of the different color channels do not have the same number of slices (equivalent to not the same file size) or (2) that the signals in the stacks touch the image edges or (3) that there are no signals left over after applying the gray value and object thresholds.

d) The error message '*… out of memory...*' indicates that the calculated distance files exceed the memory capacity of the respective computer. This problem can be solved by reducing the amount of measured signals by deleting a randomly chosen subset of signal voxels.

- Generating a control channel:

To test measured signal distributions for their non-randomness, a control distribution on the entire 3D volume of an HCC nucleus, which comprises HCC bundles plus the entire interchromatin compartment and nucleoli has to be generated. This control channel was generated as a black and white mask, obtained by applying the 'Signal Cutter', an algorithm provided by T. Thormeyer over the course of his diploma thesis (Thormeyer, 2005). This program opens the HCC bundle channel, which gets filtered, expanded and filled until a best-fitting mask, covering the entire 3D nuclear volume is obtained. Measuring the distance distribution of all voxels belonging to this mask against the HCC bundle surface provides a control distribution as displayed in Fig. 23B (yellow bars)

- Gray value threshold dependency:

Working with distance measurements against folded surfaces like the one of HCC bundles demands to test for the dependency of the resulting distributions on the gray value thresholds applied in the program. Since all evaluated images were subjected to deconvolution, the potential error of segmenting out-of-focus light was diminished (see 6.1.7). In several diploma studies (Musoski, 2005; Thormeyer, 2005; Zunhammer, 2006), supervised over the course of this thesis, it was demonstrated that applying a range of gray value thresholds above or below the user chosen optimal threshold had no major effect on the distance distributions of the signals. Varying the threshold for the reference structure (HCC-bundles), however, led to significant shifts of the distributions. Nevertheless, different signal distributions shifted in the same directions and to similar extents keeping their relative arrangement to each other constant. This demonstrated the reliability of relative statements (signal A in relation to B, if both measured against C) but the threshold dependency of direct statements (signal A has a distance of x µm to C).

6 RESULTS

6.1 Deconvolution

Since diffracted light is present in all confocal optical sections it hinders the choice of a single threshold segmenting whole nuclei to a satisfying extent in all nuclear sub-regions. Deconvolution, a method that reduces this diffracted light, was not commonly used on confocal images at the beginning of this study. Accordingly, the first aim was to test and eventually modify protocols for deconvolution of confocal images. At this point it is important to stress that the final goal was not to enhance image resolution to a maximal level by applying deconvolution with optimal parameters. In fact, deconvolution in this context would already be defined reliable, if [1] diffracted light got diminished to an extent allowing proper segmentation by a single threshold and simultaneously [2] the generation of artifacts was excludable. Different approaches on how to test deconvolution are presented.

6.1.1 Measuring the Point-Spread-Function (PSF)

Before performing deconvolution, the point-spread-function (PSF) of each objective and excitation wavelength used had to be measured. For this purpose, 3D data sets of fluorescent nano-spheres (175 nm) were collected separately for each laser line. These data sets were imported in the Huygens deconvolution software and their PSFs were calculated and saved for subsequent deconvolution of confocal data sets. The quality of the PSFs that were obtained in this manner was controlled visually from the symmetry of the resulting data set in lateral and axial direction. An example of a good PSF is displayed in Figure 2. The typical elongated appearance is caused by the dissimilar lateral and axial resolution in confocal microscopy (lateral >200 nm; axial >500 nm).

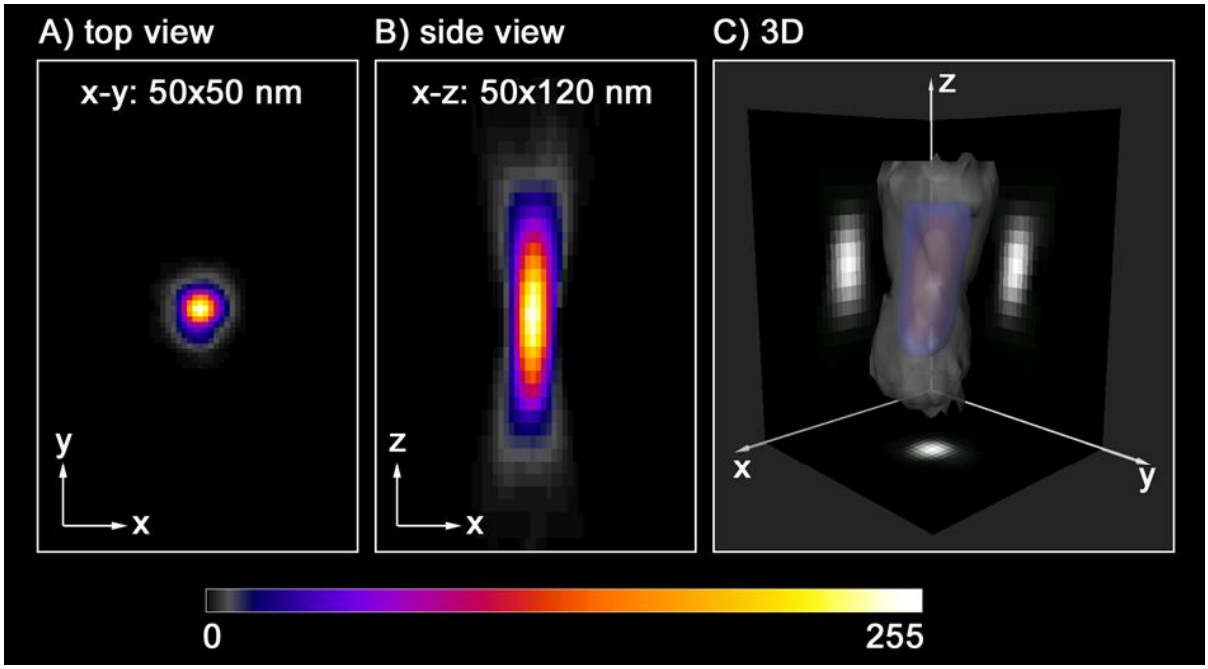

Figure 2: Example of a PSF for a 1.4 NA oil objective and 488 nm excitation

Top- (**A**), side- (**B**) and 3D-view (**C**) of a typical PSF measured on the Leica SP2 confocal microscope using the plan Apo 63x/1.4 oil objective and an excitation wavelength of 488 nm (Argon-Laser). Images were recorded with a voxel size (x-y-z) of 50-50-120 nm. Intensity values in (**A**) and (**B**) are displayed false-colored according to the assigned color table (0-255).

6.1.2 Restoration of volume and shape of fluorescent nano-beads

As a first approach to test deconvolved confocal images, the geometry of synthetic fluorescent nano-spheres of known volume and shape was measured before and after deconvolution of 3D confocal data sets. According to the manufacturer these spheres have a diameter of 500 ± 20 nm and an almost spherical geometry (Fig. 3). Deconvolution led to a clear reduction in the electronic 'noise' detectable as single voxels in the low threshold range in raw images (e.g. Fig. 3A: raw image) due to the intrinsic filtering in the deconvolution process. At first glance, small values for the signal-to-noise ratio (SNR: 5-20) reached the best restoration in terms of regular shape whereas higher values for the SNR yielded increasingly irregular geometries. To quantify this data, the volume (3D) and circularity (2D in mid-sections) of the nano-spheres (n>20) were measured and plotted against thresholds ranging from 20 to 200 (Fig. 3). Since deconvolution can not completely compensate for the anisotropic resolution of confocal microscopy (see Fig. 2), the best volume that could be obtained was of elongated appearance and accordingly slightly larger than the ideal sphere volume plotted here. Nevertheless, the values obtained for deconvolved images showed on the whole less deviation from the theoretical ideal volume (Fig. 3B: green line) than the values of the raw data set.

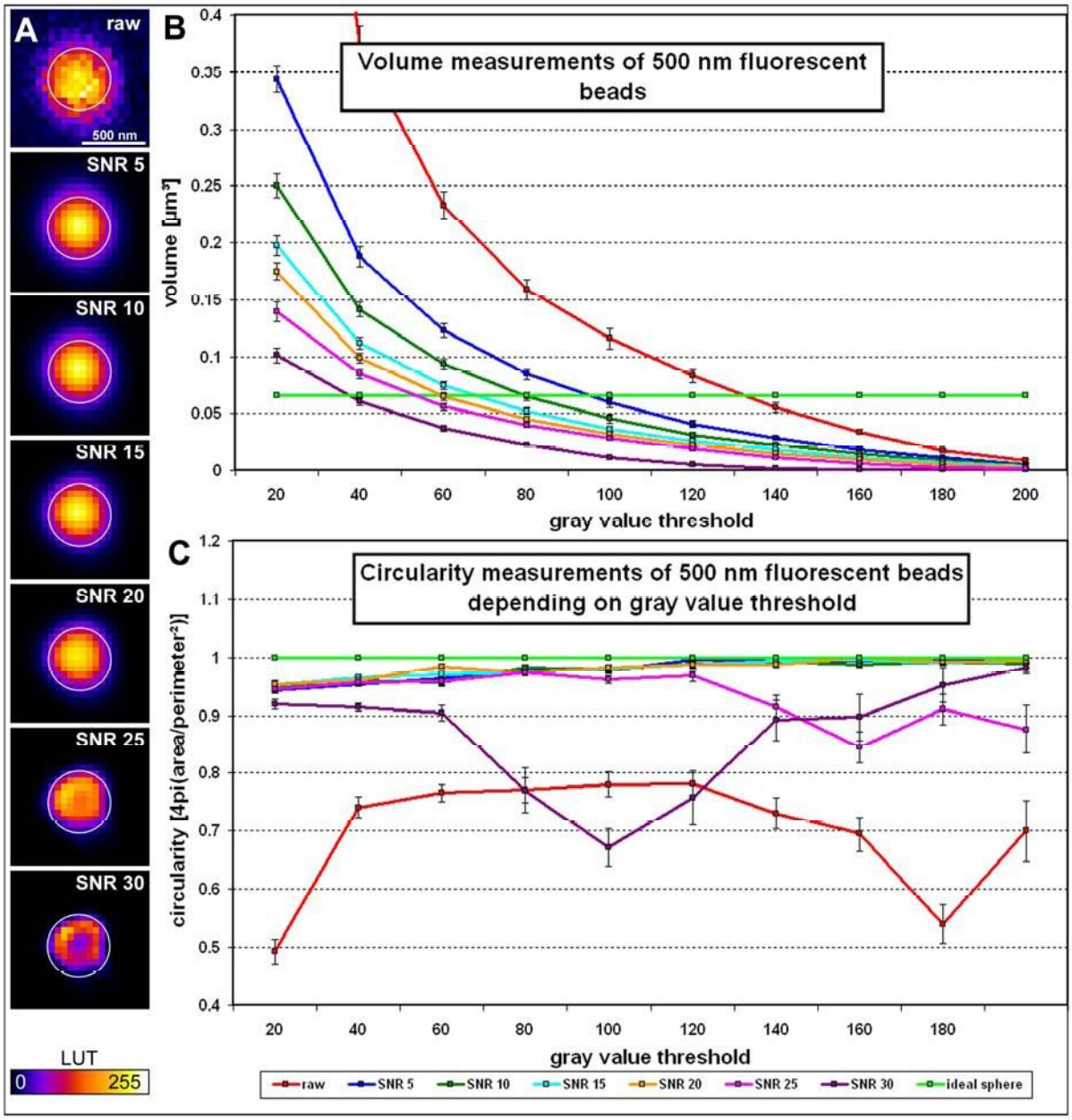

Figure 3: Restoration of volume and shape of fluorescent 500 nm nano-spheres after deconvolution

A) Confocal mid-sections (xy view) of a 500 nm nano-sphere (excitation 488 nm / emission 515 nm).). 8-bit images are displayed with the assigned lookup table (LUT) before (raw) and after deconvolution with the SNR values 5, 10, 15, 20, 25 or 30. Superimposed white circles show the theoretical perfect shape (500 nm diameter) Note the improved sphere-like appearance of the nano-spheres after deconvolution (SNR 5-20) and the increasing irregularity in shape with higher SNR values (25-30). (Bar = 500 nm)

After applying the indicated thresholds, the volume (**B**) and circularity (**C**) of the 500 nm fluorescent nano-spheres were measured in raw (red) and confocal data sets after deconvolution with increasing values for the SNR (5, 10, 15, 20, 25 and 30). The mean values for >20 nano-spheres were plotted against the applied threshold. The bright green line shows (**B**) the theoretical volume (~0.07µm³) and (**C**) the theoretical circularity (c=1) of a 500 nm sphere. Error bars indicate standard error of the mean.

Furthermore, the circularity ($c = 4\pi$ X area/perimeter^2) of the same nano-spheres was measured in mid-sections of the 3D confocal data sets before and after deconvolution (Fig. 3C). This result indicates that deconvolution improved the quality of images in terms of the shape of objects: Circularity values calculated from deconvolved images were closer to the optimum than the raw data values. However, too high values of SNR (25 and 30, purple and pink lines) led to deviations from the ideal value.

6.1.3 Adopting the parameters for deconvolution

A problematic issue concerns the arbitrary nature of values assigned by the user to parameters, such as the SNR or the maximal number of iterations. A biased choice of the user is a potential cause of errors. Different SNR values and a series of iterations were therefore tested and the changing effect on the restored images was monitored. For this purpose, objects having a more complex morphology were chosen for investigation, i.e. fluorescently-stained cell nuclei visualized either by the DNA dye DAPI or by the expression of histone H2B-GFP. In these models, the chromatin compaction level varies across the nuclear volume, leading to variations in signal intensities in the imaged nuclei.

A typical nucleus of the cervix carcinoma cell line HeLa displays a complex morphology and harbors more compact, more intensely stained chromatin at the periphery (Fig. 4A: arrowheads) and a mostly DNA-free and weakly stained nucleolus (Fig. 4A: arrow) in the nuclear interior. Applying deconvolution clearly increased the contrast and enhanced the separation between chromatin and non-chromatin regions (Fig. 4A: SNR 15 and 30). Nevertheless, it was noticed that setting the SNR to 30 led to the partial loss of fine substructures close to the periphery of the nucleus after a higher number of iterations (Fig. 4A:asterisks in 80 it. and 160 it.).

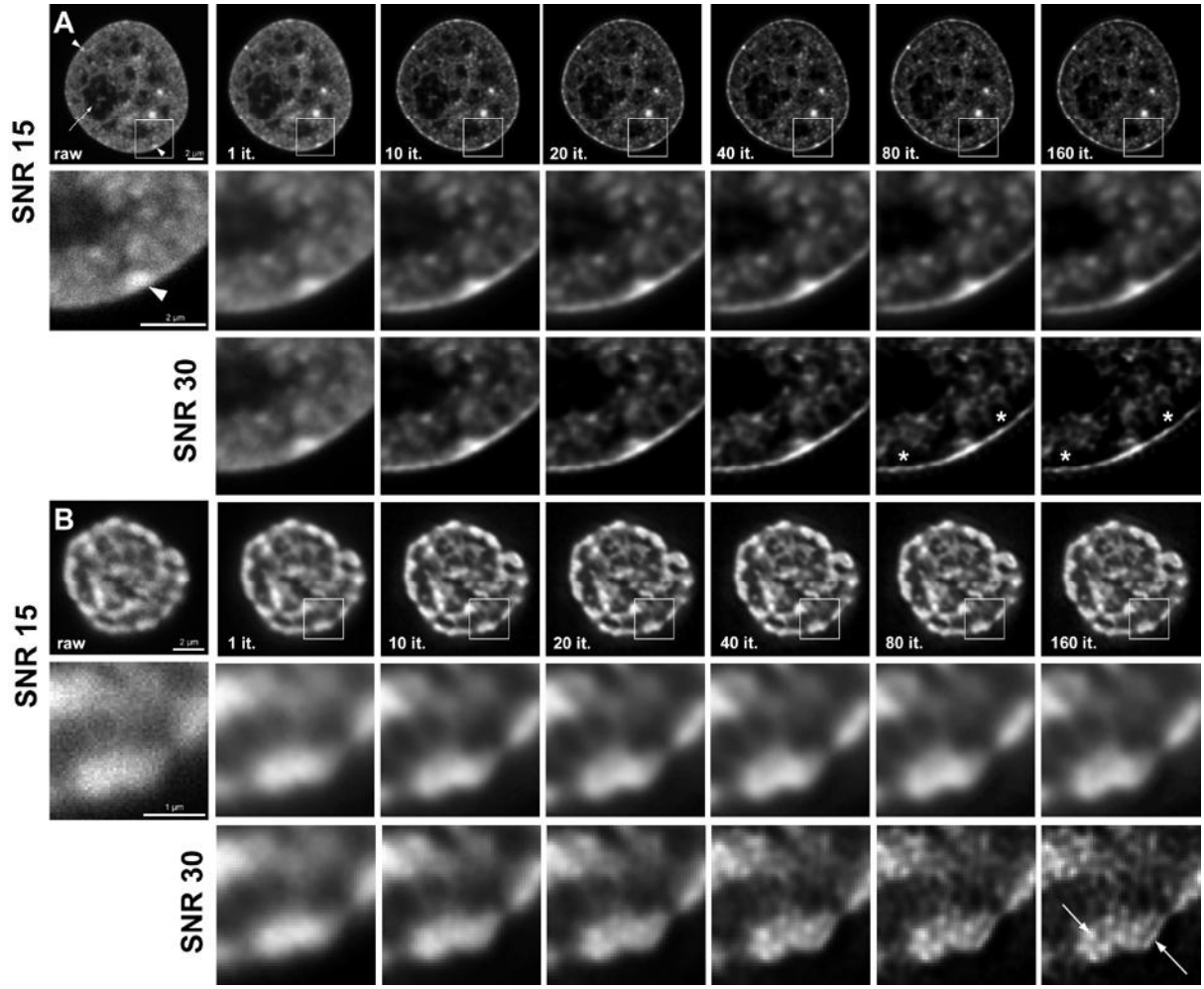

Figure 4: Comparison of raw and deconvolved confocal mid-sections for the impact of the SNR

A) Raw confocal and corresponding deconvolved mid-sections of a histone H2B-GFP labeled HeLa cell nucleus (excitation 488 nm / emission 508 nm). In the raw images the brighter rim which corresponds to more compact heterochromatin at the nuclear periphery (arrowheads) and the very weakly stained DNA free nucleolus (arrow) can be distinguished. Deconvolution with different values for the SNR (15 and 30) leads to improved contrast (entire nuclei only shown for SNR 15). When setting the SNR to 30, however, a loss of substructures (asterisks) can be observed after high number of iterations (e.g. 80 it. and 160 it.).

B) Raw and deconvolved confocal mid-section of a human lymphoblastoid nucleus with hypercondensed chromatin visualized by DAPI staining (excitation 405 nm / emission 461 nm). Again an increase in contrast can be observed after deconvolution (entire nucleus only shown for SNR 15). Setting the SNR to 30, led to an increased accumulation of spot- and stripe-like artifacts after high number of iterations (arrows in SNR 30, 160 it.).

Another example of a cell nucleus is displayed in Figure 4B. The chromatin of this human lymphoblastoid was hypercondensed by hyper-osmotic treatment, which results in a 3D network of compact chromatin bundles characterized by a less complex morphology. This phenomenon is described in detail in subsequent chapters (see 6.2). This example demonstrates another potential artifact that can occur with too high estimations of the SNR. Besides the desirable increase in contrast between the raw and deconvolved data, fine substructures appeared. These became especially evident with setting the SNR to 30 and

applying a high number of iterations and were recognizable by their spot- or stripe-like appearance (Fig. 4B: arrows). It should be noted, however, that such structures were never detected in deconvolved images with an SNR set to 15.

Thus, it was concluded that the setting of the SNR has to be considered with caution. Indeed, it was observed that performing deconvolution with a too high SNR increases the chance of introducing artifacts. Since these artifacts were never detected when applying the standard settings of SNR=15, maximum number of iterations=40 and quality factor=0.1, these settings were used for all subsequent experiments.

6.1.4 Deconvolution of different channels delineating the same object

Another way to test for artifacts is to compare signals of different deconvolved data sets which delineate the same object. In the event of proper deconvolution congruence between the two data sets was expected. In the event that artifacts accumulate due to the deconvolution procedure (e.g. due to incorrect estimations on the SNR), divergence of the two data sets was expected. Chromatin of a HeLa cell nucleus was visualized by the expression of histone H2B-GFP (Fig. 5A-D) and additionally with the DNA dye DAPI (Fig. 5E-H) and these signals were recorded separately. Since the same object was visualized twice, a high degree of similarity between both channels was expected. However, it is important to note that DAPI stains preferentially AT-rich DNA sequences whereas the H2B-GFP fusion protein visualizes all chromatin without any preference. Nevertheless, as the recorded raw images demonstrate, this preference at the molecular level has only a small - if any - impact on the global view of HeLa cell nuclei presented here. Highly similar raw images were obtained for both channels (compare Fig. 5A and 5E). If artifacts were to accumulate during deconvolution, a concomitant divergence and loss of similarity would be expected. This expectation could be clearly ruled out by viewing the results of deconvolution with SNR 15: a high similarity between the two channels was observed (compare Fig. 5C and 5G). Setting the SNR to 30, however, led to an increasing divergence between the two channels (compare Fig. 5D and 5H).

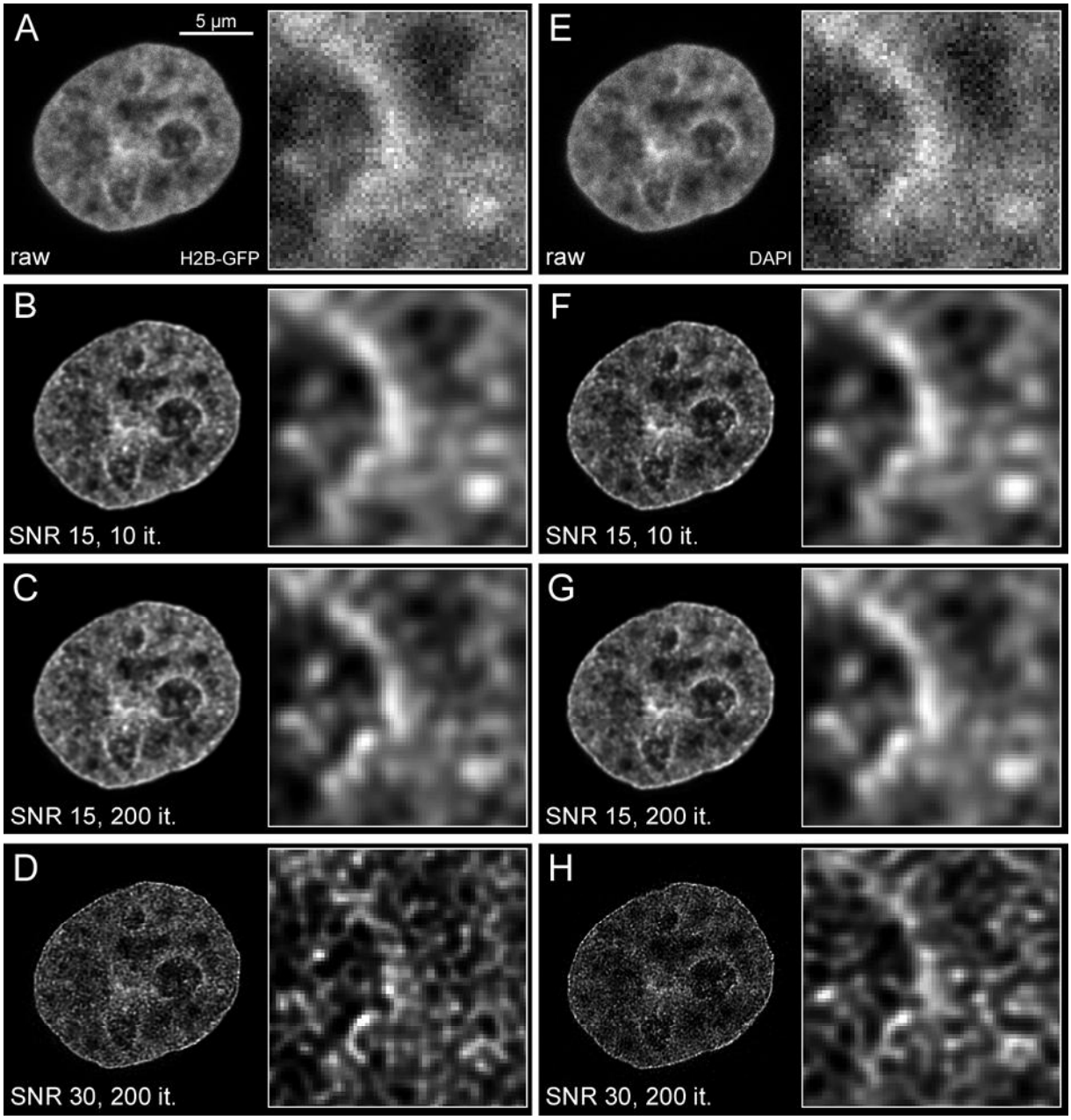

Figure 5: The same HeLa cell nucleus visualized with different fluorochromes in separate channels
A mid-section of a HeLa cell nucleus visualized by expression of histone H2B-GFP (**A-D**) or by DNA counterstaining with DAPI (**E-H**): The raw images (**A and E**) are highly similar. This similarity is still observed after deconvolution with a SNR of 15 (**B and F**) even after conducting 200 iterations (**C and G**). However reconstructed images displayed increased dissimilarity when 200 iterations were conducted for deconvolution with a SNR of 30 (**D and H**).

6.1.5 Comparison of confocal with other LM approaches

Up to this point, confocal data sets were only compared at different stages of image processing. One of the strength of the presented approach was that it was managed to record the same nucleus with different microscopy approaches. This allowed testing if the changes obtained by deconvolution were only detected by confocal microscopy. Raw and deconvolved confocal data sets were compared with images obtained by the other

approaches and it was considered unlikely that different microscopy techniques could lead to similar results if image processing introduced artifacts.

First raw and deconvolved confocal data sets were compared with corresponding deconvolved wide-field (WF) data sets (Fig. 6). Examples of raw and deconvolved WF mid-sections of a histone H2B-GFP labeled HeLa cell nucleus (Fig. 6A and 6C) are shown with the corresponding mid-section recorded at the confocal microscope (Fig. 6B and 6D). Since WF images are dramatically affected by out-of-focus light (Fig. 6A) the application of deconvolution is extremely helpful to distinguish fine morphological features and routinely performed. The mid-sections would not match perfectly because the different magnification factor and the tilting of the specimen due to differences in microscope setups can lead to misalignments. In addition, it was not expected that the optical sections would be focused on exactly the same planes. Notwithstanding these technical limitations, a global view of the corresponding images already suggested that the deconvolved confocal data set matched the deconvolved WF data better than did the raw confocal data set. This impression was confirmed by plotting a fluorescence intensity profile over a line drawn across the nuclear rim (Fig. 6A-D: enlargements). This plot revealed a steep increase in intensity starting from the nuclear edge inwards. This increase is considerably steeper (meaning a higher contrast) in the deconvolved confocal image (Fig. 6D) compared to the raw confocal image (Fig. 6B) and demonstrates a localization of a compact nuclear rim adjacent to less compacted chromatin in the interior. Nearly the same curve was observed for deconvolved WF images (Fig. 6C) but not for the raw WF data (Fig. 6A). In a HeLa cell nucleus with hypercondensed chromatin (Fig. 6E-H) the same microscope images (raw versus deconvolved) were compared. Bundles of hypercondensed chromatin are enlarged to show the gain in contrast in the deconvolved data sets (Fig. 6G-H). In summary, the two light microcopy approaches demonstrated the same trend of image improvement obtained by deconvolution of confocal data sets.

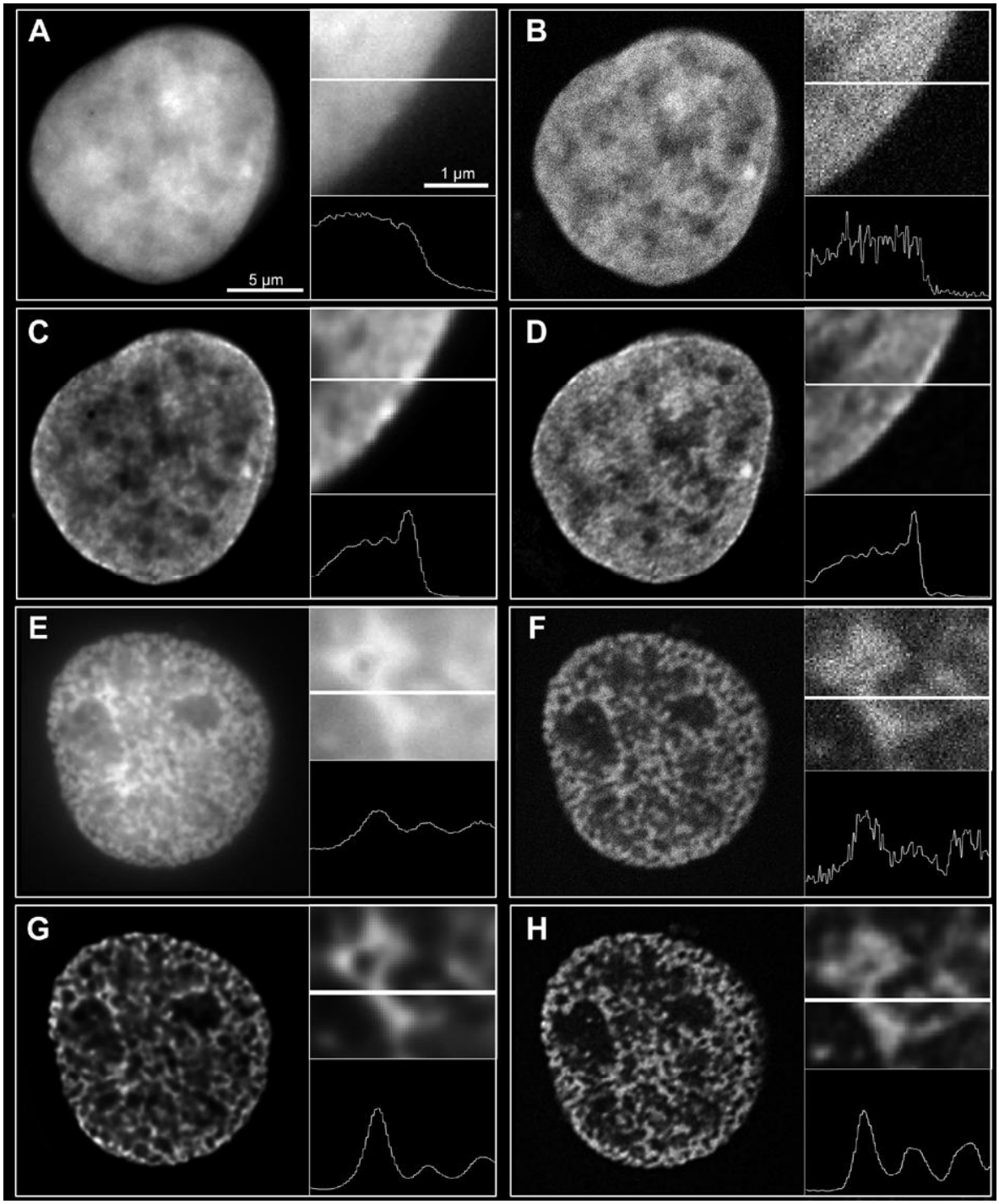

Figure 6: Deconvolution of WF and confocal microscope data shows the same trend of image improvement

Mid-sections of histone H2B-GFP labeled HeLa cell nuclei with normal (**A-D**) or hypercondensed chromatin (**E-H**). Raw (**A and E**) and deconvolved (**C and G**) wide-field microscopy images were compared with raw (**B and F**) and deconvolved confocal (**D and H**) images. The enlargements demonstrate the same level of improvement for the deconvolved compared to the raw images in WF as well as in confocal data sets. This improvement was especially evident when comparing intensity profiles along the indicated lines at corresponding sites. **A-D**) A steep increase in intensity at the nuclear edge followed by a drop in the nuclear interior was observed in all deconvolved data sets, but not in the raw data. **E-H**) Bundles of hypercondensed chromatin become strikingly contrasted in the deconvolved data sets. Bars in (**A**) = 5µm respectively 1 µm (enlargement).

6.1.6 Comparison of deconvolved confocal with EM images

To ensure that the observed similarities between images generated by different fluorescence light microscope approaches did not reflect the existence of a similar response of light microscope images to deconvolution or image enhancement, corresponding mid-sections of the same HeLa cell nuclei obtained by confocal microscopy and by electron microscopy (EM) were compared. Initial EM preparations comprising cell treatment, fixation and resin embedding were performed in Munich. The final preparation steps as well as all EM microscopy work was kindly performed in the laboratory of Prof. S. Fakan in Lausanne by Lorella Vecchio and Cinzia Tiberi. The two approaches (confocal light versus electron microscopy) differ dramatically in their methodology that they delineate the object of interest: in the case of confocal microscopy, images were recorded by optical sectioning (steps size 120 nm; z-resolution >500 nm) of fluorescent signals (histone H2B-GFP) using laser excitation and collection of emitted light through a photomultiplier detection system. By contrast, in the case of EM the nucleus was physically sectioned (80 nm) with an ultramicrotome, contrasted with a Feulgen-type staining method and objects were detected thereafter based on the semi-transparency of the specimen for electrons. An enlarged view of a region in the nuclear interior (Fig. 7A-C) revealed once more a strong enhancement of contrast when comparing the raw (Fig. 7A) and the deconvolved (Fig. 7B) confocal image. Although the electron microscope (Fig. 7C and 7F) generates images in much more details due to the high resolution and thinner section size, the fact that chromatin in the deconvolved confocal image was strongly contrasted against a mostly unstained interchromatin space as seen in the EM image was obvious. Comparing images of a HeLa cell nucleus with hypercondensed chromatin (Fig. 7D-F) confirmed the gain in image quality obtained by deconvolution for structures having a less complex morphology. The enlarged detail demonstrates how lacunas become clearly contrasted against the surrounding chromatin after deconvolution (Fig. 7E), consistent with the EM image (Fig. 7F) but not the raw confocal image (Fig. 7D).

It was considered unlikely that these two microscope approaches, differing completely in the ways they delineate the object of interest, could generate such a similar result just by chance.

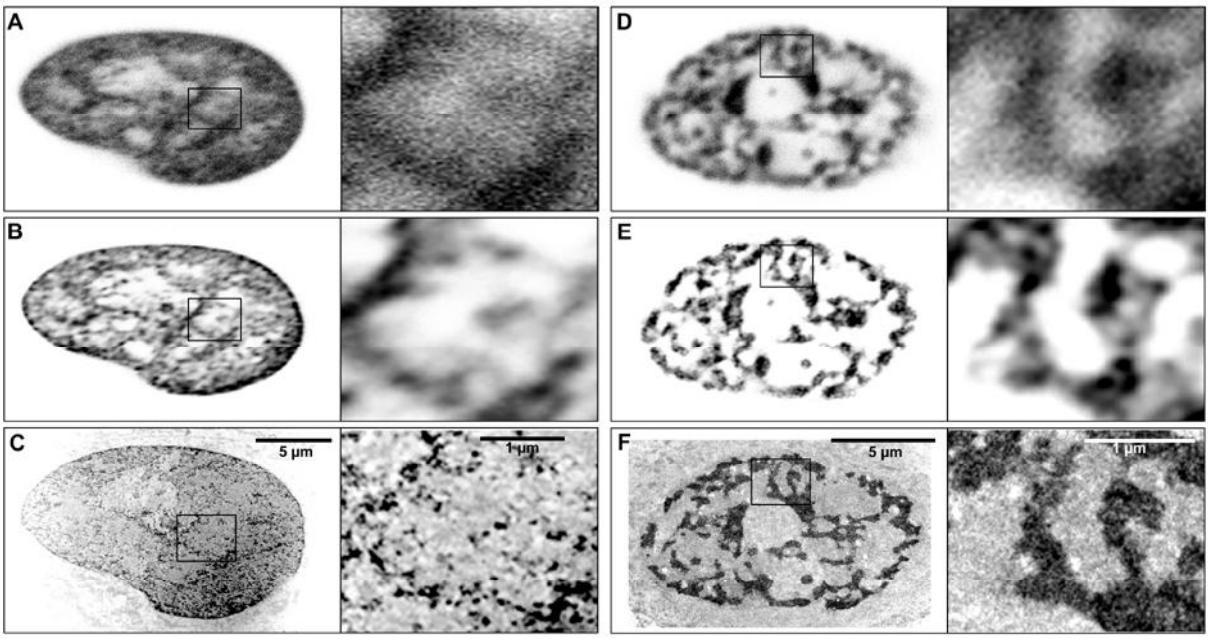

Figure 7: Comparison of images obtained by confocal microscopy and electron microscopy (EM)
Mid-sections of histone H2B-GFP labeled HeLa cell nuclei with normal (**A-C**) and hypercondensed chromatin (**D-F**). Since ultramicrotome sectioning leads to a slight deformation of the nuclei, the light microscopy images had to be stretched (**A, B, D, E**) to fit the outline of the EM images (**C**) and (**F**). Additionally light microscopy images were inverted to obtain the same orientation of intensities (low gray values = true signal, high gray values = no signal) as displayed in the EM images. Raw (**A**) and (**D**) and deconvolved (**B**) and (**E**) confocal images are compared with the corresponding EM images (**C**) and (**F**). For EM, chromatin was specifically contrasted with osmium ammine by a Feulgen-type staining reaction. Enlargements show the enhancement in image quality gained by deconvolution: blurred regions in the raw data become more contrasted, comparable with the corresponding regions observed by EM. (Images A-E: Tiberi C., Lausanne)

6.1.7 Deconvolved images allow correct thresholding

The improvement in image quality after deconvolution not only helps to resolve fine morphological structures in the data sets, it also facilitates the quantification of these data sets. Most of the quantification software currently used requires the input of a threshold value (TH) in order to separate the signal from background before performing measurements. Accordingly, the second aim, in addition to the avoidance of artifacts, was to test if the segmentation of a fluorescent object by gray value thresholding got facilitated after deconvolution. An exemplary HeLa cell nucleus is displayed in Figure 8 with enlarged views of two regions: [1] the nuclear periphery, comprising the bright rim and less intense adjacent chromatin with fine channels and [2] the centrally localized nucleolus with its clearly contrasted border between chromatin and non-chromatin regions. Thresholded images are displayed in black and white. The setting of a low TH for the raw data set (TH = 50) led to a good segmentation of the nucleolus (green frame) but the channels at the nuclear rim were not resolved (red frame). To reveal these finer structures, a much higher TH was required (TH = 80), at which the outline of the nucleolus vanished (red frame). An intermediate gray

value (TH = 65) neither segmented the nucleolus nor the fine channels to a satisfying extent. Thus, it was not possible to find a single TH that would resolve known nuclear structures in the raw data sets, as either too many or too few signal voxels were included. However, a single TH could be easily defined for the same regions in the deconvolved confocal data set. At this gray value (TH = 35), both the nucleolus and the channels were properly segmented (green frames). Neither lower (TH = 20) nor higher values (TH = 50) improved this segmentation. This example demonstrated that deconvolution clearly facilitated the choice of an optimal TH to segment complex morphological structures.

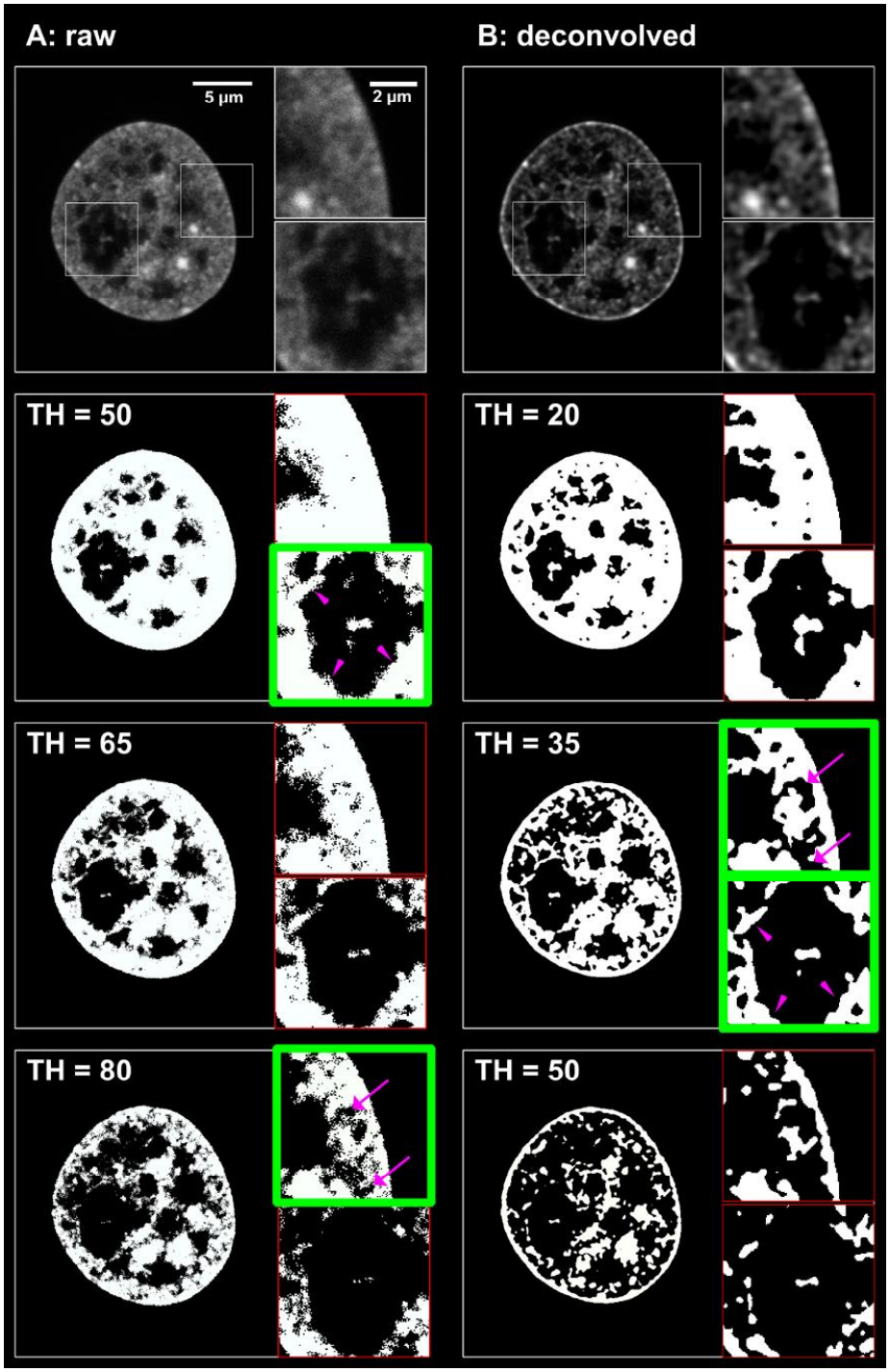

Figure 8: Deconvolved images can be segmented with a single TH better than raw images

Raw (**A**) and deconvolved (**B**) confocal mid-section of a HeLa cell nucleus. Thresholded images are shown in black and white. Two enlarged regions show [1] the brighter rim and fine channels at the nuclear periphery (upper enlargement) and [2] the nucleolus (lower enlargement). A TH value was considered to be satisfying (green frames) if it allowed the visualization of fine channels (pink arrows) and/or of the nucleolar border (pink arrowheads). In the case of the raw data set, a low gray value (TH = 50) was needed for proper segmentation of the nucleolus whereas segmentation of the fine channels at the nuclear periphery could only be achieved at a high value (TH = 80), at which the nucleolar border disappeared. An intermediate value (TH = 65) yielded no satisfying segmentation for either of the two regions. In the deconvolved data set, however, a single value (TH = 35) could be found in order to yield a good segmentation of both regions simultaneously. Lower (TH = 20) as well as higher values (TH =50) did not improve the segmentation of the deconvolved data set.

6.1.8 Conclusion on deconvolution of confocal data sets

Deconvolution of confocal images facilitates the proper segmentation by an optimal gray value threshold. This was proven by the better restoration of the volume and shape of fluorescent nano-spheres and the comparisons of images of the same object, visualized with different microscopy approaches including WF and EM. These comparisons delivered a striking similarity of the images, which can only unlikely be considered as a random result. The tested settings of deconvolution parameters did not lead to the creation of artifacts and were additionally sufficient to allow a proper segmentation by subsequent gray value thresholding. Accordingly, deconvolution was routinely applied on 3D confocal data sets if TH demanding quantifications had to be performed in the subsequent experiments.

6.2 Induced formation of hypercondensed chromatin (HCC)

Nuclear architecture was manipulated by performing a protocol leading to the formation of hypercondensed chromatin (HCC). Incubation of living cells for 10 min in medium with an osmolarity of 570 mOsm led to a condensation of chromatin (Fig. 9). The shape of nuclei of adherent cells did not change in the xy-extension but shrinkage of ~25% was observed in the z-extension. The pattern of condensed chromatin slightly reminded of prophase nuclei, since condensation, instead of forming a single compact chromatin clump, led to the formation of numerous chromatin bundles with typical diameters of 500 to 900 nm in HeLa cell nuclei.

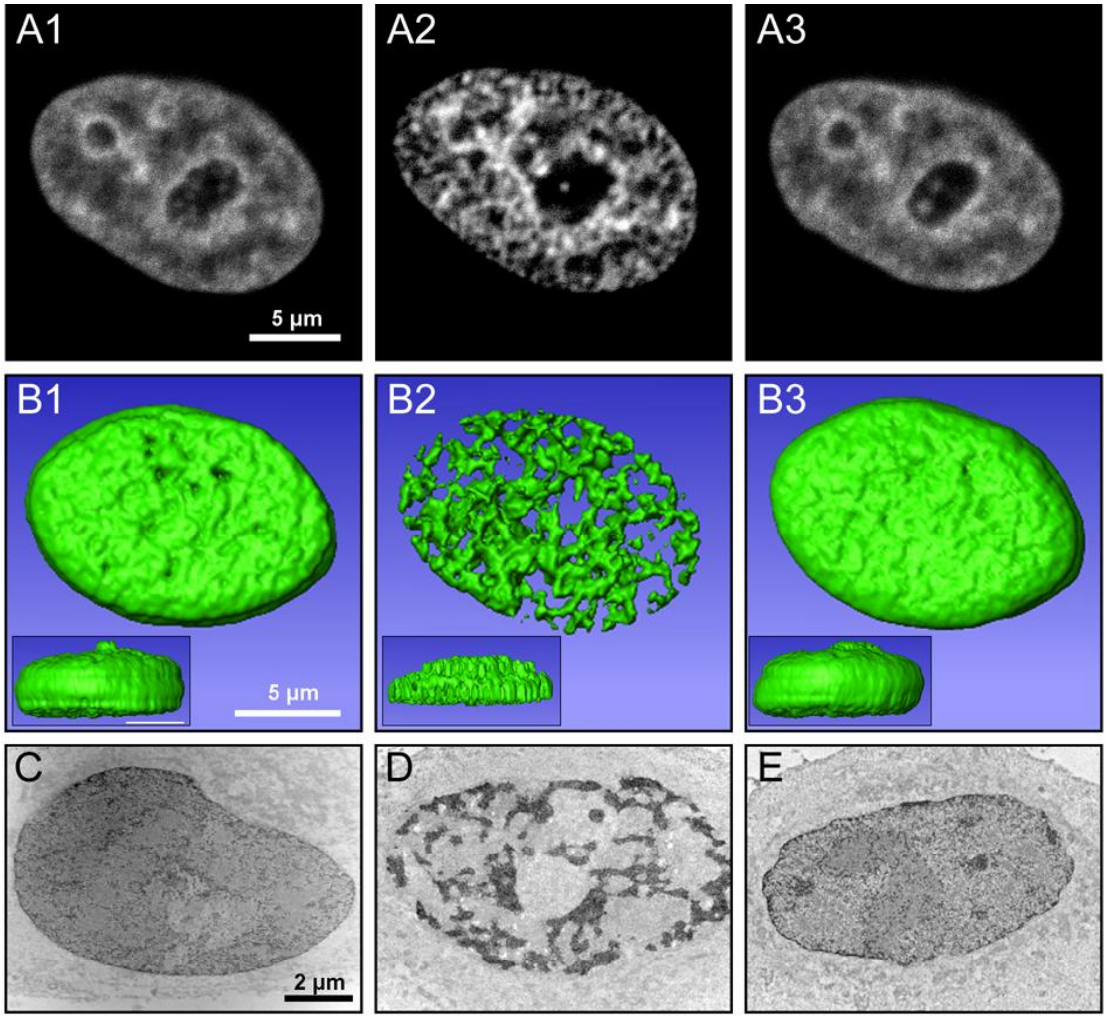

Figure 9: Induced formation of hypercondensed chromatin (HCC)

HCC formation and restoration on normally condensed chromatin (NCC) in HeLa cell nuclei. **A)** Confocal midsections of a nucleus (H2B-GFP) of a living HeLa cell in physiological medium (A1, 290 mOsm), after formation of HCC in medium with 570 mOsm (A2) and after restoration of NCC (A3). **B)** 3D reconstructions (top view) of a nucleus with NCC (B1), HCC (B2) and restored NCC (B3) reveal a pattern of interconnected H2B-GFP tagged HCC bundles together with a largely increased interchromatin space (B2). Side views (insets) show shrinkage in the z-extension. **C-E)** EM midsections of HeLa cell nuclei fixed in physiological medium (**C**), during the HCC state (D) and after restoration of NCC (E) stained by the osmium ammine technique. Note the complete restoration of the normal chromatin architecture (C) after recovery of NCC (E). (Images C-E: Tiberi C., Lausanne)

HCC formation could be induced in each cell line or cell culture tested including HeLa cells, human neuroblastoma cell lines (Kelly and LAN-5), the human breast cancer cell line MCF-7, human colon carcinoma cells (DLD-1) and Chinese hamster ovary cells (CHO), as well as in normal diploid human fibroblasts (HFb), lymphocytes (HLy) and amniotic fluid cells (AFC) (Fig. 10).

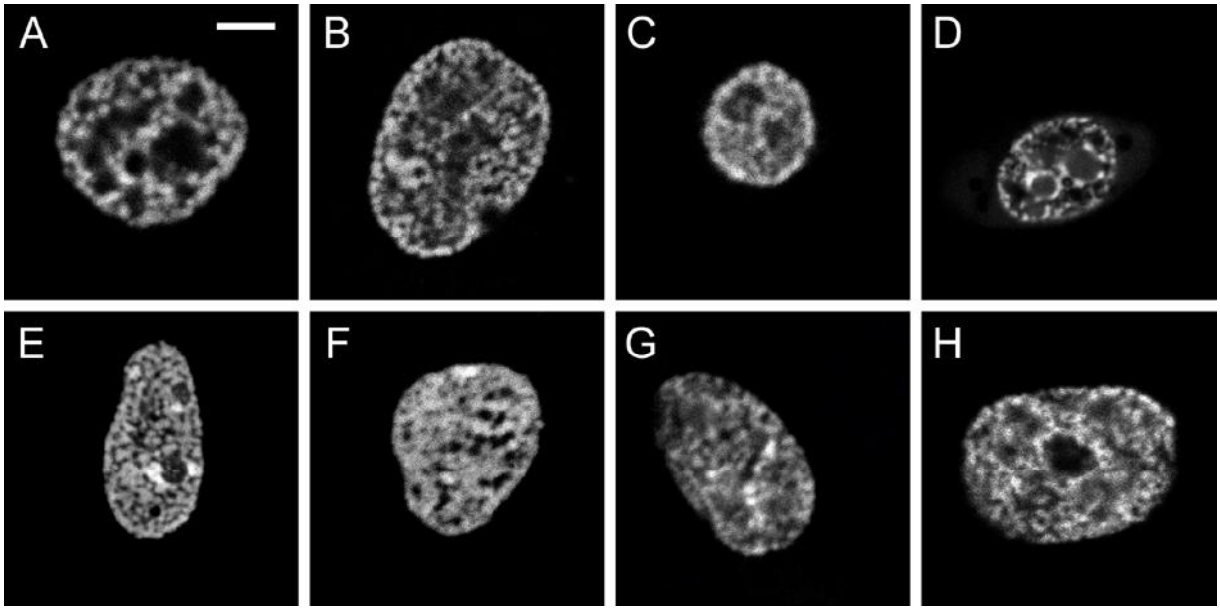

Figure 10: Nuclei of different cell lines with HCC

HCC formation was inducible in all tested cell lines. Displayed are confocal mid-sections of DAPI stained nuclei. **A)** HeLa **B)** HFb **C)** HLy **D)** CHO **E)** LAN-5 **F)** Kelly **G)** AFC **H)** MCF-7. Bar in (**A**) = 5µm

6.2.1 Reversibility of HCC formation

Releasing living cells with HCC to physiological conditions immediately led to the reversal of the effect and a reformation of normally condensed chromatin (NCC) (Fig. 9). To quantify such a NCC-HCC-NCC cycle the frequency of voxel intensities was plotted for a living cell nucleus (Fig. 11). Since the complete nuclear volume was analyzed, a direct comparison of the three states was possible after normalizing to the total intensity of each state which compensates for the loss of fluorescence by photobleaching. As expected, a shift to higher voxel intensities was observed, which was almost completely compensated after 5 min of recovery of physiological medium conditions.

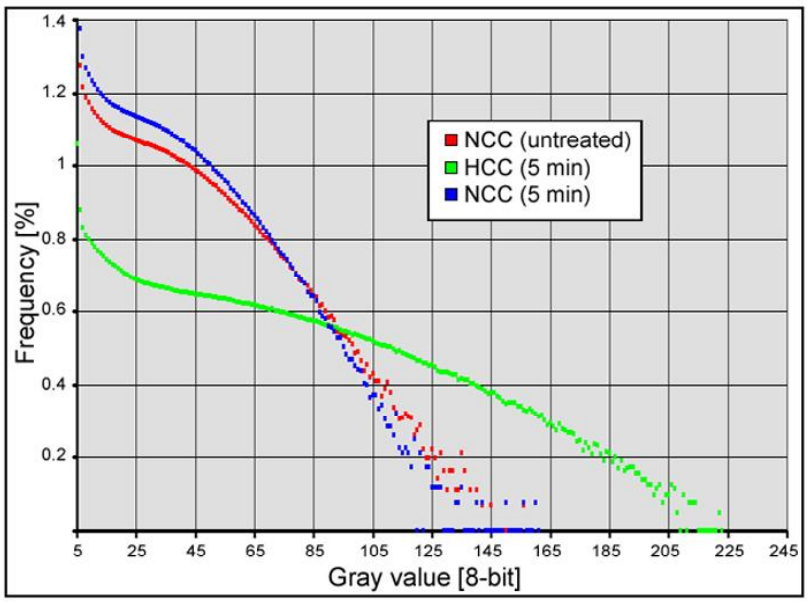

Figure 11: Quantitative ascertainment of chromatin conformation changes over an NCC-HCC-NCC cycle

The frequency of gray values (>4) of all voxels of 3D confocal data sets were plotted for the same living cell nucleus before any treatment (NCC, red), during the HCC state (green) and after 5 min of recovery of NCC (blue). To correct for loss of intensity due to photobleaching, frequencies (plotted with a logarithmic scale) were normalized to the total amount of fluorescence at each stage. A shift in voxel intensities to higher gray values was observed for the HCC state, followed by the complete recovery of the original intensity distribution.

6.2.2 Global chromatin positioning in nuclei with HCC

Are the impressive changes in chromatin morphology observed during HCC formation accompanied by global chromatin repositioning? To address this question the topology of early replicating chromatin as well as the topology of centromeres and CTs was monitored over an entire NCC-HCC-NCC cycle in living HeLa cells stably expressing histone H2B-GFP (Fig. 12). The replication pattern was visualized by the *in-vivo* replication labeling technique (see 5.3.2), which leads to the incorporation of fluorochrome tagged nucleotides in active replication foci. Since these foci are persistent chromatin compartments they were termed '~1 Mb chromatin domains' (Ma et al., 1998; Nakamura et al., 1986) according to their roughly estimated DNA content (see 4.1.4). According to established classification schemes (Nakamura et al., 1986; O'Keefe et al., 1992), the exemplary pattern of replication foci (shown in Fig. 12G-I) was assigned to early replicating chromatin. The position of centromeres was monitored in living cells after transient transfection of dsRED coupled CENP-B, a major component of the centromere binding kinetochore complex. CTs were visualized *in-vivo* by replication labeling and subsequent long term incubation (3-5 days), leading to the segregation and separation of labeled ~1 Mb chromatin domains (former replication foci) of single CTs after several (6-9) cell divisions (Zink et al., 1998). Note that living cell replication labeling only tags chromatin with a particular replication timing, since the incorporation of directly labeled nucleotides is technically limited to a short time window (~1 h). Accordingly, the label does not cover all ~1 Mb chromatin domains of a given CT but only a sub-fraction with similar replication timing. Nevertheless, the extent of labeling is

adequate to determine the localization of a CT as well as its approximate shape (Zink et al., 1998).

At the global view presented here, neither CT (Fig. 12A-C) nor centromere positioning (Fig. 12D-F) displayed remarkable shifts towards each other or in regard to the nuclear periphery. The arrangements of these compartments are especially similar comparing the untreated and the recovered nuclei. Monitoring the more complex pattern of early replicating chromatin over the NCC-HCC-NCC cycle (Fig. 12G-I) confirmed this result. The arrangement of these early replicated foci, displayed here in a confocal mid-section of the monitored nucleus, remained remarkably constant.

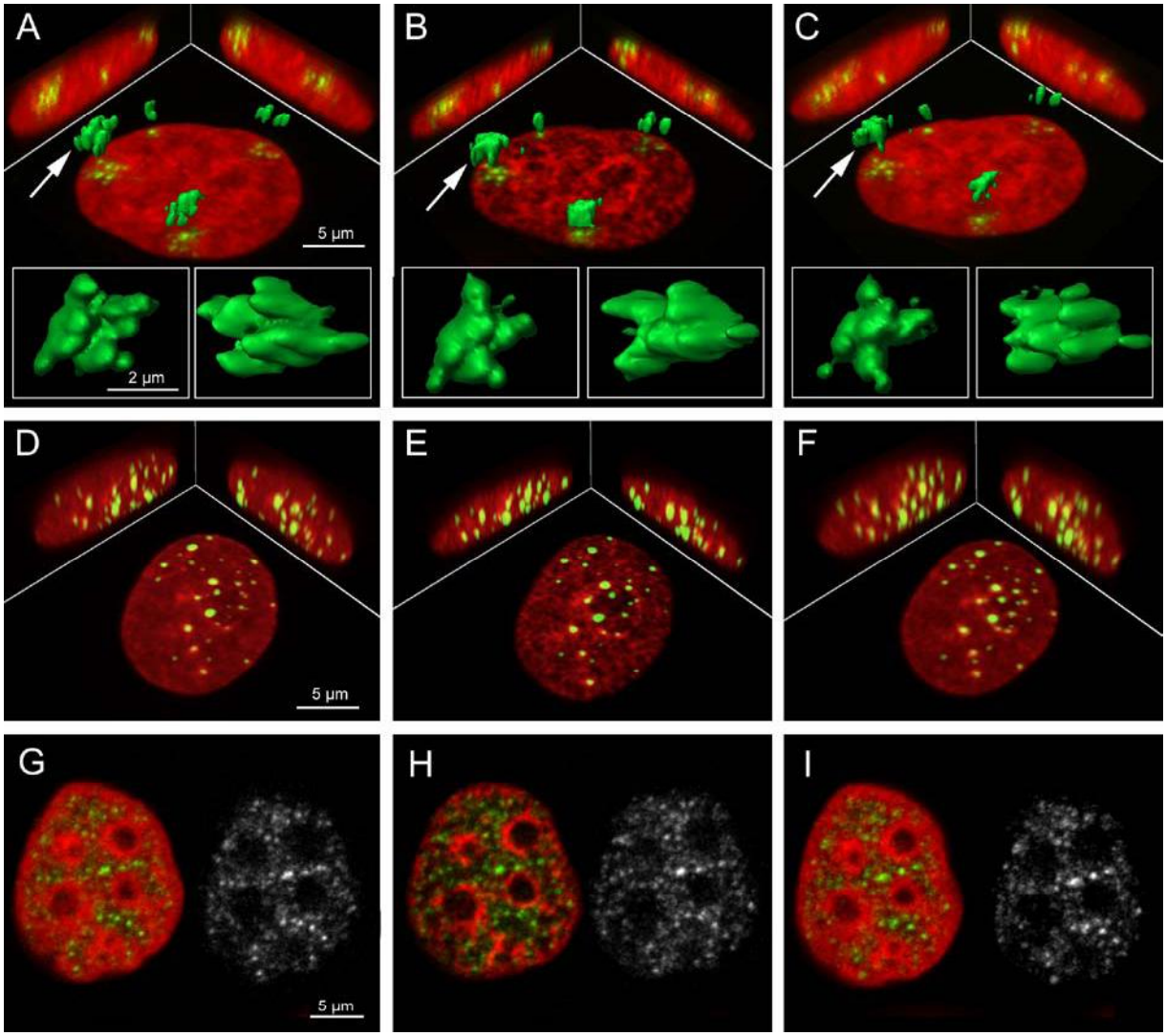

Figure 12: Positioning of CTs, centromeres and replication foci over an entire NCC-HCC-NCC cycle

H2B-GFP tagged chromatin (red) and CTs (A-C, green), centromeres (D-F, green) and early replication foci (G-I, green) were monitored over a NCC-HCC-NCC cycle. Displayed are maximum Z, X- and Y projections of confocal image stacks (A-F) or confocal mid-sections (G-I) or 3D reconstructions (A-C) for typical nuclei before (A, D, G) and during HCC state (B, E, H), as well as after re-establishing NCC (C, F, I). CTs maintained their shape (A-C, 3D reconstructions, enlarged CT marked by arrow) and relative positions in the nucleus (A-C, projections). Similarly, no remarkable changes in topology were observed for centromeres (D-F, projections) or early replication foci (G-I, mid-section).

6.2.3 HCC formation and the cell cycle stage

An unsynchronized growing culture of HeLa cells with H2B-GFP tagged chromatin was subjected to hyper-osmolarity (570 mOsm) including cells during mitosis and various interphase stages to check if the response to changed medium conditions depends on the actual cell cycle stage (Fig. 13 and Movie 1). To distinguish early, mid and late S-phase stages, cells were pulse-labeled for 20 min with BrdU before induction of HCC formation, and immuno-detection of the incorporated bromide was carried out after fixation. The three main replication patterns described for different time-points during S-phase in NCC nuclei (Nakamura et al., 1986; O'Keefe et al., 1992) were easily recognized in nuclei with HCC, confirming the global preservation of higher order nuclear architecture reported in the previous chapter. Nuclei lacking BrdU labeling (non S-phase) were tentatively assigned to G1 (small) or G2 (large). All nuclei of this unsynchronized HeLa cell culture displayed HCC, irrespective of the cell cycle stage they were going through. Mitotic chromosomes, already condensed before the treatment, exhibited a slight additional condensation (compare Movie 2).

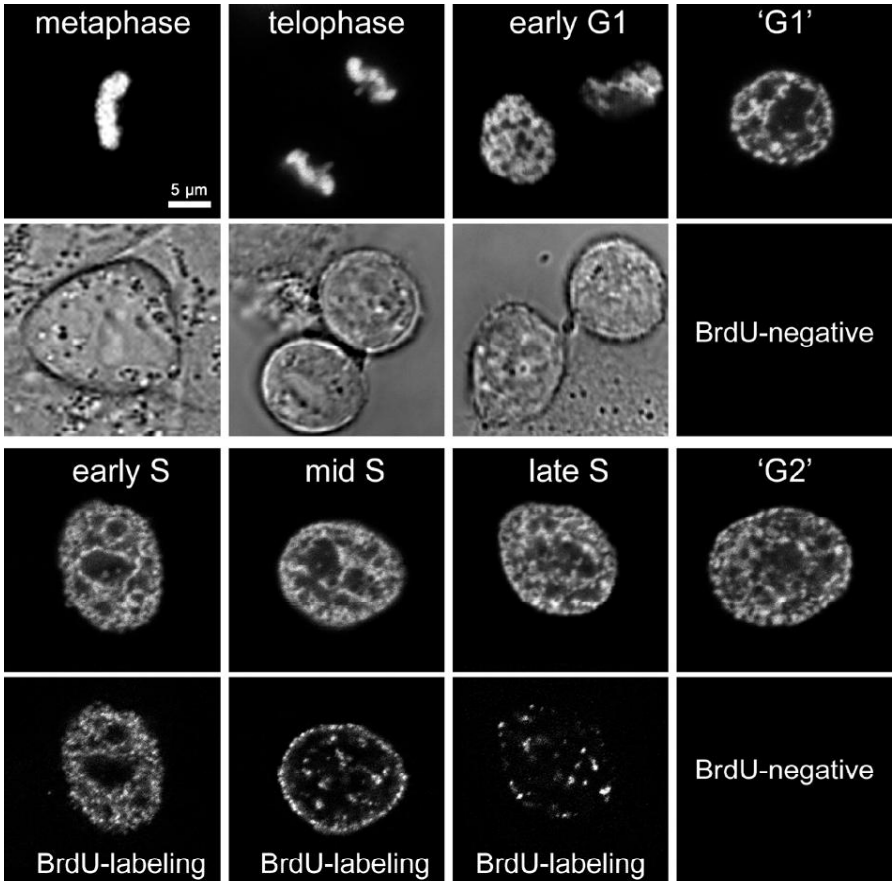

Figure 13: HCC formation can be induced in every cell cycle stage

A growing culture of HeLa cells with H2B-GFP tagged chromatin was subjected to hyper-osmotic (570 mOsm) conditions. This culture included cells during mitosis and various interphase stages. The effect of HCC formation on mitotic chromosomes is further demonstrated in the enclosed Movie 2. To distinguish early, mid and late S-phase stages, cells were pulse-labeled with BrdU 20 min before the change to hyper-osmotic conditions. HCC formation was observed in every nucleus of this unsynchronized cell culture. Note that replication patterns typical for the three S-phase stages were easily recognized in nuclei with HCC indicating the global preservation of higher order nuclear architecture in spite of chromatin hypercondensation. Small nuclei lacking BrdU labeling were subjectively assigned to G1, large nuclei to G2.

6.2.4 Comparison of hyper- and hypo-osmotic treatments

HeLa cells were incubated for 10 min in hypo-osmotic conditions (~140 mOsm) to compare the effects on chromatin morphology of the converse treatment (Fig. 14). Incubation in hypo-osmotic conditions gave rise to a decondensed chromatin morphology with an overall diffuser appearance of chromatin. To test if the observed global de-/condensation of chromatin induced by hypo- or hyper-osmotic conditions can be ascribed to a local de-/condensation of small chromatin domains, size differences of ~1 Mb chromatin domains were compared after the hyper- resp. hypo-osmotic treatments. The maximal diameter of all round profiles ($n > 150$) found in the 3D data stacks were detected automatically and plotted according to their frequency. The shapes of all three distributions (hyper-, hypo-osmotic and physiological) were similar; the median and mean foci diameters were only very slightly smaller (<5%) under hyper-osmotic conditions than the corresponding values for the two other treatments. This difference on the level of single ~1 Mb chromatin domains, however, was too small to have a considerable impact on the global chromatin condensation.

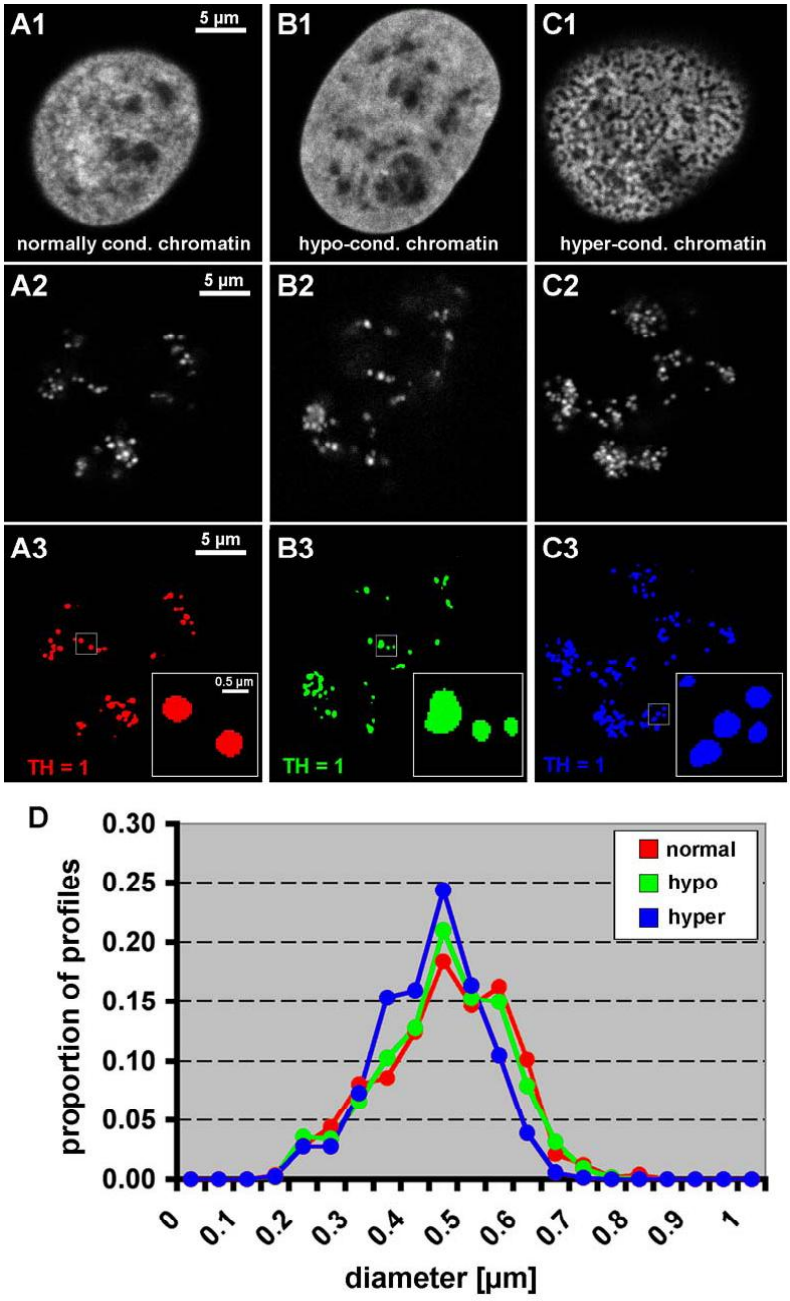

Figure 14: Size distribution of ~1 Mb chromatin domains in normal, hyper- and hypo-osmotic conditions

A-C) Displayed are confocal mid - sections of HeLa cell nuclei (H2B-GFP, A1-C1), with labeled ~1 Mb chromatin domains (A2-C2) after different treatments: (A) untreated, normally condensed chromatin (NCC), (B) 10 min incubation in hypo-osmotic medium, hypo-condensed chromatin and (C) 10 min incubation in hyper-osmotic medium, hypercondensed chromatin (HCC). A3-C3) Signals of the same ~1 Mb chromatin domains after deconvolution. All pixels with gray values above 0 are colored. Enlargements display typical examples of foci. **D**) In order to compare size differences of ~1 Mb domains after the different treatments, the maximal diameter of all round profiles (n>150) found in the 3D data stacks were detected automatically and plotted according to frequency. Median and mean foci diameters under hyper-osmotic conditions were only <5% smaller, than the corresponding values for the other two treatments.

6.2.5 Local changes in chromatin topology

Since no major effect on chromatin arrangement was detected with regard to the positioning of CTs, centromeres or replication patterns and since no significant change of chromatin domain sizes was measurable at the local level of ~1 Mb chromatin domains, what affects the global hypercondensation of chromatin? Instead of getting compressed or blown-up under the tested conditions, ~1 Mb chromatin domains may be subjected to positional changes in response to the applied treatments. Indeed, living cell observations of ~1 Mb chromatin domains assigned to different replication timing supported the assumption that small scale positional shifts lead to HCC formation (Fig. 15). Domains, originally labeled during mid- or late S-phase, showed no obvious changes with respect to the underlying

global chromatin pattern (Fig. 15A-F). Domains originally labeled during early S-phase, however, displayed topological changes (Fig. 15G-I). Since this experiment was carried out on only a small number of nuclei (3 per S-phase stage) and no quantification has been performed yet, these observations have to be considered as preliminary. Nevertheless, positional changes at the level of ~1 Mb chromatin domains match the hypothesis that early replicating / active chromatin, decondensed in nuclei with NCC, got retracted towards late replicating / inactive chromatin during HCC formation.

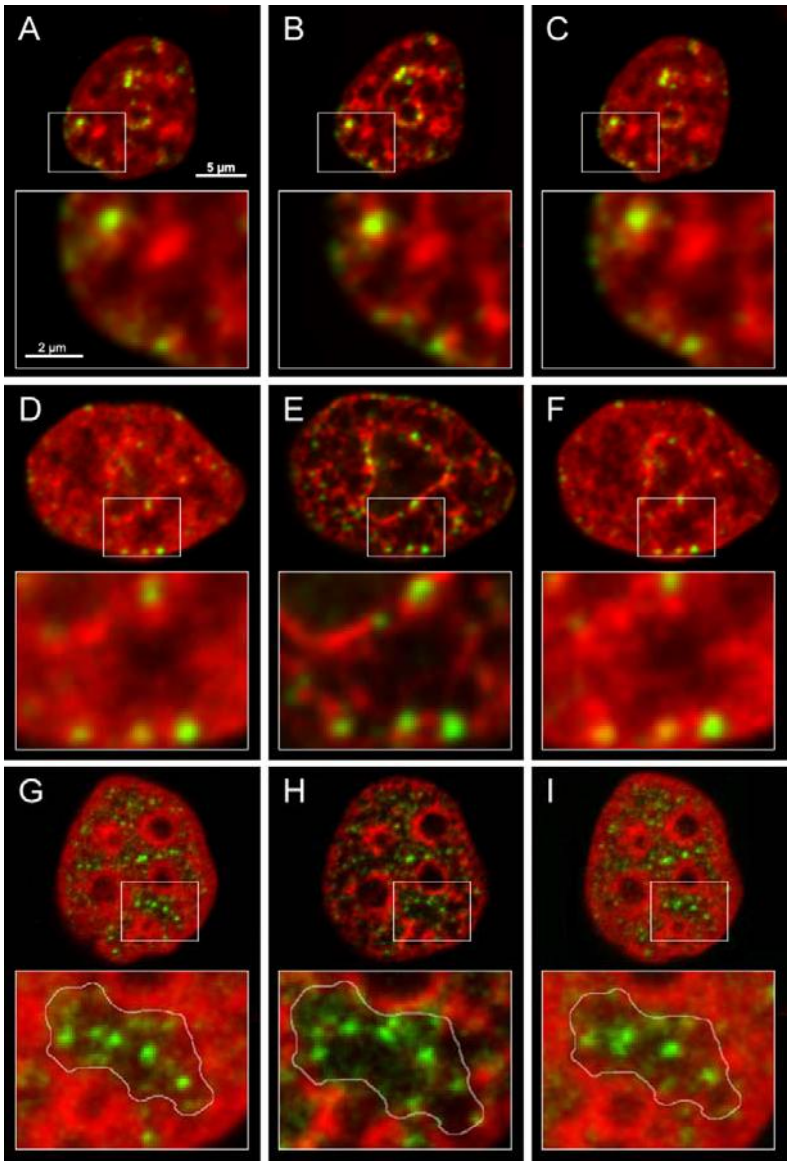

Figure 15: Monitoring of differently replication timed chromatin domains over a NCC-HCC-NCC cycle

Displayed are confocal mid-sections of living HeLa cell nuclei (H2B-GFP, red), with labeled ~1 Mb chromatin domains (Cy3dUTP, green) of different replication timing: late replicating (**A-C**), mid replicating (**D-F**) and early replicating (**G-I**) chromatin domains. The three classes of replication timing were assigned according to Nakamura et al., 1986 and O'Keefe et al., 1992. An NCC-HCC-NCC cycle was performed and each nucleus was monitored before any treatment (NCC: A, D, G), after HCC formation (B, E, H) and after recovery (NCC: C, F, I). Enlargements display a few labeled ~1 Mb chromatin domains and the surrounding chromatin. Inactive/mid-to-late replicating chromatin seems to be fixed while active/early replicating chromatin seems to be shifted in its position and dragged to more compact chromatin regions.

Accordingly, inactive and more compact chromatin regions would serve as the stationary scaffold for the HCC bundle formation. These postulations will be followed up in a subsequent chapter where investigations on the architecture of HCC bundles are presented (see 6.4.2).

6.2.6 HCC formation and physiological parameters

6.2.6.1 Hyper-osmolarity triggers HCC formation only indirectly

To investigate if the increase in osmolarity of the culture medium directly triggers the effect of HCC formation or if it is only a consequence of the specific impact of increased concentrations of particular ions, different hyper-osmotic media with similar osmolarity were prepared by the addition of different salts (NaCl or KCl or NaAc) as well as of saccharose. The resulting HCC formation was essentially the same after incubations in every of the tested hyper-osmotic media (Fig. 16C-F) compared with the hyper-osmotic medium prepared by the addition of 20x PBS (Fig. 16B).

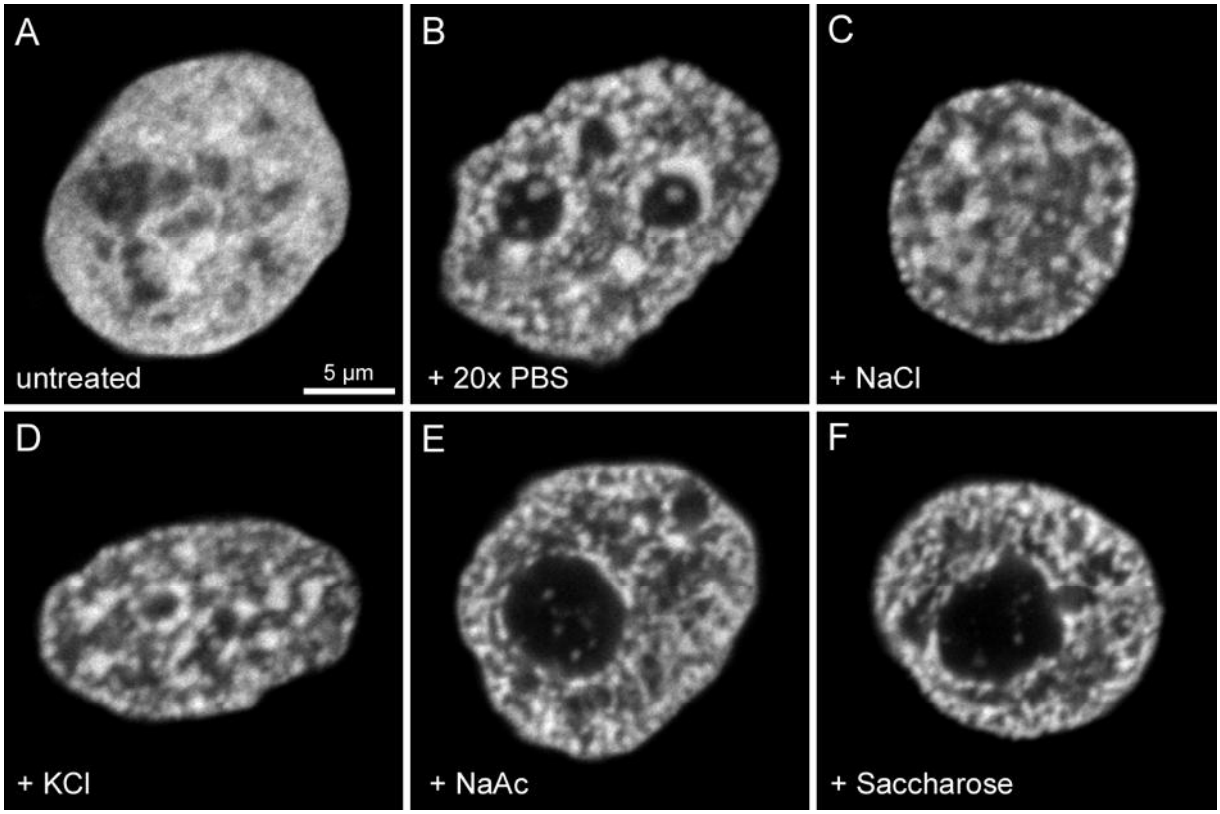

Figure 16: HCC formation can be induced by every hyper-osmotic medium

Confocal midsections of HeLa cell nuclei (H2B-GFP). **A**) untreated nucleus exhibiting NCC. **B-F**) Chromatin morphology after formation of HCC. Similar HCC morphology was observed after incubation in media with increased osmolarity (~500-800 mOsm, see Methods, 5.7.1) achieved by supplemental of salts or saccharose.

An intact semi-permeable cell membrane, however, was obligatory for HCC formation mediated by a hyper-osmotic medium. In cells with membranes permeabilized by a mild digitonin treatment (Fig. 17), HCC formation could no longer be induced by an increase in the concentration of just monovalent cations (Fig. 17B-D). An increase in the concentration of only divalent cations (Mg^{2+} and Ca^{2+}) still affected condensation of chromatin (Fig. 17E and 17F). However, the condensed chromatin exhibited a morphology differing

from that of nuclei with HCC in intact cells. Here, condensed chromatin appeared more concentrated around nucleoli and the nuclear periphery. In summary it was concluded that the increase in osmolarity of the medium had an only indirect effect on intact cells most likely by an increase of intracellular components due to the loss of water over the semi-permeable membrane. Divalent cations may play a role, but also other potential mediators will be discussed (see Discussion, 7.3).

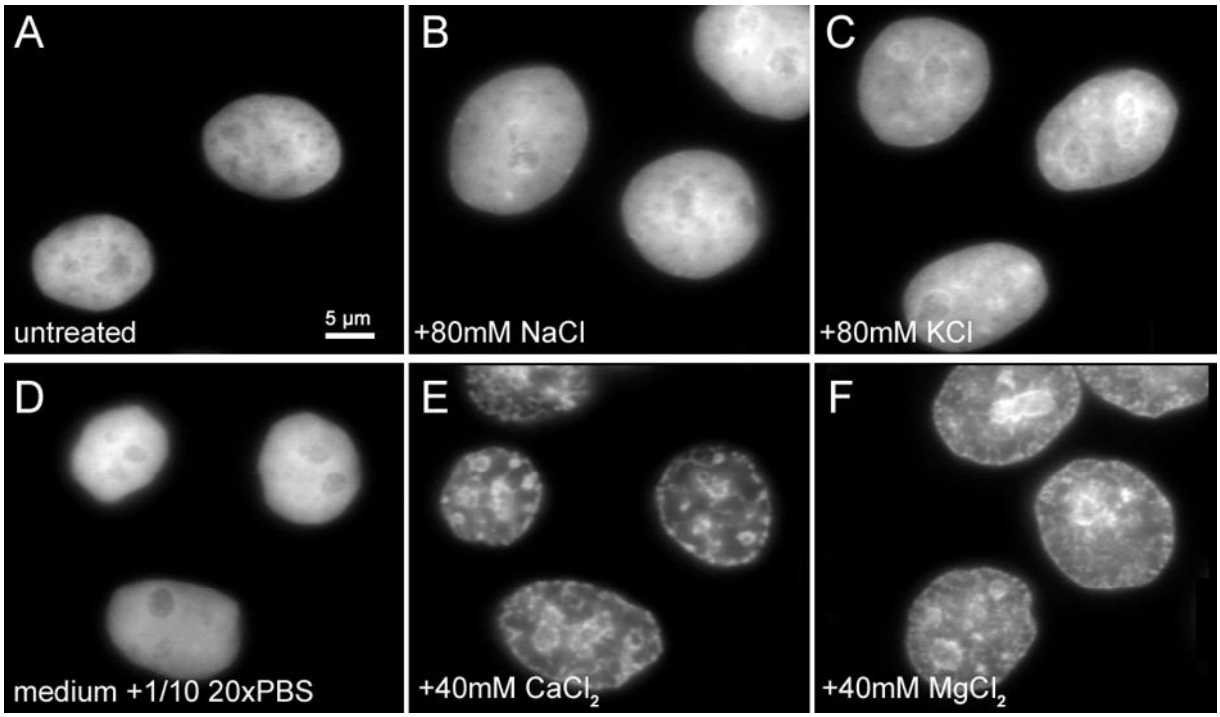

Figure 17: Hyper-osmotic treatment of living cells with permeabilized membranes

HeLa cells permeabilized by incubation with digitonin (40 µg/ml) for 2 min. Displayed are epifluorescent midsections of nuclei (H2B-GFP). **A**) Digitonin treatment per se had no effect on nuclear morphology of permeabilized cells. **B-C**) An increase of the concentration of monovalent cations (80 mM NaCl resp. 80 mM KCl) did not lead to HCC formation. **D**) The standard treatment (medium +20x PBS) to induce HCC formation in intact cells (see Methods 5.6.2) had no effect on chromatin of permeabilized cells. **E-F**) An increase of the concentration of divalent cations (40 mM $CaCl_2$ resp. 40 mM $MgCl_2$), however, led to hyper-condensation of chromatin.

6.2.6.2 Nuclear functions are stalled during the HCC state

As already demonstrated by the observation of HCC formation in a colony of H2B-GFP expressing HeLa cells (Movie 1), cell division is stalled during the HCC state but recovered immediately after the release from hyper-osmotic conditions. This was especially impressing while monitoring a colony of cells including mitotic cells over several NCC-HCC-NCC cycles (Movie 2). The attention should be drawn to a prophase and a metaphase nucleus with the latter harboring chromosomes organized in the metaphase plate just before anaphase separation (Movie 2: lower left corner). The local movements of CTs, typically observed at this state of mitosis (see pre-treatment observation), were immediately brought to a stop, when HCC formation was induced. The treatment led to a further compaction of already

condensed mitotic chromosomes and kept them firmly 'frozen' in their present configuration. No movements were observed until the hyper-osmotic medium was removed and physiological conditions were restored. After this change, chromosomes instantly started to move and arrange in preparation for the imminent anaphase chromatid separation. All movements were again immediately halted after reestablishing hyper-osmotic conditions. On the whole, four cycles of NCC-HCC-NCC (10 min-5 min-10 min) were performed spanning a total observation period of 70 min. After final returning to normal conditions and subsequent long-term incubation (>17 h), anaphase proceeded regularly, chromatids separated successfully and daughter nuclei formed without any obvious sign of damage or suffering. This example impressively demonstrated the plastic nature of chromatin architecture, which enabled all monitored cells to survive the repeated hyper-osmotic treatments and to continue cell cycle progression. HeLa cells could be kept up to 60 min in the HCC state without any significant sign of cell suffering or increased cell death rate during the HCC state or in a long term observation period after the release from the HCC state (Movie 1). However, incubating cells for >1 h in the HCC state led to massive cell death during and after the release from the HCC state (Movie 3).

In addition to the interruption of the cell cycle, neither DNA nor RNA synthesis could be detected, when living HeLa cells were pulse-labeled for 10 min with Cy3-dUTP and BrUTP after HCC formation (Fig. 18B). To control that this negative finding was not caused just by an ineffective nucleotide uptake during the HCC state, cells were pulse-labeled in the same way but subsequently incubated in physiological conditions. These cells generated the pattern of incorporated BrUTP respectively Cy3dUTP indistinguishable from control cells (Fig. 18C).

When cells with NCC were loaded with BrUTP immediately before induction of HCC formation, RNA synthesis was absent in the nucleoplasm but still detected in nucleoli (Fig. 18D). These findings indicate that the transcription of genes by RNA polymerase II was quickly stalled after the beginning of HCC formation, whereas RNA polymerase I was still active during early stages of HCC formation. In accordance with this result, selective inhibition of RNA polymerase II transcription in control cells by α-amanitin (2 µg/ml) delivered BrUTP incorporation exclusively into nascent nucleolar (ribosomal) RNA (Fig. 18E).

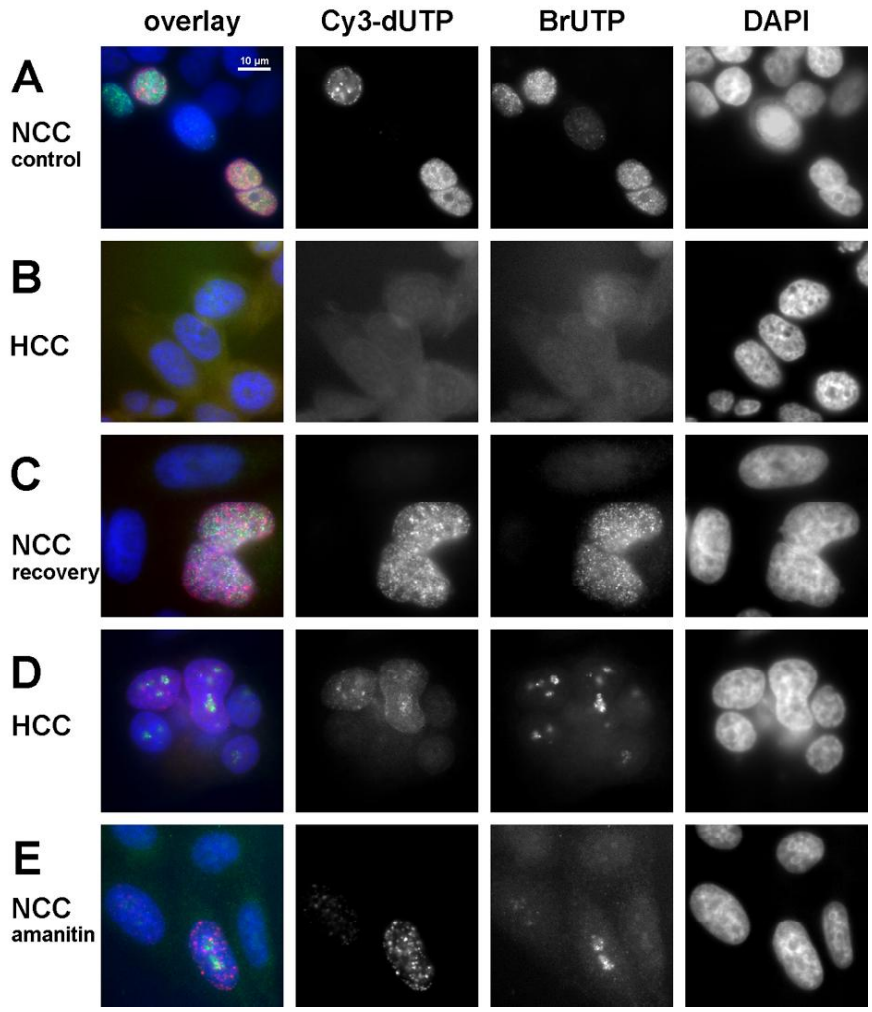

Figure 18: RNA and DNA synthesis is stalled after formation of HCC, but quickly resumes following restoration of NCC

Epifluorescent images of HeLa cell nuclei with nascent replication- and transcription-sites following scratch labeling of cells with BrUTP and Cy3-dUTP for 10 min. Overlay images show nascent RNA (green), nascent DNA (red) and DAPI-stained DNA (blue). **A-C)** Labeling patterns of control nuclei (A) and from nuclei labeled and released from HCC state (C) show patterns undistinguishable from each other, while no detectable labeling was observed in nuclei labeled during HCC (B). **D)** Labeling immediately before HCC formation, followed by 10 min incubation in the HCC state, gave rise to signals indicating BrUTP incorporation only in the nucleoli, but not in the nucleoplasm. Slightly Cy3dUTP labeled replication foci indicate reduced but not completely stalled DNA synthesis (D). These results suggest that HCC formation inhibits the activity of RNA polymerase II to a much larger extent than the activity of RNA polymerase I and DNA polymerase. **E)** A similar pattern of nucleotide incorporation was found when labeling was performed under physiological conditions in medium supplemented with α-amanitin, which selectively inhibits RNA polymerase II. As expected, cells only displayed a nucleolar BrUTP pattern, while DNA replication was not affected.

Transcription and DNA-replication were observed in cells that were pulse-labeled immediately after recovery of the NCC state (Fig. 19). Already after 5 min of incubations (Fig. 19C) patterns indistinguishable from those found in control cells were detected (compare Figs. 18 A, 18C and 19D). Moreover, 2 min of recovery and incubation with the labeled nucleotides were already sufficient to generate the known incorporation patterns (Fig. 19B), albeit the intensity of the signals was only low.

This rapid restoration of nuclear functions comprising cell division, transcription and DNA replication was unexpected considering the drastic difference of higher order chromatin compaction between nuclei with HCC and NCC.

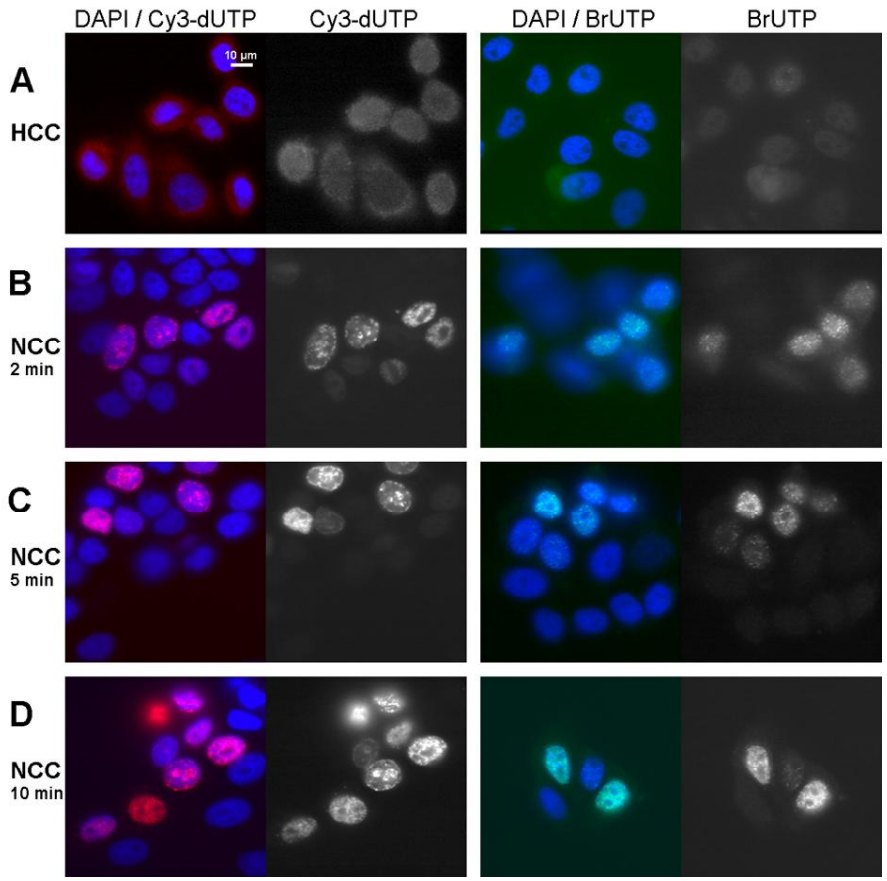

Figure 19: Immediate recovery of RNA and DNA synthesis

Epifluorescent images of HeLa cell nuclei with nascent replication- and transcription-sites following scratch labeling of cells with BrUTP and Cy3-dUTP respectively. Overlay images show nascent RNA (green), nascent DNA (red) and DAPI-stained DNA (blue). **A)** Labeling and incubation for 10 min during the HCC state resulted in no incorporation of the labeled nucleotides. **B)** Labeling during the HCC state and subsequent incubation for 2 min in physiological medium gave rise to the typical incorporation patterns with a low intensity of signals. **C-D)** Incubations in recovered physiological conditions for 5 or 10 min gave rise to patterns indistinguishable from control nuclei (compare Fig. 18A and 18C)

6.2.6.3 Is HCC formation an ATP dependent process?

To test for the ATP dependency of the HCC formation phenomenon, established ATP depletion protocols were applied followed by the incubation of cells in hyper-osmotic conditions (Fig. 20). ATP-depletion protocols (see Methods, 5.2.2) work by incubating cells in medium supplemented with sodium azide, which blocks the respiratory chain and thereby inhibits the synthesis of new ATP. Simultaneously, glucose is substituted in the medium by 2-deoxyglucose, which inhibits the glycolysis, the second possible cellular pathway of ATP generation. Incubating cells in these conditions leads to the exhaustion of cellular ATP levels (Dingwall et al., 1987; Phair and Misteli, 2000). This process on itself, however, led to condensation of chromatin in control cells kept in physiological medium (Fig. 20B), an effect already described in literature (Shav-Tal et al., 2004). Incubation of such cells in hyper-osmotic medium had an additional, but no substantial effect on further chromatin compaction (Fig. 20C). The test of ATP dependence of HCC formation could therefore not be addressed by the available protocols.

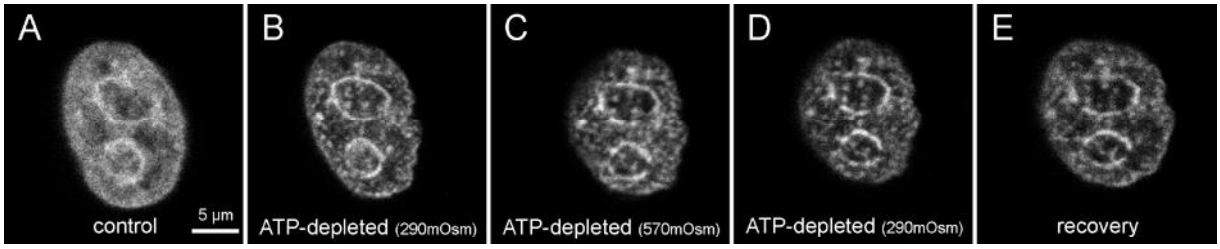

Figure 20: Effect of ATP depletion on HCC formation

A) Nucleus of a living HeLa cell with H2B-GFP tagged chromatin and normal ATP levels incubated in physiological medium. **B)** The same cell after incubation for 30 min in physiological (290 mOsm), glucose free medium supplemented with sodium azide (10 mM) and 2-deoxy-glucose (6 mM) already affected chromatin condensation compared to controls as previously described (see text). **C)** Moderate increase of chromatin compaction was observed after an increase of the osmolarity of the medium described in (B) to 570 mOsm. **D)** The ATP depleted cell revealed the same level of chromatin compaction 10 min after re-incubation in physiological medium as described in (B). **E)** Further incubation of the cell for 30 min in physiological medium did not yield a normalization of chromatin condensation (compare A and E).

6.3 Visualization of the interchromatin space

HCC formation occurred within 1 min after the increase of osmolarity (Fig. 21). Time lapse images recorded during the first 90 sec after the replacement of physiological medium (290 mOsm) with hyper-osmotic medium (570 mOsm) demonstrated that HCC formation was accompanied by an enlargement of large interchromatin lacunas already detected in untreated nuclei (Fig. 21A:arrowhead). Alternatively, the osmolarity of the medium was stepwise increased from 290 to 750 mOsm (Fig. 21B). This procedure resulted in a stepwise increase of chromatin condensation together with a stepwise widening of the pre-existent interchromatin space (Fig. 21B: arrowhead). Additional channels became apparent, which were not visible in untreated nuclei (Fig. 21B: arrows). Due to the limited resolution of light microscopy, it was not possible to determine whether such channels were already present in untreated nuclei or were too narrow to be detected. Nevertheless, the majority of the DNA free space observed between HCC bundles reflects the widening of a pre-existing interchromatin space. The relative volume occupied by the widened interchromatin space including nucleoli was in the order of 60% in HeLa cells.

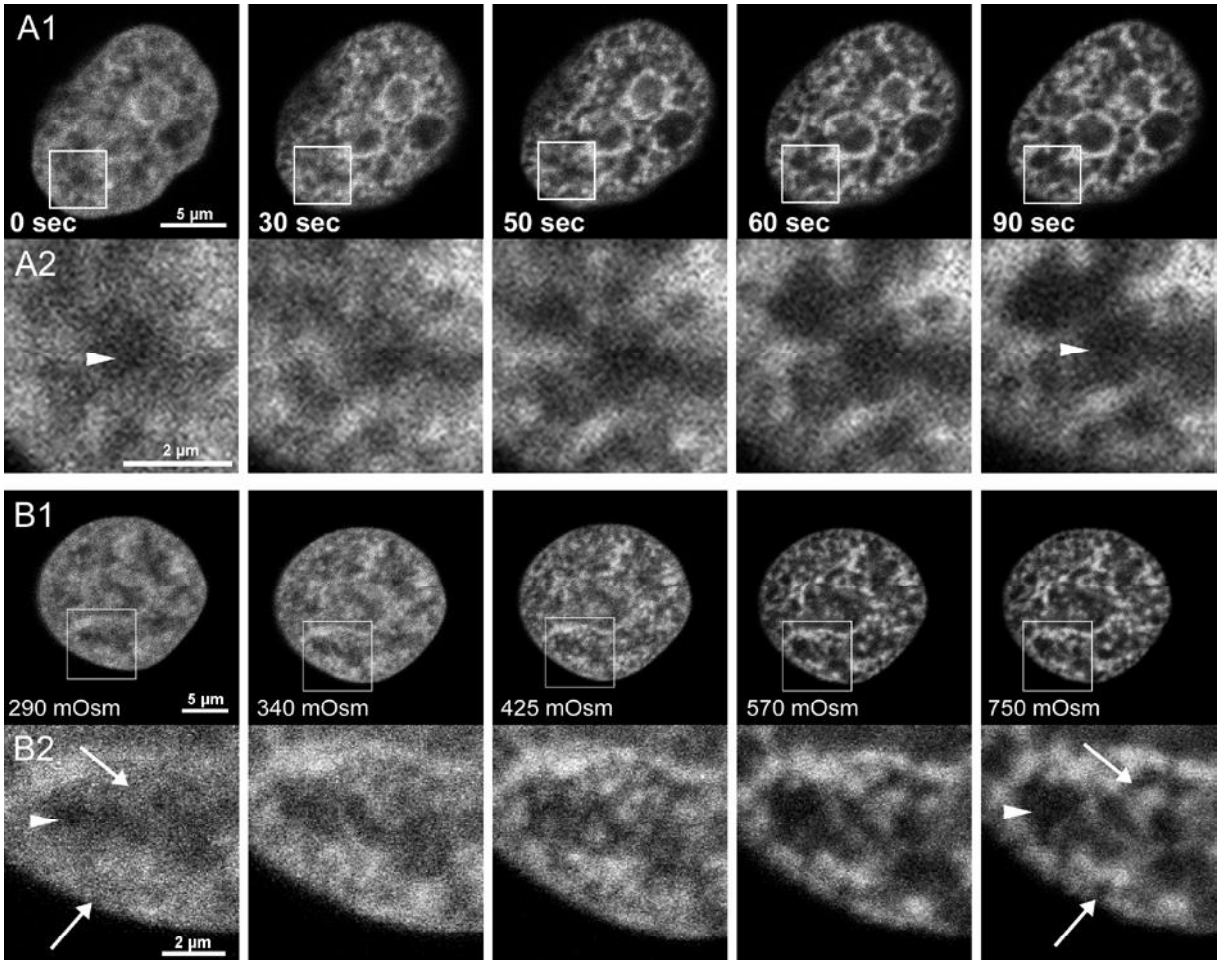

Figure 21: HCC formation is accompanied by the enlargement of interchromatin space

A) Time-lapse recording of confocal midsections from the nucleus of a living HeLa cell (H2B-GFP) before the treatment (0 s) and subsequently at 30, 50, 60 and 90 s after subjection to hyper-osmotic medium (570 mOsm). HCC formation implied an expansion of IC lacunas already visible under physiological conditions (A2, arrowheads). Maximum condensation was obtained after about 60 s. A similar time-scale was found for the decondensation process (data not shown).

B) Exemplary confocal midsections from the nucleus of a living HeLa cell with H2B-GFP tagged chromatin in physiological medium (290 mOsm) and after incubation for 5 min each in medium with increasing osmolarity (340 mOsm; 425 mOsm; 570 mOsm; 750 mOsm). Chromatin hypercondensation increases from 340 to 570 mOsm. No further increase is apparent at 750 mOsm. Corresponding close-ups (B2) indicate that the space between HCC bundles was generated at last to a large extent by the expansion of the pre-existing interchromatin space (arrowheads) and additional interchromatin channels (arrows) not visible in untreated nuclei.

6.3.1 Topology of functional processes

The finding that the interchromatin space gets enlarged by HCC formation allowed testing postulations of the CT-IC model on the localization of functional processes. Therein the interchromatin space is termed interchromatin compartment (IC) to place emphasis on its functional relevance. Processes like transcription or replication are accordingly expected to preferentially locate at the perichromatin region, the border zone between the chromatin and the interchromatin compartment (IC). Having widened the IC in nuclei with HCC, should

accordingly enable to locate these processes at the surface of the HCC bundles. Since an anticipated complex network of IC channels in untreated nuclei would only roughly be delineated by HCC formation, an only global trend of preferential localization of active processes at the HCC bundle surface was expected. To test for this expectation, various immuno-labeling experiments were performed with antibodies directed against proteins or nucleotides involved in two of the major nuclear functions: transcription and DNA replication.
For the sake of comparability the immuno-detection (Fig. 22) and measured localization (Fig. 23) of these active nuclear processes are displayed together with results on the topology of other nuclear components dealt with in subsequent chapters.

6.3.1.1 Transcription

To mark sites of ongoing transcription, RNA polymerases were detected with specific antibodies (Fig. 22C). In a second approach cells were incubated with BrUTP for 10 min followed by subsequent HCC formation and fixation thereafter (Fig. 22A). Since BrUTP gets incorporated in nascent transcripts, these nucleotides were detectable at sites of ongoing transcription by specific antibodies. All signals, obtained with these immuno-labeling approaches were measured for their closest distance to the next surface of the HCC bundles (Fig. 23A). The frequencies of distances were plotted in distance classes of 200 nm. Hence, the y-axis (0 on the x-axis) represents the surface of HCC bundles, positive distance values display signals located in the IC (=‘outside' of HCC bundles), whereas signals with negative values correspond to locations 'inside' the HCC bundles. One should note that these measurements were performed on 3D confocal data sets limited by an inherent axial resolution of ~500 nm. Nevertheless, a preferential localization of the signals was obtained in a window of ±200 nm around the chromatin bundle surfaces (Fig. 23A). Since absolute statements, e.g. on the mean distance of signals from the surface are limited due to the microscopy setup properties, the distribution was compared with an even distribution (Fig. 23B: yellow bars), obtained by measuring an artificial channel which covered the entire nuclear volume (including chromatin, nucleoli and the widened interchromatin compartment). Accordingly, the measured distance frequencies for these artificial control signals represent a distribution without any preference and served as a control distribution. The distributions for the signals obtained for molecules involved in transcription differed significantly from this control distribution ($p < 0.001$, Wilcoxon U-test). For a second control, which revealed the distribution of chromatin in nuclei with HCC, the distance distribution of the HCC signal itself was measured against its surface (Fig. 23B: red bars).

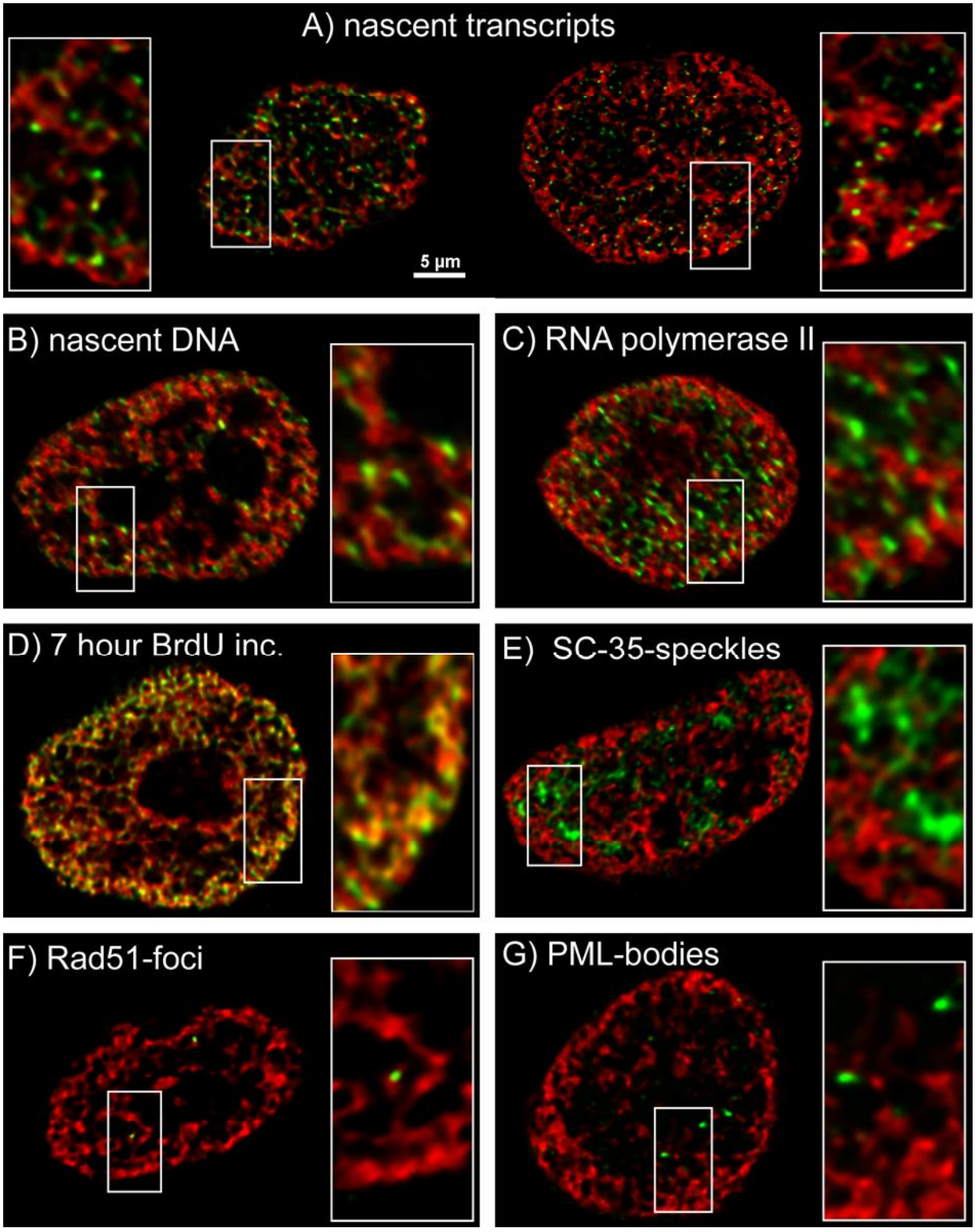

Figure 22: Immuno-detection of nuclear components in nuclei with HCC

Visualization of nascent RNA, DNA, RNA polymerase II, SC-35 speckles and nuclear bodies in HeLa cell nuclei with HCC. In addition to HCC bundles (H2B-GFP, red) the following components (green) were visualized directly or by immunocytochemistry (Methods, 5.3 and 5.5): **A**) nascent transcripts after 10 min incorporation of BrUTP, **B**) nascent DNA after 10 min pulse-labeling with Cy3-dUTP, **C**) RNA polymerase II (large sub-unit), **D**) DNA after 7 h BrdU labeling, **E**) SC-35 speckles, **F**) Rad51-foci and **G**) PML-bodies.

Naturally, measurements of the same channel against its own surface can only deliver negative values ('inside' the HCC bundles), which was also highly significant different from the distributions of signals comprising ongoing transcription (BrUTP and RNA Pol-II: p<=0.001, U-test). As an additional control distribution, chromatin was labeled by a long term BrdU incubation which gets incorporated in chromatin in S-phase nuclei. A potential bias due to tagging only parts of the chromatin was prevented by extending the pulse to more than 7 h. Under these conditions, a wide coverage of the entire chromatin was obtained by immuno-detection of the incorporated BrdU (Fig. 22D). Measuring these signals against the surface of chromatin visualized by the expression of H2B-GFP, gave rise to a distribution with >70% of the signals inside of HCC bundles confirming the reliability of the approach (Fig. 23B: orange bars). The remaining <30% of BrdU tagged chromatin located outside of H2B-GFP points to the limitations of the microscopy approach used.

Nevertheless, both distributions delineating transcription sites differed highly significantly from this chromatin control distribution (BrUTP and RNA Pol-II: p<=0.001, U-test). The detection of signals deep inside of HCC bundles, like observed for the detection of BrdU (Figs. 22D and 23B), additionally confirmed that the interior regions of HCC bundles were accessible for antibodies with the immuno-detection protocol applied.

The specific localization of nascent transcripts at the surface of HCC bundles was additionally investigated by electron microscopy (Fig. 24). As a first control, normally condensed chromatin of ultrathin sections of HeLa cells was contrasted with the Feulgen type osmium ammine staining reaction (Cogliati and Gautier, 1973). This method is used to specifically label chromatin which becomes dark contrasted against a less stained interchromatin space (Fig. 24A-1 and 24A-3). The complexity of interchromatin channels and lacunas gets especially obvious, when chromatin regions are highlighted with a false-color (Fig. 24A-2 and 24A-4: red signals). Additionally, chromatin and DNA have been immuno-detected with specific primary and gold-coupled secondary antibodies in a HeLa cell expressing H2B-GFP. The gold grains differing in size for DNA (anti-DNA, 15 mm) and chromatin (anti-GFP, 10 mm) were additionally highlighted with false colors (green resp. blue) and demonstrate the existence of a mostly chromatin free interchromatin space (arrows) since they predominantly overlap with the dark contrasted chromatin (Fig. 24A-4).

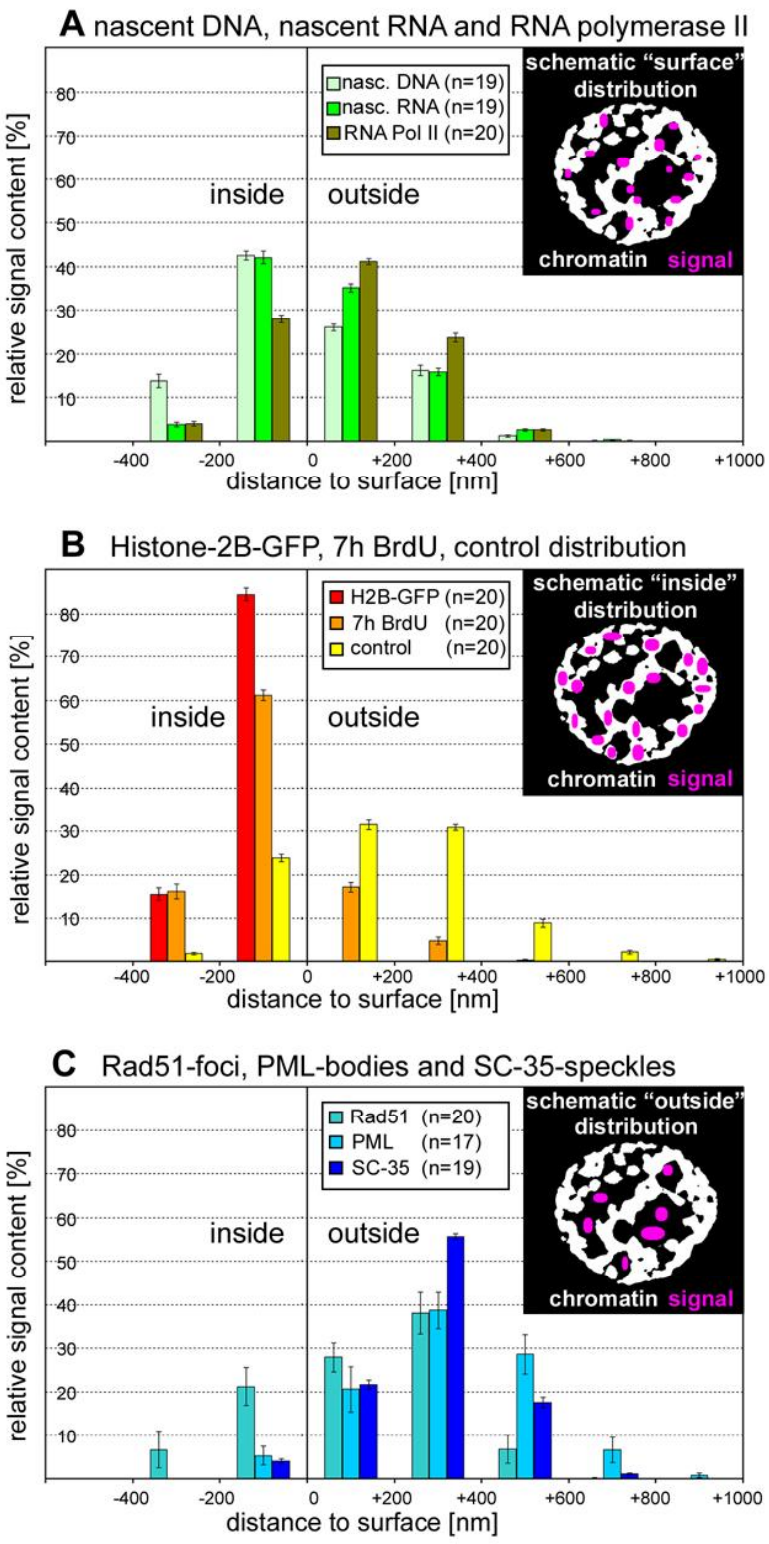

Figure 23: Quantitative analysis of the topography of nuclear components in nuclei with HCC

A) 3D distance values for signal voxels attributed to nascent DNA (bright green bars), nascent transcripts (dark green bars) and RNA polymerase II (olive bars) demonstrate the location of most of these signals close to the surface of HCC bundles (compare scheme in the inset). **B**) H2B-GFP signals (red bars), as expected, were located exclusively inside of HCC bundles. BrdU signals (orange bars) recorded after 7 h BrdU labeling were also mainly located within HCC bundles (comparable to a schematic distribution drawn in the inset). Yellow bars display a control distribution (see 5.10.7), covering the entire nuclear volume. **C**) More than 90% of signal voxels from PML bodies (bright blue) and SC-35 speckles (dark blue) located within the expanded IC (compare scheme in the inset). In contrast, only about 70% of signal voxels attributed to Rad51 foci (turquoise) located outside of HCC bundles, the remaining fraction suggests a more intimate connection with HCC bundles.

Since the osmium ammine staining technique largely destroys molecules other than chromatin, a detection of transcripts had to be carried out with another chromatin contrasting technique ('EDTA regressive staining', Bernhard, 1968) leaving chromatin less contrasted against a higher contrasted nucleoplasm (Fig. 24B). When BrUTP molecules incorporated in nascent transcripts were immuno-detected with specific primary antibodies and secondary antibodies coupled with gold particles the localization in regard to chromatin was observable

at a high resolution level (Fig. 24B-3 and 24B-4). These images demonstrate a preferential localization of nascent RNA labeling at the surface of HCC bundles, thus confirming the measurements performed on 3D confocal data sets.

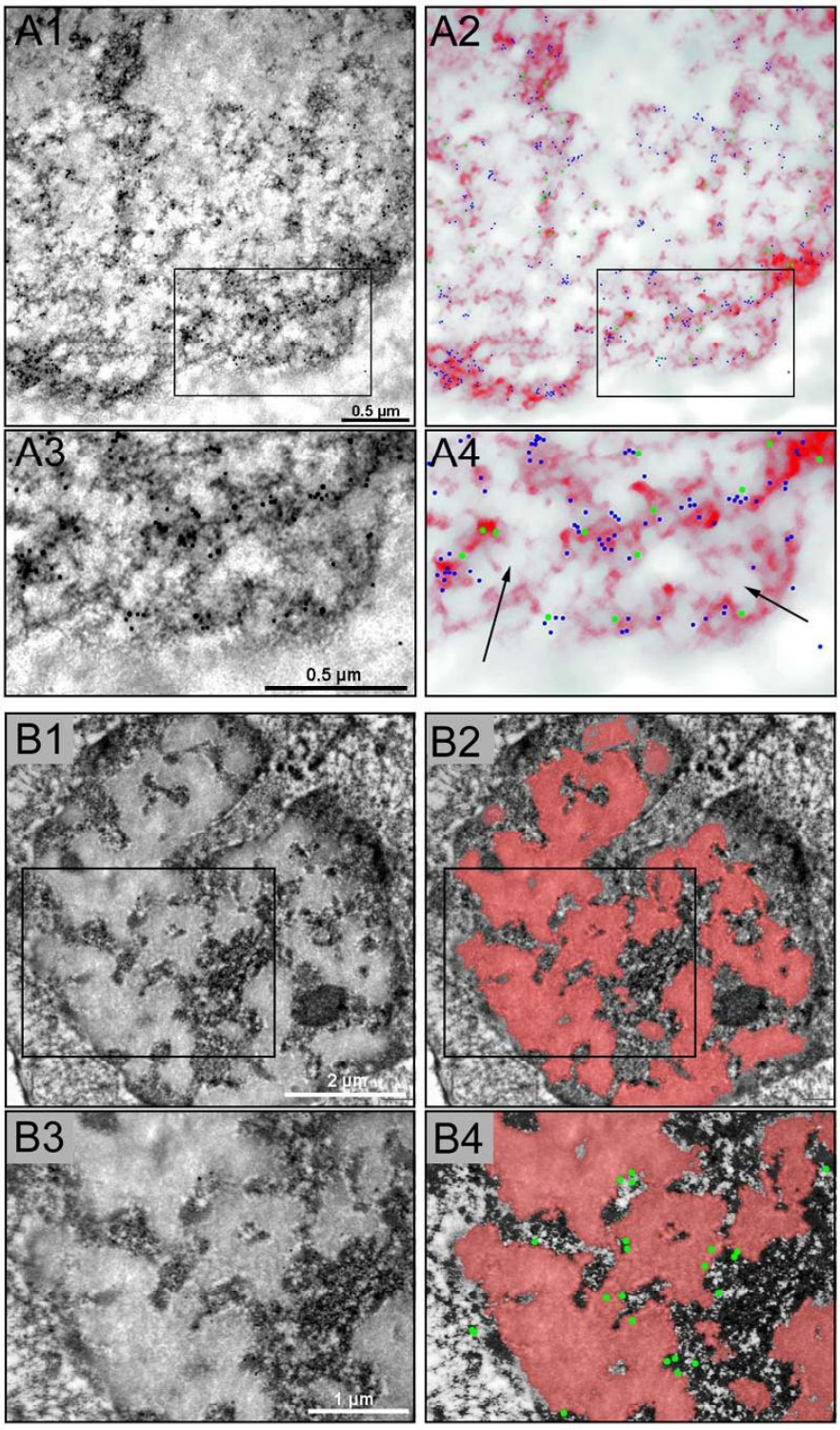

Figure 24: EM provides evidence for interchromatin space and localization of nascent transcripts

A) Immunoelectron microscopic visualization of DNA and GFP tagged histone H2B on a HeLa cell nucleus after double-labeling with specific anti-DNA and anti-GFP antibodies and colloidal gold markers of 15 nm and 10 nm, respectively. The ultrathin section was contrasted by a Feulgen-type staining specific for DNA. A1) Raw electron micrograph and enlargement (A3). A2 and A4) Same images with DNA contrast enhanced by red color, 15 nm gold particles (anti-DNA) colored in green and 10 nm particles (anti-GFP) colored in blue. A4) IC channels (arrows) expand between chromatin regions marked by the red DNA and the false colored gold particles.

B) Immunoelectron microscopic visualization of nascent transcripts in a Hela cell nucleus with HCC after 10 min incorporation of BrUTP detected with specific antibodies and colloidal gold markers. The ultrathin section was treated by the EDTA regressive staining (see text), leaving chromatin less contrasted. B1) Raw electron micrograph and enlargement (B3). B2 and B4) Same images with chromatin and antibody signals highlighted with false colors (red respectively green). Nascent RNA was preferentially found at the surface of HCC bundles. (Images A1-4: Vecchio L.; B1-4 Tiberi C., Lausanne)

6.3.1.2 Replication

Long term incubation of S-phase cells with BrdU led to a labeling distribution of signals largely covering the HCC bundles (see Figs. 22D and 23B). Following the postulations of the CT-IC model, however, ongoing replication would be expected to take place only at the surface of HCC bundles, the border zone between chromatin and the IC. Short term incubation with BrdU, incorporated in nascent DNA in S-phase cells, was used to address this question. Incubation with BrdU nucleotides was limited to 10 min before HCC formation and immediate subsequent fixation. The obtained signals of nascent replicates (Fig. 22B) were measured against the surface of HCC bundles as described above. In fact the obtained distance distribution (Fig. 23A: green bars) differed significantly ($p<=0.001$, U-test) from the long-term BrdU labeling distribution (Fig. 23B: orange bars). A localization around the surface of HCC bundles, with >70% of all measured signals in classes of ±200 nm was obtained. This signal distribution for active replication sites delivered a similar distribution as obtained for the sites of ongoing transcription, supporting the claim of this border zone being the shared compartment of active nuclear processes.

Rad51-foci

Rad51 is a protein involved in the repair of double-strand-breaks (DSBs) and was reported to form nuclear bodies in S-phase cells (Tashiro et al., 2000). Being involved in nuclear functions localization at the surface of HCC bundles was expected following the postulations of the CT-IC model (see above). Measured distances for the anti-Rad51 signals (Figs. 22F and 23C: turquoise bars), however, delivered a signal distribution mostly in the IC, but no significant difference to the control distribution ($p= 0.756$, U-test). Accordingly, it has to be concluded that Rad51-foci localized with no preference for the surface, interior or exterior of HCC bundles. This result might reflect that not all labeled foci were located at sites of ongoing repair but that some may additionally serve as storage sites ('inside' the IC) or may stay at sites already repaired ('inside' the HCC bundles) for a longer period.

6.3.2 Topology of nuclear speckles and bodies

SC35-speckles

Nuclear speckles or interchromatin granule clusters as termed in electron micrographs locate in chromatin free areas in nuclei with NCC as reported by light- and electron microscopy studies (Lamond and Spector, 2003, see Introduction, 4.4.1). Immuno-detection of the splicing factor SC-35, one of the major components of nuclear speckles, in nuclei with HCC delivered as expected signals inside the widened IC (Fig. 22F). The measured frequency distribution of these signals displayed >70% of the values in distances more than 200 nm apart from the HCC bundle surface (Fig. 23C: blue bars). This distribution differed highly

significant not only from the control distributions (both with p<=0.001, U-test) but also from the distributions of the sites of ongoing transcription and replication (both with p<= 0.001, U-test). It is important to note that the structures visualized and measured here do not delineate sites of ongoing splicing but only depict the prominent splicing speckles, which are mostly considered as storage sites for splicing factors (Fay et al., 1997; Lamond and Spector, 2003).

PML-bodies

Other prominent nuclear compartments are the PML bodies (Ching et al., 2005). Similar to the nuclear speckles they have been reported to locate in the chromatin free areas in untreated nuclei. Whether these compartments do play a functional role is not known, but it was proposed that they may serve as storage sites for a large variety of proteins. One of these is the pro-myelotic leukemia (PML) protein. It was discovered since its typical aggregated appearance ('bodies') gets lost over the course of the pro-myelotic leukemia but PML signals become more diffuse. Measuring the distribution of immuno-detected PML signals in nuclei with HCC demonstrated their preferential localization in the widened IC similar to the SC-35 signal distribution (Fig. 22G). Again >70% of all measured signals located more than 200 nm from the closest HCC bundle surface (Fig. 23: bright blue bars). The PML distribution was tested to be significantly different from the control distributions (both with p<= 0.001, U-test) as well as from the distribution of the sites of ongoing transcription and replication (both with p<= 0.001, U-test).

6.3.3 Topology of 'nuclear matrix' associated proteins

The reversible manipulation of chromatin morphology by the induced formation of HCC opened a new avenue to explore the question where a 'nuclear matrix' potentially involved in higher order chromatin organization is localized. This question was mainly addressed in the Diploma thesis of Tobias Thormeyer who was supervised in the course of this thesis (Thormeyer, 2005). The observation that nuclear function and organization got rapidly re-established after restoration of physiological conditions led to the postulation that topological relationships of chromatin and the 'nuclear matrix' had to be conserved to a certain extent during an entire NCC-HCC-NCC cycle. A ‘nuclear matrix’ was expected to locate either within chromatin bundles, if it served as a scaffold organizing chromatin from the interior or within the IC, if it served as an anchoring site for decondensed active chromatin. Following the argument that 'nuclear matrix' preparations are only precipitations of interchromatin proteins, a preferential localization of 'nuclear matrix' proteins inside the widened IC would be expected.

Scaffold attachment factor A (SAF-A)

One of the numerous proteins detected in 'nuclear matrix' preparations is the scaffold attachment factor A (SAF-A or 'hnRNP U'='heterogeneous nuclear ribonucleoprotein U' with RNA binding sites and affinity for DNA scaffold attachment regions, SARs). Immuno-detected signals displayed a preferential localization of SAF-A at the surface of HCC bundles (Fig. 25B and 25C: green bars). The measured closest distances to the HCC bundles gave rise to a signal distribution very similar to the one demonstrated for the sites of ongoing transcription or replication. Accordingly, the SAF-A distribution was tested to be highly significant different from the control distributions (both with $p <= 0.001$, U-test), but not from the distributions of nascent transcripts ($p=0.332$, U-test), RNA polymerase-II ($p=0.227$, U-test) or nascent DNA ($p=0.421$, U-test). Since the incorporated BrdU was detectable in the interior of HCC bundles with the immuno-detection protocol used (compare Figs. 22D and 23B: orange bars), a methodological limitation in the access to the HCC bundle interior could be excluded. This finding rules out the claim of a localization of the 'nuclear matrix' in the interior of compact chromatin.

Lamin A/C

The nuclear lamina has been demonstrated to have a considerable impact on the structural organization of the nucleus. Immuno-detections of the lamins A/C or B in nuclei with NCC typically delineate the lamina at its peripheral localization in close contact with chromatin. According to several reports, however, lamins A/C should additionally be detectable in the nuclear interior (Hozak et al., 1995). It was postulated that these intermediate filaments were essential components of the 'nuclear matrix' serving as its structural basis. However, besides the perinuclear layer, no interior lamins A/C were detectable in HeLa cell nuclei under the conditions sufficient to detect BrdU in nuclei with NCC as well as after formation of HCC (Thormeyer, 2005). This failure of detection made judgments on the localization of the 'nuclear matrix' on basis of intranuclear lamins A/C impossible. Notably, the close contact of the peripheral lamins and chromatin dense regions got partly lost in nuclei with HCC (Fig. 25A). The distances of these peripheral lamin signals to the surface of HCC bundles delivered a wide distribution with >60% of the signals located remote (>250 nm) from the HCC bundles (Fig. 25A and 25C: blue bars).

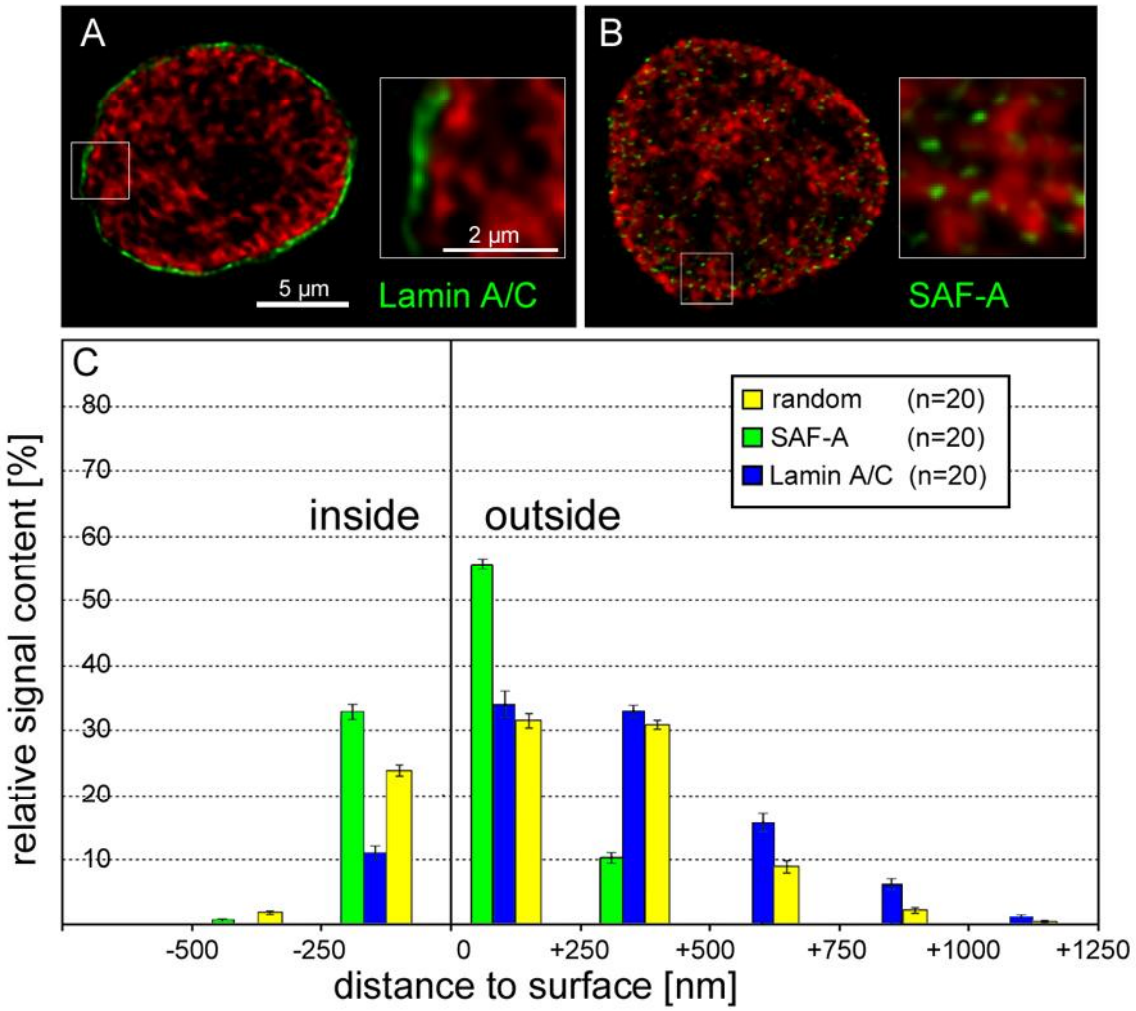

Figure 25: Topology of 'nuclear matrix' associated proteins in nuclei with HCC

A) Immuno-detection of Lamin A/C (green) in a HeLa cell nucleus (H2b-GFP, red). Besides the peripheral layer, no lamins A/C were detected in the nuclear interior. The enlargements point to a region, where the close junction of the lamina with chromatin is lost. **B**) Immuno-detection of SAF-A (α-hnRNP-U, green) in a HeLa cell nucleus (H2b-GFP, red). A preferential localization at the surface of HCC bundles was observed. C) Quantitative measurements on the topology of lamins A/C (blue bars) and SAF-A (green bars) in comparison with the random distribution (yellow bars).

6.4 The architecture of HCC bundles

6.4.1 Chromosome territories are interconnected in a 3D network

3D image reconstructions of nuclei of all tested cell lines with HCC revealed a contiguous chromatin signal. No visual separation of CTs just based on the chromatin counterstain was possible as demonstrated with 3D reconstructions and corresponding confocal mid-sections of a HeLa H2B-GFP nucleus with HCC (Fig. 26). The chromatin signal could only be separated in a larger number of smaller bodies if very high gray value thresholds were applied (Fig. 26F). In such cases, however, bright signals were excluded and most of the occurring separated bodies were too small to comprise whole CTs.

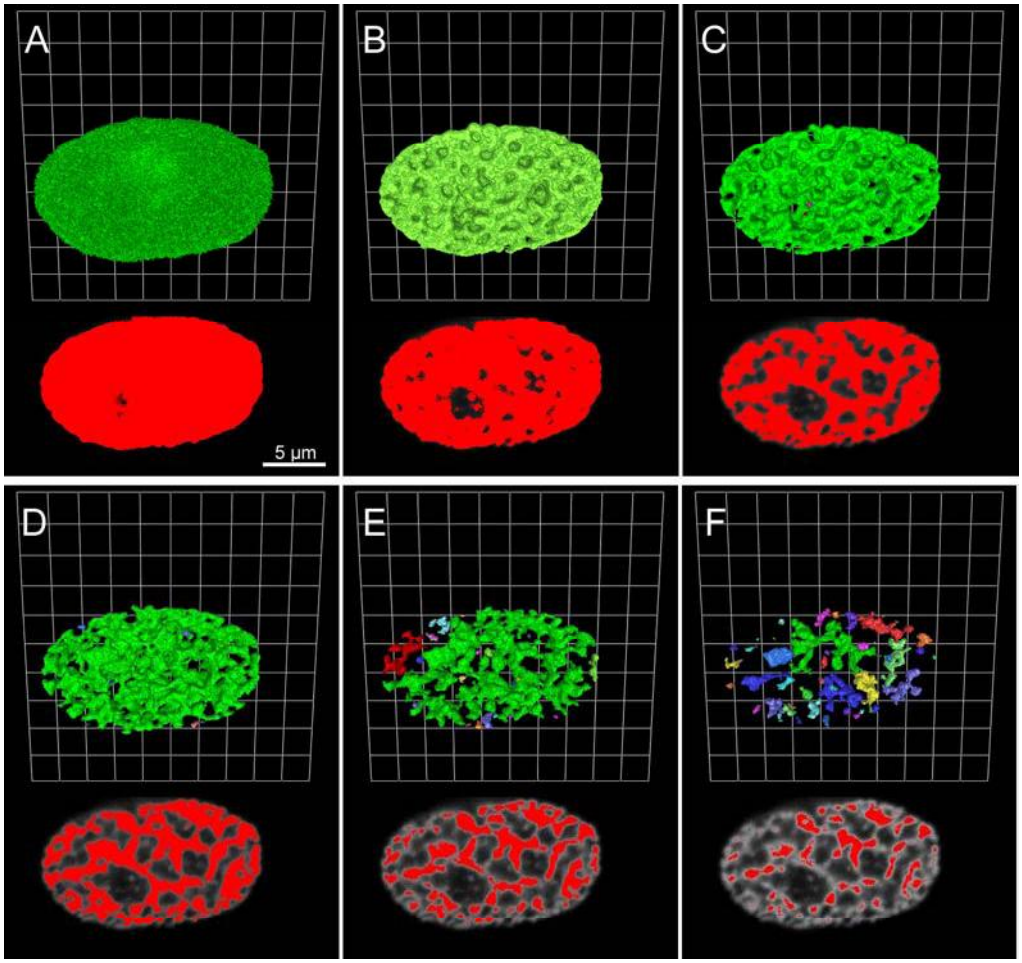

Figure 26: 3D reconstructions and corresponding confocal mid-sections of a nucleus with HCC

A HeLa cell nucleus with HCC, visualized by expression of H2B-GFP is displayed after applying a gray value threshold of 20 (**A**), 40 (**B**), 70 (**C**), 100 (**D**), 130 (**E**) and 160 (**F**) on the 3D confocal data set (8-bit format). 3D reconstructions (green for the biggest body, differently colored for all smaller bodies) and corresponding confocal mid-sections (gray= original data / red=segmented data after applying the TH) are shown to demonstrate the failure of segmenting single chromosomes just based on the chromatin staining. The chromatin signal only fell apart in separated bodies (each displayed with a different color) after applying a very high TH (**F**), which excluded intense signals (gray in mid-section) and the obtained bodies were mostly too small to comprise whole CTs (compare 3D reconstruction and mid-section).

Hence, CTs are tightly interconnected in a 3D chromatin network (Fig. 27A-1 and A-2: green). This 3D chromatin network is co-aligned by a 3D network of the enlarged interchromatin channels and lacunas (Fig. 27A-1 and A-3: red). 3D FISH with paint probes for HSA 7 and 8 in nuclei of human fibroblasts with HCC (Fig. 27B) revealed spatially discrete, differentially painted CTs. Typically CTs occupied the complete diameter of a bundle and displayed a clear contrasted border to neighboring chromatin. In nuclei in which the two painted CTs were accidentally located side by side, persistent connections of HCC bundles from one CT to the next were observed (Fig. 27B-2 to B-4). Without the FISH paints (Fig. 27B-2), however, no separation at the site of CT interconnection was observed.

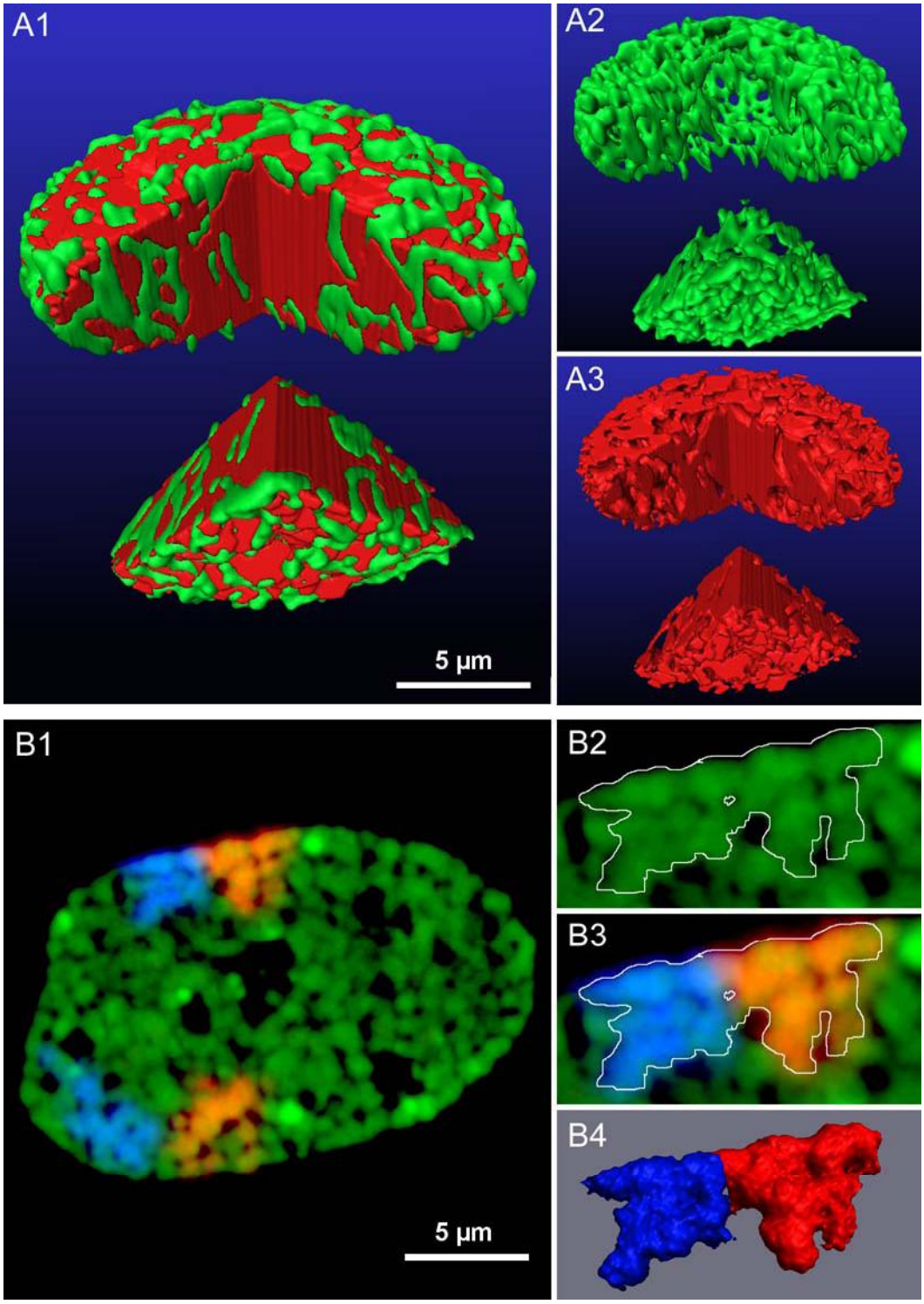

Figure 27: 3D networks of HCC bundles and interchromatin channels.

A1) 3D reconstruction of a HeLa cell nucleus (H2B-GFP, green) after HCC formation. The space between HCC bundles (red) represents both the expanded IC space and the nucleoli. Removal of a nuclear segment allows a view into the nuclear interior. The hypercondensed chromatin (**A2**) and expanded IC space (**A3**) form two contiguous networks. **B1**) Confocal midsection of a human fibroblast nucleus after HCC formation with painted CT 7 (red) and 8 (blue) and TO-PRO-3 stained chromatin (green) indicates a complex folding of CTs with IC channels expanding from the territory periphery to the interior. Close-up views of HCC bundles with and without chromosome painting (**B2 and B3**) suggest a direct connection between the chromatin of two adjacent CTs further emphasized by 3D reconstructions (**B4**).

6.4.1.1 Stability of chromatin network pattern

To test, whether the observed chromatin network was the result of a random chromatin clustering, repeated NCC-HCC-NCC cycles were performed. In case of random formation of HCC bundles the exposure of living cells to repeated NCC-HCC-NCC cycles was expected to lead to highly variable chromatin patterns. Individual HeLa cells with histone H2B-GFP tagged chromatin were followed through three consecutive NCC-HCC-NCC cycles of 5 min in hyper-osmotic medium (570 mOsm) followed by 5 min in physiological medium (290 mOsm). During each cycle confocal serial sections were recorded from nuclei with HCC and NCC (Fig. 28A-1 to A-6). Best fit overlays from maximum intensity projections recorded at subsequent cycles were generated for nuclei with NCC (not shown) and nuclei with HCC, respectively (Fig. 28A-7 to A-9). In addition, 3D reconstructions of the same nuclei were generated for comparison (Fig. 28A-10 to A-12). The apparent reproducibility of the observed higher order chromatin patterns during repeated NCC-HCC-NCC cycles supports the hypothesis that structural patterns observed in nuclei with HCC reflect a higher order chromatin and interchromatin topology that already exists in nuclei with NCC. The observed similarity was confirmed by measuring the differences between 3D data sets with a histogram-based approach, which provides the mean-square-error MSE (see Methods, 5.10.5). This approach was developed at the division 'Intelligent Bioinformatics Systems' at the DKFZ in Heidelberg by Karl Rohr and colleagues in a collaborative project. MSE values are small for a comparison of similar input data (MSE = 0 for identical data sets), while a comparison of increasingly dissimilar data sets yields increasingly larger MSE values. The comparison of repeated NCC and HCC states of the same nucleus yielded MSE-values of 7.7 ± 1.5 and 8.8 ± 1.9 respectively (n=15), while the pair-wise comparison of MSE-values for 54 different nuclei yielded significantly higher MSE-values of 28 ± 2.9 for NCC and 25 ± 2.7 for HCC ($p < 0.001$, U-test). To further test the reproducibility of higher order chromatin arrangements during repeated NCC-HCC-NCC cycles, stripes were bleached into HeLa cell nuclei with H2B-GFP tagged chromatin using an intense laser beam (Fig. 28B). The stripes were fully maintained during repeated cycles both in the nuclear periphery and in the nuclear interior demonstrating once more the non-randomness of HCC formation and concomitant IC enlargement.

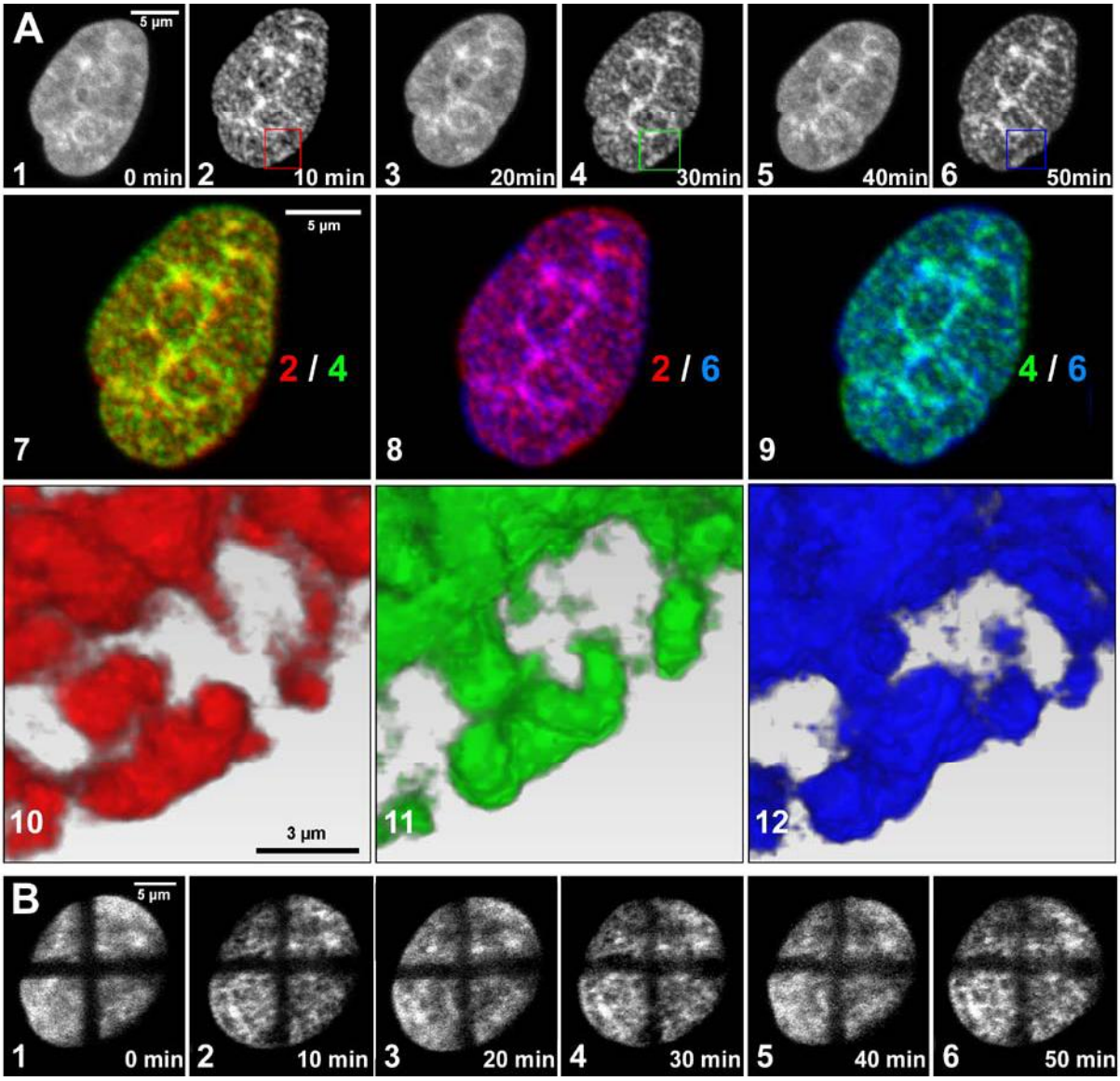

Figure 28: Repeated NCC-HCC-NCC cycles reveal reproducible chromatin and IC patterns.

A-1 to A-9) Nucleus of a living HeLa cell (H2B-GFP, confocal maximum Z projections) during repeated cycles of HCC formation (A-2, A-4, A-6) and release (A-1, A-3, A-5). Overlays of pseudo-colored projections (A-2 red; A-4 green; A-6 blue) revealed merged colors expected in case of a high reproducibility of the patterns of HCC bundles. **A-10 to A-12)** 3D reconstructions of the image stacks recorded from nuclei with HCC (compare A-2, A-4 and A-6) further demonstrate the reproducibility of the HCC networks, suggesting that these were formed on the basis of a structure pre-existing in nuclei with NCC. **B)** Crosswise stripes of bleached chromatin are maintained during repeated NCC-HCC-NCC cycles. Crosswise stripes of chromatin were bleached in the nucleus (H2B-GFP) of a living HeLa cell by an intense laser beam (B-1). Confocal midsections of the nucleus were obtained during repeated HCC formation (B-2, B-4, B-6) and release (B-3, B-5). The first image (B-1) was obtained 5 min after bleaching, the others (B-2 to B-6) thereafter at time intervals of 10 min. The bleached cross remained visible during all cycles.

6.4.2 Localization of active and inactive chromatin in HCC bundles

In consideration of the fact that transcriptional and replicational processes were located at the surface of HCC bundles, the question arising was whether active respectively inactive chromatin sites would be specifically arranged in the HCC bundles. Accordingly active chromatin would be expected to predominately locate at the periphery of HCC bundles whereas inactive chromatin would be expected to be preferentially found in the very interior. Such a topology was further suggested by the *in-vivo* observations (see 6.2.5), which indicated early replicating chromatin (i.e. gene-rich) to shift towards late replicating chromatin (i.e. gene-poor) during HCC bundle formation.

6.4.2.1 Comparison of different chromatin counterstains

As a first approach the general topology of chromatin counterstained by DNA dyes differing in their affinity to AT- or GC-rich DNA sequences was investigated. Since gene-rich chromatin in human cells generally exhibits a higher content of GC base pairs compared to gene-poor regions comprising an enrichment of AT base pairs, dyes differing in their DNA binding affinity were expected to display the specific topological arrangement postulated above. The counterstains used were 4',6-Diamidino-2-phenylindol (DAPI) and the cyanine monomer ToPro-3 (both with an AT-affinity), 7-aminoactinomycin D (7-AAD; GC-affinity) and propidium iodide (PI; no preference). Since ToPro and PI stain single stranded RNA as well, an RNase digestion was performed in all experiments before DNA counterstaining (see Methods, 5.4.2).

This global approach of DNA staining, however, revealed no apparent differences in the staining pattern in regard to the staining of HCC bundles (Fig. 29). Slight differences in staining intensities might reflect differences in the AT versus GC content of the respective chromatin regions. However, these differences followed no obvious topology in regard to the periphery or inside of HCC bundles. This negative finding is naturally not sufficient to generally reject the hypothesis of preferential chromatin arrangement in HCC bundles in regard to GC- or AT-content at local levels, but only rules out the existence of a pronounced global arrangement of these regions.

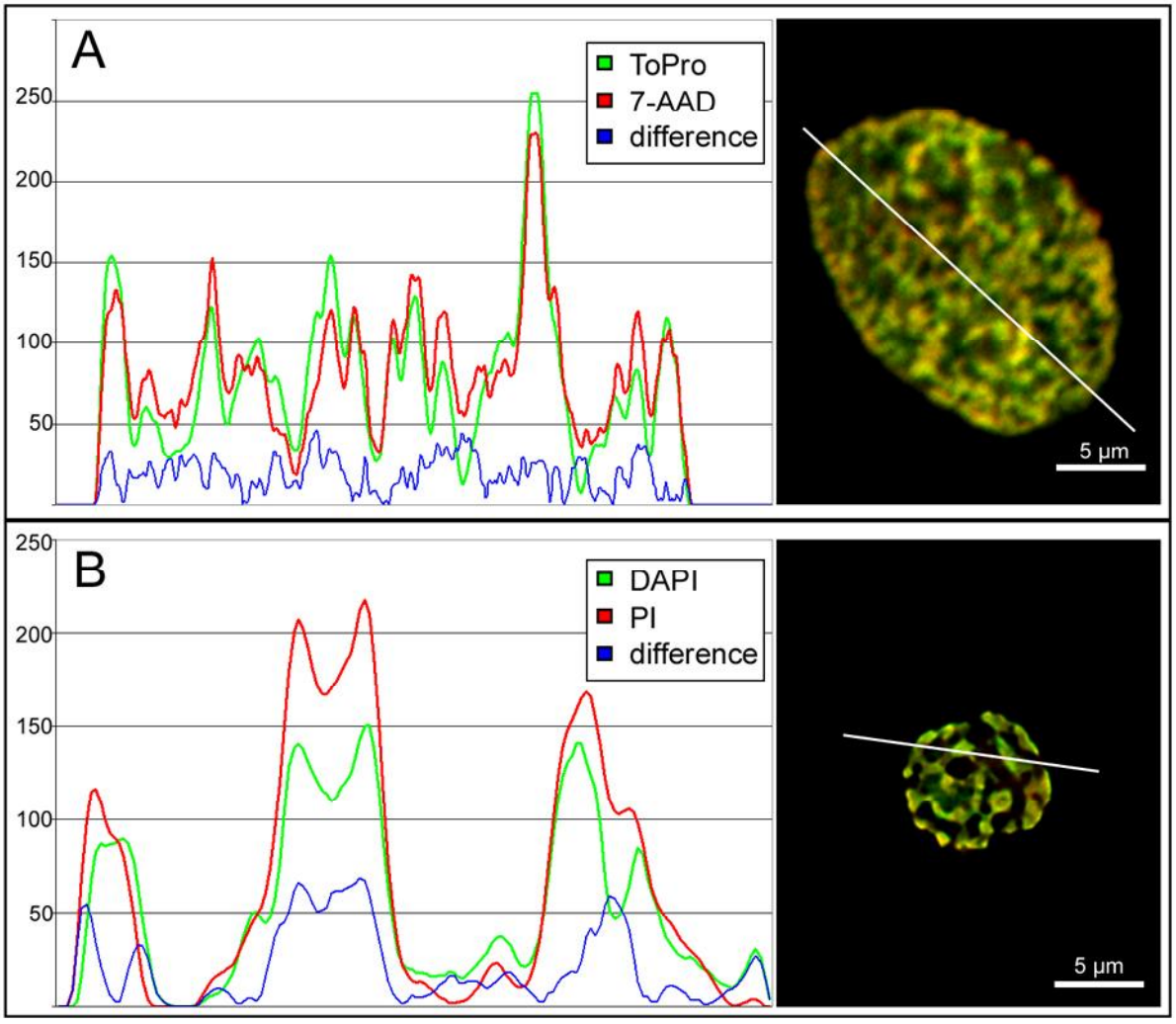

Figure 29: Different counterstains (AT versus GC affinity) reveal no obvious architecture in HCC bundles

A) Nucleus of a HeLa cell visualized by ToPro (green) and 7-AAD (red). The intensity profile displays the intensity fluctuations along the line indicated in the confocal mid-section. No clear topological difference (blue line) between ToPro (AT-preference, green line) and 7-AAD (GC preference, red line) was detectable.

B) Nucleus of a human lymphoblastoid visualized by DAPI (green) and PI (red). The intensity profile was plotted as described in (A). Again, no clear topological difference (blue line) between DAPI (AT-preference, green line) and PI (no preference, red line) was detected. The blue lines delineate the absolute intensity difference calculated between the respective red and green lines (ToPro and 7-AAD resp. DAPI and PI).

6.4.2.2 Comparison of epigenetic markers for active and inactive chromatin

Since no global pattern of HCC architecture with respect to AT/GC richness was found, a more focused approach on the topology of chromatin regions defined by differences in their functional status was attempted. To this, specific histone modifications correlating with the functional status of chromatin were detected in nuclei with HCC. The main work in this context was performed in the Diploma thesis of A. Zunhammer (Zunhammer, 2006) supervised within the scope of this thesis. Since all antibodies used for the detection of the histone modifications derived from the same animal source (all raised in rabbit) and since comparisons between the localization of the modifications were to be carried out

simultaneously in the same nuclei, a sequential immuno-detection protocol preventing antibody cross-talk had to be adopted (see Methods, 5.5.2). The detected histone modifications were the trimethylated lysine 9 at histone H3 (H3K9me3) and the trimethylated lysine 4 at histone H3 (H3K4me3). These two modifications were selected since their functional relevance is best described in literature and correlates with distinguishable grades of chromatin activity states (see Introduction, 4.1.6). Accordingly, H3K9me3 held as a marker for constitutive inactive chromatin whereas active chromatin could be delineated by the detection of H3K4me3.

Measurements of the shortest distances between the immuno-detected signals and the surface of HCC bundles were performed using the EDMT program (see Methods, 5.10.7) and the obtained distance frequencies were plotted in distance classes of 200 nm. Both distributions were tested to be highly significant different (both with $p <= 0.001$, Wilcoxon-test) compared to the control distribution (yellow bars). More than 80% of both chromatin modifications located in distances of only ±200 nm to the HCC bundle surface as expected for markers of chromatin. Nevertheless, a significant tendency of localization expected for the tested epigenetic modifications, was found in HLy and HFb cell nuclei: H3K4me3 marked active chromatin localized more towards the periphery than inactive chromatin marked by H3K9me3 (HFb: $p <= 0.001$; HLy: $p <= 0.001$). Figure 30 exemplarily reproduces the absolute measurements for human fibroblast nuclei with HCC. Here, ~20% of H3K9me3 (red bars) signals located more internally than the signals of H3K4me3 (green bars), measured in the same nuclei. Since these differences manifested in ranges below the optical resolution of the confocal microscope, no absolute statement on the localization of both modifications were possible. Another factor hampering these analyses is the choice of a proper gray value threshold. This problem was diminished since all analyzed images were deconvolved, which facilitates the choice of a threshold value as demonstrated in a previous chapter (see Results, 6.1). Nevertheless, massive shifts of the respective threshold values naturally led to shifts in the absolute distance distributions of the signals. Since such shift were tested to be only significant when changing the threshold of HCC counterstain segmentation (Albiez et al., 2006; Musoski, 2005; Thormeyer, 2005) and since two signal distributions always shifted in the same direction (Albiez et al., 2006; Musoski, 2005), the relative arrangements of two distributions to each other could be considered as being independent on the gray value threshold.

A. Zunhammer additionally investigated the localization of H3K27me3, a marker for facultative inactive chromatin. Though not consistently reproducible, H3K27me3 was found more in the interior of HCC bundles in comparison to H3K4me3 (DLD-1 nuclei) and in a similar interior localization in comparisons with H3K9me3 (in DLD-1 and HFb nuclei, see Zunhammer, 2006).

In summary, the topology of specific histone modifications in HCC bundles supports the hypothesis of preferential arrangements of active versus inactive chromatin regions at the surface or in the interior of HCC bundles respectively.

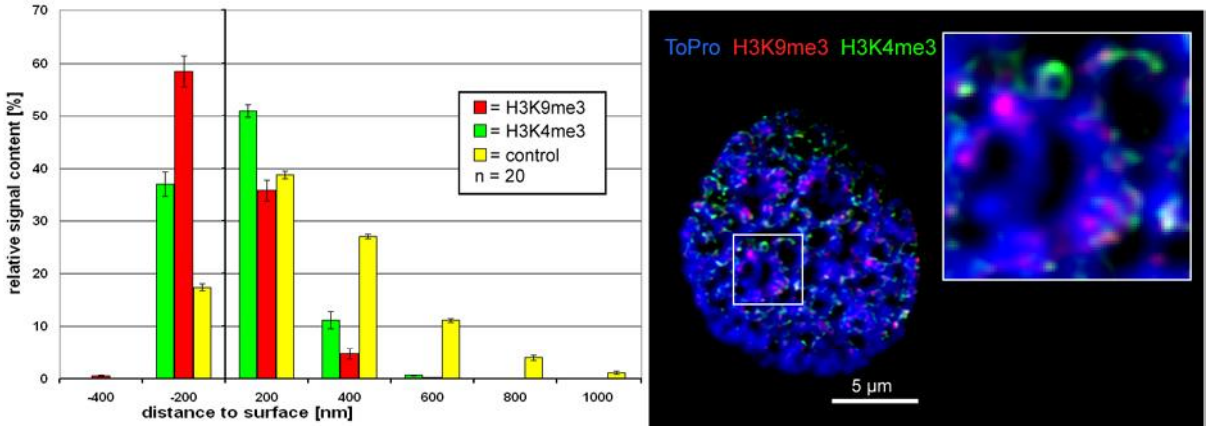

Figure 30: Topography of chromatin modifications with respect to HCC bundle surfaces in HFb nuclei

The active chromatin marker H3K4me3 (green) and the marker for constitutive inactive chromatin H3K9me3 (red) were simultaneously detected in HFb cell nuclei (ToPro, blue). Relative frequencies of the shortest distances of the respective signals to the closest surface of HCC bundles (0 on x-axis), were plotted in distance classes of 200 nm. Both distributions, H3K9me3 (red bars) and H3K4me3 (green bars) differed highly significantly from the control distribution (yellow bars), which covered the entire nuclear volume (chromatin+interchromatin, see Methods, 5.10.7). A significant preferential localization of H3K9me3 in the interior and of H3K4me3 at the periphery of the HCC bundles was obtained (Wilcoxon-signed rank test: p<=0.001). Error bars represent the standard error of the mean. (Image: Zunhammer A.)

6.4.2.3 Highly expressed chromatin regions

In the context of active chromatin, special attention was drawn to highly transcribed regions. Several such loci have been detected to locate considerably far away (>2 µm) from their respective CTs when detected by FISH (see Introduction, 4.1.4). Two exemplary regions demonstrated to protrude from their respective CTs are the MHC-locus on HSA 6p21.3 in interferon-γ stimulated lung fibroblasts (Musoski, 2005; Volpi et al., 2000) and the telomeric region on HSA 11p15.5 in normal human fibroblasts (Albiez et al., 2006; Kupper et al., 2007; Mahy et al., 2002a). In the context of the topology of these regions, two questions were addressed: [1] Are highly expressed and out-looped regions organized in 30 nm fibers or are they further compacted in higher order structures? [2] Where do highly expressed and protruded loci locate with respect to the HCC bundle surface? The experiments addressing these questions were performed in co-operation with Sandy Dittrich, Katrin Küpper, Marion Cremer (HSA 11p15.5) and Saban Musoski and Marion Cremer (HSA 6p21.3).

Highly expressed chromatin regions in nuclei with NCC

For the complete visualization of the gene-dense region of 11p15.5, 3D FISH with a bacterial artificial chromosome (BAC) contig of 2.35 Mb was performed. When tested individually each BAC yielded a dot-like FISH signal in the nucleus. Typically the signals were observed at the border or outside the painted HSA 11 territory. In a multicolor experiment, the two terminal as well as two BACs located in the middle of the contig as dot-like signals were detected (Fig. 31). The BAC at the telomeric end of the contig contains 11 genes, many of them highly transcribed in human fibroblasts (Albiez et al., 2006; Kupper et al., 2007), while the BAC at the centromeric end contains only one gene with low transcriptional activity (Kupper et al., 2007). The telomeric BAC was typically located further away from the HSA 11 CT body than the centromeric BAC. Notably, both BACs revealed dot-like chromatin structures and it was not possible to detect a clear size difference. The two BACs chosen from the middle of the contig always revealed a single compact signal (Fig. 31), although a region of about 350 kb between these BACs was not covered. To test, whether the out-looped region is composed of a thin 30 nm fiber meandering in the vicinity of the HSA 11 CT core, the experiment was modified so that the two BACs representing the telomeric and centromeric ends of the contig were visualized in red and green as before, while all other BACs in between were visualized in yellow (Fig. 31). In this experiment typically finger-like chromatin protrusions were observed, which extended from the CT periphery with a maximal length of up to 3 µm and a width of typically several hundred nanometers (Albiez et al., 2006; Dittrich, 2006). Occasionally a thicker part of the protrusion was connected by a much thinner fiber segment (Fig. 31: arrow). However, a dispersed pattern of BAC signals, expected in case of elongated 30 nm fibers was never observed but the signals always exhibited a compact sphere-like appearance. In some cases the contig probes revealed rather compact structures at the CT surface (Fig. 31). In any case, the compaction rates of ~ 1:300, estimated for this 2.35 Mb segment, argued against a sheer 30 nm fiber (compaction ~ 1:30 to 1:40) randomly meandering in the neighborhood of the corresponding CT.

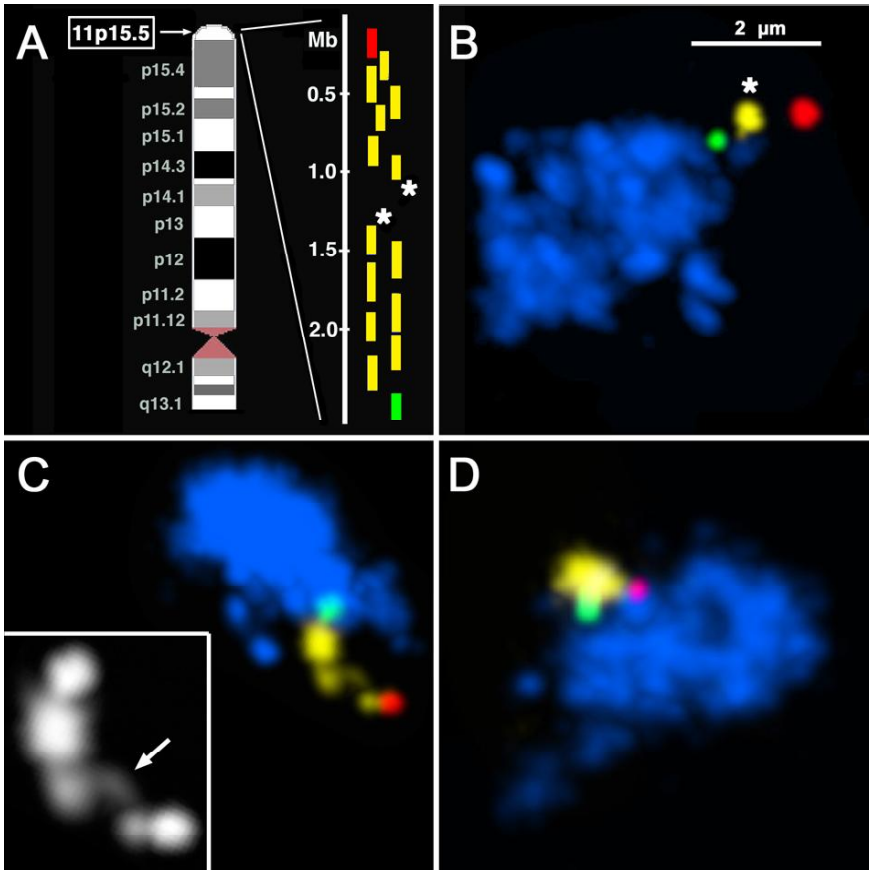

Figure 31: Multicolor 3D FISH on a human fibroblast of a 2.35 Mb region on HSA 11p15.5

A) Schematic draft of the 15 BACs used for the contiguous delineation of this region (with one interruption of 350 kb in the middle). The most telomeric (red), the most centromeric (green) clone and the intermediate clones (yellow) are labeled in different colors. **B-D)** Maximum Z projections after 3D-FISH of the CT 11 (blue) and the 11p15.5 clones as indicated in the schematic draft. **B)** In addition to the two BACs marked green and red, two BACs marked by an asterisk in (A) were visualized together with the CT 11. **C-D)** Here, the most telomeric (red) and centromeric (green) BAC were visualized together with all other BACs (yellow). **B-C)** The stained region forms a finger-like chromatin protrusion with a compaction factor of ~1:300 expanding from CT 11. The inset in (C) outlines the contiguous structure of the full length contig, delineated by all BACs. The arrow points to a much thinner fiber segment connecting the thicker parts of the protrusion. **D)** Here, the stained region presents itself as an even more condensed structure. (Images: Dittrich S.)

Basically similar results were obtained on the higher order structure of the MHC-locus on HSA 6p21.3 (Musoski, 2005). Localization apart from the painted territory (>1 µm) was observed in ~30% of all recorded CTs for interferon-γ stimulated fibroblasts. Protruded regions always exhibited a stem or finger like configuration arguing against a decondensed meandering giant 30 nm fiber (Fig. 32).

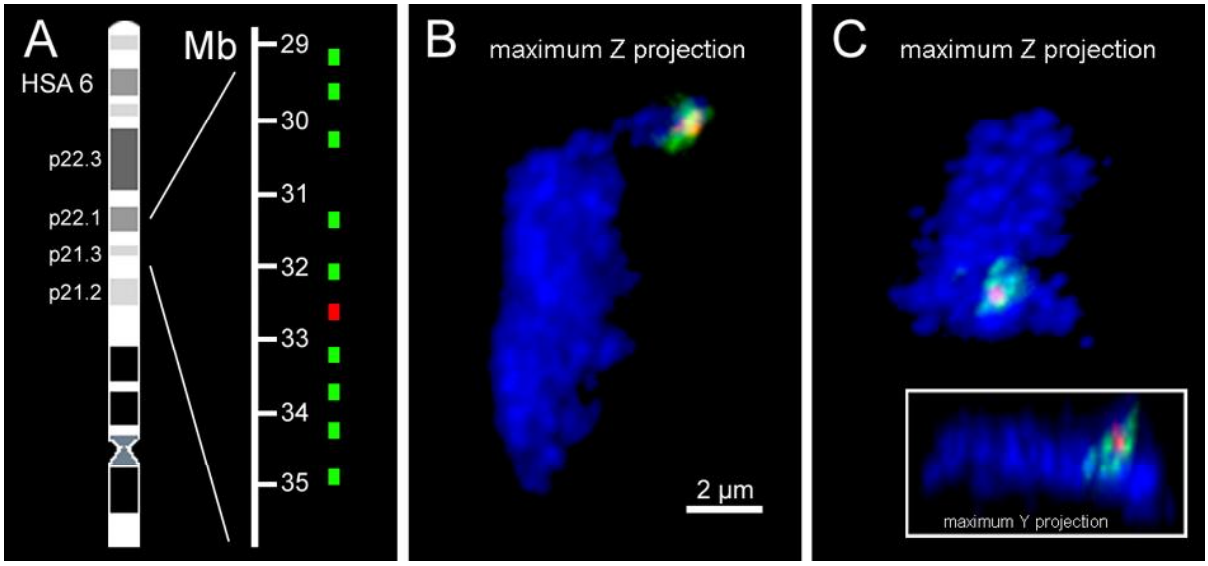

Figure 32: Multicolor 3D FISH on a human fibroblast of the MHC locus on HSA 6p21.3

A) Schematic draft of the 10 BACs used for the delineation of MHC region. The clone used in (Volpi et al., 2000) depicted in red, was flanked by 4 resp. 5 clones on each side (green, for details see Musoski, 2005) **B)** Maximum Z projections after 3D-FISH of the CT 6 (blue) and the 6p21.3 clones as indicated in the schematic draft. This stained region locates at the tip of a finger-like chromatin protrusion extending from the CT 6 and represents a conformation displayed by ~30% of all recorded CTs. **C)** The other ~70% of all CTs exhibited this region in a more compact form as displayed in this maximum Z projection. The insert shows a maximum Y projection to demonstrate that the region is located at the periphery of the respective CT 6. (Images B-C: Musoski S.)

Highly expressed chromatin regions in nuclei with HCC

The question on the topography of highly expressed chromatin regions was addressed with multicolor FISH experiments with the respective whole CT paint probes and clones depicted in Figures 31 and 32 on human fibroblasts fixed after formation of HCC (collaboration with M. Cremer and S. Musoski). In case of the MHC locus the fibroblasts were pre-treated by interferon-γ stimulation as described in Musoski, 2005. However unexpected methodological problems in applying FISH on nuclei with HCC were faced. While whole CT paint probes worked mostly well, all smaller FISH probes like single BACs or BAC pools gave hardly rise to analyzable signals. Infrequent high quality results for one color channel were always accompanied by unacceptable efficiencies of the simultaneously detected further channels. Lots of variations of the FISH methodology including e.g. prolonged pepsinization treatments were tested, but the finally reached quality level of hybridized signals kept always below the accustomed quality of standard FISH experiments.

Additionally, tested clones for the HSA 6p21.3 region as depicted in Figure 32, gave always rise to doublets of signals in single territories for the single BAC as well as for the contig probes. Since the BACs used and the HSA 6p21.3 region were carefully checked with the published data bases, the reason for this effect remains unknown but may be a special feature of the fibroblast cell line used. These circumstances have to be kept in mind when viewing the following results and these experiments should be considered as only preliminary. Further experiments with further enhanced methodological setups are in progress.

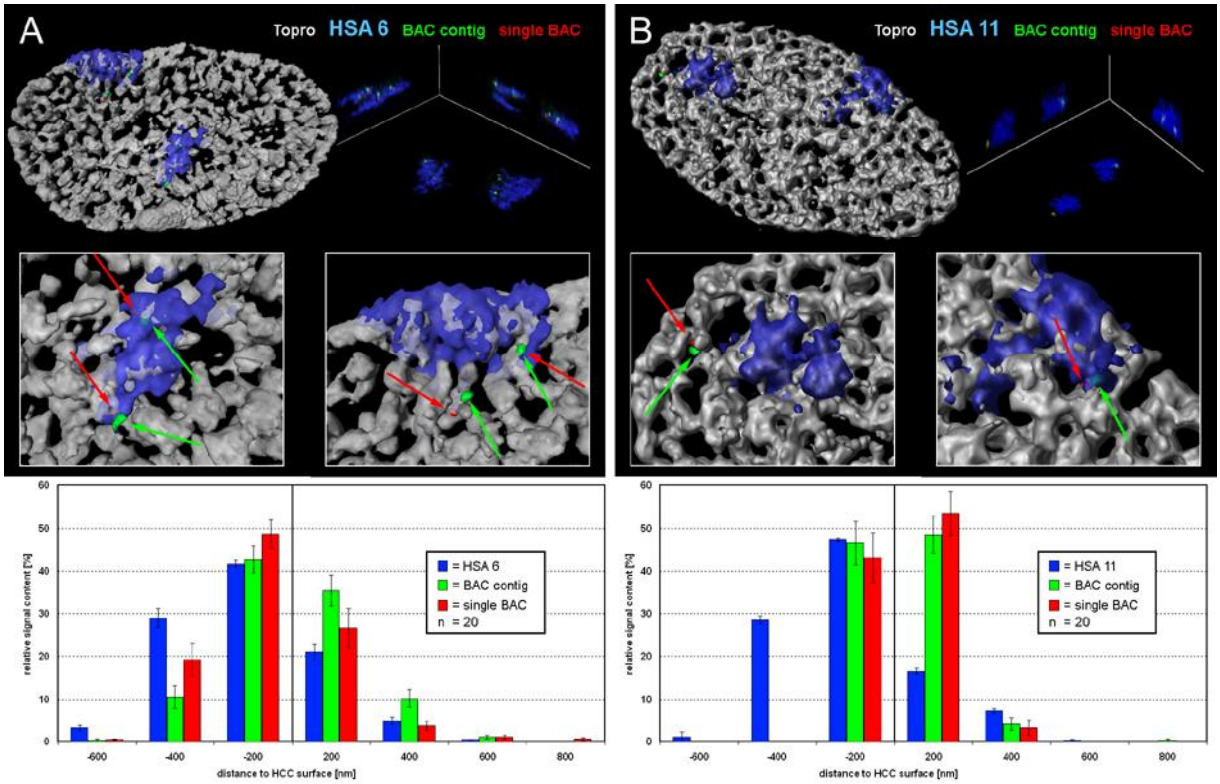

Figure 33: Topography of the HSA 6p21.3 and HSA 11p15.5 in HFb nuclei with HCC

A) Multicolor 3D FISH on a human fibroblast of the MHC locus on HSA 6p21.3. 3D reconstructions display the entire HFb nucleus stained with ToPro (silver), HSA 6 (blue), the single BAC (red) and BAC contig (green) which correspond to the clones depicted in Figure 32. For unknown reasons, always doublets of the BAC signals were detected for each CT. Maximum intensity projections display the CT and BACs. Arrows in the enlargements of the 3D reconstruction point to the location of the respective BAC signals. Absolute distance measurements from the CT, BAC contig and single BAC to HCC surfaces are plotted in the graph below. Only the BAC contig differed significantly from the respective HSA 6 distribution (Wilcoxon $p<=0.001$), whereas no difference was found between the single BAC and the HSA 6 (Wilcoxon $p=0.113$). In addition also no difference was found between both BAC distributions (Wilcoxon $p=0.043$).

B) Multicolor 3D FISH on a human fibroblast of the MHC locus on HSA 11p15.5. 3D reconstructions display the entire HFb nucleus stained with ToPro (silver), HSA 11 (blue), the single BAC (red) and BAC contig (green) which correspond to the most telomeric respectively the intermediate clones depicted in Figure 31. According to the absolute distance measurements to the HCC bundle surface, plotted in the graph below, both the single BAC and the BAC contig located more peripheral than the respective CT (Wilcoxon for both $p<=0.001$), while no difference was found between the single BAC and BAC contig (Wilcoxon for both $p=0.91$).

Figure 33 shows two exemplary nuclei for the delineation of the HSA 6p21.3 and HSA 11p15.5 regions in fibroblast nuclei with HCC taken from the two experiment series with best quality. Visual judgment and counting of protrusions delivered percentages as obtained for nuclei with NCC (Musoski, 2005). EDMT measurements were performed to analyze the topography of both regions with respect to HCC bundle surfaces as described above (see 6.3.1). For both regions, a preferential localization at the periphery of HCC bundles was observed. In case of the MHC locus, a further comparison was performed on the localization of the same locus in interferon-γ activated and non-activated cells (Musoski, 2005). The activation led, as expected, to a shift of the former randomly localized signal towards the interchromatin space.

Higher order organization of protruded chromatin regions

To test whether the conclusion that chromatin protrusions are organized with a higher order compaction (see above) could be extended to the entire genome, living HeLa cells harboring a few CTs partially labeled by fluorescent ~ 1 Mb chromatin domains were generated, while the majority of CTs remained unlabeled (see Methods, 5.3.2). In Figure 34 a typical nucleus with three distinct clusters of labeled ~1 Mb chromatin domains is shown. Each area represents one or possibly several adjacent labeled CTs. Chromatin was simultaneously visualized by expression of histone H2B-GFP (Fig. 34A-1). Nuclear regions between the three intensely labeled areas revealed evenly distributed signals similar to background fluorescence outside the nucleus after applying a low threshold (Fig. 34B-1). A slight accumulation of weak fluorescence signals is seen in the close vicinity of intensively labeled clusters of ~1 Mb chromatin domains (Fig. 34B-1), which disappeared after application of a higher threshold (Fig. 34B-2). After deconvolution, measured fluorescence intensities in non-labeled areas within labeled CTs were not higher compared to nuclear zones occupied by non-labeled CTs (Fig. 34C-1 and C-2). This finding conforms to the assumption that most, if not all, fluorescence observed in the vicinity of ~1 Mb chromatin domains resulted from out-of-focus light, and not from looping-out of labeled chromatin fibers.

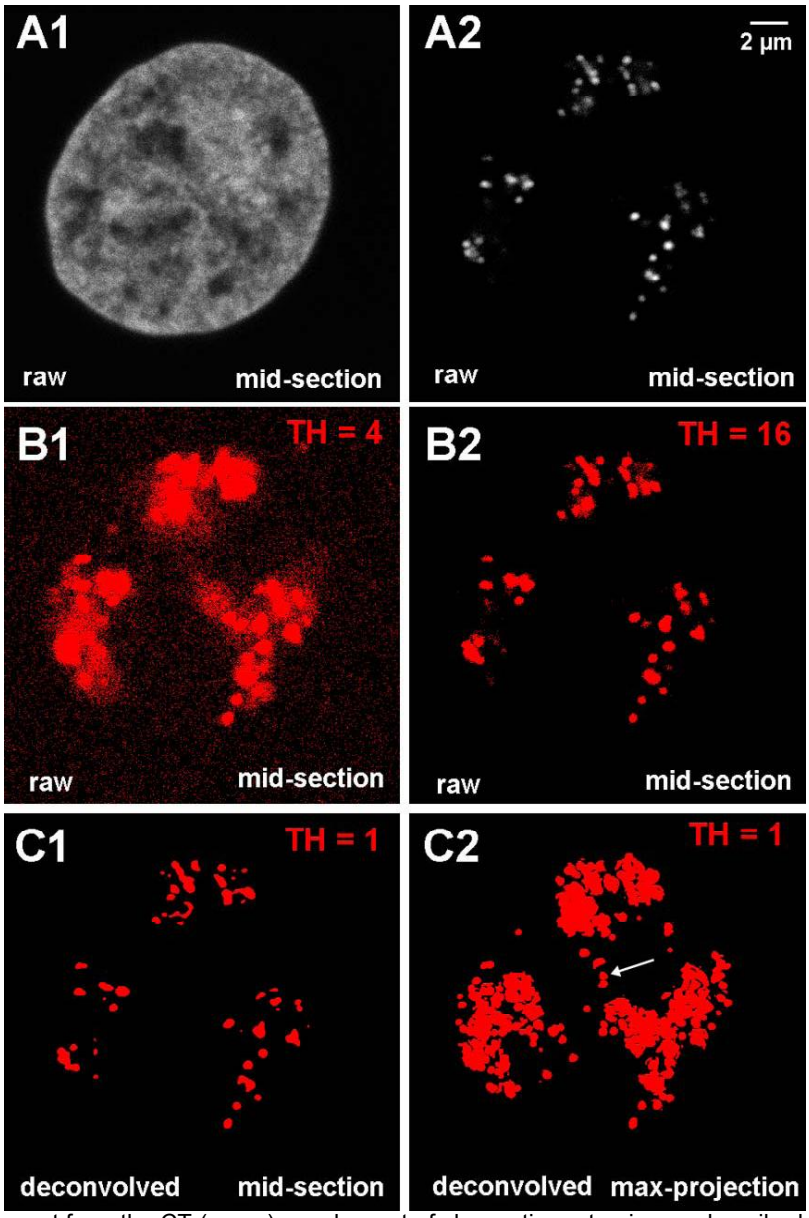

Figure 34: Fixed HeLa cell nucleus with a few in-vivo-labeled CTs

A) Midsection of a fixed HeLa nucleus reveals GFP tagged histone H2B (A-1) and three clusters of densely located ~ 1 Mb chromatin domains (A-2) representing (at least) three fluorescently labeled CTs. **B)** Pixels with gray values above the assigned thresholds (TH) are highlighted in red. The low threshold image reveals a cloud of fluorescence in the immediate vicinity of CTs, as well as between labeled domains. **C-1)** Same mid-section as shown in (B) after deconvolution of the original 3D image stack (12-bit format) and conversion to the eight-bit format. Note that detectable fluorescent signal is now restricted to the compact, labeled ~ 1 Mb chromatin domains. **C-2)** Maximum Z projection of the deconvolved image stack reveals clusters with all labeled ~ 1 Mb chromatin domains representing CTs. A few labeled ~ 1 Mb chromatin domains found apart from the CT (arrow) may be part of chromatin protrusion as described in Figures 31 to 33.

The maximum intensity projection of all deconvolved light-optical sections, which comprise all labeled foci present in this nucleus, reveals a few ~1 Mb chromatin domains located between the three intensely labeled nuclear areas (Fig. 34C-2: arrow). These domains may be part of higher-order chromatin protrusions expanding from a labeled CT body as described above (compare Figs. 31 to 33). These findings are typical for numerous nuclei harboring fluorescently labeled CTs observed in this and previous studies (Walter et al., 2003).

Furthermore, living HeLa cells with a few labeled CTs were followed from one cell cycle to the next (Fig. 35). In case of a sizeable fraction of labeled giant loops expanding from a given CT, the retraction of such loops during the formation of the corresponding prometaphase chromosome would be expected to result in a much smaller and accordingly more intensely labeled halo around the condensing CT. The reverse event should take place, when mitotic chromosomes form CTs during the telophase/early G1 transition. However, besides a modest shrinkage (Fig. 35C, G2>prometaphase) and swelling (Fig. 35C, prometaphase>G1) of the observed CTs this expectation could be ruled out. These evidences argue against the hypothesis that extended 30 nm giant chromatin loops represent a major part of the DNA of a given CT.

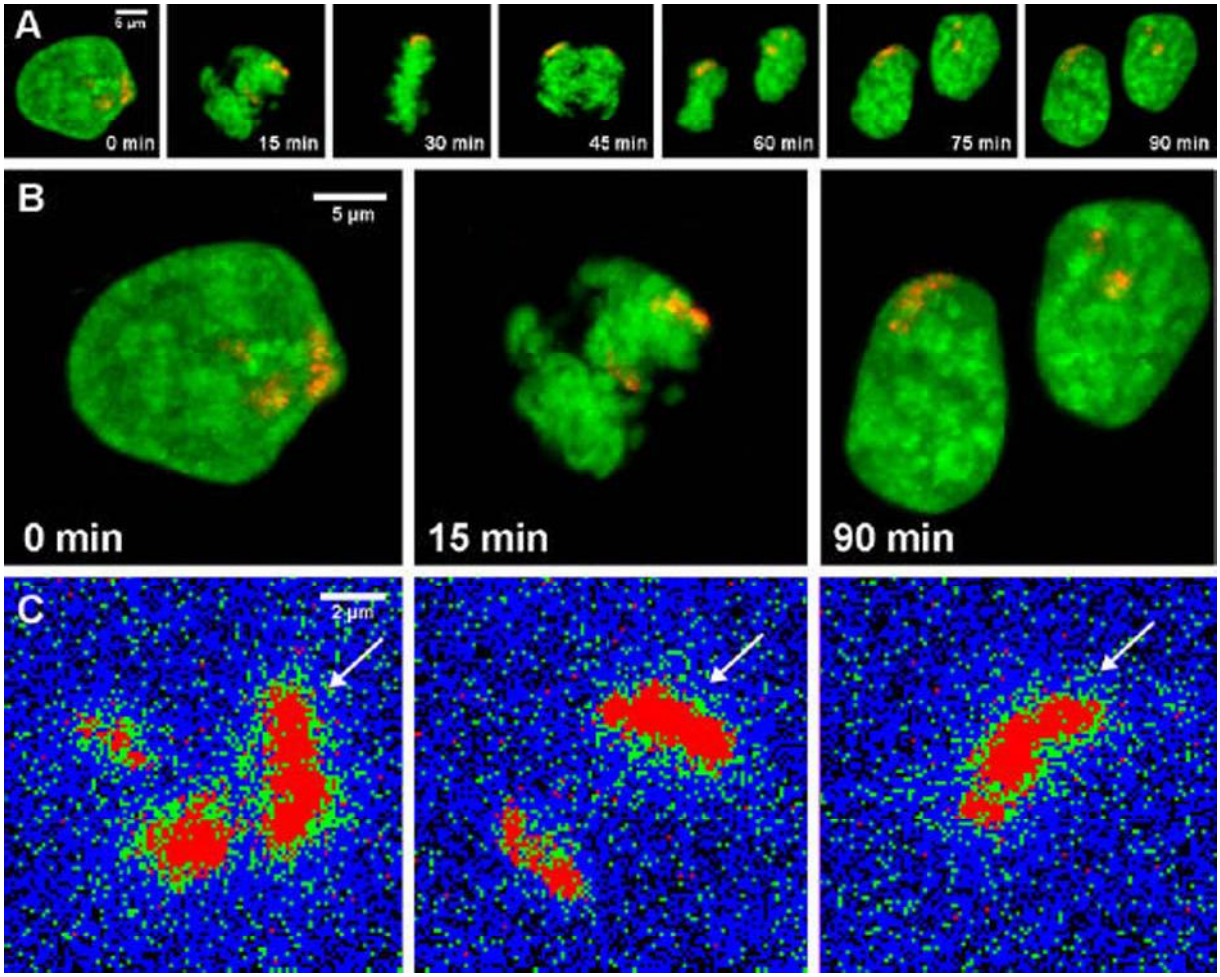

Figure 35: Live observation of a G2-M-G1 transition of a HeLa cell with three fluorescently labeled CTs

A) Live cell observation of a HeLa cell nucleus (H2B-GFP, green) with fluorescently labeled CTs (red) covering a complete cell division. **B)** Nucleus (H2B-GFP, green) of a living HeLa cell with labeled CTs (red) in late G2 (0 min), prometaphase (15 min) and one of the two daughter nuclei in G1 (90 min). **C)** Signals of CTs and mitotic chromosomes, respectively, displayed at higher magnification. Arrows point to a single CT and corresponding mitotic chromosome followed from late G2 to early G1. Images are displayed in the unprocessed 8-bit data format with colors assigning the intensity of the pixels (black = 0-4; blue = 5-14; green = 15-23; red > 23). Note that no thresholding was applied. (Images: Schermelleh L.)

7 DISCUSSION

7.1 Deconvolution of 3D confocal data sets

Unprocessed confocal data sets contain out-of-focus light arising from light diffracted according to the PSF of the microscope system (Wallace et al., 2001). Deconvolution is a mathematical procedure designed to diminish this blur and deliver images of higher quality (Wallace et al., 2001). The fact that deconvolution of confocal data is not applied routinely is mainly due to the fear that artifacts will be introduced by the procedure. It is difficult to determine with certainty whether an image processing algorithm indeed improves image quality or rather introduces artifacts (Wallace et al., 2001). Studies on this question usually compare real or simulated data sets of fluorescent beads with regard to the quality of reconstruction before and after deconvolution (Boutet de Monvel et al., 2001; Kriete et al., 2001). In the present work, three additional ways to demonstrate the reliability of image improvements gained by deconvolution were tested: [1] comparison of raw with deconvolved confocal images applying different parameters for deconvolution, [2] delineation of the same object with different light microscopy techniques and [3] comparison of raw and deconvolved images with corresponding images obtained using another microscopy approach, namely EM.

None of these approaches on its own can prove the reliability of the observed image improvements. However, the use of complementary approaches greatly strengthens the evidence. Objects of known size and shape were better reconstructed and deconvolution of confocal images delineated the same morphological features found in the corresponding images obtained using other microscopy approaches. Finally the choice of a single optimal TH was facilitated by deconvolution. Having said that, it was also observed that deconvolution can generate artifacts caused by over- or underestimations of some of the values of deconvolution parameters (Conchello and Lichtman, 2005; Dey et al., 2006; Markham and Conchello, 2001; Wallace et al., 2001). These became obvious when deconvolution was performed with too high SNR values (Landmann, 2002). A second important source of error could be the refractive index mismatch between the embedding medium and the coverslip in the described experiments. This mismatch could have been avoided using another embedding medium. However, other embedding media could lead to destruction of specimen morphology. Nevertheless, it was found that the generation of artifacts could be prevented by performing deconvolution with the SNR set to 15. As demonstrated here, the choice of a proper threshold value to satisfactorily delineate nuclear substructures was in fact facilitated after deconvolution under these conditions.

Deconvolution is a time-consuming process by itself and due to the demands it places on image acquisition. Indeed, according to image acquisition theories (Nyquist theorem), a small z step (e.g. ~150 nm for the wavelengths used in this study) is necessary to fulfill the requests for proper image acquisition and is obligatory for deconvolution, a fact which doubles the acquisition time if one is normally working with z steps of 200 – 300 nm. Therefore, it is important to note that, despite the improvement in image quality, deconvolution is not always necessary to quantify confocal data sets. For example, the coordinates of intensity barycenters or centroids of fluorescent objects do not significantly shift between raw and deconvolved data sets so that quantifications based on these values are not affected.

For colocalization analyses on the other hand deconvolution has been shown to deliver better results when compared to filtering techniques (Landmann, 2002; Sedarat et al., 2004). Since the increase in resolution gained by deconvolution rises arbitrarily with the number of iterations, it is difficult to define the resolution level reached at the end of the deconvolution procedure. This matter has to be kept in mind when evaluating absolute measurements based on user set thresholds on deconvolved images. Nonetheless, the error caused by including out-of-focus signals in the quantitative image analysis is substantially diminished by working with deconvolved data sets.

In conclusion deconvolution improves image quality and is recommended when working with threshold-dependent evaluations of confocal microscope images. Software tools, developed in the future are expected to allow an evaluation of confocal data sets to be performed without the need to set a threshold. In the meantime, deconvolved and thereby better reconstructed images remain of great help to gain insights into the morphology of cellular organelles.

7.2 Formation of hypercondensed chromatin

The phenomenon of the inducible formation of hypercondensed chromatin (HCC) was rediscovered in the preceding diploma thesis (Albiez, 2003). After its first observation in the beginning of the 20th century (Bank, 1939; Belar, 1930; Sakamura, 1927) HCC formation was applied only in a few studies in the 1970th, where the effect was compared with prophase condensation (Pederson and Robbins, 1970; Robbins et al., 1970).

In the present study HCC formation was used as a tool to globally manipulate the architecture of chromatin in living cell nuclei. In the following chapters, the obtained results are discussed with respect to the mechanism underlying HCC formation (7.3) and the relevance of the newly discovered features of nuclear architecture (7.4 and 7.5). Finally, present model views on chromatin and interchromatin organization presented in the Introduction will be revisited in the light of the obtained results (7.6) and an updated

chromosome territory-interchromatin compartment (CT-IC) model will be presented (7.7) together with an attempt to link EM evidences with the updated CT-IC model (7.8).

7.3 Mediators of HCC formation

Little is known about the mechanism of HCC formation. The increased osmolarity led to a loss of water from the cells and a concomitant decrease of the nuclear volume (Fig. 9). These changes are necessarily accompanied by a concomitant increase in the concentration of other cellular components. Two potential candidates, which may be able to trigger chromatin hypercondensation in these conditions, are cations and macromolecules.

7.3.1 Cations

An increase in the concentration of divalent cations may play an essential role since it could result in a neutralization of the negatively charged DNA backbone (Hansen, 2002; Horn and Peterson, 2002). *In-vitro* studies demonstrated that divalent cations (Mg^{2+}, Ca^{2+}) applied on stretched chromatin fibers lead to their condensation (Garcia-Ramirez et al., 1992; Hansen et al., 1989; Marko and Poirier, 2003; Poirier and Marko, 2003; Schwarz and Hansen, 1994). Measurements on the ion levels on condensed mitotic chromosomes revealed that only Na^{+}, K^{+}, Mg^{2+} and Ca^{2+} were detected on mitotic chromosomes but no other ones. Increased concentrations of Ca^{2+} were found along the axis of mitotic chromosomes (Strick et al., 2001). The authors concluded that their findings implicate that Na^{+}, K^{+}, Mg^{2+} and Ca^{2+} play a role in higher order chromosome structure through electrostatic neutralization (Strick et al., 2001). In accordance with this claim is the observation that formation of hypercondensed chromatin in cells with a permeabilized membrane was possible only if the concentration of divalent cations was raised in the surrounding medium (see 6.2.6). Monovalent cations were not sufficient to trigger a condensation effect in the concentrations tested. The pattern of hypercondensed chromatin induced by divalent cations in permeabilized cells was further different from the HCC pattern normally observed in intact cells. These results hint that the chromatin condensation effect observed for the standard hyper-osmotic treatment may differ from the effect obtained by DNA electrostatic neutralization mediated by increased concentrations of cations. Since not only ion concentrations but also the concentration of other nuclear components including proteins and macromolecules were increased in the hyper-tonic conditions, further factors could be considerable mediators of HCC formation.

7.3.2 Macromolecular crowding effects

A biophysical concept, recently adapted on nuclear architecture (Cook, 2002; Hancock, 2004a; Hancock, 2004b; Hancock, 2007) is macromolecular crowding (Zimmerman and Minton, 1993). This concept argues for a changing response of molecular interactions in

regard to the change of crowding conditions. Crowding is thereby defined as the occurrence of macromolecular molecules occupying volume and thereby decreasing the effective volume ingestible for other molecules. A concentration dependent response of molecular interactions to changes in macromolecular crowding is postulated to induce the formation/deformation of nuclear compartments built up by interacting molecules. The initially widespread molecules will form compact compartments in a crowded system (Cook, 2002; Hancock, 2004b), since a higher compaction leads to less excluded volume roamed by the molecules themselves and thereby provides a higher entropy level of the system in total. The application of this idea to the formation of nuclear compartments was first applied in the group of Ronald Hancock, which tested effects of macromolecular crowding on nuclear compartments like PML bodies and nucleoli (Hancock, 2004b). To decrease the crowding force, isolated nuclei were incubated in low ionic (=low osmotic) media, water was taken up by the nuclei and their volume increased. Since this treatment reduces the molecular crowding force (enlarged volume but constant molecular content) they expected and experimentally confirmed that PML bodies and nucleoli disappeared (Hancock, 2004b). When inert macromolecules (Polyethylene glycol), which enter the nuclear membrane were added subsequently, the reformation of PML bodies as well as of nucleoli was observed (Hancock, 2004b). In the light of the CT-IC model, also chromatin polymers could be considered as crowding macromolecules occupying nuclear volume, concomitantly leading to the formation of compartments in the interchromatin space. Furthermore chromatin itself could be affected by a crowded nuclear environment (Hancock, 2007) which may trigger the self-organization of CTs and the formation of densely packed 'heterochromatin', if one assumes molecular interactions between e.g. heterochromatic histone modifications and their binding partners. This argument may also provide a way to explain the observed polarity of chromatin arrangements in the nuclear volume, with compact ‘heterochromatic’ chromatin compartments found preferentially at the periphery or perinucleolar: The reason for this edge-affine topography may be that the effective excluded volume of interacting molecules is further minimized, if compartments were formed at physical borders like the nuclear membrane respectively nucleoli.

On the other hand, a significant decondensation of chromatin, expected under hypo-osmotic conditions (diminished crowding) was not observed on fluorescently labeled ~1 Mb chromatin domains (see 6.2.4). The effect may be too small or not existent at the level of single ~1 Mb chromatin domains. Nevertheless it was striking, that the overall chromatin appeared diffuser under hypo-osmotic conditions, matching the expectations of the nuclear crowding theory (Fig. 14). Following the opposite way by incubating cells in hyper-osmotic media (exactly as performed in this study), should - following the crowding theory - lead to increased crowding forces and concomitantly to a more contrasted compartmentalization in the nucleus. The

observation that chromatin hypercondenses in these conditions matches exactly this expectation. In conclusion, the data of the Hancock group and of the present study match the postulations of the crowding theory and accordingly provide support for a new biophysical approach in investigating and understanding the organization of nuclear architecture. It is worth considering that the organization of nuclear compartments just based on molecular crowding forces works with no demand for an additional structural organizer like the 'nuclear matrix' (Hancock, 2004b, see 7.6.2).

7.4 Interconnected chromosome territories

The induction of HCC formation revealed a contiguous network of chromatin bundles (Fig. 27). No visual separation just based on chromatin counterstaining was possible neither at the light (e.g. Fig. 27) nor electron microscopy level of observation (e.g. Figs 9 and 24). This result implies that CTs are interconnected forming a global 3D chromatin network. The interconnection sites displayed distinct borders between adjacent CTs labeled by FISH (Fig. 27). An interconnection between chromosomes was formerly proposed in a study where the authors attempted to pull-out single chromosomes of interphase nuclei. No matter which chromatin region was harpooned, subsequent extraction led to the sequential removal of the entire chromatin (Maniotis et al., 1997a). Finally elongated stretches of chromatin were obtained with larger chromatin clumps interconnected by thin fiber-like segments (Maniotis et al., 1997a). Since these interconnections could only be interrupted by DNase but not by RNase, protease or formamide treatments, Maniotis et al. claimed that chromosomes in interphase were interconnected by strands of DNA (Maniotis et al., 1997a). The same postulation was raised for mitotic chromosomes, where the same results were obtained when harpooning single condensed chromosomes (Maniotis et al., 1997a; Marko and Poirier, 2003; Poirier and Marko, 2003).

The claim that CTs are interconnected was further supported by EM micrographs, where chromatin was contrasted with the highly specific osmium ammine staining (Cogliati and Gautier, 1973), and CTs were detected by immuno-gold detection of BrdU, which was integrated during S-phase and subsequently segregated (Visser et al., 2000). The demarcation between these labeled CTs and adjacent non-labeled chromatin displayed no gap of chromatin staining and suggested a tight connection or at least a close spatial proximity of neighboring CTs (Visser et al., 2000). The stability of CT interconnections was especially intriguing when monitoring nuclei over several NCC-HCC-NCC cycles, which repeatedly gave rise to the same 3D chromatin network (Fig. 28).

The discovery of stable CT interconnections adds to the understanding of overall stability of chromatin architecture after the establishment of radial chromatin arrangements in early G1 (Gerlich et al., 2003; Walter et al., 2003). The reported global immobility of chromatin over

interphase (Lanctot et al., 2007; Molenaar et al., 2003; Walter et al., 2003) can now be explained by mainly two architectural landmarks: [1] chromatin is anchored to the lamina at the nuclear periphery (Gruenbaum et al., 2005; Hutchison, 2002) and [2] chromatin in the nuclear interior is stabilized by firm interconnections of CTs building up a stable 3D chromatin network.

7.4.1 Sites of chromosome territory interconnections

The result that CTs are interconnected raised the question on the nature of the interconnecting sites. Since this architectural feature is largely unexplored, the search on potential candidates mediating these interconnections reminded on the search for the needle in the haystack. The experiments performed by Maniotis et al. (Maniotis et al., 1997a) implied that DNA itself is involved in these interconnections. As a first approach the location of defined DNA compartments in regard to CT-CT interconnections was investigated in the diploma thesis of Jens Nagel supervised over the course of this thesis (Nagel, 2006). Since centromeres (cen) as well as telomeres (tel) form clusters in interphase nuclei (Nagele et al., 2001; Weierich et al., 2003, see Introduction), these regions were considered as first candidates. FISH paints of the human chromosomes 7, 8, 11 and 12 revealed that each chromosome forms at minimum three but frequently up to nine interconnections with its CT neighbors in the HCC bundle network in human fibroblasts (Nagel, 2006). This observation excludes that solely cen-cen and/or tel-tel interactions take place, since such configurations could only allow for a total of three interconnections per chromosome (1x cen, 2x tel). Nevertheless it was assumed that centromeric and telomeric regions could act as sites of interconnections if even just one (and only rarely both) of the involved CTs contributed with a centromere or telomere. This assumption would allow for three interconnections made up by the respective CT plus up to three further interconnections made up by every of its CT neighbors.

FISH experiments with CT paint probes (7, 8, 11 and 12) were performed on HFb and DLD-1 nuclei after formation of HCC (Nagel, 2006). Additionally, chromosome specific probes for either the respective cens or tels were hybridized. Subsequently, the frequency of cens and tels localizing at interconnection sites were counted. It is important to note that this quantification was based on a subjective judgment counting signals as 'localized at the interconnection' if they touched the edge of the paint signal at a site of interconnection. Roughly 55% of cens and 96% of tels were localized at sites of CT interconnections (Nagel, 2006). To further elucidate these findings, new experiments are currently in progress to simultaneously label all tels and cens in nuclei with HCC in addition to two painted CTs. These experiments will demonstrate whether or not each interconnection site is accompanied by at least one cen or tel.

In addition to cen/tel mediated interconnections other non-covalent or possibly also covalent protein-protein, DNA-protein, DNA-DNA and DNA-RNA interactions may play a role as inter-chromatin 'linkers' (for a recent review see Adkins et al., 2004). Specific and stable chromatin linker patterns established during terminal cell differentiation may ensure the long-term stability of cell type specific chromatin arrangements. Evidence for cell type specific changes of higher order chromatin arrangements during postmitotic differentiation (Martou and De Boni, 2000; Moen et al., 2004; Solovei et al., 2004a; Su et al., 2004) raises the question on the mechanism(s) responsible for this plasticity of nuclear architecture. Attempts to identify the molecular nature, plasticity and possible cell type specific diversity of interchromatin linkers will likely become a major focus of future analysis.

7.5 The topography of active processes

The interchromatin space contains nuclear speckles and bodies, such as Cajal (coiled) bodies, PML-bodies or Rad51-foci (Ching et al., 2005; Tashiro et al., 2000; Zirbel et al., 1993). In accordance with studies on untreated cells, nuclei with HCC displayed a preferential localization of these nuclear bodies and speckles in the widened interchromatin space (Figs. 22 and 23). The interchromatin space is separated from the interior of compact higher order chromatin domains by the perichromatin region, which was structurally defined by EM studies as a narrow border zone of decondensed chromatin at the surface of compact chromatin clumps in untreated nuclei. It represents a functionally important nuclear compartment, where DNA and RNA synthesis, as well as co-transcriptional splicing takes place (for reviews see Fakan, 2004a; Fakan, 2004b). In the present study most nascent DNA, nascent RNA and RNA polymerase II were detected within a region of about ± 200 nm from the surface of HCC bundles (Fig. 23). Within the limits of light microscopy resolution these results confirmed the ultrastructural observations from RNA labeling experiments (Cmarko et al., 1999; Fakan and Bernhard, 1971; Spector et al., 1991; Verschure et al., 1999). An overestimation of this localization at the periphery of chromatin domains due to insufficient antibody penetration could be excluded by successful detection of incorporated BrdU nucleotides (Figs. 22 and 23) or histone modifications (Fig. 30) in the most interior of HCC bundles. Furthermore, an ultrastructural control on the distribution of nascent RNA in nuclei with HCC revealed the same peripheral localization as obtained for the light microscopic investigation (Fig. 24).

The results that [1] the obtained distinct 3D chromatin compartment was repeatedly formed with a high degree of similarity in sequentially performed NCC-HCC-NCC cycles (Fig. 28) and that [2] the distribution of active nuclear processes was restricted to the surface of this 3D chromatin network, argue in summary for a higher order compartmentalization of

chromatin and the interchromatin space and a clear correlation between higher order nuclear architecture and the topography of nuclear functions.

The observed rapid recovery of nuclear functions like transcription, replication and cell cycle progression further argues that the topography of these processes was largely maintained in nuclei with HCC. Accordingly, rapid functional recovery after HCC-NCC transition should require movements of DNA and functional machineries only on a small scale. This assumption is in accordance with the results obtained by monitoring only slight positional shifts of ~1 Mb chromatin domains towards each other (Fig. 15). Since untreated interphase nuclei exhibit a freedom of chromatin domain movements in the order of 0.5 µm (Abney et al., 1997; Lanctot et al., 2007; Walter et al., 2003), the formation of HCC could be fully explained just on present knowledge of chromatin mobility without any additional claim for significant changes of these parameters.

7.5.1 Highly transcribed chromatin regions

Motivated by studies on the topology of highly transcribed gene clusters like the HSA 11p15.5 region or the MHC locus on HSA 6p21.3 (Chubb and Bickmore, 2003; Mahy et al., 2002a; Volpi et al., 2000), the higher order architecture of these regions and their localization was investigated by the FISH technique (Albiez et al., 2006; Dittrich, 2006; Kupper et al., 2007; Musoski, 2005). Delineation of a contig of BACs spanning 2.35 Mb on HSA 11p15.5 in untreated nuclei revealed compact signals for all labeled single BACs (Figs. 31-33). The contig as a whole thereby displayed a globular formation, but in addition in some cases a finger like protrusion extending from the HSA 11 chromosome territory and reaching a total length of up to 3 µm (Albiez et al., 2006; Dittrich, 2006). This observation is consistent with the data of preceding studies reporting extensions for the HSA 11p15.5 region as well as for the MHC locus for up to 1.5 µm measured from the respective CTs surface (Mahy et al., 2002a; Volpi et al., 2000). The whole region did, however, not light up as an extended and widely meandering 30 nm fiber (Chubb and Bickmore, 2003), but exhibited an estimated compaction ratio of 1:300, according to its measured total length and known Mb content (Albiez et al., 2006; Dittrich, 2006).

To test if the described extensions of chromatin regions from the respective CTs were a common feature of chromatin architecture, living cell experiments monitoring tagged CTs over the entire cell cycle were performed. In case of extended meandering chromatin fibers in the order of 30 nm fibers, a halo around interphase CTs would have been expected. Following such a CT into its condensed state during prophase should accordingly display a loss of this halo, when the extended fibers get retracted to their 'core' CT. The reverse case was expected when this condensed mitotic chromosome entered G1 state, where the halo should reconstitute by extending chromatin fibers. However, no such halo was observed in

any state from G2 to G1 (Fig. 35) arguing against a major contribution of such extended 30 nm fibers to the architecture of CTs. This result was gained in this study as well as in previous studies investigating CTs in living cells (Walter et al., 2003). This conclusion was further supported by data of fixed nuclei harboring several *in-vivo* labeled CTs. The labeled signals corresponding to CTs displayed mainly distinct patches with no halo of thin fibers surrounding those (Fig. 34). Additionally a few of these patches (Fig. 34) displayed finger-like protrusions built up by ~1 Mb chromatin domains, comparable to the topography observed for highly transcribed regions as described above (Fig. 31-33).

Bickmore and colleagues found such protrusions of the HSA 11p15.5 preferentially in untreated cells, whereas cells with inhibited transcriptional activity displayed a preferential localization of the HSA 11p15.5 locus at the surface of the HSA territory (Chubb and Bickmore, 2003; Mahy et al., 2002a). These observations were based on measurements of the most distal BAC of the contig used in the present study without further delineating the rest of the contig making up the connection to the CT paint signal. Though their schematic sketch provided in Chubb and Bickmore 2003 suggests an organization of this highly active region on the base of a 30 nm fiber (Chubb and Bickmore, 2003), Bickmore and colleagues state that '[…] *the decondensed regions must still retain higher-order structure beyond the 30 nm fiber*' (Gilbert et al., 2004).

Investigations of both regions (HSA 6p21.3 and HSA 11p15.5) in nuclei with HCC implied that these regions preferentially locate at the surface of HCC bundles (Fig. 33), suggesting that they extended along pre-existing interchromatin channels.

7.6 Revisiting present model views on nuclear architecture

The results obtained by induced formation of HCC add to the understanding of nuclear architecture and enable to critically revisit the postulations of present model views. Which model views are compatible with observations of interconnected CTs, a reproducibly expandable interchromatin space and the lack of observing giant chromatin loops?

7.6.1 Giant chromatin loops

Are giant chromatin loops major elements of nuclear architecture as proposed by the random walk-giant loop (RW-GL) computer model (Sachs et al., 1995) or by experimental observations on the localization of HSA11p15.5 (Mahy et al., 2002a)? The relevance of the RW-GL model was already discussed in the Introduction (see 4.3.4). Experimental data correlating with the theoretical RW-GL calculations was also fully compatible with the multi-loop subcompartment (MLS) model where no giant loops are implemented.

The presented experiments of this study do also not support any claims for the existence of giant 30 nm fiber chromatin loops. No extended fields of out-looped DNA fibers (Fig. 1D) were observed around CTs in fixed as well as in living cell nuclei. In fact, investigations focused on the highly expressed and protruded regions of HSA 11p15.5 and HSA 6p21.3 revealed that even these are built from higher order chromatin with compaction ratios much beyond that of sheer 30 nm fibers (Fig. 31). These results rule out the claim of extended chromatin 'out-looping', which was indirectly concluded from incomplete visualizations of only parts of these regions (Chubb and Bickmore, 2003; Mahy et al., 2002a). The presented results, however, do match postulations of the MLS-model (Fig.1 C) for the existence of small scale chromatin loops building up sub-compartments. These sub-compartments could correspond to the observed ~1 Mb chromatin domains as well as to the chromomeres observed by Wanner and Formanek, 2000. A chain of such domains could accordingly extend from the respective CT building up protruded regions like observed for the investigated highly expressed loci (see also subsequent chapter, 7.7). An organization of chromatin in small scale sub-compartments would additionally demand much less orchestration during the conformational changes over a NCC-HCC-NCC cycle compared to a model claiming entangled giant loops.

Applying the 'Occam's razor' principle the simpler explanation of an observation should be preferred. Since no tenable evidence for extended out-looped 30 nm chromatin fibers could be provided, this postulation is actually not favored.

7.6.2 'Nuclear matrix'

The 'nuclear matrix', a postulated scaffold organizing chromatin in interphase nuclei is another nuclear component, whose existence is questioned (Hancock, 2000; Pederson, 1998; Pederson, 2000). Again, if its proposed function could be adopted by more simple and already demonstrated principles, postulations for its existence would be challenged (Cremer et al., 1995; Hancock, 2000; Hancock, 2004b; Pederson, 2000). In that line of argument it was discussed that the structural organization of a cell nucleus could largely be triggered by macromolecular crowding effects with no need for an additional scaffold (Hancock, 2004b). Kreth et al demonstrated that the existence of distinct CTs could be fully explained with a computer model just based on sphere-like ~1 Mb chromatin domains interconnected by short flexible chromatin linkers (Cremer and Cremer, 2001; Kreth et al., 2004b).

Factors proposed to be components of the 'nuclear matrix' (e.g. SAF-A) preferentially localize in the interchromatin space and at the surface of HCC bundles as demonstrated in this study (Fig. 25). Since these seem to be the regions subjected to small scale movements during HCC formation (Fig. 15), a potential 'nuclear matrix' would necessarily be considerably flexible. However, if the 'nuclear matrix' would be responsible for the stable organization of

chromatin, how could it fulfill this function, granting the strikingly similar patterns of HCC, although it itself gets massively subjected to global topological changes whilst HCC formation? These considerations would rather suggest a 'nuclear matrix' to be located in the interior of HCC bundles, potentially at the bases of multi-loop sub-compartments (Munkel et al., 1999; Sadoni et al., 2004) and acting as a backbone for the emerging HCC bundles at their central axis. On the other hand, since the 'nuclear matrix' is also postulated to be involved in the stable anchoring of active small scale chromatin loops (Cook, 1999), a localization at sites of functional activity would be expected. However, as demonstrated in this study, these sites were localized at the HCC bundles surfaces.

In summary, the results presented are contradictory to an organizing 'nuclear matrix' and go better with a view that 'nuclear matrix' preparations lead to the precipitation of interchromatin proteins, which in part are involved in nuclear functions (Cremer et al., 1995; Pederson, 2000). This matches with the localization of 'nuclear matrix' proteins at the periphery of HCC bundles and is additionally in accordance with the rapid recovery of all tested nuclear functions, when the massive conformational changes of chromatin were reversed.

Still, the question whether and how small scale loops of active chromatin are tethered remains open. In the view of Peter Cook, not the polymerases are the mobile entities while transcription or replication is processed, but the DNA template is pulled through a fixed factory of polymerases and additional factors (Cook, 1999). This claim derives from reflections of the entwining and replication/transcription processes, which would necessarily lead to extensive entanglement of the replicates/transcripts with their respective templates in case of an immobile DNA template. The question on how these factories are fixed remains to be addressed.

7.6.3 Interchromatin space

The observed widening of interchromatin spaces in a non-random reproducible pattern supports the claim for the existence of a channel-like compartment as postulated by the chromosome territory-interchromatin compartment (CT-IC) model (Cremer and Cremer, 2001, Fig. 1H). According to the CT-IC model, the observed 3D interchromatin network would represent a widened interchromatin compartment. Since functional processes are postulated to be restricted to the surface of chromatin domains, a preferential localization of these processes at the surface of the HCC bundles would have been expected according to the CT-IC model. Indeed, nascent RNA, nascent DNA and RNA polymerases located around the surface of chromatin bundles (Fig. 22 and 23).

The older interchromatin domain model postulating interchromatin spaces to completely surround every CT (Zirbel et al., 1993, Fig. 1G), could be ruled out by the presented results. Formation of HCC revealed that CTs are not organized as single entities embedded in

interchromatin space, but are interconnected in a 3D chromatin network aligned by a 3D interchromatin channel system.

Preferential localizations of nuclear functions as postulated by the CT-IC model and as found in this study are hard to interpret in the light of the interchromatin network (ICN) model (Branco and Pombo, 2006; Branco and Pombo, 2007). The extensive chromatin intermingling postulated to lead to the ICN (Fig. 1E) would necessarily be expected to either [1] maintain the extent of intermingling during the HCC state leading to extensively intermingled fibers in the HCC bundles with no higher order of active versus inactive sites or lead to [2] de-mingling of chromatin fibers, which would be unlikely to yield the same chromatin pattern in repeated treatments. Such a reproducibility of HCC pattern formation would demand a complex and organized orchestration of intermingling chromatin fibers to assure their correct de-mingling when retracted and correct and organized re-intermingling when recovering the NCC state. Branco et al. deduced their postulation of wide fields of intermingling fibers between neighboring CTs from the observed overlap of fluorescent signals in thin (150 nm) cryosections. Although their approach allowed a much better resolution compared to confocal microscopy of intact nuclei, their images still suffered from out-of-focus light, were still limited by an axial resolution of ~200-300 nm and their evaluations were largely depending on the user set gray value thresholds. Considering these limitations, (Albiez et al., 2006) came to the conclusion, that the overlap of neighboring CTs was very much overestimated by (Branco and Pombo, 2006). In fact, an updated CT-IC model given below (see 7.7), is fully compatible with a partial overlap of ~1 Mb chromatin domains of neighboring CTs in 150 nm thick cryosections without the claim for any intermingling fibers (see supplemental in Albiez et al., 2006).

7.6.4 Chromatin conformation

The ICN model was supported by observations at the resolution level of EM revealing chromatin structures in the order of 30 nm fiber (Dehghani et al., 2005). The deduced lattice-model describes the entire chromatin to form a network of chromatin fibers with no order in respect to the space in between (Dehghani et al., 2005) Fig. 1F). Indeed, a huge channel system of interchromatin spaces cannot be distinguished with the electron spectroscopic imaging (ESI) method, which delineates and distinguishes the distribution of phosphorus and nitrogen in ultrathin EM sections. However, the conclusion, that the observed distribution of the two elements indeed reflects the distribution of only DNA and proteins respectively has to be critically scrutinized. First of all, RNA contains phosphorus as well, hindering a distinguishing between DNA and RNA (Cremer and Cremer, 2006b). As soon as RNA transcription is terminated, the transcript may get released to the interchromatin channel system and thereby blurring the topography of DNA as delineated by the ESI technique.

Furthermore heavily phosphorylated proteins could hamper a proper separation of the signals (Cremer and Cremer, 2006b). Applying the osmium ammine staining technique, which is supposed to solely stain DNA by a Feulgen-type reaction (Cogliati and Gautier, 1973), lacunas and channels in the order as described in this and previous studies are detected (Cremer and Cremer, 2001; Verschure et al., 1999; Visser et al., 2000).
Nevertheless, also the osmium ammine approach delivers images which suggest a structural organization of at least some nuclear regions in the order of 30 nm fibers (e.g. Fig 24). Where are the ultrastructural counterparts of the ~1 Mb chromatin domains observed at the light microscopic level? Dheghani et al. claim that ~1 Mb chromatin domains are misperceptions of local concentrations of 30 nm fibers (Dehghani et al., 2005). However their statement may as well be a misinterpretation of local chromatin arrangements, missing to view larger regions as organized entities. A comprehensive view on these considerations is given at the end of this discussion (see 7.8).

7.7 Updated chromosome territory-interchromatin compartment model

In Figure 36, an updated chromosome territory-interchromatin compartment (CT-IC) model implementing the results obtained in this study is presented (Albiez et al., 2006; Lanctot et al., 2007). This cartoon shows a part of an interphase nucleus with differentially colored higher-order chromatin domains (red and green) from neighboring CTs separated by the interchromatin compartment (IC, white). This model postulates that the nucleus and each CT is built up from two structurally distinct compartments: a 3D network of chromatin domains with compaction levels beyond an extended 30 nm fiber and an integrated IC channel network with nuclear speckles and bodies (blue), which expands between these domains, independently of whether they belong to the same or different CTs. The width of the IC varies from the micrometer scale, e.g. IC lacunas containing large nuclear speckles, to nanometer scales (Fig. 36B).
One argument against the CT-IC model, recently raised by the ICN model concerns the frequencies of interchromosomal translocations. Branco et al. claim that no such events could occur in a strict territorial organization of chromosomes, since no neighboring CTs would have sufficient contact to build translocations. Their ICN model on the other hand demonstrated that the extents of ‘intermingling’ between chromosome pairs as measured by them, enabled translocations and correlated with the translocation frequencies measured for the same pairs of chromosomes in the same cell line (Branco and Pombo, 2006). In fact, intrachromosomal as well as interchromosomal rearrangements can occur within the constraints of the CT-IC model when double-strand breaks are induced in neighboring ~1 Mb chromatin domains of the same respectively different CTs. Possibilities for rearrangements

are increased by constrained Brownian movements of neighboring chromatin domains resulting in a transient decrease of the width of small IC channels.

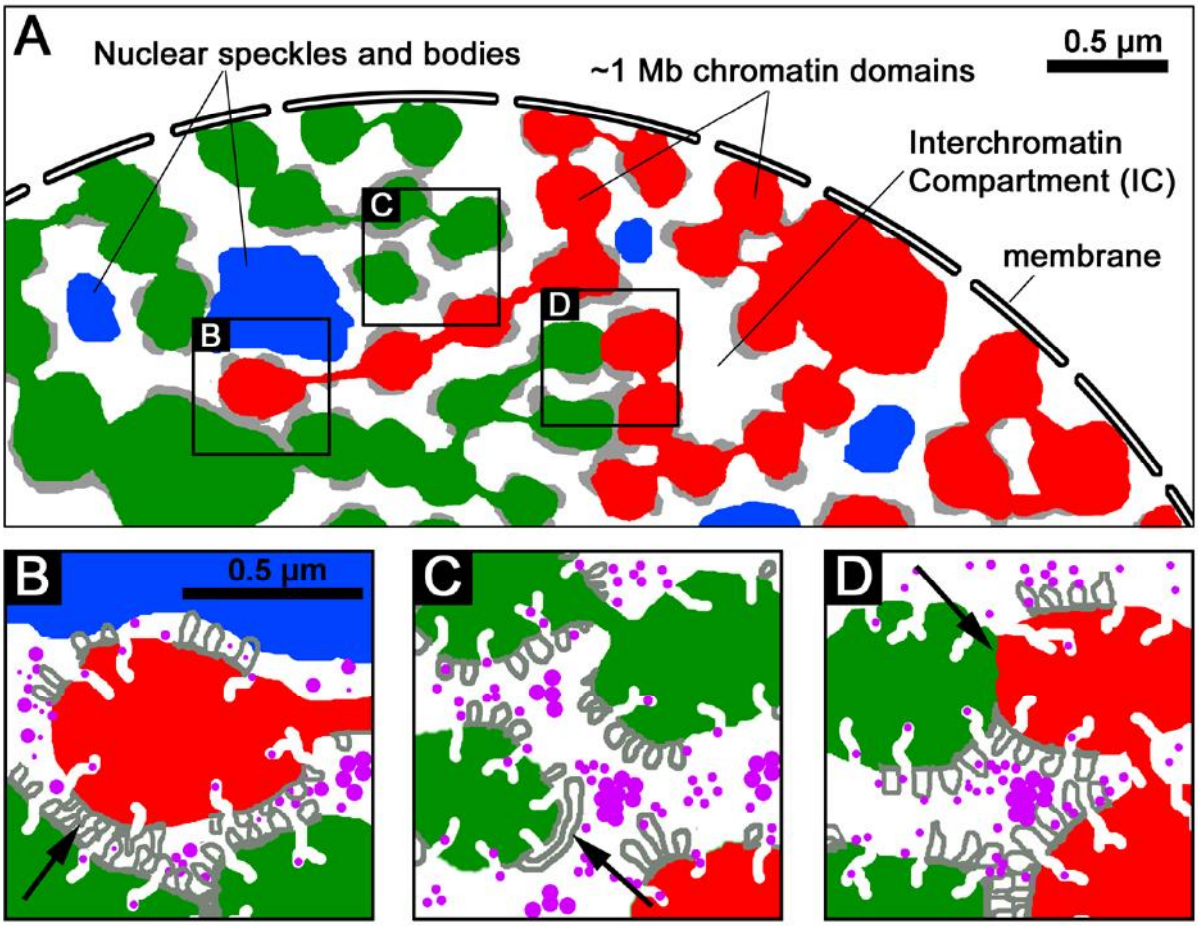

Figure 36: Updated chromosome territory-interchromatin compartment (CT-IC) model

A) Schematic section of a nucleus with two territories (red and green). Each territory is built up by ~1 Mb chromatin domains depicted as sphere-like bodies. The surface of these domains is partly covered by the perichromatin region (gray). Interchromatin channels (white) expand between and in the CTs. Nuclear speckles and bodies (blue) locate in the interchromatin space.

B-D) Enlargements indicated in (A) which demonstrate spatial proximity between neighboring CTs at the tip of a protruded region (B), an extended small scale chromatin loop expanding along the perichromatin regions (C) and a tight interconnection between neighboring CTs (D). For details see text.

When considering the proven gene-density related preferential radial position of chromosomes (Boyle et al., 2001), measured and modeled translocation frequencies do highly correlate within the constraints of the CT-IC model as well (Kreth et al., 2002; Kreth et al., 2004a).

The claim of Branco et al. that the CT-IC model would not allow for chromosomal rearrangements can therefore not be sustained.

In the updated CT-IC model, the perichromatin region (Fig. 36: gray regions) is located at the periphery of chromatin domains and forms a functionally important border zone (100-200 nm)

with certain genes or segments thereof poised for, or in the process of, transcription (Albiez et al., 2006). Although the CT-IC model postulates that permanently silenced genes are hidden in the interior of compact chromatin domains, the possibility that most or all genes are located at chromatin domain borders is not excluded. Enlargements of nuclear sites (Fig. 36B-D: indicated in 36A) display ~1 Mb chromatins domains (red and green) and the interchromatin space (white) with nuclear speckles and bodies (blue), as well as preformed modules of the transcription and splicing machineries (pink). Diffusion of individual proteins into the interior of compact chromatin domains is likely not prevented. Several ~1 Mb chromatin domains may still form larger domains as seen in EM images as chromatin clumps. The finest branches of the IC with a width of ~100 nm may penetrate into the interior of ~1 Mb chromatin domains and end between ~100 kb loop domains (not shown). An exemplary higher-order chromatin protrusion, which expands from the respective CT into the interior of a neighboring CT, is depicted in Figure 36B. Expansions of such higher-order protrusions are guided by the IC. Locally decondensed chromatin loops contribute to the perichromatin region (gray). Note that the narrow IC channel allows for direct contact of loops from neighboring ~1 Mb chromatin domains (arrow). Large out-looping (on a small scale size of some 100 kb) may expand along the perichromatin region (Fig. 36C). Neighboring CTs have sites of close interactions (Fig. 36D). The possible intermingling of chromatin fibers in the updated CT-IC model is limited to sites where neighboring ~1Mb chromatin domains of the same or neighboring CTs come in close spatial proximity (e.g. Fig. 36B or 36D) and is restricted to small scale chromatin loops of some 100 kb (gray loops).

The updated CT-IC model does not demand any scaffold since the stability of chromatin arrangements in the nuclear interior is granted by stable CT-CT interconnections. However, if a scaffold existed, it would be expected to locate in the very interior axis of HCC bundles.

7.8 Linking EM images with the updated CT-IC model

How can a schematic view as provided in Figure 36, be linked with electron microscopic sections, showing much less ordered chromatin arrangements? Especially, how are ~1 Mb chromatin domains organized at the ultrastructural level and why are they not discernable in counterstained ultrathin sections in the EM?

Here, I would like to provide an attempt to interpret EM images on the base of the updated CT-IC model. In Figure 37A, the EM section of a HeLa cell nucleus (taken from Fig. 24A-4) contrasted by the osmium ammine staining technique is displayed. Chromatin was highlighted with red color and immunostaining of DNA and chromatin is detected as black dots (for details see Fig. 24). An enlargement depicted in Figure 37B with implemented 30 nm violet bars demonstrates that the usual chromatin fiber size in this particular region is in the order of 30 nm. Indeed, when schematically highlighting the 30 nm fibers in red

(Fig. 37C: fibers drawn to scale), the entire section could be viewed as a fiber network just as proposed by Branco and Pombo, 2006 or as a lattice of chromatin fibers as proposed by (Dehghani et al., 2005). However, even this seemingly entangled fiber network could as well be interpreted as a close spatial association of ~1 Mb chromatin domains, if one assumes that these domains are built up by loops and coils of 30 nm fibers (superimposed violet circles in Fig. 37D). The size of the circles (~500 nm) reflects the hypothetical appearance of labeled replication foci at the resolution level of a confocal light microscope. Since these foci have been demonstrated to be persistent over several cell divisions (see Introduction, 4.1.4), and since they were not expandable in hypo-tonic conditions (Fig. 14), it is likely that these domains are kept together by presently unknown linkers. This view goes very well with the MLS model (see Introduction, 4.3.4) postulating sub-compartments (~1 Mb chromatin domains) built from multiple 30 nm chromatin loops (Fig. 1C).

These sub-compartments light up as spheres in the confocal microscope only due to the resolution limit but may have a relatively variable configuration based on folded 30 nm fibers. This comprehensive view is consistent with experimental data delineating only parts of the chromatin (e.g. the HSA 11p15.5) by the FISH technique with BAC probes (Fig. 37E). The continuous sphere-like appearance of BAC signals could be interpreted as sub-compartments built by folded 30 nm fibers. In Figure 37F, the signal of a FISH painted HSA 6 territory on an ultrathin (150 nm) cryosection is displayed (reproduced from (Branco and Pombo, 2006). Such images were taken as evidence for intermingling chromatin fibers. However, as presented here, they can also be interpreted as ~1 Mb chromatin domains (violet circles) interconnected by small linkers (green dots).

The reason, why these sub-compartments of the CT are better discernable in this experiment as compared to the blue HSA 11 paint signal in Figure 37E may be due to the improved resolution when imaging thin cryosections. The hypothetical ultrastructure of the HSA 11p15.5 (Fig. 37E) and the HSA 6 (Fig. 37F) could be anticipated as shown in Figure 37G and 37H. Folded and coiled 30 nm fibers (red and gray) are forming sub-compartments (violet circles) interconnected by linkers (green dots). Without the red highlighting of the domains depicted as violet circles, the entire sections would be misinterpreted as only networks of 30 nm fibers.

The presented comprehensive view has naturally to be taken as a hypothetical suggestion since the direct experimental link between light microscopic ~1 Mb chromatin domains and corresponding EM structures is still lacking.

Nevertheless, this view demonstrates that both, electron and light microscopists need to be open-minded about the results of the others. Seemingly homogeneous structures like ~1 Mb chromatin domains or entire nuclei visualized by light microscopy are composed of much more complex sub-structures than the images suggest. At the same time, highly complex

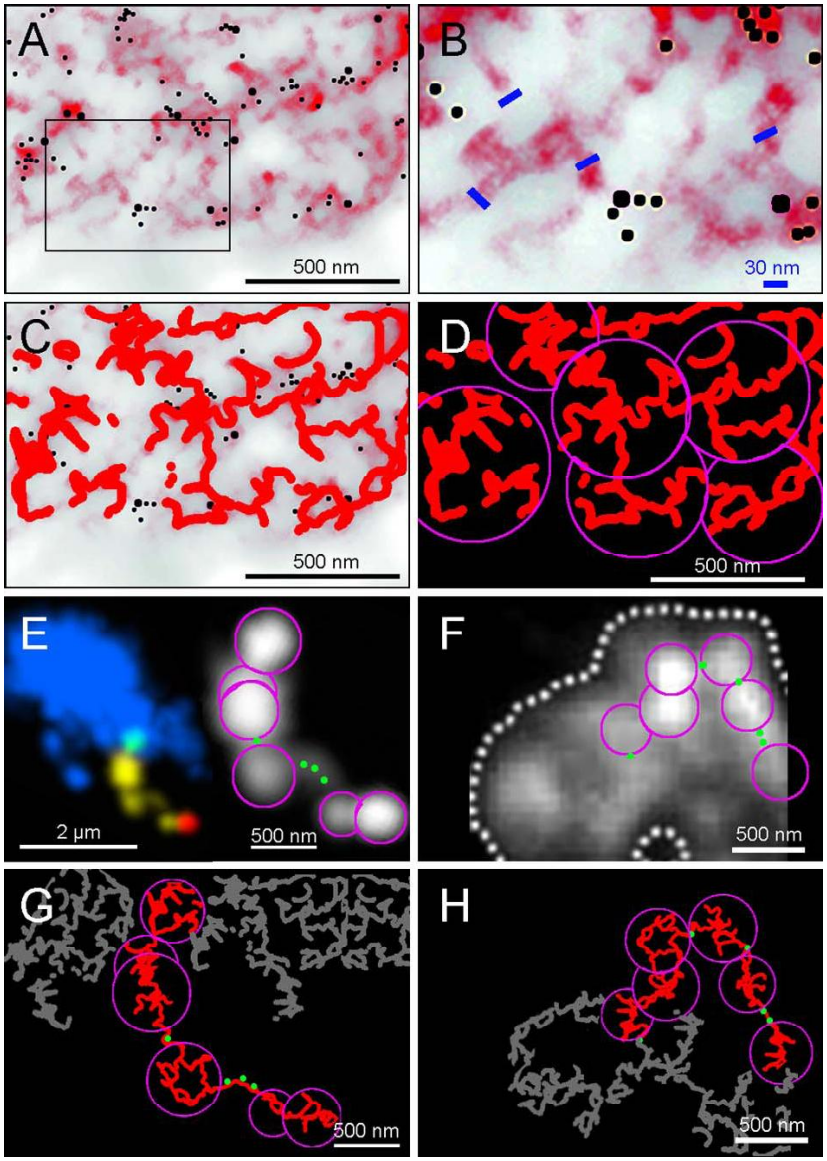

Figure 37: Linking EM images with the updated CT-IC model
A) Part of an ultrastructural section of a HeLa cell nucleus contrasted with the osmium ammine staining technique and visualized by EM. Chromatin is highlighted in red and black dots represent immuno-detected DNA and chromatin (for details see Fig. 24). **B)** Enlargement as indicated in (A) with bue bars of 30 nm length. **C)** Same image as (A) with 30 nm fibers artificially traced in red. **D)** Same image as shown in (C) without real data background and with hypothetical ~1 Mb chromatin domains superimposed on the hypothetical drawn 30 nm fiber network. **E)** Experimental FISH data on HSA 11 (blue) with the 11p15.5 region (green, yellow and red) as described in detail in Figure 31. Gray spheres display the enlarged 11p15.5 region with hypothetically superimposed ~1 Mb chromatin domains (violet circles) and chromatin linkers (green dots). **F)** Image taken form Branco and Pombo, 2006, showing parts of FISH painted HSA 6 on a 150 nm thick cryosection with superimposed hypothetical ~1 Mb chromatin domains (violet circles) and linkers (green dots). **G-H)** Hypothetical ultra-resolved view of the region depicted in (E) respectively (F) to suggest a hypothetical link between the 30 nm fiber network (red and green) frequently seen in EM sections and the higher order organization in ~1 Mb chromatin domains (violet circles) and linkers (green dots) as postulated by the updated CT-IC model.

structures revealed by electron microscopy not necessarily refute the existence of higher order compartments which are indiscernible at that high level of resolution ('not see the wood for the trees').

The example of ~1 Mb chromatin domains demonstrates the need for further efforts in comparing EM and other high resolution approaches with light microscopy images. Deconvolution of confocal images will thereby partially help to bridge the resolution gap. The combination of the respective advantages of each of the imaging techniques will then help to approach a more complete view on the architecture of the cell nucleus.

8 APPENDIX

8.1 Cells types, cell lines, expression constructs

The listed cells were cultured in either D-MEM (medium A) or RPMI-1640 (medium B) with the appropriate supplements (see methods).

Cells types /Cell lines	**medium**	**kindly provided by:**
baby hamster kidney fibroblast **BHK**-21	A	Prof. Goldman, Northwestern University, Chicago
Chinese hamster ovary cells **CHO**	A	Dr. Jos Broers, University of Maastricht
human amniotic fluid cell **AFC**	B	Prof. T. Meitinger, TU München
human breast cancer **MCF-7**	B	Dr. P. Meltzer, NIH, Bethesda, USA
human cervix cancer **HeLa** subclone 6	B	Prof. W. Franke, DKFZ, Heidelberg
human colon cancer **DLD-1**	A	Dr. C. Lengauer, John Hopkins Hospital, Baltimore
human fibroblast **HFb**	A	Prof. T. Meitinger, TU München
human granulocyte **HGc**	B	own peripheral blood sample
human lung fibroblast **LFb**	A	Prof. D. Sheer, Lincoln's Inn Fields Laboratories, London
human lymphoblastoid **HLb** LB-575	B	Dr. S. Müller, LMU, München
human lymphocyte **HLy**	B	own peripheral blood sample
human neuroblastoma **KELLY**	B	Prof. M. Schwab, DKFZ, Heidelberg
human neuroblastoma **LAN**	B	Prof. M. Schwab, DKFZ, Heidelberg

Expression construct	Resistance	Kindly provided by:
Histone-2B-GFP (H2B-GFP)	none	K. Sullivan
Histone-2B-monomeric RFP (H2B-RFP)	none	M. Ziegler, GSF, Munich
RNA-Pol-II-GFP (Pol-II-GFP)	α-Amanitin (2 µg/ml)	Prof. D. Eick, GSF, Munich
RNA-Pol-II-GFP delta 5 (Pol-II-GFPΔ5)	α-Amanitin (2 µg/ml)	Prof. D. Eick, GSF, Munich
RNA-Pol-II-GFP delta 266 (Pol-II-GFPΔ266)	α-Amanitin (2 µg/ml)	Prof. D. Eick, GSF, Munich
RNA-Pol-II-GFP delta 0 (Pol-II-GFPΔ0)	α-Amanitin (2 µg/ml)	Prof. D. Eick, GSF, Munich
Prolif.-Cell-Nuclear-Antigene-GFP (PCNA-GFP)	Kana	Prof. H. Leonhardt, LMU, Munich
Rad51-GFP	Neomycin	Dr. S. Tashiro, Hiroshima University
Scaffold-Attachment-Factor-A-GFP (SAF-A-GFP)	Kana R	Prof. R. Grosschedl, Genzentrum, Munich
Lamin-A/C-GFP	none	Prof. R. Goldman, Northw. University, Chicago
Lamin-B-GFP	none	Prof. R. Goldman, Northw. University, Chicago
Centromere-bind.-Protein-B-GFP (CENP-B-GFP)	none	Dr. M. Ziegler, GSF, Munich
SATb2-GFP	Kana R	Prof. R. Grosschedl, Genzentrum, Munich
SC35-GFP	None	M. Ziegler, GSF, Munich

8.2 Antibodies

Antibodies	Dilution	Distributor
Donkey α-goat-Cy3	1: 500	Rockland
Donkey α-rat-Cy3	1: 500	Jackson ImmunResearch
Goat α-mouse-Alexa488 (h.c.a.)	1: 200	Molecular Probes,
Goat α-rabbit (Fab) (un-conj.)	1: 50	gift by Dr. F. Spada, LMU, Munich
Goat α-rabbit-Cy3	1: 500	Amersham
Goat α-rabbit-Cy3 (Fab)	1: 100	Dianova
Human α-CREST	1: 100	Euroimmun
Mouse α-BrdU	1: 200	Roche
Mouse α-Ki67	1: 100	Roche
Mouse α-Lamin-A/C	1: 100	Santa Cruz Biotechnology
Mouse α-Lamin-B	1: 50	Santa Cruz Biotechnology
Mouse α-PML	1: 200	Santa Cruz Biotechnology
Mouse α-Pol-II (3/3)	1: 10	gift by Prof. D. Eick, GSF, Munich
Mouse α-Rad51	1: 200	gift by Dr. S. Tashiro, Hiroshima
Mouse α-SAF-A (hnRNP)	1: 100	Santa Cruz Biotechnology
Mouse α-SC35	1: 1000	Sigma-Aldrich
Mouse α-TRF2	1: 50	Imgenex
Mouse α-WG16	1: 1	gift by Prof. D. Eick, GSF, Munich
Rabbit α-triH3K27	1: 400	gift by Prof. T. Jenuwein, IMP, Vienna
Rabbit α-triH3K4	1: 500	Abcam
Rabbit α-triH3K9	1: 400	gift by Prof. T. Jenuwein, IMP, Vienna
Rabbit α-triH4K20	1: 400	gift by Prof. T. Jenuwein, IMP, Vienna
Rat α-Pol-II--phospho-S2 (sup.nat.)	1: 10	gift by Prof. D. Eick, GSF, Munich
Rat α-Pol-II--phospho-S5 (sup.nat.)	1: 10	gift by Prof. D. Eick, GSF, Munich
Rat α-Pol-II--phospho-S7 (sup.nat.)	1: 10	gift by Prof. D. Eick, GSF, Munich
Rat α-Pol-II--phospho-T4 (sup.nat.)	1: 10	gift by Prof. D. Eick, GSF, Munich
Sheep α-mouse-Cy3	1: 500	Dianova
Sheep α-mouse-FITC	1: 200	Sigma-Aldrich

8.3 Chemicals, reagents, media and solutions

Chemicals and Reagents	Distributor
Alexa-633 (Alexa 633 Fluor hydrazide)	Molecular Probes, Invitrogen
α-Amanitin	Sigma-Aldrich
7-AAD (7-amino actinomycin D)	Sigma-Aldrich
2-deoxyglucose	Sigma-Aldrich
Aphidicolin	Calbiochem
BrdU (Bromo-2'-doexyuridinBrdU)	Sigma-Aldrich
BSA (bovine serum albumin, Fraction V)	Roche
CaCl (calcium chloride)	Merck
Cy3-dUTP (Cyanin-3-deoxy-triphosphate)	gift by D. Köhler, LMU Munich
DAPI (diamidino-2-phenylindole)	Sigma-Aldrich
Digitonin powder	Sigma-Aldrich
DMSO (dimethyl sulphoxide)	Merck
DNase I	Roche
Ethanol absolute (type 642, 510)	Bundesmonopolverwaltung
FITC (Fluorescein isothiocyanate)-dextran	Molecular Probes, Invitrogen
Glycerol	Merck
HCl [1N] (hydrochloric acid)	Merck
Isopropanol	Merck
KCl (potassium chloride)	Merck
KH_2PO_4 (potassium hydrogen phosphate)	Merck
Meliseptol	B.Braun Biotech International
$MgCl_2$ (magnesium chloride)	Merck
Na_2HPO_4 (disodium hydrogen phosphate dihydrate)	Merck
NaAc (sodium acetate)	Merck
NaAz (sodium azide)	Merck
NaCl (sodium chloride)	Merck
NaOH (sodium hydroxide)	Merck
Nitrogen (liquid)	Messer Griesheim GmbH
Paraformaldehyde	Merck
Resin LR White	Electron Microscopy Sciences
RNase A	Roche
Triton X-100	Merck

Chemicals and Reagents	**Distributor**
To-Pro-3 iodide	Molecular Probes, Invitrogen
Trolox™	Sigma Aldrich
Tris-Base	Sigma Aldrich
Trypan blue (0.5%)	Seromed Biochrom
Trypsin / EDTA (10x, 0.5%/0.2%)	Seromed Biochrom
Tween 20	Merck
Vectashield (embedding medium, antifade)	Vector

Media and Media supplements	**Distributor**
D-MEM (**D**ulbeccos **M**odified-**E**agle-**M**edium)	Seromed Biochrom
D-MEM: glucose-free	Seromed Biochrom
RPMI-1640 (**R**oswell-**P**ark-**M**emorial-**I**nstitute)	Seromed Biochrom
RPMI-1640 with 25 mM HEPES	Seromed Biochrom
FCS (fetal calf serum)	Seromed Biochrom
Penicillin / Streptomycin: 10000 I.E. / 10000 µg/ml	Seromed Biochrom

Solutions (commercial)	**Distributor**
dd H_2O	
Poly-L-Lysine (10 mg/ml)	Sigma-Aldrich
DRAQ5	Biostatus
PI (propidium iodide, 500 µg/ml)	Sigma-Aldrich
Formaldehyde stock solution (37%)	Sigma-Aldrich

Solutions (self-made)	**Solvent**
7-AAD (7-aminoactinomycin D, 100 µM)	in DMSO, use 10 µM in PBST
2-deoxyglucose (60 mM)	in dd H_2O
Alexa-633 (10 mM)	in dd H_2O
α-Amanitin stock solution (2 mg/ml)	in dd H_2O
Aphidicolin (5 µg/µl)	in EtOH, store at -20°C
BrdU stock solution (50 mM)	in 50% DMSO, dd H_2O
CMF-PBS (Ca^{2+} and Mg^{2+} free-)	PBS w/o NaAz
DAPI (stock: 5 mg/ml)	in dd H_2O; use: 1:100 in PBST

Solutions (self-made)	Solvent
Digitonin (stock: 10 mg/ml)	in dd H_2O, store at +4°C
DNase (stock: 2U/µl; 1mg=2000U)	in 0.3M NaCl, 50% Glycerin
Ethanol (30%,50%,70%,90%)	in dd H_2O
PBS (5% 20xPBS)	in dd H_2O; pH:7.4 (HCl/NaOH)
20x PBS (2800 mM NaCl; 54 mM KCl; 130 mM Na_2HPO_4; 30 mM KH_2PO_4, 15 mM NaAz)	in dd H_2O; pH:7.4 (HCl/NaOH)
PBST (PBS + 0.01% Tween)	
PI (25 µg/ml)	dilute stock 1:20 in PBS
Poly-L-Lysine (use: 1 mg/ml)	dilute stock 1:10 in dd H_2O
Rnase stock solution (1% =10mg/ml)	in Tris-HCl
Soerensen phosphate buffer (0.1M: 7.13 g Na_2HPO_4, 1.32 g NaH_2PO_4)	in 500 ml dd H_2O; pH 7.33 (HCl/NaOH)
NaAz stock solution (1 M)	in CMF-PBS
To-Pro-3 (1mM)	in DMSO
Trolox (100 mM)	for protocol see Schermelleh, 2003
Tris-HCl (1M)	in dd H_2O, adjust with HCl
Trypsin / EDTA solution (0.05%/0.02%)	dilute stock 1:10 in CMF-PBS

8.4 Consumables and technical equipment

Consumables	Distributor
6-well plates	Greiner
microinjection capillary (Femtotip)	Eppendorf
coverslips gridded (CELLocate)	Eppendorf
coverslips (round: 40, 42 mm)	Assistent
coverslip (15x15 mm)	Superior
Embedding capsules (BEEM)	Electron Microscopy Sciences
Fluorescent beads 175 nm (PS-Speck™)	Molecular Probes, Invitrogen
Fluorescent beads: Tetraspeck 500 nm	Molecular Probes, Invitrogen
FuGene 6 transfection Kit	Roche
Hypodermic needle (0.9x40 mm)	B.Braun Biotech International
Microloader tip	Eppendorf
Nail polish	miscellaneous
Object slide (76x26 mm)	Langenbrinck

Consumables	Distributor
Paper wipes	Kimberley-Clark
Parafilm	Pechiney Plastic Packaging
Petri-dishes (35 mm, 60 mm)	Becton Dickinson
Pipettes - Serological (5, 20, 25, 50 ml)	Becton Dickinson
Syringe (Omnifix Luer Lock)	B.Braun Biotech International
Culture flasks (25 cm², 75 cm²)	Becton Dickinson
Tubes Cryotubes	Greiner
Tubes (1.5 ml, 2 ml)	Eppendorf
Tubes (15 ml, 50 ml)	Falcon

Technical equipment	Distributor
Autoclave	H+P Labortechnik GmbH
Balance	Sartorius
Bunsen burner (gasprofi)	WLD-TEC
Centrifuge (C 3i)	Jouan
Centrifuge (Biofuge pico)	Hereaus
Centrifuge (miniCentrifuge)	Neolab
Freezing box (filled with isopropanol)	Nalgene
Forceps	Dumont
Freezer -80°C (VXE 380)	Jouan
Freezer -20°C	Quelle
Freezing point Osmometer with tubes	Gonotec
Fridge +4°C	Quelle
Glass embryo dishes	Electron Microscopy Sciences
Laminar flow (Hera safe)	Hereaus
Ice machine	Scotsman
Incubator B 5060 and BB 6220	Hereaus, Hanau
Liquid nitrogen tank with rackets	Cryotherm
Living cell culture dish µ-slide I	ibidi
Living cell chamber system: FCS-II	Bioptechs
Living cell chamber system: POC	Bachofer
Magnetic stirrer	Ika Labortechnik
Metal box with lid	Schubert
Microinjection device (FemtoJet / InjectMan)	Eppendorf

Technical equipment	Distributor
pH-meter	WTW, Weilheim
Pipette Aid, accu-jet BRAND	Schubert&Weiss
Pipette Tips (white, green, blue)	Greiner
Pipettes (2µl, 10 µl, 20 µl, 200 µl, 1 ml,)	Gilson
Reflex-camera (Ricoh XR/KR 10-M)	Ricoh
Vortex	Ika Labortechnik
Water baths	GFL, Lauda, Julabo

Epifluorescence microscope: Axiophot 2	**Carl Zeiss**
Objectives:	Filters:
Plan-Neofluar 16x / 0.5	DAPI (BP 365, FT 395, LP 450-490 mm)
Plan-Neofluar 40x / 1.3 oil	FITC (BP 450-490, FT 510, LP 515-565 mm)
Plan-Apochromat 63x / 1.4 oil	Cy3 (BP 546, FT 580, LP 590 mm)
Plan-Neofluar 100x / 1.3 oil	Cy5 (BP 575-625, FT 645, LP 660-710 mm)
Camera:	Software:
Coolview CCD (Applied Imaging)	CytoVision (Applied Imaging)

Phase contrast microscope: Axiovert 25 C	**Carl Zeiss**
Objectives:	
CP Achromat 5x / 0.12	
CP Achromat 10x / 0.25 Ph1	
LD Achrostigmat 20x / 0.3 Ph1	
LD Achrostigmat 40x / 0.55 Ph2	

Confocal laser scanning microscope: LSM 410	**Carl Zeiss**
Objectives:	Software:
Plan-Apochromat 63x / 1.4 oil	LSM 410 software v 3.95
Plan-Neofluar 10x / 0.3	
Lasers:	Emission Filters:
Ar+-laser 488 nm, 15 mW	BP 502-542 nm: 'green'
HeNe-laser 543 nm / 0.5mW	BP 575-640 nm: 'orange'
HeNe-laser 633 nm / 5mW	LP 650 nm: 'red-infrared'

Confocal laser scanning microscope: LSM 510	**Carl Zeiss**
Objectives:	Software:
Plan-Apochromat 63x / 1.4 oil	Zeiss LSM 510 Image Browser v3.2
Lasers:	
Ar+-laser 488 nm, 35 mW; HeNe-laser 543 nm / 1mW	
Heating unit (37°C) for POC chamber	
3 photomultipliers with continuously adjustable bandwidth	

Confocal laser scanning microscope: TCS SP2	**Leica**
Objectives:	Software:
Plan-Apochromat 63x / 1.4 oil	TCS SP software v 2.61
heating chamber: 'the cube' (light imaging services)	
Lasers:	
Diode-laser 405 nm / 25 mW; Argon-laser 488 nm / 200 mW; DPSS-laser 561 nm / 10 mW;	
HeNe-laser 594 nm / 2.5 mW; HeNe-laser 633 nm / 10 mW	
4 photomultipliers with continuously adjustable bandwidth	

8.5 Software and deconvolution parameters

Software	**Distributor**
AfterEffects 5.5	Adobe
Amira 3.1.1.	TGS Europe
Cytovision	Appl. Imaging International
Huygens Essential 3.2	Scientific Volume Imaging
EDMT v 3.00a and Filemaker 2.10	Courtesy of T. Thormeyer
Endnote 9.0	Thomson
ImageJ 1.3.7c	Wayne Rasband, NIH
Imaris 4.5	Bitplane
Irfan View 3.9.2	Irfan Skilijan
Leica TCS	Leica
LSM 410 (v. 3.98)	Zeiss
LSM 510	Carl Zeiss

Software	Distributor
Microsoft Office 2003	Microsoft
Photoshop 7.0	Adobe
Quicktime 4.0	Apple
SigmaStat 3.00	SPSS
SPSS 12.0	SPSS
TIKALpro 1.0	Courtesy of C. Bacher, DKFZ
Volocity 3.0	Improvision
Zeiss LSM Image Browser 3.2	Carl Zeiss

Deconvolution parameters

The parameters to be set in the Huygens Essential 3.2 software for the PSF generation as well as for the deconvolution were adjusted under consideration of the 'Huygens Essential User Guide' (http://www.svi.nl/download/guides.php) as follows:

Numerical aperture of the objectives: 1.4

Since the highest possible resolution was desired, only objectives with the highest numerical aperture were chosen for confocal microscopy.

Refractive indices: Immersion oil 1.518; Embedding medium *Vectashield*: 1.457.

Since these two values differ, a 'refractive index mismatch' was inherent in the recording system. Such a mismatch causes spherical aberration and a loss of light due to total internal reflection. It could be avoided, if the values were adapted by either choosing a smaller numerical aperture or a different embedding medium with a higher refractive index. However, both adaptations would worsen image quality, since either the resolution is decreased (numerical aperture) or compromises in regard to the preservation of the specimen are made (embedding medium). A major impact of this mismatch on image quality, however, occurs only in thicker specimen with several 10^{th} of microns and is less obvious in recordings of thin cell nuclei (<15 µm). Furthermore, potential artifacts derived from refractive indices (amongst others) could be prevented by adapting other parameters, especially the SNR (see 6.1).

Voxel size (x-y-z): Zeiss LSM 410: 50-50-100 nm; Leica SP2: 50-50-120 nm

Images, which ought to be deconvolved, have to meet the so called 'Nyquist Criterion', which describes the sampling size for the respective excitation wavelength needed for proper deconvolution (Pawley, 2006). Since normally several channels were recorded in the same run, the values were set as a standard as reported above.

Excitation wavelength: The wavelengths of the lasers used were set for each channel as excitation wavelength.

Emission wavelength: The emission maxima of the fluorochromes / fluorescent beads used were set for each channel as emission wavelength.

Size of back-projected pinhole: Zeiss LSM 410: 315 nm (for all lasers); Leica SP2: 176 nm (for 405 nm laser line), 213 nm (for 488 nm laser line), 244 nm (for 561 nm laser line) and 276 nm (for 633 nm laser line). This is a general parameter with 'back-projected' meaning the size of the pinhole as it appears in the specimen plane. This value can be looked up in tables or be computed by formulas, both given in the 'Huygens Essential Deconvolution Recipes Guide': (http://www.svi.nl/download/guides.php).

Excitation photon count: 1 (no 2-photon approach was used)

Signal to noise ratio (SNR): This parameter is estimated on the image quality and can range from <10 (=noisy), 10<20 (=moderate noise) and >20 (low noise). The deconvolved data sets, investigated in this thesis were all set to 15 (unless otherwise stated in the text).

Background estimation: The mean gray value of the background (region outside of fluorescent object) was always accepted of the estimated value calculated on the input images by Huygens with the therein recommended 'lowest value'-tool (according to this automated procedure the background gray values usually were below 10).

Maximum iterations: Deconvolution based on the CMLE algorithm is an iterative and in principle endless procedure. To stop the calculation one has to determine a stopping criterion. The number of proceeded iterations after which the deconvolution was stopped was set to 40, unless otherwise stated in the text.

Quality threshold: In the Huygens software, the deconvolution procedure can be alternatively set to end when a given quality level is reached. As soon as the quality of the image is not improved beyond that resulting from the preceding iteration, the procedure is stopped. As a standard this value was set to 0.1. In order to control precisely the process of deconvolution only by using a maximum number of iterations, this function was deactivated by setting a very high quality criterion (e.g. 0.0001).

Iteration mode: From the two modes offered in the Huygens Essential software, always the 'high quality mode' was applied. The additional 'fast mode' - offered to speed up the MLE-algorithm - was of no advantage, since the computing time was no limiting factor.

Bleaching correction: Since bleaching during the acquisition of confocal images was minimal, this feature was deactivated.

8.6 List of Publications

Albiez, H., Viña, J., Zinner, R., Tiberi, C., Vecchio, L., Weierich, C., Strickfaden, H., van der Voort, H., Fakan, S., Cremer, T.
Deconvolution of 3D confocal microscope data sets enhances images of biological samples.
In prep.

von Hase, J., Kuepper, K., **Albiez, H.**, Weierich, C., Köhler, D., Kreth, G., Mills, K., Cremer, C.
Euclidean Distance Transform in images from fluorescence microscopy
Biophysical Journal, submit.

Albiez, H., Cremer, M., Tiberi, C., Vecchio, L., Schermelleh, L., Dittrich, S., Küpper, K., Joffe, B., Thormeyer, T., von Hase, J., Yang, S., Rohr, K., Leonhardt, H., Solovei, I., Cremer, C., Fakan, S., Cremer, T. 2006.
Chromatin domains and the interchromatin compartment form structurally defined and functionally interacting nuclear networks.
Chromosome Research 14 (7), 707-733

Walter J., Joffe B., Bolzer A., **Albiez H.**, Benedetti P. A., Müller S., Speicher M. R., Cremer T., Cremer M., Solovei I. 2006
Towards many colors in FISH on 3D-preserved interphase nuclei.
Cytogenetic and Genome Research 114, 367-378

Zinner, R., **Albiez, H.**, Walter, J., Peters, A.H.F.M., Cremer, T., Cremer, M. 2006.
Histone lysine methylation patterns in human cell types are arranged in distinct three-dimensional nuclear zones.
Histochemistry and Cell Biology 125, 3-19.

Lux, C., **Albiez, H.** (**joint first authors**), Chapman, R. D., Heidinger, M., Meininghaus, M., Brack-Werner, R., Lang, A., Ziegler, M., Cremer, T., and Eick, D. 2005.
Transition from initiation to promoter proximal pausing requires the CTD of RNA polymerase II.
Nucleic Acids Research 33, 5139-5144.

Solovei I., Schermelleh L., **Albiez H.**, Cremer T. 2005.
Detection of the cell cycle stages in situ in growing cell populations.
In: Celis J, Editor. Cell Biology Handbook: A Laboratory Manual, 3rd Edition. San Diego: Academic Press, NYP

Cremer M., Zinner R., Stein S., **Albiez H.**, Wagler B., Cremer C., Cremer T. 2004.
Three dimensional analysis of histone methylation patterns in normal and tumor cell nuclei.
European Journal of Histochemistry 48,1:15-28

8.8 Bibliography

Abney, J.R., B. Cutler, M.L. Fillbach, D. Axelrod, and B.A. Scalettar. 1997. Chromatin dynamics in interphase nuclei and its implications for nuclear structure. *J. Cell Biol.* 137:1459-68.

Abranches, R., A.F. Beven, L. Aragon-Alcaide, and P.J. Shaw. 1998. Transcription sites are not correlated with chromosome territories in wheat nuclei. *J. Cell Biol.* 143:5-12.

Adkins, N.L., M. Watts, and P.T. Georgel. 2004. To the 30-nm chromatin fiber and beyond. *Biochim Biophys Acta*. 1677:12-23.

Adolphs, K.W., S.M. Cheng, J.R. Paulson, and U.K. Laemmli. 1977. Isolation of a protein scaffold from mitotic HeLa cell chromosomes. *Proc Natl Acad Sci U S A*. 74:4937-41.

Alberts, B., Johnson, A., Lewis, J., Raff, M., Roberts, K., and Walter, P. 2002. Molecular Biology of the Cell. *Garland Science, New York*.

Albiez, H. 2003. Induzierte Chromatinkondensation. *In* Diplomarbeit an der Fakultät für Biologie, LMU München.

Albiez, H., M. Cremer, C. Tiberi, L. Vecchio, L. Schermelleh, S. Dittrich, K. Kupper, B. Joffe, T. Thormeyer, J. von Hase, S. Yang, K. Rohr, H. Leonhardt, I. Solovei, C. Cremer, S. Fakan, and T. Cremer. 2006. Chromatin domains and the interchromatin compartment form structurally defined and functionally interacting nuclear networks. *Chromosome Res*. 14:707-733.

Alexandrova, O., I. Solovei, T. Cremer, and C.N. David. 2003. Replication labeling patterns and chromosome territories typical of mammalian nuclei are conserved in the early metazoan Hydra. *Chromosoma*. 112:190-200.

Bacher, C.P., M. Guggiari, B. Brors, S. Augui, P. Clerc, P. Avner, R. Eils, and E. Heard. 2006. Transient colocalization of X-inactivation centres accompanies the initiation of X inactivation. *Nat Cell Biol*. 8:293-9.

Bank, O. 1939. Abhaenigigkeit der Kernstruktur von der Ionenkonzentration. *Protoplasma*. 32:20-30.

Belar, K. 1930. Ueber die reversible Entmischung des lebenden Protoplasmas. *Protoplasma*. 9:209-244.

Belmont, A.S., and K. Bruce. 1994. Visualization of G1 chromosomes: a folded, twisted, supercoiled chromonema model of interphase chromatid structure. *J. Cell Biol.* 127:287-302.

Belmont, A.S., J.W. Sedat, and D.A. Agard. 1987. A three-dimensional approach to mitotic chromosome structure: evidence for a complex hierarchical organization. *J. Cell Biol.* 105:77-92.

Berezney, R., and D.S. Coffey. 1974. Identification of a nuclear protein matrix. *Biochem. Biophys. Res. Commun.* 60:1410-7.

Berezney, R., D.D. Dubey, and J.A. Huberman. 2000. Heterogeneity of eukaryotic replicons, replicon clusters, and replication foci. *Chromosoma*. 108:471-84.

Berezney, R., M.J. Mortillaro, H. Ma, X. Wei, and J. Samarabandu. 1995. The nuclear matrix: a structural milieu for genomic function. *Int. Rev. Cytol.*:1-65.

Bernhard, W. 1968. [A method of regressive colaration with use of the electron microscope]. *C R Acad Sci Hebd Seances Acad Sci D.* 267:2170-3.

Bernstein, B.E., M. Kamal, K. Lindblad-Toh, S. Bekiranov, D.K. Bailey, D.J. Huebert, S. McMahon, E.K. Karlsson, E.J. Kulbokas, 3rd, T.R. Gingeras, S.L. Schreiber, and E.S. Lander. 2005. Genomic maps and comparative analysis of histone modifications in human and mouse. *Cell*. 120:169-81.

Bolzer, A., G. Kreth, I. Solovei, D. Koehler, K. Saracoglu, C. Fauth, S. Muller, R. Eils, C. Cremer, M.R. Speicher, and T. Cremer. 2005. Three-dimensional maps of all chromosomes in human male fibroblast nuclei and prometaphase rosettes. *PLoS Biol*. 3:e157.

Boutanaev, A.M., L.M. Mikhaylova, and D.I. Nurminsky. 2005. The pattern of chromosome folding in interphase is outlined by the linear gene density profile. *Mol Cell Biol*. 25:8379-86.

Boutet de Monvel, J., S. Le Calvez, and M. Ulfendahl. 2001. Image restoration for confocal microscopy: improving the limits of deconvolution, with application to the visualization of the mammalian hearing organ. *Biophys J*. 80:2455-70.

Boyle, S., S. Gilchrist, J.M. Bridger, N.L. Mahy, J.A. Ellis, and W.A. Bickmore. 2001. The spatial organization of human chromosomes within the nuclei of normal and emerin-mutant cells. *Hum Mol Genet*. 10:211-219.

Branco, M.R., and A. Pombo. 2006. Intermingling of Chromosome Territories in Interphase Suggests Role in Translocations and Transcription-Dependent Associations. *PLoS Biol*. 4:e138.

Branco, M.R., and A. Pombo. 2007. Chromosome organization: new facts, new models. *Trends Cell Biol*. 17:127-34.

Bridger, J.M., S. Boyle, I.R. Kill, and W.A. Bickmore. 2000. Re-modelling of nuclear architecture in quiescent and senescent human fibroblasts. *Curr. Biol.* 10:149-52.

Bridger, J.M., H. Herrmann, C. Münkel, and P. Lichter. 1998. Identification of an interchromosomal compartment by polymerization of nuclear-targeted vimentin. *Journal of Cell Science*. 111:1241-1253.

Bridger, J.M., C. Kalla, H. Wodrich, S. Weitz, J.A. King, K. Khazaie, H.G. Krausslich, and P. Lichter. 2005. Nuclear RNAs confined to a reticular compartment between chromosome territories. *Exp Cell Res*. 302:180-93.

Caille, N., O. Thoumine, Y. Tardy, and J.J. Meister. 2002. Contribution of the nucleus to the mechanical properties of endothelial cells. *J Biomech*. 35:177-87.

Caron, H., B. van Schaik, M. van der Mee, F. Baas, G. Riggins, P. van Sluis, M.C. Hermus, R. van Asperen, K. Boon, P.A. Voute, S. Heisterkamp, A. van Kampen, and R. Versteeg. 2001. The human transcriptome map: clustering of highly expressed genes in chromosomal domains. *Science*. 291:1289-92.

Chadwick, B.P., and H.F. Willard. 2004. Multiple spatially distinct types of facultative heterochromatin on the human inactive X chromosome. *Proc Natl Acad Sci U S A*. 101:17450-5.

Chambeyron, S., N.R. Da Silva, K.A. Lawson, and W.A. Bickmore. 2005. Nuclear re-organisation of the Hoxb complex during mouse embryonic development. *Development*. 132:2215-23.

Cheutin, T., A.J. McNairn, T. Jenuwein, D.M. Gilbert, P.B. Singh, and T. Misteli. 2003. Maintenance of stable heterochromatin domains by dynamic HP1 binding. *Science*. 299:721-5.

Ching, R.W., G. Dellaire, C.H. Eskiw, and D.P. Bazett-Jones. 2005. PML bodies: a meeting place for genomic loci? *J Cell Sci*. 118:847-54.

Chuang, C.H., A.E. Carpenter, B. Fuchsova, T. Johnson, P. de Lanerolle, and A.S. Belmont. 2006. Long-range directional movement of an interphase chromosome site. *Curr Biol*. 16:825-31.

Chubb, J.R., and W.A. Bickmore. 2003. Considering nuclear compartmentalization in the light of nuclear dynamics. *Cell*. 112:403-6.

Claussen, U. 2005. Chromosomics. *Cytogenet Genome Res*. 111:101-6.

Cmarko, D., P.J. Verschure, T.E. Martin, M.E. Dahmus, S. Krause, X.D. Fu, R. van Driel, and S. Fakan. 1999. Ultrastructural analysis of transcription and splicing in the cell nucleus after bromo-UTP microinjection. *Mol. Biol. Cell*. 10:211-23.

Cogliati, R., and A. Gautier. 1973. [Demonstration of DNA and polysaccharides using a new "Schiff type" reagent]. *C R Acad Sci Hebd Seances Acad Sci D*. 276:3041-4.

Conchello, J.A., and J.W. Lichtman. 2005. Optical sectioning microscopy. *Nat Methods*. 2:920-31.

Cook, P.R. 1999. The organization of replication and transcription. *Science*. 284:1790-5.

Cook, P.R. 2002. Predicting three-dimensional genome structure from transcriptional activity. *Nat Genet*. 32:347-52.

Cook, P.R., and F. Gove. 1992. Transcription by an immobilized RNA polymerase from bacteriophage T7 and the topology of transcription. *Nucleic Acids Res*. 20:3591-8.

Craig, J.M. 2005. Heterochromatin--many flavours, common themes. *Bioessays*. 27:17-28.

Cremer, C., T. Cremer, M. Fukuda, and K. Nakanishi. 1980. Detection of laser--UV microirradiation-induced DNA photolesions by immunofluorescent staining. *Hum. Genet.* 54:107-10.

Cremer, C., T. Cremer, and J.W. Gray. 1982. Induction of chromosome damage by ultraviolet light and caffeine: correlation of cytogenetic evaluation and flow karyotype. *Cytometry*. 2:287-90.

Cremer, M., J. von Hase, T. Volm, A. Brero, G. Kreth, J. Walter, C. Fischer, I. Solovei, C. Cremer, and T. Cremer. 2001. Non-random radial higher-order chromatin arrangements in nuclei of diploid human cells. *Chromosome Res*. 9:541-67.

Cremer, M., R. Zinner, S. Stein, H. Albiez, B. Wagler, C. Cremer, and T. Cremer. 2004a. Three dimensional analysis of histone methylation patterns in normal and tumor cell nuclei. *Eur J Histochem*. 48:15-28.

Cremer, T., and C. Cremer. 2001. Chromosome territories, nuclear architecture and gene regulation in mammalian cells. *Nat Rev Genet*. 2:292-301.

Cremer, T., and C. Cremer. 2006a. Rise, fall and resurrection of chromosome territories: a historical perspective. Part I. The rise of chromosome territories. *Eur J Histochem*. 50:161-76.

Cremer, T., and C. Cremer. 2006b. Rise, fall and resurrection of chromosome territories: a historical perspective. Part II. Fall and resurrection of chromosome territories during the 1950s to 1980s. Part III. Chromosome territories and the functional nuclear architecture: experiments and models from the 1990s to the present. *Eur J Histochem*. 50:223-72.

Cremer, T., M. Cremer, S. Dietzel, S. Muller, I. Solovei, and S. Fakan. 2006. Chromosome territories--a functional nuclear landscape. *Curr Opin Cell Biol*. 18:307-16.

Cremer, T., S. Dietzel, R. Eils, P. Lichter, and C. Cremer. 1995. Chromosome territories, nuclear matrix filaments and interchromatin channels: A topological view on nuclear architecture and function. *In* Kew Chromosome Conference IV. P.E. Brandham and M.D. Bennett, editors. Royal Botanic Gardens, Kew, Royal Botanic Gardens, Kew. 63-81.

Cremer, T., K. Kupper, S. Dietzel, and S. Fakan. 2004b. Higher order chromatin architecture in the cell nucleus: on the way from structure to function. *Biol Cell*. 96:555-67.

Dehghani, H., G. Dellaire, and D.P. Bazett-Jones. 2005. Organization of chromatin in the interphase mammalian cell. *Micron*. 36:95-108.

Dey, N., L. Blanc-Feraud, C. Zimmer, P. Roux, Z. Kam, J.C. Olivo-Marin, and J. Zerubia. 2006. Richardson-Lucy algorithm with total variation regularization for 3D confocal microscope deconvolution. *Microsc Res Tech*. 69:260-6.

Dietzel, S., A. Jauch, D. Kienle, G. Qu, H. Holtgreve-Grez, R. Eils, C. Munkel, M. Bittner, P.S. Meltzer, J.M. Trent, and T. Cremer. 1998. Separate and variably shaped chromosome arm domains are disclosed by chromosome arm painting in human cell nuclei. *Chromosome Res.* 6:25-33.

Dingwall, C., S.M. Dilworth, S.J. Black, S.E. Kearsey, L.S. Cox, and R.A. Laskey. 1987. Nucleoplasmin cDNA sequence reveals polyglutamic acid tracts and a cluster of sequences homologous to putative nuclear localization signals. *Embo J*. 6:69-74.

Dittrich, S. 2006. Zwei besondere Bereiche: Die genarme Centromerregion von HSA 19 und die genreiche region HSA 11p15.5. *In* Diplomarbeit an der Fakultät für Biologie, LMU München.

Earnshaw, W.C., and M.M. Heck. 1985. Localization of topoisomerase II in mitotic chromosomes. *J. Cell Biol.* 100:1716-1725.

Earnshaw, W.C., and U.K. Laemmli. 1983. Architecture of metaphase chromosomes and chromosome scaffolds. *J. Cell Biol.* 96:84-93.

Esquivel, C., G.H. Vazquez-Nin, and O. Echeverria. 1989. Evidence of repetitive patterns of chromatin distribution in cell nuclei of rat liver. *Acta Anat (Basel)*. 136:94-8.

Fakan, S. 1994. Perichromatin fibrils are in situ forms of nascent transcripts. *Trends Cell Biol*. 4:86-90.

Fakan, S. 2004a. The functional architecture of the nucleus as analysed by ultrastructural cytochemistry. *Histochem Cell Biol*. 122:83-93.

Fakan, S. 2004b. Ultrastructural cytochemical analyses of nuclear functional architecture. *Eur J Histochem*. 48:5-14.

Fakan, S., and W. Bernhard. 1971. Localisation of rapidly and slowly labelled nuclear RNA as visualized by high resolution autoradiography. *Exp Cell Res*. 67:129-41.

Fakan, S., and R. Hancock. 1974. Localization of newly-synthesized DNA in a mammalian cell as visualized by high resolution autoradiography. *Exp Cell Res*. 83:95-102.

Fakan, S., and E. Puvion. 1980. The ultrastructural visualization of nucleolar and extranucleolar RNA synthesis and distribution. *Int. Rev. Cytol.* 65:255-99.

Fakan, S., E. Puvion, and G. Sphor. 1976. Localization and characterization of newly synthesized nuclear RNA in isolate rat hepatocytes. *Exp Cell Res*. 99:155-64.

Fawcett, D.W. 1966. On the occurrence of a fibrous lamina on the inner aspect of the nuclear envelope in certain cells of vertebrates. *Am J Anat*. 119:129-45.

Fay, F.S., K.L. Taneja, S. Shenoy, L. Lifshitz, and R.H. Singer. 1997. Quantitative digital analysis of diffuse and concentrated nuclear distributions of nascent transcripts, SC35 and poly(A). *Exp Cell Res*. 231:27-37.

Federico, C., S. Saccone, and G. Bernardi. 1998. The gene-richest bands of human chromosomes replicate at the onset of the S-phase. *Cytogenet. Cell Genet.* 80:83-8.

Ferreira, J., G. Paolella, C. Ramos, and A.I. Lamond. 1997. Spatial organization of large-scale chromatin domains in the nucleus: a magnified view of single chromosome territories. *J Cell Biol*. 139:1597-610.

Festenstein, R., S.N. Pagakis, K. Hiragami, D. Lyon, A. Verreault, B. Sekkali, and D. Kioussis. 2003. Modulation of heterochromatin protein 1 dynamics in primary Mammalian cells. *Science*. 299:719-21.

Finch, J.T., and A. Klug. 1976. Solenoidal model for superstructure in chromatin. *Proc Natl Acad Sci U S A*. 73:1897-901.

Foster, H.A., and J.M. Bridger. 2005. The genome and the nucleus: a marriage made by evolution. Genome organisation and nuclear architecture. *Chromosoma*. 114:212-29.

Fuchs, J., D. Demidov, A. Houben, and I. Schubert. 2006. Chromosomal histone modification patterns--from conservation to diversity. *Trends Plant Sci*. 11:199-208.

Galiova, G., E. Bartova, and S. Kozubek. 2004. Nuclear topography of beta-like globin gene cluster in IL-3-stimulated human leukemic K-562 cells. *Blood Cells Mol Dis*. 33:4-14.

Garcia-Ramirez, M., F. Dong, and J. Ausio. 1992. Role of the histone "tails" in the folding of oligonucleosomes depleted of histone H1. *J Biol Chem*. 267:19587-95.

Gazave, E., P. Gautier, S. Gilchrist, and W.A. Bickmore. 2005. Does radial nuclear organisation influence DNA damage? *Chromosome Res*. 13:377-88.

Gerlich, D., J. Beaudouin, B. Kalbfuss, N. Daigle, R. Eils, and J. Ellenberg. 2003. Global chromosome positions are transmitted through mitosis in mammalian cells. *Cell*. 112:751-64.

Gilbert, N., S. Boyle, H. Fiegler, K. Woodfine, N.P. Carter, and W.A. Bickmore. 2004. Chromatin architecture of the human genome: gene-rich domains are enriched in open chromatin fibers. *Cell*. 118:555-66.

Gladilin, E., K. Rohr, and R. Eils. 2006. Image-based analysis of mechanical cell response with respect to uniaxial stretching. *In* CMBBE. FIRST Numerics Ltd., Antibes.

Goren, A., and H. Cedar. 2003. Replicating by the clock. *Nat Rev Mol Cell Biol*. 4:25-32.

Gorisch, S.M., K. Richter, M.O. Scheuermann, H. Herrmann, and P. Lichter. 2003. Diffusion-limited compartmentalization of mammalian cell nuclei assessed by microinjected macromolecules. *Exp Cell Res*. 289:282-94.

Gruenbaum, Y., A. Margalit, R.D. Goldman, D.K. Shumaker, and K.L. Wilson. 2005. The nuclear lamina comes of age. *Nat Rev Mol Cell Biol*. 6:21-31.

Habermann, F.A., M. Cremer, J. Walter, G. Kreth, J. von Hase, K. Bauer, J. Wienberg, C. Cremer, T. Cremer, and I. Solovei. 2001. Arrangements of macro- and microchromosomes in chicken cells. *Chromosome Res*. 9:569-84.

Hancock, R. 2000. A new look at the nuclear matrix. *Chromosoma*. 109:219-225.

Hancock, R. 2004a. Internal organisation of the nucleus: assembly of compartments by macromolecular crowding and the nuclear matrix model. *Biol Cell*. 96:595-601.

Hancock, R. 2004b. A role for macromolecular crowding effects in the assembly and function of compartments in the nucleus. *J Struct Biol*. 146:281-90.

Hancock, R. 2007. Packing of the polynucleosome chain in interphase chromosomes: evidence for a contribution of macromolecular crowding. *Sem Cell Dev Biol*. in press.

Hansen, J.C. 2002. Conformational dynamics of the chromatin fiber in solution: determinants, mechanisms, and functions. *Annu Rev Biophys Biomol Struct*. 31:361-92.

Hansen, J.C., J. Ausio, V.H. Stanik, and K. van Holde. 1989. Homogenous reconstituted oligonucleosomes, evidence for salt-dependent folding in the absence of histone H1. *Biochemistry*. 28:9129-9136.

Heun, P., T. Laroche, M.K. Raghuraman, and S.M. Gasser. 2001. The positioning and dynamics of origins of replication in the budding yeast nucleus. *J Cell Biol*. 152:385-400.

Hiraoka, Y., J.W. Sedat, and D.A. Agard. 1990. Determination of three-dimensional imaging properties of a light microscope system. Partial confocal behavior in epifluorescence microscopy. *Biophys J*. 57:325-33.

Horn, P.J., and C.L. Peterson. 2002. Molecular biology. Chromatin higher order folding--wrapping up transcription. *Science*. 297:1824-7.

Hozak, P., A.M. Sasseville, Y. Raymond, and P.R. Cook. 1995. Lamin proteins form an internal nucleoskeleton as well as a peripheral lamina in human cells. *J Cell Sci*. 108 (Pt 2):635-44.

Hsu, T.C. 1975. A possible function of constitutive heterochromatin: the bodyguard hypothesis. *Genetics*. 79 Suppl:137-50.

Hu, Q., Z. Hou, and W.L. Nowinski. 2006. Supervised range-constrained thresholding. *IEEE Trans Image Process*. 15:228-40.

Hutchison, C.J. 2002. Lamins: building blocks or regulators of gene expression? *Nat Rev Mol Cell Biol*. 3:848-58.

Jackson, D.A. 2003. The anatomy of transcription sites. *Curr Opin Cell Biol*. 15:311-7.

Jackson, D.A., and A. Pombo. 1998. Replicon clusters are stable units of chromosome structure: evidence that nuclear organization contributes to the efficient activation and propagation of S phase in human cells. *J. Cell Biol.* 140:1285-95.

Jaunin, F., and S. Fakan. 2002. DNA replication and nuclear architecture. *J Cell Biochem*. 85:1-9.

Jaunin, F., A.E. Visser, D. Cmarko, J.A. Aten, and S. Fakan. 2000. Fine structural in situ analysis of nascent DNA movement following DNA replication. *Exp Cell Res*. 260:313-23.

Jenuwein, T., and C.D. Allis. 2001. Translating the histone code. *Science*. 293:1074-80.

Koberna, K., A. Ligasova, J. Malinsky, A. Pliss, A.J. Siegel, Z. Cvackova, H. Fidlerova, M. Masata, M. Fialova, I. Raska, and R. Berezney. 2005. Electron microscopy of DNA replication in 3-D: evidence for similar-sized replication foci throughout S-phase. *J Cell Biochem*. 94:126-38.

Kreth, G., P. Edelmann, C. Münkel, J. Langowski, and C. Cremer. 2002. Translocation frequencies for X and Y chromosomes predicted by computer simulations of nuclear structure. *In* Some aspects of Chromosome Structure and Functions. R.C. Sobti, G. Obe, and R.S. Athwal, editors. Narosa Publ House, New Delhi. 57-71.

Kreth, G., J. Finsterle, and C. Cremer. 2004a. Virtual radiation biophysics: implications of nuclear structure. *Cytogenet Genome Res*. 104:157-61.

Kreth, G., J. Finsterle, J. von Hase, M. Cremer, and C. Cremer. 2004b. Radial arrangement of chromosome territories in human cell nuclei: a computer model approach based on gene density indicates a probabilistic global positioning code. *Biophys J*. 86:2803-12.

Kriete, A., M. Naim, and L. Schafer. 2001. Quality measures in applications of image restoration. *Scanning*. 23:313-9.

Kupper, K., A. Kolbl, D. Biener, S. Dittrich, J. von Hase, T. Thormeyer, H. Fiegler, N.P. Carter, M.R. Speicher, T. Cremer, and M. Cremer. 2007. Radial chromatin positioning is shaped by local gene density, not by gene expression. *Chromosoma*.

Kuroda, M., H. Tanabe, K. Yoshida, K. Oikawa, A. Saito, T. Kiyuna, H. Mizusawa, and K. Mukai. 2004. Alteration of chromosome positioning during adipocyte differentiation. *J Cell Sci*. 117:5897-903.

Kurz, A., S. Lampel, J.E. Nickolenko, J. Bradl, A. Benner, R.M. Zirbel, T. Cremer, and P. Lichter. 1996. Active and inactive genes localize preferentially in the periphery of chromosome territories. *J. Cell Biol.* 135:1195-205.

Lachner, M., R.J. O'Sullivan, and T. Jenuwein. 2003. An epigenetic road map for histone lysine methylation. *J Cell Sci*. 116:2117-24.

Laemmli, U.K., S.M. Cheng, K.W. Adolph, J.R. Paulson, J.A. Brown, and W.R. Baumbach. 1978. Metaphase chromosome structure: the role of nonhistone proteins. *Cold Spring Harb Symp Quant Biol*. 42 Pt 1:351-60.

Lamond, A.I., and D.L. Spector. 2003. Nuclear speckles: a model for nuclear organelles. *Nat Rev Mol Cell Biol*. 4:605-12.

Lanctot, C., T. Cheutin, M. Cremer, G. Cavalli, and T. Cremer. 2007. Dynamic genome architecture in the nuclear space: regulation of gene expression in three dimensions. *Nat Rev Genet*. 8:104-15.

Landmann, L. 2002. Deconvolution improves colocalization analysis of multiple fluorochromes in 3D confocal data sets more than filtering techniques. *J Microsc*. 208:134-47.

Langowski, J. 2006. Polymer chain models of DNA and chromatin. *Eur Phys J E Soft Matter*. 19:241-9.

Lawrence, J.B., R.H. Singer, and L.M. Marselle. 1989. Highly localized tracks of specific transcripts within interphase nuclei visualized by in situ hybridization. *Cell*. 57:493-502.

Lemke, J., J. Claussen, S. Michel, I. Chudoba, P. Muhlig, M. Westermann, K. Sperling, N. Rubtsov, U.W. Grummt, P. Ullmann, K. Kromeyer-Hauschild, T. Liehr, and U. Claussen. 2002. The DNA-based structure of human chromosome 5 in interphase. *Am J Hum Genet*. 71:1051-9.

Liu, L.F., and J.C. Wang. 1987. Supercoiling of the DNA template during transcription. *Proc Natl Acad Sci U S A*. 84:7024-7.

Ma, H., J. Samarabandu, R.S. Devdhar, R. Acharya, P.C. Cheng, C. Meng, and R. Berezney. 1998. Spatial and temporal dynamics of DNA replication sites in mammalian cells. *J. Cell Biol.* 143:1415-25.

Maeshima, K., M. Eltsov, and U.K. Laemmli. 2005. Chromosome structure: improved immunolabeling for electron microscopy. *Chromosoma*. 114:365-75.

Maeshima, K., and U.K. Laemmli. 2003. A two-step scaffolding model for mitotic chromosome assembly. *Dev Cell*. 4:467-80.

Mahy, N.L., P.E. Perry, and W.A. Bickmore. 2002a. Gene density and transcription influence the localization of chromatin outside of chromosome territories detectable by FISH. *J Cell Biol*. 159:753-63.

Mahy, N.L., P.E. Perry, S. Gilchrist, R.A. Baldock, and W.A. Bickmore. 2002b. Spatial organization of active and inactive genes and noncoding DNA within chromosome territories. *J Cell Biol*. 157:579-89.

Manders, E.M., F.J. Verbeek, and J.A. Aten. 1993. Measurement of co-localization of objects in dual-colour confocal images. *Journal of Microscopy*. 169:375-387.

Maniotis, A.J., K. Bojanowski, and D.E. Ingber. 1997a. Mechanical continuity and reversible chromosome disassembly within intact genomes removed from living cells. *J Cell Biochem*. 65:114-30.

Maniotis, A.J., C.S. Chen, and D.E. Ingber. 1997b. Demonstration of mechanical connections between integrins, cytoskeletal filaments, and nucleoplasm that stabilize nuclear structure. *Proc Natl Acad Sci U S A*. 94:849-54.

Manuelidis, L. 1985. Individual interphase chromosome domains revealed by in situ hybridization. *Hum. Genet.* 71:288-93.

Markham, J., and J.A. Conchello. 2001. Artefacts in restored images due to intensity loss in three-dimensional fluorescence microscopy. *J Microsc*. 204:93-8.

Marko, J.F., and M.G. Poirier. 2003. Micromechanics of chromatin and chromosomes. *Biochem Cell Biol*. 81:209-20.

Marsden, M.P., and U.K. Laemmli. 1979. Metaphase chromosome structure: evidence for a radial loop model. *Cell*. 17:849-58.

Marshall, W.F., J.C. Fung, and J.W. Sedat. 1997. Deconstructing the nucleus: global architecture from local interactions. *Curr Opin Genet Dev*. 7:259-63.

Martin, C., and Y. Zhang. 2005. The diverse functions of histone lysine methylation. *Nat Rev Mol Cell Biol*. 6:838-49.

Martin, S., and A. Pombo. 2003. Transcription factories: quantitative studies of nanostructures in the mammalian nucleus. *Chromosome Res*. 11:461-70.

Martou, G., and U. De Boni. 2000. Nuclear topology of murine, cerebellar Purkinje neurons: changes as a function of development. *Exp Cell Res*. 256:131-9.

Mayer, R., A. Brero, J. von Hase, T. Schroeder, T. Cremer, and S. Dietzel. 2005. Common themes and cell type specific variations of higher order chromatin arrangements in the mouse. *BMC Cell Biol*. 6:44.

McNally, J.G., T. Karpova, J. Cooper, and J.A. Conchello. 1999. Three-Dimensional Imaging by Deconvolution Microscopy. *Methods*. 19:337-385.

Meaburn, K.J., T. Misteli, and E. Soutoglou. 2007. Spatial genome organization in the formation of chromosomal translocations. *Semin Cancer Biol*. 17:80-90.

Misteli, T. 2001. Protein dynamics: implications for nuclear architecture and gene expression. *Science*. 291:843-7.

Misteli, T. 2004. Spatial positioning; a new dimension in genome function. *Cell*. 119:153-6.

Moen, P.T., Jr., C.V. Johnson, M. Byron, L.S. Shopland, I.L. de la Serna, A.N. Imbalzano, and J.B. Lawrence. 2004. Repositioning of muscle-specific genes relative to the periphery of SC-35 domains during skeletal myogenesis. *Mol Biol Cell*. 15:197-206.

Molenaar, C., K. Wiesmeijer, N.P. Verwoerd, S. Khazen, R. Eils, H.J. Tanke, and R.W. Dirks. 2003. Visualizing telomere dynamics in living mammalian cells using PNA probes. *Embo J*. 22:6631-41.

Monneron, A., and W. Bernhard. 1969. Fine structural organization of the interphase nucleus in some mammalian cells. *J. Ultrastruct. Res.* 27:266-88.

Morey, C., N.R. Da Silva, P. Perry, and W.A. Bickmore. 2007. Nuclear reorganisation and chromatin decondensation are conserved, but distinct, mechanisms linked to Hox gene activation. *Development*. 134:909-19.

Munkel, C., R. Eils, S. Dietzel, D. Zink, C. Mehring, G. Wedemann, T. Cremer, and J. Langowski. 1999. Compartmentalization of interphase chromosomes observed in simulation and experiment. *J Mol Biol*. 285:1053-65.

Munkel, C., and J. Langowski. 1998. Chromosome structure predicted by a polymer model. *Phys. Rev. E*. 57:5888-5896.

Murmann, A.E., J. Gao, M. Encinosa, M. Gautier, M.E. Peter, R. Eils, P. Lichter, and J.D. Rowley. 2005. Local gene density predicts the spatial position of genetic loci in the interphase nucleus. *Exp Cell Res*. 311:14-26.

Musoski, S. 2005. Untersuchungen zur Lokalisation des MHC-Lokus von Chromosom 6 mittels FISH und ICC in menschlichen Fibroblasten. *In* Diplomarbeit an der Fakultät für Biologie, LMU München.

Nagel, J. 2006. Untersuchungen zur Architektur von hyperkondensiertem Chromatin in humanen Zellkernen. *In* Diplomarbeit an der Fakultät für Biologie, LMU München.

Nagele, R., T. Freeman, L. McMorrow, and H.Y. Lee. 1995. Precise spatial positioning of chromosomes during prometaphase: evidence for chromosomal order. *Science*. 270:1831-5.

Nagele, R.G., T. Freeman, J. Fazekas, K.M. Lee, Z. Thomson, and H.Y. Lee. 1998. Chromosome spatial order in human cells: evidence for early origin and faithful propagation. *Chromosoma*. 107:330-8.

Nagele, R.G., A.Q. Velasco, W.J. Anderson, D.J. McMahon, Z. Thomson, J. Fazekas, K. Wind, and H. Lee. 2001. Telomere associations in interphase nuclei: possible role in maintenance of interphase chromosome topology. *J Cell Sci*. 114:377-88.

Nakamura, H., T. Morita, and C. Sato. 1986. Structural organization of replicon domains during DNA synthetic phase in the mammalian nucleus. *Experimental Cell Research*. 165:291-297.

Nash, R.E., E. Puvion, and W. Bernhard. 1975. Perichromatin fibrils as components of rapidly labeled extranucleolar RNA. *J Ultrastruct Res*. 53:395-405.

Neri, L.M., Y. Raymond, A. Giordano, S. Capitani, and A.M. Martelli. 1999. Lamin A is part of the internal nucleoskeleton of human erythroleukemia cells. *J Cell Physiol*. 178:284-95.

Nickerson, J.A. 2001. Experimental observations of a nuclear matrix. *J Cell Sci*. 114:463-474.

Nickerson, J.A., G. Krockmalnic, K.M. Wan, and S. Penman. 1997. The nuclear matrix revealed by eluting chromatin from a cross-linked nucleus. *Proc. Natl. Acad. Sci. USA*. 94:4446-50.

O'Keefe, R.T., S.C. Henderson, and D.L. Spector. 1992. Dynamic organization of DNA replication in mammalian cell nuclei: spatially and temporally defined replication of chromosome-specific alpha-satellite DNA sequences. *J. Cell Biol.* 116:1095-110.

Okada, T.A., and D.E. Comings. 1979. Higher order structure of chromosomes. *Chromosoma*. 72:1-14.

Okada, Y., Q. Feng, Y. Lin, Q. Jiang, Y. Li, V.M. Coffield, L. Su, G. Xu, and Y. Zhang. 2005. hDOT1L links histone methylation to leukemogenesis. *Cell*. 121:167-78.

Olins, D.E., and A.L. Olins. 2003. Chromatin history: our view from the bridge. *Nat Rev Mol Cell Biol*. 4:809-14.

Parada, L.A., P.G. McQueen, and T. Misteli. 2004. Tissue-specific spatial organization of genomes. *Genome Biol*. 5:R44.

Parada, L.A., P.G. McQueen, P.J. Munson, and T. Misteli. 2002. Conservation of relative chromosome positioning in normal and cancer cells. *Curr Biol*. 12:1692-7.

Paulson, J.R., and U.K. Laemmli. 1977. The structure of histone-depleted metaphase chromosomes. *Cell*. 12:817-28.

Pawley, J.B. 2006. Handbook of biological confocal microscopy. Springer, New York.

Pederson, T. 1998. Thinking about a nuclear matrix. *J. Mol. Biol.* 277:147-59.

Pederson, T. 2000. Half a century of "the nuclear matrix". *Mol. Biol. Cell*. 11:799-805.

Pederson, T., and E. Robbins. 1970. RNA synthesis in HeLa cells. Pattern in hypertonic medium and its similarity to synthesis during G2-prophase. *J Cell Biol*. 47:734-44.

Peters, A.H., S. Kubicek, K. Mechtler, R.J. O'Sullivan, A.A. Derijck, L. Perez-Burgos, A. Kohlmaier, S. Opravil, M. Tachibana, Y. Shinkai, J.H. Martens, and T. Jenuwein. 2003. Partitioning and plasticity of repressive histone methylation states in mammalian chromatin. *Mol Cell*. 12:1577-89.

Phair, R.D., S.A. Gorski, and T. Misteli. 2004. Measurement of dynamic protein binding to chromatin in vivo, using photobleaching microscopy. *Methods Enzymol*. 375:393-414.

Phair, R.D., and T. Misteli. 2000. High mobility of proteins in the mammalian cell nucleus. *Nature*. 404:604-9.

Plehn-Dujowich, D., P. Bell, A.M. Ishov, C. Baumann, and G.G. Maul. 2000. Non-apoptotic chromosome condensation induced by stress: delineation of interchromosomal spaces. *Chromosoma*. 109:266-79.

Poirier, M.G., and J.F. Marko. 2003. Micromechanical studies of mitotic chromosomes. *Curr Top Dev Biol*. 55:75-141.

Politz, J.C. 1999. Use of caged fluorochromes to track macromolecular movement in living cells. *Trends Cell Biol.* 9:284-7.

Politz, J.C., E.S. Browne, D.E. Wolf, and T. Pederson. 1998. Intranuclear diffusion and hybridization state of oligonucleotides measured by fluorescence correlation spectroscopy in living cells. *Proc. Natl. Acad. Sci. USA*. 95:6043-8.

Politz, J.C., R.A. Tuft, T. Pederson, and R.H. Singer. 1999. Movement of nuclear poly(A) RNA throughout the interchromatin space in living cells. *Curr. Biol.* 9:285-91.

Pombo, A., and P.R. Cook. 1996. The localization of sites containing nascent RNA and splicing factors. *Exp. Cell Res.* 229:201-3.

Postberg, J., O. Alexandrova, T. Cremer, and H.J. Lipps. 2005. Exploiting nuclear duality of ciliates to analyse topological requirements for DNA replication and transcription. *J Cell Sci*. 118:3973-83.

Raap, A.K., F.M. van de Rijke, R.W. Dirks, C.J. Sol, R. Boom, and M. van der Ploeg. 1991. Bicolor fluorescence in situ hybridization to intron and exon mRNA sequences. *Exp Cell Res*. 197:319-22.

Rabl, C. 1885. Über Zelltheilung. *In* Morphologisches Jahrbuch. Vol. 10. C. Gegenbaur, editor. 214-330.

Ragoczy, T., M.A. Bender, A. Telling, R. Byron, and M. Groudine. 2006. The locus control region is required for association of the murine beta-globin locus with engaged transcription factories during erythroid maturation. *Genes Dev*. 20:1447-57.

Ragoczy, T., A. Telling, T. Sawado, M. Groudine, and S.T. Kosak. 2003. A genetic analysis of chromosome territory looping: diverse roles for distal regulatory elements. *Chromosome Res*. 11:513-25.

Reichenzeller, M., A. Burzlaff, P. Lichter, and H. Herrmann. 2000. In vivo observation of a nuclear channel-like system: evidence for a distinct interchromosomal domain compartment in interphase cells. *J. Struct. Biol.* 129:175-85.

Richter, K., M. Reichenzeller, S.M. Gorisch, U. Schmidt, M.O. Scheuermann, H. Herrmann, and P. Lichter. 2005. Characterization of a nuclear compartment shared by nuclear bodies applying ectopic protein expression and correlative light and electron microscopy. *Exp Cell Res*. 303:128-37.

Robbins, E., T. Pederson, and P. Klein. 1970. Comparison of mitotic phenomena and effects induced by hypertonic solutions in HeLa cells. *J Cell Biol*. 44:400-16.

Rougeulle, C., J. Chaumeil, K. Sarma, C.D. Allis, D. Reinberg, P. Avner, and E. Heard. 2004. Differential histone H3 Lys-9 and Lys-27 methylation profiles on the X chromosome. *Mol Cell Biol*. 24:5475-84.

Sachs, R.K., G. van den Engh, B. Trask, H. Yokota, and J.E. Hearst. 1995. A random-walk/giant-loop model for interphase chromosomes. *Proc. Natl. Acad. Sci. USA*. 92:2710-4.

Sadoni, N., M.C. Cardoso, E.H. Stelzer, H. Leonhardt, and D. Zink. 2004. Stable chromosomal units determine the spatial and temporal organization of DNA replication. *J Cell Sci*. 117:5353-65.

Sadoni, N., S. Langer, C. Fauth, G. Bernardi, T. Cremer, B.M. Turner, and D. Zink. 1999. Nuclear organization of mammalian genomes. Polar chromosome territories build up functionally distinct higher order compartments. *J. Cell Biol.* 146:1211-26.

Sadoni, N., K.F. Sullivan, P. Weinzierl, E.H. Stelzer, and D. Zink. 2001. Large-scale chromatin fibers of living cells display a discontinuous functional organization. *Chromosoma*. 110:39-51.

Sadoni, N., and D. Zink. 2004. Nascent RNA synthesis in the context of chromatin architecture. *Chromosome Res*. 12:439-51.

Saitoh, Y., and U.K. Laemmli. 1994. Metaphase chromosome structure: bands arise from a differential folding path of the highly AT-rich scaffold. *Cell*. 76:609-22.

Sakamura, T. 1927. Chromosomenforschung am frischen Material. *Protoplasma*. 1:537-565.

Santos-Rosa, H., R. Schneider, A.J. Bannister, J. Sherriff, B.E. Bernstein, N.C. Emre, S.L. Schreiber, J. Mellor, and T. Kouzarides. 2002. Active genes are tri-methylated at K4 of histone H3. *Nature*. 419:407-11.

Schardin, M., T. Cremer, H.D. Hager, and M. Lang. 1985. Specific staining of human chromosomes in Chinese hamster x man hybrid cell lines demonstrates interphase chromosome territories. *Hum Genet*. 71:281-7.

Schermelleh, L. 2003. Dynamic organization of chromosomes in the mammalian cell nucleus. *In* Dissertation an der Fakultät für Biologie, LMU München.

Schermelleh, L., I. Solovei, D. Zink, and T. Cremer. 2001. Two-color fluorescence labeling of early and mid-to-late replicating chromatin in living cells. *Chromosome Res.* 9:77-80.

Schwarz, P.M., and J.C. Hansen. 1994. Formation and stability of higher order chromatin structures. Contributions of the histone octamer. *J Biol Chem*. 269:16284-9.

Sedarat, F., E. Lin, E.D. Moore, and G.F. Tibbits. 2004. Deconvolution of confocal images of dihydropyridine and ryanodine receptors in developing cardiomyocytes. *J Appl Physiol*. 97:1098-103.

Sedat, J., and L. Manuelidis. 1978. A direct approach to the structure of eukaryotic chromosomes. *Cold Spring Harb. Symp. Quant. Biol.* 42:331-50.

Seligson, D.B., S. Horvath, T. Shi, H. Yu, S. Tze, M. Grunstein, and S.K. Kurdistani. 2005. Global histone modification patterns predict risk of prostate cancer recurrence. *Nature*. 435:1262-6.

Shav-Tal, Y., X. Darzacq, S.M. Shenoy, D. Fusco, S.M. Janicki, D.L. Spector, and R.H. Singer. 2004. Dynamics of single mRNPs in nuclei of living cells. *Science*. 304:1797-800.

Shaw, P.J., and D.J. Rawlins. 1991. The point spread function of a confocal microscope: its measurement and use in deconvolution of 3D data. *Journal of Microscopy*. 163:151-165.

Shopland, L.S., C.R. Lynch, K.A. Peterson, K. Thornton, N. Kepper, J. Hase, S. Stein, S. Vincent, K.R. Molloy, G. Kreth, C. Cremer, C.J. Bult, and T.P. O'Brien. 2006. Folding and organization of a contiguous chromosome region according to the gene distribution pattern in primary genomic sequence. *J Cell Biol*. 174:27-38.

Sobczak-Thepot, J., F. Harper, Y. Florentin, F. Zindy, C. Brechot, and E. Puvion. 1993. Localization of cyclin A at the sites of cellular DNA replication. *Exp Cell Res*. 206:43-8.

Solovei, I., N. Grandi, R. Knoth, B. Volk, and T. Cremer. 2004a. Positional changes of pericentromeric heterochromatin and nucleoli in postmitotic Purkinje cells during murine cerebellum development. *Cytogenet Genome Res*. 105:302-310.

Solovei, I., L. Schermelleh, K. During, A. Engelhardt, S. Stein, C. Cremer, and T. Cremer. 2004b. Differences in centromere positioning of cycling and postmitotic human cell types. *Chromosoma*. 112:410-23.

Spector, D.L. 2001. Nuclear domains. *J Cell Sci*. 114:2891-3.

Spector, D.L., X.D. Fu, and T. Maniatis. 1991. Associations between distinct pre-mRNA splicing components and the cell nucleus. *Embo J.* 10:3467-81.

Stadler, S., V. Schnapp, R. Mayer, S. Stein, C. Cremer, C. Bonifer, T. Cremer, and S. Dietzel. 2004. The architecture of chicken chromosome territories changes during differentiation. *BMC Cell Biol*. 5:44.

Strick, R., P.L. Strissel, K. Gavrilov, and R. Levi-Setti. 2001. Cation-chromatin binding as shown by ion microscopy is essential for the structural integrity of chromosomes. *J Cell Biol*. 155:899-910.

Su, R.C., K.E. Brown, S. Saaber, A.G. Fisher, M. Merkenschlager, and S.T. Smale. 2004. Dynamic assembly of silent chromatin during thymocyte maturation. *Nat Genet*. 36:502-6.

Sullivan, H.S. 1896. The tall office building artistically considered. *Lippincott's Magazine*.

Sun, H.B., J. Shen, and H. Yokota. 2000. Size-dependent positioning of human chromosomes in interphase nuclei. *Biophys. J.* 79:184-90.

Tanabe, H., F.A. Habermann, I. Solovei, M. Cremer, and T. Cremer. 2002a. Non-random radial arrangements of interphase chromosome territories: evolutionary considerations and functional implications. *Mutat Res*. 504:37-45.

Tanabe, H., K. Kupper, T. Ishida, M. Neusser, and H. Mizusawa. 2005. Inter- and intra-specific gene-density-correlated radial chromosome territory arrangements are conserved in Old World monkeys. *Cytogenet Genome Res*. 108:255-61.

Tanabe, H., S. Muller, M. Neusser, J. von Hase, E. Calcagno, M. Cremer, I. Solovei, C. Cremer, and T. Cremer. 2002b. Evolutionary conservation of chromosome territory arrangements in cell nuclei from higher primates. *Proc Natl Acad Sci U S A*. 99:4424-9.

Tashiro, S., J. Walter, A. Shinohara, N. Kamada, and T. Cremer. 2000. Rad51 accumulation at sites of DNA damage and in postreplicative chromatin. *J. Cell Biol.* 150:283-91.

Thoma, F., T. Koller, and A. Klug. 1979. Involvement of histone H1 in the organization of the nucleosome and of the salt-dependent superstructures of chromatin. *J Cell Biol*. 83:403-27.

Thormeyer, T. 2005. Untersuchungen zur Lokalisation der nukleären Matrix in Zellkernen nach induzierter Chromatinkondensation. *In* Diplomarbeit an der Fakultät für Biologie, LMU München.

Trentani, A., P.S. Testillano, M.C. Risueno, and M. Biggiogera. 2003. Visualization of transcription sites at the electron microscope. *Eur J Histochem*. 47:195-200.

van der Voort, H.T.M., and K.C. Strasters. 1995. Restoration of confocal images for quantitative image analysis. *J Microsc*. 178:165-181.

van Driel, R., and P. Fransz. 2004. Nuclear architecture and genome functioning in plants and animals: what can we learn from both? *Exp Cell Res*. 296:86-90.

Varambally, S., S.M. Dhanasekaran, M. Zhou, T.R. Barrette, C. Kumar-Sinha, M.G. Sanda, D. Ghosh, K.J. Pienta, R.G. Sewalt, A.P. Otte, M.A. Rubin, and A.M. Chinnaiyan. 2002. The polycomb group protein EZH2 is involved in progression of prostate cancer. *Nature*. 419:624-9.

Vasilic, B., and F.W. Wehrli. 2005. A novel local thresholding algorithm for trabecular bone volume fraction mapping in the limited spatial resolution regime of in vivo MRI. *IEEE Trans Med Imaging*. 24:1574-85.

Verschure, P.J., I. Van Der Kraan, J.M. Enserink, M.J. Mone, E.M. Manders, and R. Van Driel. 2002. Large-scale chromatin organization and the localization of proteins involved in gene expression in human cells. *J Histochem Cytochem*. 50:1303-12.

Verschure, P.J., I. van der Kraan, E.M. Manders, D. Hoogstraten, A.B. Houtsmuller, and R. van Driel. 2003. Condensed chromatin domains in the mammalian nucleus are accessible to large macromolecules. *EMBO Rep*. 4:861-6.

Verschure, P.J., I. van Der Kraan, E.M. Manders, and R. van Driel. 1999. Spatial relationship between transcription sites and chromosome territories. *J. Cell Biol.* 147:13-24.

Versteeg, R., B.D. van Schaik, M.F. van Batenburg, M. Roos, R. Monajemi, H. Caron, H.J. Bussemaker, and A.H. van Kampen. 2003. The human transcriptome map reveals extremes in gene density, intron length, GC content, and repeat pattern for domains of highly and weakly expressed genes. *Genome Res*. 13:1998-2004.

Vinogradov, A.E. 1998. Buffering: a possible passive-homeostasis role for redundant DNA. *J Theor Biol*. 193:197-9.

Vinogradov, A.E. 2005. Genome size and chromatin condensation in vertebrates. *Chromosoma*. 113:362-9.

Visser, A.E., F. Jaunin, S. Fakan, and J.A. Aten. 2000. High resolution analysis of interphase chromosome domains. *J. Cell Sci.* 113:2585-93.

Volpi, E.V., E. Chevret, T. Jones, R. Vatcheva, J. Williamson, S. Beck, R.D. Campbell, M. Goldsworthy, S.H. Powis, J. Ragoussis, J. Trowsdale, and D. Sheer. 2000. Large-scale chromatin organization of the major histocompatibility complex and other regions of human chromosome 6 and its response to interferon in interphase nuclei. *J. Cell Sci.* 113:1565-76.

Vourc'h, C., D. Taruscio, A.L. Boyle, and D.C. Ward. 1993. Cell cycle-dependent distribution of telomeres, centromeres, and chromosome-specific subsatellite domains in the interphase nucleus of mouse lymphocytes. *Exp. Cell Res.* 205:142-51.

Wallace, W., L.H. Schaefer, and J.R. Swedlow. 2001. A workingperson's guide to deconvolution in light microscopy. *Biotechniques*. 31:1076-8, 1080, 1082 passim.

Walter, J., L. Schermelleh, M. Cremer, S. Tashiro, and T. Cremer. 2003. Chromosome order in HeLa cells changes during mitosis and early G1, but is stably maintained during subsequent interphase stages. *J Cell Biol*. 160:685-97.

Wanner, G., and H. Formanek. 2000. A new chromosome model. *J Struct Biol*. 132:147-61.

Wanner, G., E. Schroeder-Reiter, and H. Formanek. 2005. 3D analysis of chromosome architecture: advantages and limitations with SEM. *Cytogenet Genome Res*. 109:70-8.

Wansink, D.G., W. Schul, I. van der Kraan, B. van Steensel, R. van Driel, and L. de Jong. 1993. Fluorescent labeling of nascent RNA reveals transcription by RNA polymerase II in domains scattered throughout the nucleus. *J. Cell Biol.* 122:283-93.

Weierich, C., A. Brero, S. Stein, J. von Hase, C. Cremer, T. Cremer, and I. Solovei. 2003. Three-dimensional arrangements of centromeres and telomeres in nuclei of human and murine lymphocytes. *Chromosome Res*. 11:485-502.

Weise, A., H. Starke, A. Heller, H. Tonnies, M. Volleth, M. Stumm, S. Gabriele, A. Nietzel, U. Claussen, and T. Liehr. 2002. Chromosome 2 aberrations in clinical cases characterised by high resolution multicolour banding and region specific FISH probes. *J Med Genet*. 39:434-9.

Williams, R.R., S. Broad, D. Sheer, and J. Ragoussis. 2002. Subchromosomal positioning of the epidermal differentiation complex (EDC) in keratinocyte and lymphoblast interphase nuclei. *Exp Cell Res*. 272:163-75.

Williams, R.R., and A.G. Fisher. 2003. Chromosomes, positions please! *Nat Cell Biol*. 5:388-90.

Wischnitzer, S. 1973. The submicroscopic morphology of the interphase nucleus. *Int. Rev. Cytol.* 34:1-48.

Wolfe, S.L. 1993. Molecular and Cellular Biology. Wadsworth, Belmont.

Woodcock, C.L., and S. Dimitrov. 2001. Higher-order structure of chromatin and chromosomes. *Curr Opin Genet Dev*. 11:130-5.

Yi, Q., and M.G. Coppolino. 2006. Automated classification and quantification of F-actin-containing ruffles in confocal micrographs. *Biotechniques*. 40:745-6, 748, 750 passim.

Yokota, H., G. van den Engh, J.E. Hearst, R.K. Sachs, and B.J. Trask. 1995. Evidence for the organization of chromatin in megabase pair-sized loops arranged along a random walk path in the human G0/G1 interphase nucleus. *J. Cell Biol.* 130:1239-49.

Zimmerman, S.B., and A.P. Minton. 1993. Macromolecular crowding: biochemical, biophysical, and physiological consequences. *Annu Rev Biophys Biomol Struct*. 22:27-65.

Zink, D., T. Cremer, R. Saffrich, R. Fischer, M.F. Trendelenburg, W. Ansorge, and E.H. Stelzer. 1998. Structure and dynamics of human interphase chromosome territories in vivo. *Hum Genet*. 102:241-51.

Zinner, R., H. Albiez, J. Walter, A.H. Peters, T. Cremer, and M. Cremer. 2006. Histone lysine methylation patterns in human cell types are arranged in distinct three-dimensional nuclear zones. *Histochem Cell Biol*. 125:3-19.

Zirbel, R.M., U.R. Mathieu, A. Kurz, T. Cremer, and P. Lichter. 1993. Evidence for a nuclear compartment of transcription and splicing located at chromosome domain boundaries. *Chromosome Res*. 1:93-106.

Zunhammer, A. 2006. Untersuchung zur Lokalisation von Histonmodifikationen in Zellkernen mit hyperkondensiertem Chromatin. *In* Diplomarbeit an der Fakultät für Biologie, LMU München.

DANKSAGUNG

An erster Stelle möchte ich meinem Doktorvater Herrn Prof. Thomas Cremer für sein großes Vertrauen, seine Bemühungen und Unterstützungen jeglicher Art sehr herzlich danken. Die Zeit in seiner Arbeitsgruppe war eine große Erfahrung für mich in wissenschaftlicher wie auch persönlicher Hinsicht und wird mir in prägender Erinnerung bleiben.

Des Weiteren danke ich Herrn Prof. Peter Becker für die Übernahme des Zweitgutachtens.

Sehr zum erfolgreichen Gelingen dieser Arbeit haben vor allem die in dieser Arbeitsgruppe etablierte russisch-heidische Laborорganisation, das jederzeit verfügbare zellkernige Assistenten- und Postdocwissen, sowie eine ausgefeilte Finanzjonglage beigetragen. In diesem Zusammenhang möchte ich speziellen Dank an meine langjährige Tischnachbarin richten: für Ihr Ringen mit FISH on HCC, für das Korrekturlesen dieser Arbeit sowie für die vielen schönen wissenschaftlichen aber auch privaten Diskussionen.

Besonders spannend war die Zellkernforschung, wenn man sich lanctotisch dem Einfluss von Energie und Zeit näherte und danach vogelwuid auf die Baumdinge spielte. Großer Dank für Ihre HCC-Arbeiten geht an die diplomierte mazedonisch-sächsisch-bayerisch-badische Fraktion. Vielen Dank auch an diejenigen Kollegen ohne welche die Dekonvolution konfokaler Bilder bis heute nononoch nicht convincing wäre.

Das Glück zu haben mit Kolleg(inn)en arbeiten zu dürfen, die zum Teil aber eigentlich sogar Freunde wurden ist eine weitere schöne Erfahrung, die ich in den letzten Jahren machen durfte. Die ungezählten Male martinierter Unternehmungen im Lehel oder Nymphenburg, die kulinarischen Exkursionen nach Nimes, gemächtlichen Aufenthalte in Lausanne, Reading Kicker in London oder Malkurse in Miesbach, unzählige Geburtstagsfeiern (komischerweise wurde fast nie jemand 30?) wie auch hotzenwälder Gesangsabende, geräucherte Fruchtsnacks hinter den Volieren und Millionen kleiner Brauner machten die Zeit als Doktorand auch neben der Wissenschaft äußerst angenehm! Vielen Dank Euch allen!

An dieser Stelle möchte ich meinen lieben Eltern danken, die mir meinen Lebensweg in so sichere Bahnen gelegt haben, dass das ja was werden musste.

Und lieben Dank an Meike und Lina, die stets ganz wesentlich an allem beteiligt waren.

Ehrenwörtliche Versicherung

Hiermit bestätige ich, dass ich die vorliegende Dissertation selbständig und nur mit den angegebenen Materialien und Quellen durchgeführt habe.

München, den 5. April 2007

Heiner Albiez

Erklärung über frühere Promotionsversuche

Hiermit bestätige ich, dass ich vor dieser Arbeit keine anderen Promotionsversuche unternommen habe. Dies ist meine erste Dissertation.

München, den 5. April 2007

Heiner Albiez